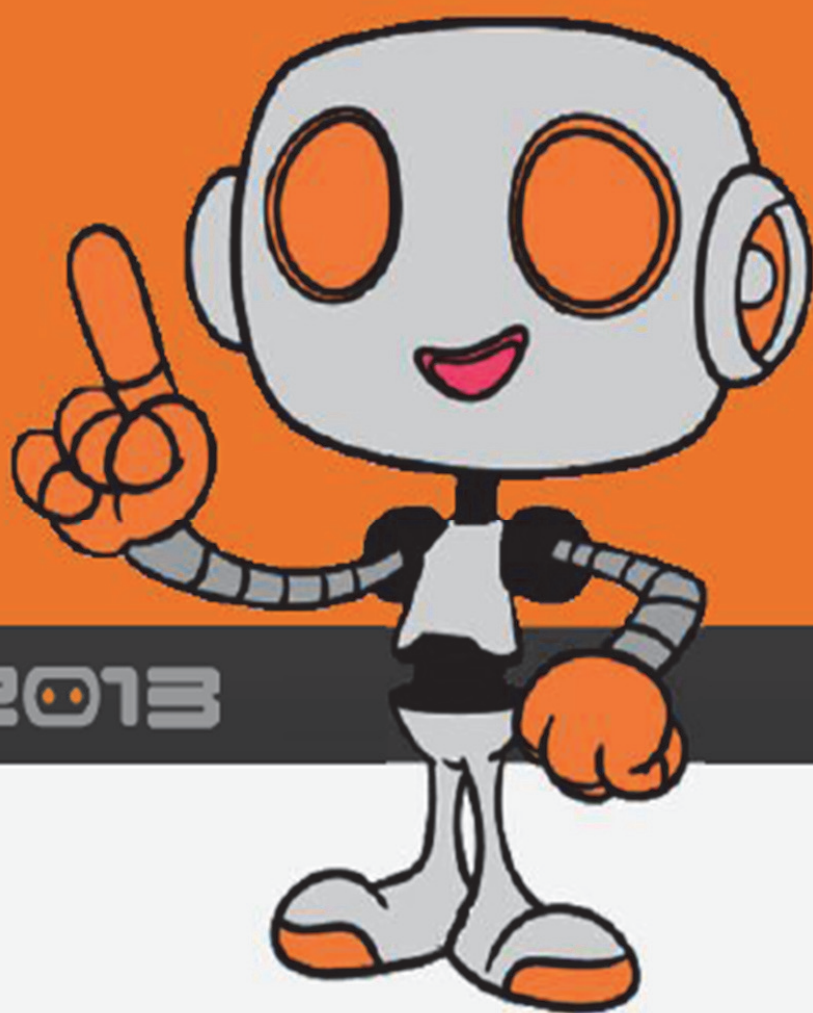


PROCEEDINGS OF THE  
13TH INTERNATIONAL CONFERENCE  
ON AUTONOMOUS ROBOT SYSTEMS AND COMPETITIONS

24 OF APRIL



ROBOTICA 2013

ISBN: 978-989-97531-2-9

# Proceedings of the 13<sup>th</sup> International Conference on Mobile Robots and Competitions

Edited by

João M. F. Calado, Luís Paulo Reis and Rui Paulo Rocha

24<sup>th</sup> April, 2013

Instituto Superior de Engenharia de Lisboa

Polytechnic Institute of Lisbon

Portugal

ISBN: 978-989-97531-2-9

*© 2013 IEEE. Personal use of this material is permitted. Permission from IEEE must be obtained for all other uses, in any current or future media, including reprinting/republishing this material for advertising or promotional purposes, creating new collective works, for resale or redistribution to servers or lists, or reuse of any copyrighted component of this work in other works.*

Organizers:



Sponsors:



Patrons:



**Hosted:**



**Cover Design:**

Catarina Sampaio

**Secretariat:**

Maria da Conceição Ribeiro

**Website Design:**

Sérgio Fernandes Palma

**Website:**

<http://www.dem.isel.pt/Robotica2013>

**Organizing Committee**

João M. Ferreira Calado  
[jcalado@dem.isel.ipl.pt](mailto:jcalado@dem.isel.ipl.pt)  
 Instituto Superior de Engenharia de  
 Lisboa  
 Área Departamental de Engenharia  
 Mecânica

Luís Paulo Reis  
[lpreis@dsi.uminho.pt](mailto:lpreis@dsi.uminho.pt)  
 Universidade do Minho  
 Dep. Sistemas de informação  
 Lab. Inteligência Artificial e Ciência  
 de Computadores

Rui Paulo Rocha  
[rprocha@isr.uc.pt](mailto:rprocha@isr.uc.pt)  
 Universidade de Coimbra  
 Dep. de Engenharia Eletrotécnica e  
 de Computadores  
 Instituto de Sistemas e Robótica

**Steering Committee**

Alexandro De Luca (URoma-IT)  
 Bruno Siciliano (UNINA-IT)  
 Toshio Fukuda (UNagoya-JP)

Alicia Casals (UPC-SP)  
 Hideki Hashimoto (UTokyo-JP)

**International Program Committee**

A. Fernando Ribeiro (UMinho-PT)  
 Alexandre Simões (UNESP-BR)  
 Alicia Casals (UPC-SP)  
 Alexandro De Luca (URoma-IT)  
 André Marcato (UJuizFora-BR)  
 Andreas BirK (UJacobs-D)  
 Angel Sappa (UAB-SP)  
 Aníbal Matos (FEUP-PT)  
 António Bandera (UM-SP)  
 António P. Moreira (FEUP-PT)  
 António Pascoal (IST-PT)  
 Armando Sousa (FEUP-PT)  
 Bernardo Cunha (UAveiro-PT)  
 Bruno Siciliano (UNIMA-IT)  
 Carlos Cardeira (IST-PT)  
 Carlos Carreto (IPG-PT)  
 Danilo Tardioli (UZaragoza-SP)  
 Denis Wolf (USão Paulo-BR)  
 Dimos Dimarogonas (KTH-S)  
 Enric Cervera (UJaume I-SP)  
 Estela Bicho (UMinho-PT)  
 Fernando Melício (ISEL-PT)  
 Fernando Pereira (FEUP-PT)  
 Flavio Tonidandel (CUFEI-BR)  
 Gabriel Oliver (UIB-SP)  
 G. Kratzschmar (UBonn-Rhein-D)  
 Gil Lopes (UMinho-PT)

Hans Du Buf (UAlgarve-PT)  
 Helder Araújo (UCoimbra-PT)  
 Hideki Hashimoto (Utokyo-JP)  
 Hugo Costelha (IPLeiria-PT)  
 Isabel Ribeiro (IST-PT)  
 João Calado (ISEL-PT)  
 João Palma (ISEL-PT)  
 João Pinto (IST-PT)  
 João Sequeira (IST-PT)  
 Jorge Dias (UCoimbra-PT)  
 Jorge Ferreira (UAveiro-PT)  
 Jorge Lobo (UCoimbra-PT)  
 Jorge Pais (ISEL-PT)  
 José Igreja (ISEL-PT)  
 José Lima (IPBragança-PT)  
 José Luís Azevedo (UAveiro-PT)  
 José Sá da Costa (IST-PT)  
 José Tenreiro Machado (ISEP-PT)  
 Jun Ota (UTokyo-JP)  
 Luca Locchi (URome-IT)  
 Lucia Pallottino (UPisa-IT)  
 Luís Almeida (FEUP-PT)  
 Luís Gomes (UNINOVA-PT)  
 Luís Louro (UMinho-PT)  
 Luís Merino (UPOLaive-SP)  
 Luís Mota (ISCTE-PT)  
 Luís Paulo Reis (UMinho-PT)

Luís S. Lopes (UAveiro-PT)  
 Luiz Chaimowicz (UFMG-BR)  
 Manuel Lopes (INRIA-FR)  
 Manuel Silva (ISEP-PT)  
 Mário Mendes (ISEL-PT)  
 Nuno Lau (UAveiro-PT)  
 Nuno Ferreira (ISEC-PT)  
 Norberto Pires (UCoimbra-PT)  
 Patrícia Vargas (UHeriot-Watt-UK)  
 Patrício Nebot (UJaume-I-SP)  
 Paulo Costa (FEUP-PT)  
 Paulo Fiorini (UNIVR-IT)  
 Paulo Gonçalves (IPCB-PT)  
 Paulo Menezes (UCoimbra-PT)  
 Paulo Oliveira (IST-PT)  
 Pedro U. Lima (IST-PT)  
 René van de Molengraft (TUE-NL)  
 Reinaldo Bianchi (FEI-BR)  
 Rodrigo Braga (USCatarina-BR)  
 Rodrigo Ventura (IST-PT)  
 Rui Cortesão (UCoimbra-PT)  
 Rui P. Rocha (UCoimbra-PT)  
 Sérgio Monteiro (UMinho-PT)  
 Toshio Fukuda (UNagoya-JP)  
 Urbano Nunes (UCoimbra-PT)  
 Vicente Matellan (ULEon-SP)  
 Vítor Santos (UAveiro-PT)

**Additional Reviewers**

Aamir Ahmad (IST/ISR-PT)  
 R. Auzuir Alexandria (UFCeará-BR)  
 José Carlos Castillo (UTrier-D)  
 Eliana Costa e Silva (UPT-PT)  
 Jonathan Grizou (EPFL-CH)

Yanjiang Huang (UTokyo-JP)  
 Simone Martini (UBologna-IT)  
 E. Montijano (CUDZaragoza-SP)  
 Gustavo Pessin (USão Paulo-BR)  
 Cristiano Premevida (UC/ISR-PT)

João Quintas (UC/ISR-PT)  
 Nima Shafii (FEUP-PT)  
 Pedro Torres (IPCB-PT)  
 Joaquín Sospedra (UJaume I-SP)

## Welcome Message

Welcome to the 13<sup>th</sup> International Conference on Autonomous Robot Systems and Competitions. Welcome to ISEL – Instituto Superior de Engenharia de Lisboa, which is the Engineering School of the Polytechnic Institute of Lisbon, Lisbon, Portugal.

This is the 2013's edition of the international scientific meeting of the Portuguese National Festival of Robotics (ROBOTICA 2013). It aims to disseminate the most advanced knowledge and to promote discussion of theories, methods and experiences in areas of relevance to the knowledge domains of Mobile Robotics and Robotic Competitions.

A total of 37 papers were submitted in response to the call for contributions. After a double blind review process, 13 papers have been accepted as regular papers for oral presentation and 9 papers have been accepted for short presentation plus poster presentation. The best papers will be selected to be published as an extended version in the Journal of Intelligent & Robotic Systems from Springer, indexed by Thomson ISI Web of Knowledge (IF=0.83). All accepted contributions are included in the proceedings book. The conference program also includes a keynote speaker, Prof. Dr. Wolfram Burgard, from the Department of Computer Science of Freiburg University, Germany, being also the Head of the Research Lab for Autonomous Intelligent Systems.

The conference is kindly sponsored by the SPR - Sociedade Portuguesa de Robótica, IEEE Robotics and Automation Society, Portugal Section RA Chapter and Instituto Politécnico de Lisboa.

We would like to thank the invaluable contribution of the Conference Patrons, Caixa Geral de Depósitos and Festo Portugal, as well as Sponsors, Steering Committee Members, International Program Committee Members, External Reviewers, Keynote Speaker, Sessions Chairs and Authors. We also thank and appreciate the collaboration of Sofia Duarte from Polytechnic Institute of Lisbon in managing the registrations and the corresponding fees payment, the collaboration of Maria da Conceição Ribeiro from ISEL in managing all administrative matters and some other local arrangements and the collaboration of Sérgio Fernandes Palma from ISEL in supporting the web site development and update. Thank you all for participating in this conference hoping you enjoy and feel it as a highly productive and sociable event.

João M. Ferreira Calado

Luís Paulo Reis

Rui Paulo Rocha

## Conference Program

**Venue:** Main Auditorium, ISEL – Instituto Superior de Engenharia de Lisboa

**Wednesday 24<sup>th</sup> April 2013**

08:15 – 08:45 **Registration**

08:45 – 09:00 **Welcome Session**

---

**09:00 – 10:00 Session 1: Keynote Speaker**

*Chair:* Luís Paulo Reis

---

09:00 – 10:00 Prof. Dr. Wolfram Burgard

*Probabilistic Techniques for Mobile Robot Navigation*

---

**10:00 – 11:15 Session 2: Perception / Educational Robotics**

*Chair:* João Calado

---

10:00 – 10:25 Kai Häussermann, Oliver Zweigle and Paul Levi. *A Framework for Anomaly Detection of Robot Behaviors.*

10:25 – 10:50 André Araújo, David Portugal, Micael Couceiro and Rui P. Rocha. *Integrating Arduino-based Educational Mobile Robots in ROS.*

10:50 – 11:15 Arthur Miranda Neto, Alessandro Correa Victorino, Isabelle Fantoni, Douglas Eduardo Zampieri and Janito Vaqueiro Ferreira. *Image Processing Using Pearson's Correlation Coefficient: Applications on Autonomous Robotics.*

---

**11:15 – 11:30 Coffee Break**

---

**11:30 – 13:10 Session 3: Humanoid Robotics / Human-Robot Interaction**

*Chair:* Pedro Lima

---

11:30 – 11:55 Koichi Koganezawa and Takumi Tamamoto. *Multi-Joint Gripper with Stiffness Adjuster.*

11:55 – 12:20 Brígida Mónica Faria, Luís Paulo Reis and Nuno Lau. *Manual, Automatic and Shared Methods for Controlling an Intelligent Wheelchair: Adaptation to Cerebral Palsy Users.*

12:20 – 12:45 Nikolaos Kofinas, Emmanouil Orfanoudakis and Michail Lagoudakis. *Complete Analytical Inverse Kinematics for NAO.*

12:45 – 13:10 Paulo Gonçalves, Pedro Torres, Fábio Santos, Ruben António, Nuno Catarino and Jorge Martins. *On the Development and Simulation of a Robotic Ultrasound Guided System for Orthopedic Surgical Procedures.*

---

**13:10 – 14:30 Lunch**

---

**14:30 – 15:45 Session 4: Localization, Mapping, and Navigation (Part I)**

*Chair:* Rui P. Rocha

---

14:30 – 14:55 Francisco Mateus Campos, Luís Correia and João Calado. *An Evaluation of Local Feature Combiners for Robot Visual Localization.*

14:55 – 15:20 Hugo Silva, Alexandre Bernardino and Eduardo Silva. *Combining Sparse and Dense Methods in 6D Visual Odometry.*

15:20 – 15:45 Fernando Carreira, João Calado, Carlos Carreira and Paulo Oliveira. *Enhanced PCA-Based Localization Using Depth Maps with Missing Data.*

---

### 15:45 – 16:30 Session 5: Posters Short Presentations

Chair: Luís Paulo Reis

---

15:45 – 15:50 Gustavo Corrente, João Cunha, Ricardo Sequeira and Nuno Lau. *Cooperative Robotics: Passes in Robotic Soccer.*

15:50 – 15:55 Anže Troppan, Eduardo Guerreiro, Francesco Celiberti, Gonçalo Santos, Aamir Ahmad and Pedro U. Lima. *Unknown-Color Spherical Object Detection and Tracking.*

15:55 – 16:00 Rui Ferreira, Nima Shafii, Nuno Lau, Luís Paulo Reis and Abbas Abdolmaleki. *Diagonal Walk Reference Generator based on Fourier Approximation of ZMP Trajectory.*

16:00 – 16:05 Frank Hoeller, Timo Röhling and Dirk Schulz. *Collective Motion Pattern Scaling for Improved Open-Loop Off-Road Navigation.*

16:05 – 16:10 Paulo Alves, Hugo Costelha and Carlos Neves. *Localization and Navigation of a Mobile Robot in an Office-like Environment.*

16:10 – 16:15 Zhenli Lu. *Design of a 3DOF Passive Rotating Platform for the Adaptive Motion Planning of a Single-Legged Robot*

16:15 – 16:20 João Ribeiro, Rui Serra, Nuno Nunes, Hugo Silva and José Almeida. *EKF-based Visual Self-Calibration Tool for Robots with Rotating Directional Cameras.*

16:20 – 16:25 Pedro Pinto, Ana Tomé and Vitor Santos. *Visual Detection of Vehicles Using a Bag-of-Features Approach.*

16:25 – 16:30 Daniel Di Marco, Oliver Zweigle and Paul Levi. *Base Pose Correction using Shared Reachability Maps for Manipulation Tasks.*

---

### 16:30 – 17:15 Coffee Break and Poster Session

### 17:15 – 18:30 Session 6: Localization, Mapping, and Navigation (Part II)

Chair: Carlos Carreira

---

17:15 – 17:40 Alfredo Martins, Guilherme Amaral, André Dias, Carlos Almeida, José Almeida and Eduardo Silva. *TIGRE: An Autonomous Ground Robot for Outdoor Exploration.*

17:40 – 18:05 Andry Pinto, António P. Moreira and Paulo Costa. *Robot@Factory: Localization Method Based on Map-Matching and Particle Swarm Optimization.*

18:05 – 18:30 André Dias, José Almeida, Pedro Lima and Eduardo Silva. *Multi-Robot Cooperative Stereo for Outdoor Scenarios.*

---

### 18:30 – 18:45 Closing Session

---

### 20:00 – 22:30 Conference Dinner / Award Ceremony

---

Notes: 25min are allocated per oral presentation for regular papers, including Q&A. 5min are allocated per oral short presentation for posters.

## Table of Contents

Cover .....	i
Organizers/Sponsors/Patrons .....	ii
Committees .....	iv
Welcome Message .....	v
Conference Program .....	vi
Table of Contents .....	viii
KEYNOTE – Probabilistic Techniques for Mobile Robot Navigation.....	1
<i>Wolfram Burgard</i>	
A Framework for Anomaly Detection of Robot Behaviors.....	2
<i>Kai Häussermann, Oliver Zweigle and Paul Levi</i>	
Integrating Arduino-based Educational Mobile Robots in ROS .....	8
<i>André Araújo, David Portugal, Micael Couceiro and Rui P. Rocha</i>	
Image Processing Using Pearson’s Correlation Coefficient: Applications on Autonomous Robotics .....	14
<i>Arthur Miranda Neto, Alessandro Correa Victorino, Isabelle Fantoni, Douglas Eduardo Zampieri and Janito Vaqueiro Ferreira</i>	
Multi-Joint Gripper with Stiffness Adjuster.....	20
<i>Koichi Koganezawa and Takumi Tamamoto</i>	
Manual, Automatic and Shared Methods for Controlling an Intelligent Wheelchair: Adaptation to Cerebral Palsy Users .....	26
<i>Brígida Mónica Faria, Luís Paulo Reis and Nuno Lau</i>	
Complete Analytical Inverse Kinematics for NAO .....	32
<i>Nikolaos Kofinas, Emmanouil Orfanoudakis and Michail Lagoudakis</i>	
On the Development and Simulation of a Robotic Ultrasound Guided System for Orthopedic Surgical Procedures .....	38
<i>Paulo Gonçalves, Pedro Torres, Fábio Santos, Ruben António, Nuno Catarino and Jorge Martins</i>	
An Evaluation of Local Feature Combiners for Robot Visual Localization .....	44
<i>Francisco Mateus Campos, Luís Correia and João Calado</i>	
Combining Sparse and Dense Methods in 6D Visual Odometry .....	50
<i>Hugo Silva, Alexandre Bernardino and Eduardo Silva</i>	
Enhanced PCA-Based Localization Using Depth Maps with Missing Data .....	56
<i>Fernando Carreira, João Calado, Carlos Cardeira and Paulo Oliveira</i>	

TIGRE: An Autonomous Ground Robot for Outdoor Exploration .....	64
<i>Alfredo Martins, Guilherme Amaral, André Dias, Carlos Almeida, José Almeida and Eduardo Silva</i>	
Robot@Factory: Localization Method Based on Map-Matching and Particle Swarm Optimization .....	70
<i>Andry Pinto, António P. Moreira and Paulo Costa</i>	
Multi-Robot Cooperative Stereo for Outdoor Scenarios .....	76
<i>André Dias, José Almeida, Pedro Lima and Eduardo Silva</i>	
Cooperative Robotics: Passes in Robotic Soccer .....	82
<i>Gustavo Corrente, João Cunha, Ricardo Sequeira and Nuno Lau</i>	
Unknown-Color Spherical Object Detection and Tracking .....	88
<i>Anže Troppan, Eduardo Guerreiro, Francesco Celiberti, Gonçalo Santos, Aamir Ahmad and Pedro U. Lima</i>	
Diagonal Walk Reference Generator based on Fourier Approximation of ZMP Trajectory .....	94
<i>Rui Ferreira, Nima Shafii, Nuno Lau, Luís Paulo Reis and Abbas Abdolmaleki</i>	
Collective Motion Pattern Scaling for Improved Open-Loop Off-Road Navigation .....	100
<i>Frank Hoeller, Timo Röhling and Dirk Schulz</i>	
Localization and Navigation of a Mobile Robot in an Office-like Environment .....	106
<i>Paulo Alves, Hugo Costelha and Carlos Neves</i>	
Design of a 3DOF Passive Rotating Platform for the Adaptive Motion Planning of a Single-Legged Robot... ..	112
<i>Zhenli Lu</i>	
EKF-based Visual Self-Calibration Tool for Robots with Rotating Directional Cameras .....	118
<i>João Ribeiro, Rui Serra, Nuno Nunes, Hugo Silva and José Almeida</i>	
Visual Detection of Vehicles Using a Bag-of-Features Approach .....	124
<i>Pedro Pinto, Ana Tomé and Vitor Santos</i>	
Base Pose Correction using Shared Reachability Maps for Manipulation Tasks .....	128
<i>Daniel Di Marco, Oliver Zweigle and Paul Levi</i>	

# Probabilistic Techniques for Mobile Robot Navigation

Wolfram Burgard  
Institut für Informatik  
Technische Fakultät  
Albert-Ludwigs-Universität Freiburg  
Georges-Köhler-Allee, Geb. 079  
D-79110 Freiburg, Germany  
burgard@informatik.uni-freiburg.de



## Abstract

Probabilistic approaches have been discovered as one of the most powerful approaches to highly relevant problems in mobile robotics including perception and robot state estimation. Major challenges in the context of probabilistic algorithms for mobile robot navigation lie in the questions of how to deal with highly complex state estimation problems and how to control the robot so that it efficiently carries out its task. In this talk, I will present recently developed techniques for efficiently learning a map of an unknown environment with a mobile robot. I will also describe how this state estimation problem can be solved more effectively by actively controlling the robot. For all algorithms I will present experimental results that have been obtained with mobile robots in real-world environments.

## Curriculum Vitae

Wolfram Burgard is a professor for computer science at the University of Freiburg, Germany where he heads the Laboratory for Autonomous Intelligent Systems. He studied Computer Science at the University of Dortmund and received his Ph.D. degree in computer science from the University of Bonn in 1991. His areas of interest lie in artificial intelligence and mobile robots. In the past, Wolfram Burgard and his group developed several innovative probabilistic techniques for robot navigation and control. They cover different aspects including localization, map-building, path planning, and exploration. He received the prestigious Gottfried Wilhelm Leibniz Prize in 2009 and an advanced ERC grant in 2010. He is fellow of the AAAI and of the ECCAI.

# A Framework for Anomaly Detection of Robot Behaviors

Kai Häussermann, Oliver Zweigle, Paul Levi

IPVS - Department of Image Understanding, University of Stuttgart, Universitätsstr. 38, 70569 Stuttgart, Germany  
email: haeussermann | zweigle | levi@ipvs.uni-stuttgart.de

**Abstract**—Autonomous mobile robots are designed to behave appropriately in changing real-world environments without human intervention. In order to satisfy the requirements of *autonomy*, the robots have to cope with unknown settings and issues of uncertainties in dynamic and complex environments. A first step is to provide a robot with cognitive capabilities and the ability of self-examination to detect behavioral abnormalities. Unfortunately, most existing anomaly recognition systems are neither suitable for the domain of robotic behavior nor well generalizable. In this work a novel spatial-temporal anomaly detection framework for robotic behaviors is introduced which is characterized by its high level of generalization, the semi-supervised manner and its high flexibility in application.

## I. INTRODUCTION

Independent of the field of robotic application, e.g. domestic-, military-, or space-robots, successful operations require robust control algorithms and behaviors. Due to the high dynamics and the unstructured nature of real-world environments, it is nearly impossible to pre-program all potential plans or consider all possible exceptions. Because of this impracticality, autonomous robots that interact in real-world environments urgently require cognitive skills to manage and detect hardware failures [1]. For instance, assume a six-wheeled mobile robot that got stuck because of a broken wheel. Instead of ending up in a failure state, the robot could adapt the motor control behavior to substitute the damaged wheel and to get out of the situation [2]. But first of all, the robot has to detect the unexpected situation and the behavioral abnormality. In this work we define behavioral abnormalities (or short *anomalies*) as patterns in observed data that do not fit to the common behaviors. The goal of the anomaly detection framework is a spatial-temporal comparison of the observation with behavioral models to check whether something has gone wrong during the execution. In contrast to the common domain of anomaly detection systems, as credit card fraud or cyber-intrusion, the proposed framework has to cope with several factors that result in uncertainty. The most typical reason for uncertainty in robotics is a noisy observation based on low-quality, contaminated or broken sensors. Further uncertainties arise due to imperfect or limited world-modeling, occlusions or in-motion unsharpness during the visual observation of a movement. In order to respect the underlying uncertainty, the framework employs probabilistic reasoning and obtains traceable conclusions.

To achieve a highly general anomaly detection framework, which is able to cope with uncertainties adequately and which

is independent of the underlying robot platform and the number and kinds of sensors, we propose to couple Kohonen-Feature Maps (*SOM*) [3] with the concepts of Probabilistic Graphical Models (*PGM*) [4].

### A. Related Work

All existing anomaly detection methods can be classified into three subclasses. *Supervised anomaly detection methods* assume the availability of pre-labeled training data tagged as normal or abnormal classes [5], [6]. This class of methods is not able to detect unforeseen faults and it is often impossible to obtain abnormal training-data for robots (since it would be extremely costly). Thus, *semi-supervised anomaly detection techniques* have been developed, assuming a pre-labeled training set for the normal data. The goal is to classify all observations as anomaly which deviate from the normal model [7]. In contrary, the class of *unsupervised anomaly detection methods* does not require any training data. The key idea is the assumption that normal instances are statistically more frequent than anomalies in the observation. Thus, the goal is to identify individual outliers as an anomaly [1], [8]. In respect to this definition, our proposed framework is currently trained semi-*unsupervised*, i.e. the spatial context is trained fully unsupervised, while strictly speaking, the temporal context is trained in a semi-supervised manner. In [9] the authors propose an anomaly-detection system for surveillance tasks to find spatial anomalies in the environment. Here, an autonomous mobile robot follows a predefined path and is equipped with a monocular panoramic camera. During navigation the robot detects visual differences between captured and reference images. A similar scenario is proposed in [10], where the authors use discriminative CRF and MEMM to recognize human motions. [11] propose a technique to recognize two levels of actions using shared-structure hierarchical HMMs and a Rao-Blackwell particle filter. Unfortunately, most existing approaches are limited to their origin problem-domain and do not cope well with high dimensional input spaces. In contrary, our proposed framework will be able, in consequence of the SOM approach, to cope with high-level input spaces. An approach with a similar high degree of generalization as our approach was introduced by [12], proposing SVM classifier [13]. Unfortunately, SVM is not well suited to represent temporal context explicitly. Instead, the authors include the temporal information of the optical flow in form of an additional input feature to the SVM classifier. Although there exist similar extrinsic methods for SOM (e.g.

TDNN [14]) we decided to model the temporal context explicitly with PGM. This provides a statistical methodology with a flexible trade-off between computational complexity and detection robustness.

For the sake of completeness, following works base on a similar idea of combining SOMs and explicit probabilistic models and therefore have to be mentioned. The authors in [15] introduce a method for hand gesture recognition applying the Levenstein distance to find the spatial similarity of the gestures. In [16] the authors utilize a recurrent Kohonen Map and a Markov Model to predict the next position of the user and provide him with location based services. All related approaches which combine SOM with some explicit temporal modeling are specifically tailored to their application. In contrast, our method will be able to provide a general framework for anomaly detection, independent of the number of dimensions of the input space and the kind of underlying sensors spanning the input space.

## II. METHODS

### A. SOM-Algorithm

A SOM [3] is a popular method to extract characteristics of observed data and to classify data into clusters without supervision. The classical SOM algorithm provides a nonlinear mapping from an input space  $\mathbb{R}^n$  to an output space  $U^k$ , where  $n \gg k$  is usually true. The output space consists of a set of units  $U = \{u_1, \dots, u_m\}$  which are regularly arranged in a k-dimensional fix structure, e.g. lattice- or cube-structure. Beside the lateral connections of adjacent units, each unit  $u_i$  is also connected with the elements of the input vector  $v$ , represented by a weight vector  $w_i \in \mathbb{R}^n$ . The unit  $u_i$  which has the minimum (euclidean) distance  $d(v, u_i) = \|v - w_i\|$  between its weight vector  $w_i$  and the current input vector  $v$  will be called *best matching unit (bmu)*, calculated by  $bmu(v) = \operatorname{argmin}_u \{d(v, u_i)\} \forall i \in U$ .

Each *bmu* represents a prototypical subspace of the input space. During the training-phase (*unfolding-stage*) the weight vectors of the *bmu* and its neighbors are adapted according to the input vector  $v$ , to maximize the similarity (see Eq.1).

$$w_u(t+1) = w_u(t) + \alpha(t) \cdot h(bmu(v), u) \cdot d(v, u_i) \quad (1)$$

Here, the learning rate  $\alpha(t)$  is a monotonically decreasing function over time. In consequence, the weights of the units will converge. Furthermore,  $h(bmu(v), u)$  represents the neighborhood kernel which defines the influence-factor in respect to the distance. Formally:

$$h(c, j) = \exp\left(-\frac{\|u_c - u_j\|^2}{2\sigma(t)^2}\right) \quad (2)$$

where  $u_c$  and  $u_j$  correspond to the vectorial location of the units on the map and  $\sigma(t)$  corresponds to the width of the neighborhood radius, which is decreasing monotonically in time. A too small influence-radius means that units can not adapt properly, resulting in topological defects.

To estimate the quality of a output space the average *quantization error*, *topographic product* [17], or the *SOM*

*Distortion Measure* [18] can be used.

### B. Temporal Graph

To find temporal anomalies, causal dependencies of the observation sequence need to be considered. We assume the Markov-condition and follow the concept of PGM [4] to exploit well-studied graph analysis tools and to enable probabilistic reasoning. Therefore, a *temporal graph* is introduced which is represented by a directed graph  $TG = (S, E)$  that consists of temporal states  $s \in S$  and directed edges  $e_{ij} \in E$ . An edge  $e_{ij} \in E$  represents a causal dependency of state  $s_i \in S$  and the successive state  $s_j$ . States which are not connected by an edge are conditionally independent of each other. Each edge  $e_{ij}$  is equipped with a single weight value, which describes the corresponding conditional probability  $P_{ij}$ , i.e. the probability to traverse from state  $s_i$  to  $s_j$  in the following time step:

$$P_{ij} : P(s_j|s_i) = \frac{P(s_i \cap s_j)}{P(s_i)}, s_i, s_j \in S.$$

For calculating the causal probability between non-adjacent states  $S_{1:T} = (s_1, \dots, s_T)$  the joint distribution is applied by multiplying the conditional probabilities.

Formally:  $P(S_{1:T}) = \prod_{i=1}^T P(s_i|CP(s_i))$ .

Hereby,  $CP(x)$  represents the set of causal previous states of the state  $x$ . Note, that  $CP(x)$  is not limited to the first-order Markov-condition. Instead, it can model all arbitrary  $n^{th}$  ordered Markov processes. Keeping the recursive manner of the joint distribution in mind, the logic behind the temporal context is represented by a path between states in a graph following a set of probability distributions.

## III. FRAMEWORK

In order to keep a clear separation, we classify anomalies into two types: spatial anomalies and temporal anomalies. *Spatial anomalies* are classical out-liner in the observed data, e.g. data that exceed the predefined input-space. *Temporal anomalies* are defined as unusual observations in respect to the causal context. Based on this separation, the proposed framework uses SOM and a spatial-level to map the spatial context in combination with a generative probabilistic model to represent the temporal context.

### *Spatial-Training:*

In order to collect sufficient training-data, we propose an autonomous robot that observes itself during execution of pre-programmed behavior primitives randomly. This self-monitoring allows a high degree of autonomy since there is no previous labeling by an expert necessary. The self-monitored training-set consists of several sequences  $a_i \in \mathbb{A}$  of samples  $v \in \mathbb{R}^n$ . Accordingly, the training-sequence can be described as  $a_i = (v_{t1}, v_{t2}, \dots, v_m)$ , under the causal ordering  $v_{t1} \preceq v_{t2} \preceq \dots \preceq v_m$  and  $a_i \in \mathbb{A}$ . To become more robust, we extend the distance-function  $d$  by an extra modulus-vector  $m$  to  $d_m$  in order to handle the cyclic components of the input-vector which usually 'wrap-around', e.g. angular values. The *unfolding-process* of the spatial level is done as described in Section II. Two remarkable characteristics are the consequence

of the nonlinear transformation of the spatial-level: First, the distribution density of the units on the spatial-level is an approximation of the distribution density of the input space. Specifically, this means that denser sampled areas in the input space (e.g. the relevant working area of a robot arm) have a higher resolution in the output space than irrelevant areas in the input space. Second, despite the different dimensionality of the spaces, the topological order of the input space is preserved on the spatial-level. This allows a generalization of the high dimensional input space. Despite the loss of information due to the dimensional reduction, the resulting spatial-level is still sufficient to detect similar samples.

*Temporal-Training:*

In order to create the temporal graph, the spatial-level is extended by an additional list of tuples  $\psi_u$  which contain the observed successive units. Formally,  $\psi_{u_i} = \{\dots, (u_j, c_{ij}), \dots\} = \bigcup_{u_j \in h_{u_i}} (u_j, c_{ij})$ . Here, the tuple  $(u_j, c_{ij})$  is used as an occurrence counter measuring the number of visits of  $u_j$  after  $u_i$ , i.e.  $c_{ij} = \|u_i^t \wedge u_j^{t+1}\|$ . Similar to Eq. 2,  $h_s$  defines a spatial neighborhood kernel to increase the generalization of the detection. For temporal training, we assume a set of valid training sequence  $a_i$ , that is executed sequentially. Each sample  $v^n$  of  $a_i$  is projected onto the best matching spatial-unit  $u_v = bmu(v)$ . Applying this projection to the whole sequence  $a_i$ , a new sequence  $a_i^*$  is created. Furthermore, we apply a pre-filter step on  $a_i^*$  by removing all identical units following one another. Typically the resulting sequence  $a_i^*$  is smaller than the original input sequence  $a_i$ . Although the temporal aspects get lost, the shorter input sequence increases the training and recognition speed. For constructing the temporal-graph the updated list  $\psi_u, \forall u \in U$  is used. According to section II-B we define the temporal-graph  $TG = (S, E)$ , where  $S = s_1, \dots, s_m$  is constructed by applying a bijective function to the spatial-level  $U = \{u_1, \dots, u_m\}$ . Formally:  $S \rightarrow U$ , where  $s_i \rightarrow u_i$ . Since the structure of the spatial-level is fix and discrete, the temporal-graph has a well defined state set, too. The transition probabilities are calculated considering a statistical approximation based on the list  $\psi_{u_i}, \forall u_i \in U$ . Accordingly, the transition probability is calculated by  $P_{trans}(u_i|u_j) = \frac{c_{ij}}{\sum_{u_k \in \psi_{u_i}} c_{ik}}$ . In consequence of  $S \rightarrow U$ , we are able to put  $P_{trans}(u_i|u_j)$  directly on the level with the transition probability of the temporal graph  $P_{trans}(s_i|s_j)$ .

Although the current temporal graph is able to cope with temporal and spatial uncertainties, it is not fully sufficient for a reliable modeling and a robust recognition. This is based on the exclusive inclusion of the *bmus* of the spatial-level: In spite of the advantages of the quantization and generalization aspects of the SOM, the probabilistic modeling of the temporal graph shows the disadvantage of the binary *winner-takes-all*-decision: Even if there are several similar (or equal) probable units, the *winner-takes-all*-decision returns only one (the most probable) unit and drops out the others.

To increase the detection robustness the temporal graph is extended by introducing so called *path-states* and *affinity-states*.

A *path-state*  $\lambda_i \in \Lambda \subset S$  is a state on the estimated path of activated *bmus* on the spatial-level during time. In respect to  $S \rightarrow U$ , it is essential:  $(\lambda_i, \dots, \lambda_N) \rightarrow (bmu_{u_i}, \dots, bmu_{u_N})$ .

*Affinity-states*  $\phi_i \in \Phi \subset S$  are states, whose equivalent spatial-units have similar weights to the corresponding spatial *bmu*. Further, an affinity-state  $\phi \in \Phi$  is generated by the corresponding path-state  $\lambda \in \Lambda$  under an a priori unknown stochastic process, same as the concept of Hidden Markov Models.

To find the corresponding spatial-unit  $u$  of the affinity-state  $\phi$ , the mapping  $S \rightarrow U$  is exploited. We consider the spatial-level and define  $SMU_\delta(v)$  as the set of *similar matching units*, i.e. these spatial-units whose difference between their weight-vector and the weight-vector of the *bmu*( $v$ ) is under a predefined threshold  $\delta$ . *SMU* are formally calculated by:  $SMU_\delta(v) = \{smu_d(v) : d_m(u_d(v), bmu(v)) < \delta\}$ .

In respect to  $S \rightarrow U$ ,  $\Phi = (\phi, \dots, \phi_N)$  is mapped to  $(smu_{u_i}, \dots, smu_{u_N})$ . In order to estimate the conditional probability of affinity-state  $\phi_i$  under path-state  $\lambda_j$ , i.e.  $P_{aff}(\phi_i|\lambda_j)$ , we take advantage of the implicit available quantization error between the weight-vectors of the corresponding spatial-units  $u_i$  and  $u_j$ :

$$P_{aff}(\phi_i|\lambda_j) = \frac{1}{Z} \exp(-(\sigma \cdot d_m(u_i, u_j)^2)) \quad (3)$$

Here,  $\sigma$  represents a decay-parameter of the influence-factor and  $Z$  represents the normalization constant. Due to the exponential function and the distance-function  $d_m \geq 0$ , it is guaranteed that  $P_{aff}$  will be in the interval  $[0,1]$ . Furthermore, the conditional probability of that unit  $u$  with the minimum error distance, here  $u = bmu$ , becomes the maximum probability. In Fig. 1 a temporal graph is presented.

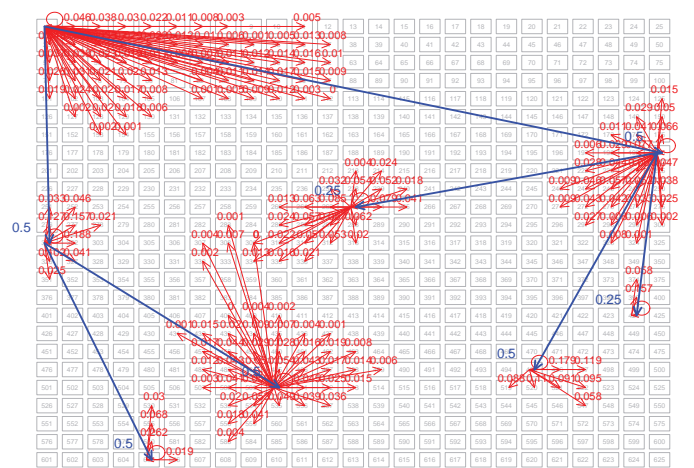


Fig. 1: Example of a temporal graph which is projected on the spatial-level. The dark-blue directed edges represent the transitions between the path-states, the light-red edges represent the conditional probabilities of the affinity-states. The numbers indicate the probability value.

Note that, despite the similarities to a HMM-approach, the current state of the framework is fully observable. I.e. it is

not required to distinguish between latent and observable states. This allows a simplified and faster creation of the models. A drawback of this approach is the vast size of the resulting models. Accordingly, it should be mentioned that if the path-states will be clustered to decrease the size of the resulting model, then the classical HMM learning process (e.g. using EM-methods as the Baum-Welch algorithm), can be used without any modification of the overall framework.

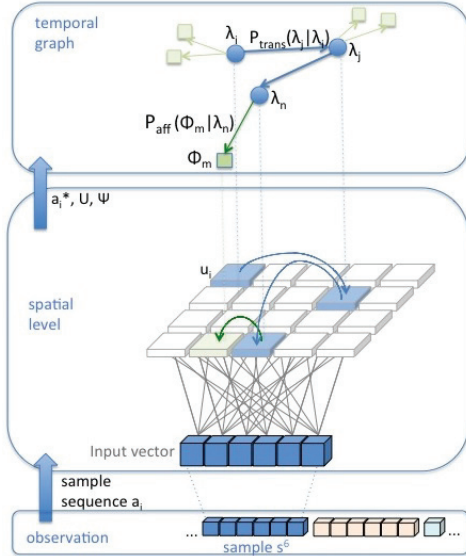


Fig. 2: Proposed framework. Bottom: The sequence  $a_i$  of observed raw sensor input-vectors  $s^n$  (here,  $n = 6$ ) is presented to the already trained spatial-level. Middle: The current input-vector is nonlinear transformed to its best-matching-unit on the spatial-level, updating the causal relations of  $\psi_{u_i}$ . Top: Based on the spatial-level  $U$ , the sequence of  $bmus$  and  $smus$  according to  $a_i^*$ , and the  $\psi_{u_i}$ , the temporal-graph is constructed.

**Anomaly-Detection:** Spatial anomalies are represented by units with a high *quantization error*, in other words: anomalies are projected to sparse regions of the output space. Formally:  $error_q(v) = \|v - w_{bmu(v)}\|$ . This is the consequence of the underlying assumption: Normal observations are statistically more frequent than anomalies during training, i.e. abnormal input vectors are seldom or never considered in the training process. To derive the probability distribution, we propose to consider the best-matching-unit (*bmu*) and the 'second'-best-matching-unit (*bmu'*), e.g.  $bmu'(v) = \operatorname{argmin}_u \{d(v, u_i)\} \forall i \in U \wedge u_i \neq bmu(v)$ , as reference. Thus, we define similar to Eq.3:  $P_{anomaly}(v) = 1 - \exp(-(\text{error}_q(v)/\sigma)^2)$ , where  $\sigma = \frac{1}{2} \cdot \|w_{bmu(v)} - w_{bmu'(v)}\|$ .

Temporal anomalies are represented by abnormal causal sequences of spatial units. In order to detect temporal anomalies and to provide a corresponding probability distribution, we make use of the already constructed temporal graph. In a first step the observation sequence  $a_i$  is converted to  $a_i^*$  by exploiting the corresponding spatial-level. For the decision whether it is a normal behavior or an anomaly, we calculate

the probability of the temporal-graph  $m$  (i.e. the normal model) to generate the observed sequence  $a_i^*$ . Formally:  $P(a_i^* | m) = \sum_{\Phi} P(a_i^*, \phi | m)$ . Since the direct calculation of the probability would be exponential in time, the well-known *forward-algorithm* [19] is utilized. The algorithm makes use of the principle of dynamic programming to efficiently compute the posterior marginals of all path-states given a sequence of observed spatial-units  $a_i^*$ . Instead of the whole sequence at once, we propose to consider several sequential and overlapping subsequences  $a_i^*[k, k+w]$  with a specific observation length  $w$  (window-size). The corresponding anomaly-probability is clearly  $P_{anomaly}(a_i^*) = 1 - P(a_i^* | m)$ .

#### IV. EXPERIMENTS

The framework was implemented in *R* [20] and the demonstration scenario was exemplary evaluated on a *CrustCrawler AX18A Smart Robotic Arm*. Although the framework is able to include all kind of sensors, we decided to use a visual observation of the scene, in order to evaluate uncertainties based on occlusions or flickering positions. Fig. 3 shows the setting of the scenario.



Fig. 3: Test bed: The position of the two-fingered gripper is estimated by a camera-based recognition system. All relevant features (gripper-fingers, robot base, objects) are marked by visually traceable markers.

First, a typical *pick-and-place* behavior will be considered. The task is to grasp an object on one side of the working area, transport the object to the opposite side and finally place the object there.

For training the spatial-level, the robot arm was programmed to approach randomized positions in the working area  $R^3$  focusing on a subspace in front. The camera system observes the positions of the markers, calculates the average position and provides these samples as a single three-dimensional input vector to the framework, i.e.  $v = \{x, y, z\}$ .

Without loss of generality, we chose the low dimension of the input space in order to enable an adequate visualization of the weight vectors in Fig. 4 for the reader. But as mentioned in the previous section, the SOM is obviously able to cope with high dimensional input spaces. Also the complexity of the temporal modeling and logical inference of the sequence is independent of scaling the dimension of the input space. Instead,



TABLE I: Spatial-temporal detection accuracy in [%] of *pick & place scenario*: 500 runs per window-size, affinity- $\delta = 0.4$ .

behavior	window size				
	1	2	7	15	30
Normal	90.38	92.84	96.13	94.276	87.67
Anomaly	31.33	40.37	75.08	99.41	100.0

is simulated by only one broken motor, an abnormal test-set could still contain some subsequences which follow the normal behavior nevertheless (compare Fig.5). In consequence, a (too) short window size of abnormal data results in less accuracy, due to more fault detections. Considering a long window size instead, the real abnormal behavior part is more likely covered by the randomly chosen subsequence and thus the accuracy is higher.

For a second experiment, the functionality of the two-fingered gripper executing an *open-gripper*-behavior was considered. Here, the 3D position of both markers on the fingers are considered to result in an input space of  $\mathbb{R}^6$ . The spatial-level was initially trained with 1068 samples over 30 epochs. The dimension and structure of the spatial-level, as well as the decreasing learning rate and neighborhood radius was the same as in the previous scenario. Here, a hardware-error was simulated by a randomly broken finger-servo. In each evaluation (à 500 runs), the subsequences of the test-set were chosen randomly (in respect to a fixed window-size) and the average accuracy was determined. See Table II for the final results.

TABLE II: Spatial-temporal detection accuracy in [%] of *open-gripper scenario*: 500 runs per window-size, affinity- $\delta = 0.2$ .

behavior	window size				
	1	2	7	15	20
Normal	90.39	92.86	97.02	98.45	72.95
Anomaly	48.36	53.04	81.14	100.0	100.0

## V. CONCLUSIONS AND FUTURE WORK

The evaluation and the experimental results emphasize the operating principles and the success of the framework to detect behavioral abnormalities in the domain of real-world autonomous robots. The coupling of SOM and PGM techniques for spatial and temporal analysis enables our framework to detect anomalies independently from the dimension size of the input data and the features. Furthermore, the proposed general framework copes with uncertainties and allows probabilistic reasoning. In the current version of the framework, the temporal graph includes the set of all path-states. In order to decrease the model size, the next optimization step will be to cluster the path-states to relevant *key-states*. A further step will be to extend the framework for a more reliable integration of variable features, since e.g. different object grasping poses

do not automatically mean an abnormal behavior. Therefore, a spatial-temporal variance-analysis of the spatial-level and the temporal graph is planned to find none but the relevant behavioral states, finally allowing more robust detection results.

## ACKNOWLEDGMENT

The research leading to these results has received funding from the European Union Seventh Framework Programme FP7/2007-2013 under grant agreement no 248942 RoboEarth.

## REFERENCES

- [1] V. Chandola, A. Banerjee, and V. Kumar. Anomaly detection: A survey. *ACM Computing Surveys (CSUR)*, 41(3):15, 2009.
- [2] B. Jakimovski, B. Meyer, and E. Maehle. Self-reconfiguring hexapod robot oscar using organically inspired approaches and innovative robot leg amputation mechanism. In *Intl Conf. on Automation, Robotics and Control Systems, ARCS-09, Orlando*, 2009.
- [3] T. Kohonen. *Self-organizing maps*, volume 30. Springer Verlag, 2001.
- [4] D. Koller and N. Friedman. *Probabilistic graphical models: principles and techniques*. MIT press, 2009.
- [5] N. Abe, B. Zadrozny, and J. Langford. Outlier detection by active learning. In *Proceedings of the 12th ACM SIGKDD international conference on Knowledge discovery and data mining*, pages 504–509. ACM, 2006.
- [6] R. Vilalta and S. Ma. Predicting rare events in temporal domains. In *Data Mining, 2002. ICDM 2003. Proceedings. 2002 IEEE International Conference on*, pages 474–481. IEEE, 2002.
- [7] R. Fujimaki, T. Yairi, and K. Machida. An approach to spacecraft anomaly detection problem using kernel feature space. In *Proceedings of the eleventh ACM SIGKDD international conference on Knowledge discovery in data mining*, pages 401–410. ACM, 2005.
- [8] S.P. Singh. Data clustering using k-mean algorithm for network intrusion detection. 2010.
- [9] P. Chakravarty, A.M. Zhang, R. Jarvis, and L. Kleeman. Anomaly detection and tracking for a patrolling robot. In *Australasian Conference on Robotics and Automation (ACRA)*. Citeseer, 2007.
- [10] C. Sminchisescu, A. Kanaujia, Z. Li, and D. Metaxas. Conditional models for contextual human motion recognition. In *Computer Vision, 2005. ICCV 2005. Tenth IEEE International Conference on*, volume 2, pages 1808–1815. IEEE, 2005.
- [11] N.T. Nguyen, D.Q. Phung, S. Venkatesh, and H. Bui. Learning and detecting activities from movement trajectories using the hierarchical hidden markov model. In *Computer Vision and Pattern Recognition, 2005. CVPR 2005. IEEE Computer Society Conference on*, volume 2, pages 955–960. IEEE, 2005.
- [12] X. Wu, Y. Ou, H. Qian, and Y. Xu. A detection system for human abnormal behavior. In *Intelligent Robots and Systems, 2005.(IROS 2005). 2005 IEEE/RSJ International Conference on*, pages 1204–1208. IEEE, 2005.
- [13] B. Schölkopf and A.J. Smola. *Learning with kernels: Support vector machines, regularization, optimization, and beyond*. MIT press, 2001.
- [14] A. Waibel, T. Hanazawa, G. Hinton, K. Shikano, and K.J. Lang. Phoneme recognition using time-delay neural networks. *Acoustics, Speech and Signal Processing, IEEE Transactions on*, 37(3):328–339, 1989.
- [15] G. Caridakis, K. Karpouzis, C. Pateritsas, A. Drosopoulos, A. Stafylopatis, and S. Kollias. Hand trajectory based gesture recognition using self-organizing feature maps and markov models. In *Multimedia and Expo, 2008 IEEE International Conference on*, pages 1105–1108. IEEE, 2008.
- [16] S.J. Han and S.B. Cho. Predicting users movement with a combination of self-organizing map and markov model. *Artificial Neural Networks–ICANN 2006*, pages 884–893, 2006.
- [17] H.U. Bauer and K.R. Pawelzik. Quantifying the neighborhood preservation of self-organizing feature maps. *Neural Networks, IEEE Transactions on*, 3(4):570–579, 1992.
- [18] E. Erwin, K. Obermayer, and K. Schulten. Self-organizing maps: ordering, convergence properties and energy functions. *Biological cybernetics*, 67(1):47–55, 1992.
- [19] L. Rabiner and B. Juang. An introduction to hidden markov models. *ASSP Magazine, IEEE*, 3(1):4–16, 1986.
- [20] R Development Core Team. *R: A Language and Environment for Statistical Computing*. R Foundation for Statistical Computing, Vienna, Austria, 2012. ISBN 3-900051-07-0.

# Integrating Arduino-based Educational Mobile Robots in ROS

André Araújo, David Portugal, Micael S. Couceiro and Rui P. Rocha

**Abstract**— This article presents the full integration of compact educational mobile robotic platforms built around an Arduino controller board in the Robotic Operating System (ROS). To that end, a driver interface in ROS was created to drastically decrease the development time, providing hardware abstraction and intuitive operation mode, allowing researchers to focus essentially in their main research motivation. Moreover, the full integration in ROS provided by the driver enables the use of several tools for data analysis, easiness of interaction between multiple robots, sensors and teleoperation devices, thereby targeting engineering education. To validate the approach, diverse experimental field tests were conducted using different Arduino-based robotic platforms.

## I. INTRODUCTION

Mobile robotics is a technological field and a research area which has witnessed incredible advances for the last decades. It finds application in areas like automatic cleaning, agriculture, support to medical services, hazard environments, space exploration, military, intelligent transportation, social robotics, and entertainment [1]. In robotics research, the need for practical integration tools to implement valuable scientific contributions is felt frequently. However, roboticists end up spending excessive time with engineering solutions for their particular hardware setup, often reinventing the wheel. For that purpose, several different mobile robotic platforms have emerged with the ability to support research work focusing on applications like search and rescue, security applications, human interaction or robotics soccer and, nowadays, almost every major engineering institute has one or more laboratories focusing on mobile robotics research.

Earlier, the focus of research was especially on large and medium systems. However, with recent advances in sensor miniaturization and the increasing computational power and capability of microcontrollers in the past years, the emphasis has been put on the development of smaller and lower cost robots. Such low-cost platforms make affordable the experimentation with a larger number of robots (*e.g.*, in cooperative robotics and swarm robotics) and are also ideal for educational purposes. With such assumptions in mind, we have been doing engineering and research work with two Arduino-based mobile platforms [2]: the TraxBot [3] and the StingBot<sup>1</sup>. The choice fell upon Arduino solutions, since it presents an easy-to-learn programming language (derived from C++) that incorporates various complex programming functions into simple commands that are much easier for students to learn. Moreover, the simplicity of the Arduino to create, modify and improve projects, as well as its open-source and reduced cost makes it among the

This work was supported by the CHOPIN research project (PTDC/EEA-CRO/119000/2010), by PhD scholarships SFRH/BD/64426/2009 and SFRH/BD/73382/2010, and by ISR-Institute of Systems and Robotics (project PEst-C/EEI/UI0048/2011), all of them funded by the Portuguese science agency "Fundação para a Ciência e a Tecnologia" (FCT).

A. Araújo, D. Portugal, M. Couceiro and R. P. Rocha are with the Institute of Systems and Robotics, University of Coimbra, Pólo II, 3030-290 Coimbra, Portugal, email: {aaraujo, davidbsp, micaelcouceiro, rprocha}@isr.uc.pt.

<sup>1</sup> <http://www.isr.uc.pt/~aaraujo/doc>

most used microcontroller solutions in the educational context [2].

Following the trend of research, in this work the focus is on educational, open-source platforms that enable researchers, students and robot enthusiasts to quickly perform real world experimentation, having access to the tools provided by the Robotic Operating System (ROS) [4]. ROS is currently the most trending and popular robotic framework in the world, reaching critical mass and being the closest one to become the standard that the robotics community urgently needed.

With the exponential growth of robotics, some difficulties have been found in terms of writing software for robots. Different types of robots can have wildly varying hardware, making code reuse nontrivial. Opposing this tendency, ROS provides libraries and tools to help software developers to create robot applications. The major goals of ROS are hardware abstraction, low-level device control, implementation of commonly-used functionally, message-passing between processes and package management. One of its gold marks is the amount of tools available for the community like the Stage simulator [5], navigation capabilities<sup>2</sup>, visual SLAM [6] and 3D point cloud based object recognition [7], among others. Regular updates enable the users to obtain, build, write and run ROS code across multiple computers.

In the next section, we review general purpose and educational mobile robots, focusing on those already integrated in ROS and briefly describe our Arduino-based robot platforms. In section III, the main contributions of this work are revealed and details on the development of the ROS driver and its features are presented. In the subsequent section, preliminary results with physical Arduino-based robots and a team of mixed real and virtual cooperating agents are presented. Finally, the article ends with conclusions and future work.

## II. RELATED WORK

The following requirements, sorted by relevance, can be expected from robots to be used for educational purposes [8][9]:

- Cost — Robots should be as cheap as possible to overcome budget limitations and evaluate multi-robot applications (*e.g.*, swarm robotics);
- Energy Autonomy — Robots should have a long battery life since they may have to operate long enough during development and experimentation;
- Communication — Robots need to support wireless communication to increase the range of applications (*e.g.*, cooperative systems);
- Sensory System — Robots should be equipped with some form of sensing capability to allow interaction between them and with their environment;
- Processing — Robots need to be able to process information about other robots and the environment (*e.g.*, sensing data).

<sup>2</sup> <http://www.ros.org/wiki/navigation>



**Fig. 1.** Well-known educational and research mobile robotic platforms: from left to right, iRobot Create, Turtlebot, Mindstorm NXT, e-puck, MarXbot, SRV-1 Blackfin and Pioneer 3-DX, respectively.

The following subsection reviews popular educational and research platforms available in the market, after which we present the Arduino-based educational platforms developed and evaluate them according to the requirements presented above.

#### A. Educational Robotic Platforms

Several off-the-shelf mobile robots with various sensors and diverse capabilities are illustrated in Fig. 1. We address their mobility within different ground environments, capabilities, size, sensing/perception, processing power, autonomous navigation and integration in ROS.

The Roomba Create [10] from iRobot was designed for students and researchers, being very popular in the robotics community due to its small size and low cost. It is a circular platform, with extra space for larger sensors (*e.g.*, 2D laser sensor or Kinect). Many choose to utilize an external computer that supports serial communication to control the Create robot, due to troublesome limitations in storage space and processing power. A ROS driver for the Roomba iCreate has already been developed (*irobot\_create\_2\_1* package in the *brown\_drivers* stack), as well as the original vacuum cleaning Roomba (*roomba\_robot* stack).

In fact, a popular off-the-shelf robot, developed at Willow Garage, has been built upon an iRobot Create: the TurtleBot<sup>3</sup>. This is a modular development platform incorporating an Xbox Kinect and an ASUS eeePC 1215N netbook. TurtleBot provides 3D functionalities and ROS out of the box (through the *turtlebot* stack), being fully open source and exploring all combined capabilities of its components.

The Mindstorms NXT [11] from Lego is an educational, academic robot kit, ideal for beginners. The robot is equipped with drive motors with encoders and a good variety of cheap sensors like an accelerometer, light, sound, ultrasound and touch sensors. Support for interfacing and controlling this robot with ROS is also available, through the *nxt* stack.

The e-puck [12] is an educational swarm platform for beginners. It has tiny dimensions with only 80mm of diameter, equipped with a vast set of sensors like microphones, infrared sensors, 3D accelerometer and a VGA camera. Similarly, the MarXbot [13] platform has 170 mm of diameter, being fully equipped with infrared range sensors, 3D accelerometer, gyroscope, and an omnidirectional camera. It has a good processing power with an ARM 11 processor at 533MHz. Both the e-puck and the MarXbot are programmed in a user-friendly scripting language, which uses ASEBA, an event-based low level control architecture. In order to interface it with ROS, a ROS/ASEBA Bridge has been released (*ethzasl\_aseba* stack<sup>4</sup>).

Additionally, the SRV-1 Blackfin [14] from Surveyor is a small-sized robot equipped with tracks with differential configuration. This robot has a good processing power with a 1000MIPS at 500MHz CPU, capable of running Linux Kernel 2.6. It is equipped with two IR rangefinders or optional ultrasonic ranging and a 1.3MP camera. It also supports Wireless 802.11b/g communication and various I2C sensors. Unlike the

previous platforms, SRV-1 Blackfin can be driven in rough terrains due to its tracking system. At the time of writing, only partial support for ROS is available through the *ros-surveyor*<sup>5</sup> stack, which offers a driver for the Surveyor Vision System in ROS.

Among the larger, more equipped and more powerful mobile robots, a reference platform for research and education is the Pioneer 3 DX from ActivMedia [15]. This is a robust differential drive platform with 8 sonars in a ring disposition, a high-performance onboard microcontroller based on a 32-bit Renesas SH2-7144 RISC microprocessor, offering great reliability and easiness of use. Compared to the previously referred robots, this robot has greater weight and less affordability. Two different drivers are available to interface the Pioneer 3 DX with ROS: *ROSARIA*<sup>6</sup> and *p2os*<sup>7</sup>.

#### B. Arduino-Based Robotic Platforms

Even though most of referred platforms provide open source software, they usually require a slow learning curve and the hardware has limited expandability. Arduino solutions have recently appeared in the market to work around such issues. For this reason, our platforms were built around an Arduino control board, which accesses the motor encoders and other information from the power motor driver like temperature and battery state, being also able to send commands to the motors, read sonar information and exchange messages natively through Zigbee. Although this section briefly describes the platforms assembled in our research laboratory, the proposed driver could be applied to any other Arduino-based platform such as the *eSwarBot* [8], the *Bot'n Roll OMNI*<sup>8</sup> and many others (*e.g.*, [1]).

The Arduino-based platforms under consideration, namely the TraxBot v1 and v2 and the Stingbot [3], are depicted in Fig. 2. All these platforms' processing units consist of Arduino Uno boards, which include a microcontroller ATmega 328p that controls the platforms motion through the use of the Bot'n Roll OMNI-3MD motor driver<sup>8</sup>.

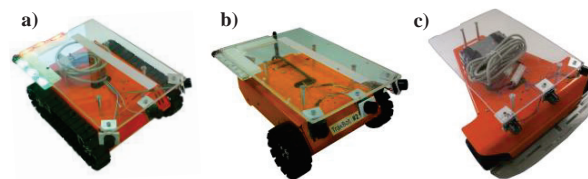


**Fig. 2.** Arduino-based robotic platforms, a) TraxBot v1; b) TraxBot v2; c) StingBot.

As for power source, two packs of 12V 2300mAh Ni-MH batteries ensure good energy autonomy to the robots. For distance sensing, 3 Maxbotix Sonars MB1300 with a range of approximately 6 meters were used. However, and as experi-

<sup>3</sup> <http://www.willowgarage.com/turtlebot>

<sup>4</sup> [http://www.ros.org/wiki/ethzasl\\_aseba](http://www.ros.org/wiki/ethzasl_aseba)

<sup>5</sup> <https://github.com/rene0/ros-surveyor>

<sup>6</sup> <http://www.ros.org/wiki/ROSARIA>

<sup>7</sup> <http://www.ros.org/wiki/p2os>

<sup>8</sup> <http://botnroll.com/omni3md>

mental results depict, the sensing capabilities of the platforms can be easily upgraded with other sensors, *e.g.*, laser range finders. Moreover, the platforms have the ability to also include a 10" netbook on top of an acrylic support, which extends the processing power and provides more flexibility. In our case, ASUS eeePC 1025C were used due to their reduced price and size. The netbook provides communication via Wireless Wi-Fi 802.11 b/g/n to the robot and is dedicated to run ROS onboard, providing the tools and means for enhanced control of the robot. Additionally, the platforms are also equipped with an Xbee Shield from Maxstream, consisting on a ZigBee communication module with an antenna attached on top of the Arduino Uno board as an expansion module. This Xbee Series 2 module is powered at 2mW having a range between 40m to 120m, for indoor and outdoor operation, respectively.

### C. Summary

Both Arduino-based platforms meet all the requirements previously pointed out, being ideal for multi-robot applications. In terms of cost, our platforms have a similar price to the Mindstorms NXT, being more affordable than the Turtlebot, e-puck, MarXbot or the Pioneer. In terms of energy autonomy, both the TraxBot and the Stingbot can operate continuously around 3 hours, which is a common operation time for compact platforms. As for communication, unlike the iRobot Create and the Pioneer, which do not offer multi-point communication out of the box, our platforms support Zigbee communication, which is extended with WiFi when using a netbook. Having distance sensors and wheel encoders with high resolution, these platforms have the flexibility to incorporate even more custom sensors, as opposed to the SRV-1 Blackfin or the Mindstorms NXT. Furthermore, its hybrid design enables not only to make use of the 24 MIPS at 26MhZ Atmega 328 microcontroller, but also the Intel Atom N2800 Dual Core at 1.86 GhZ processor of the netbook, similarly to the Turtlebot and outperforming the smaller platforms.

Additionally, when developing our educational robots other requirements were taken into account: all hardware is either made of aluminium or stainless steel, being extremely robust; their dimensions are adequate for both indoor and outdoor experiments; and they have the ability to run ROS.

## III. ROS DRIVER FOR ARDUINO-BASED ROBOTS

The key contributions of this work are the development and description of a driver that enables fast prototyping through the interface and control of custom educational platforms with ROS, which can be generalized to different Arduino-based platforms.

ROS provides tools to interface with the Arduino family of boards through the *rosserial* stack<sup>9</sup>. However, it was verified that *rosserial* is not suitable for this work, due to the high overhead imposed by its data acquisition and commands, which result in an excessive workload to the Arduino microcontroller Atmel 328p SRAM. In fact, the microcontroller presents limited SRAM memory and for standard ROS topics (float32 messages + message headers), stress tests have shown that only a maximum of 15 ROS topics can be used in parallel and the message buffer is limited to 70 standard messages.

The most important feature in *rosserial* is to add libraries to the Arduino source code, in order to emulate ROS language directly in Arduino code. This results in high overhead in communication between PC / ROS and the Arduino, due to the

structures used, for example, when publishing messages from the Arduino side. For this reason, a custom driver was created, being able to adopt a faster and more transparent communication between any Arduino board and ROS. We propose a solution based on the *serial\_communication* stack<sup>10</sup>, where the messages sent from the Arduino only consist of arrays of characters, which are parsed to integer variables on the PC / ROS side, hugely decreasing the communication load.

### A. Driver Description

The *mrl\_robots*<sup>11</sup> driver herein presented was developed for integration and control of the platform using ROS Fuerte version running on Ubuntu 11.10 "Oneiric Ocelot". The *serial\_communication* stack<sup>10</sup>, was used to establish point-to-point serial communication between the Arduino and the PC / ROS side, without the overhead of *rosserial*. This enables robust and fast communication in more complex applications, such as teleoperation, crossing of sensory information, the integration of the *navigation* stack, among others. It also has the versatility of creating protocols to exchange data between the Arduino and the PC/ROS side, which enables the creation of a customized and transparent serial communication.

The Arduino firmware code was developed taking into account all components and their features, which are required for the robots' operation. In Fig. 3 the architecture of the ROS Driver is illustrated. The power motor driver OMNI-3MD provides libraries to control the motors (*i.e.*, velocity or position control), read encoders and temperature, as well as setting the parameters for the initial configurations of the PID controller, among others. The motor driver is connected to the Arduino Uno through I2C communications. C/C++ language was used as the programming language for the ATmega328p microcontroller. Algorithm 1 illustrates the resident Robot/Arduino Firmware code.

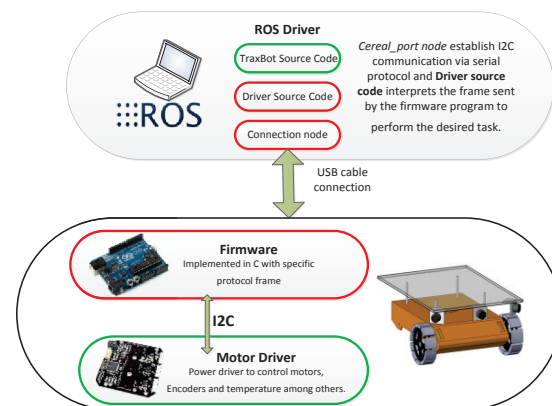


Fig. 3. ROS driver architecture diagram.

The protocol developed to interface ROS with the Arduino board consists on sending a frame with the configuration shown in Fig. 4. The character '@' is used at the beginning of every frame, and commas ',' separate the different parameters. Character 'e' identifies the end of the frame. Regarding the content of the protocol, the first parameter corresponds to the action command; like move motors, and others (Algorithm 1). Following the action command, commas separate the arguments of the designated commands which have been defined as signed integers.

<sup>9</sup> <http://www.ros.org/wiki/rosserial>

<sup>10</sup> [http://www.ros.org/wiki/cereal\\_port](http://www.ros.org/wiki/cereal_port)

<sup>11</sup> [http://www.ros.org/wiki/mrl\\_robots](http://www.ros.org/wiki/mrl_robots)

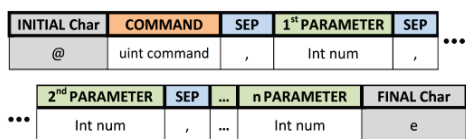


Fig. 4. Frame protocol to receive/send data from/to the Arduino Uno

Let us suppose, for instance, that we want the platform to move with a linear velocity of 0.5 m/s and an angular velocity of -0.8 rad/s, the frame would be, “@11,500,-800e” representing “@command,(lin\_vel×10<sup>3</sup>),(ang\_vel×10<sup>3</sup>)e”.

In the ROS side, a computation process (*robot\_node*) has been programmed, which starts the serial connection using the *cereal\_port* library of *serial\_communication* stack and receives streams of information from the robot. Whenever a data frame has been received, a callback is triggered, publishing the corresponding message into appropriate ROS topics, thus providing updated information to the rest of ROS ecosystem. Algorithm 2 shows how the driver works. In Fig. 5, it is shown how a ROS user application node (e.g., a mapping algorithm) can interact with *robot\_node* by sending velocity commands to the base and receiving information like sonar range, odometry, transforms, etc. One of many ROS tools, *rxgraph*, has been used to allow real time monitoring of the available nodes, as well as topics exchanged by each node. Note also the interaction with other existing nodes in ROS like the *wiimote\_node*<sup>12</sup>, used for teleoperating the robot through a Nintendo’s Wii remote controller (*WiiMote*), and the *hokuyo\_node*<sup>13</sup> to add an Hokuyo laser range sensor to the robot. ROS provides many different built-in sensor message types which are appropriately assigned to the topics of each component of the driver.

The ability to stream data from the Arduino board is an interesting feature of the driver because it does not require a synchronous communication involving requests and responses between ROS and the Arduino board. Hence, it frees the serial communication channel since it only needs a starting request and can be stopped at any time. Furthermore the *mrl\_robots* driver has the ability to enable and disable debugging options to track eventual errors.

### B. Driver Features and Potential

The driver presented in the last subsection offers several features, many of which are inherited by the direct integration with the ROS middleware. The driver enables the interface with ROS tools for data process and analysis of the platforms, like 3D visualization (*rviz*), logging real-time robot experiments and playing them offline with (*roslab/rxlog*), plotting data (*rxplot*) and visualizing the entire ROS network structure (*rxgraph*).

Beyond the easiness of using the available tools, ROS also provides effortlessly integration of new sensors without needing hardware expertise, as it will be seen in section IV. This opens a new range of possibilities since several well-known stacks from the ROS community comprise algorithms for robotics development such as the *navigation*<sup>2</sup> and *slam\_gmapping*<sup>14</sup> stacks.

<sup>12</sup> [http://www.ros.org/wiki/wiimote\\_node](http://www.ros.org/wiki/wiimote_node)  
<sup>13</sup> [http://www.ros.org/wiki/hokuyo\\_node](http://www.ros.org/wiki/hokuyo_node)  
<sup>14</sup> [http://www.ros.org/wiki/slam\\_gmapping](http://www.ros.org/wiki/slam_gmapping)

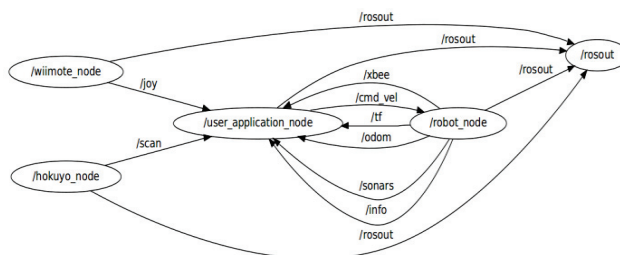


Fig. 5. Rxgraph topics and nodes provided by the *mrl\_robots* driver.

### Algorithm 1. Robot/Arduino Resident Firmware

```

1: #Omni3MD library // main motor driver command functions
2: #EEPROM library // storage robot particular specifications: robot ID,...
3: #Robot library // range sonars acquisition, calibration, PID gains
4: #RobotSerialComm library // protocol serial communication
5: #Standard libraries
6: Setup Functions(); // PID motor gains, using ports, encoders scale, set I2C
7: connection....
8: Streaming Functions():
9:   sendEncodersReads()
10:   Read encoder 1 and 2 pulses;
11:   Serial reply encoder data;
12:   sendEncodersSonarsReads()
13:   Read encoder 1 and 2 pulses;
15:   Read sonars 1, 2 and 3 ranges;
16:   Serial reply encoder and sonar data;
17:   sendRobotInfo()
18:   Read from EEPROM robot ID;
19:   Read internal board temperature;
20:   Read Omni-3MD driver firmware version;
21:   Read TraxBot battery voltage;
22:   Read firmware version;
23:   Serial reply info data;
24: Main loop():
25:   Switch (action):
26:     sendEncodersReads;
27:     sendEncodersSonarsReads;
28:     sendRobotInfo;
29:     Omni-3MD auto-calibration motors for controller purposes;
30:     Set PID gains;
31:     Receive Xbee message;
32:     Send Xbee message;
33:     Xbee node discovery;
34:     Set prescaler from encoders;
35:     Set desire encoders values;
36:     Robot info;
37:     Single encoders reading;
38:     Single sonars reading;
39:     Linear motors move with PID controller;
40:     Linear motors move;
41:     Stop motors;
42:     Reset encoders;
43:     Debug action; // (Des)Activate debug option
44:     Start streaming data; // Activate desire streaming data
45:     Stop streaming data;
    
```

### Algorithm 2. PC/ROS Driver.

```

1: #ROS_msgs library // ROS type messages
2: #Cereal_port library // protocol serial communication
3: Robot data callback():
4:   UpdateOdometry()
5:   Read encoder pulses;
6:   Pulses convert to cartesian pose (x, y, θ);
7:   Publish in ROS topic updated pose;
8:   Publish tf: odom → base_link
9:   DriveRobot()
10:   Subscribe ROS topic differential velocity commands;
11:   Send to robot angular and linear speeds;
12:   RangeUltrasonicSonars()
13:   Publish ROS topic range ultrasonic sonars;
14:   XbeeMsgs()
15:   Publish ROS topic with Xbee message received;
16:   Subscribe ROS topic with Xbee message to send from user node
17:   UpdateRobotInfo()
18:   Publish ROS topic robot information;
19: Main loop():
20:   Establish a serial connection;
21:   Receive data streaming from robot (activate callbacks);
    
```

As a result, the overall time spent in robotics research is greatly reduced due to code reuse and therefore the driver represents a valuable tool that enables fast prototyping and opens a gateway into the world of ROS.

Another interesting feature of the driver is the simplicity for enabling heterogeneous multi-robot coordination and cooperation. Running the same hardware abstraction layer in the team of robots, ROS takes care of the communication messaging system using a publish/subscribe method, which enables all kinds of interaction between members of the same team, as seen in Fig. 6, where an example of a ROS network is depicted.

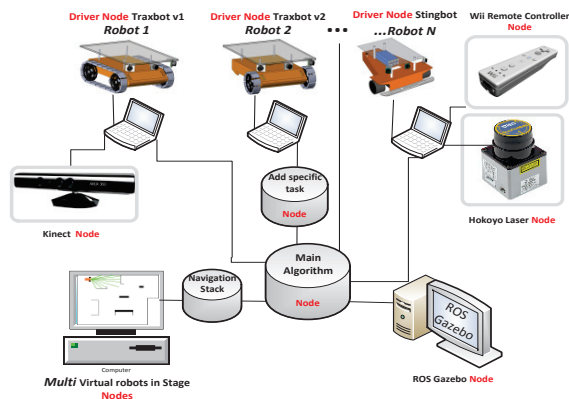


Fig. 6. Network topology example with multiple robots, sensors, tele-operation devices and applications.

ROS also has the potential to integrate mixed real and virtual robot teams. With the use of the driver herein presented, together with the Stage<sup>15</sup> multi-robot simulator, the same code can be used to drive either real robots or virtual agents running on Stage. Therefore, the developed ROS driver allows the integration of virtual robots with different sizes and driving characteristics, as seen later on. In addition, the communication between real and virtual agents is completely transparent since they are both operating in the same ROS network. This major feature is ideal to perform multi-robot tasks, allowing the use of a large population of robots, when no extra physical robots are available, being cheaper and promoting safer test scenarios by making interactions between physical and virtual world objects.

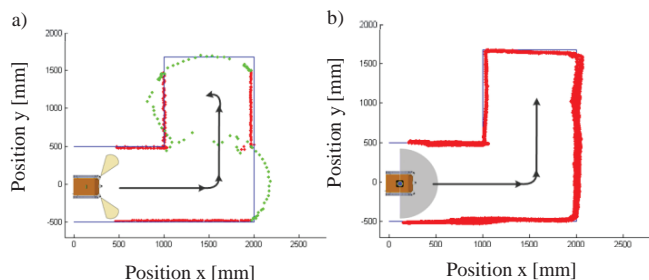


Fig. 7. Evaluation of the ROS driver in Traxbot v1 with different sensors. a) Ultrasonic Range Sensors integration; b) Hokuyo URG-04LX Laser Range Finder integration.

#### IV. RESULTS AND DISCUSSION

In order to experimentally evaluate the ROS driver, some tests were conducted using physical Arduino-based robots and

<sup>15</sup> <http://www.ros.org/wiki/stage>

stage<sup>15</sup>, which provides essential options like the information about the ground truth pose and odometry of virtual robots.

We present experimental tests that validate the aforementioned claims and we also show cooperative behaviors with real multi-robot systems, as well as mixed real and virtual robotic teams<sup>16</sup>. Therefore, the experiments will allow to evaluate the driver flexibility to different sensors, the driver portability to different robotic platforms and the driver expandability and integration with the existent ROS tools.

The first experiment aims to demonstrate the driver flexibility to integration of different sensors. The TraxBot v1 platform was equipped with a laser range finder (LRF) and its performance was compared against the native ultrasonic range sonars on a simple mapping task. The Hokuyo URG-04LX is a LRF classified as an Amplitude Modulated Continuous Wave (AMCW) sensor. In order to test the sonars performance, an L-shaped scenario of 2 m by 1.6 m was set up, with a 1 m width (Fig. 7). To perform this test, two lateral sonars placed at  $\pm 45$  degrees were used.

In this test, the robot movement relies solely on odometry. In Fig. 7a it can be seen in the first rectilinear motion, that the sonars readings are stable (red dots) and coincident with the ground truth scenario limits (blue line). Green dots represent the midpoint of sonars acoustic beam while turning. Some issues arise during the 90 degrees rotation, since the sonar beam cone has an opening of approximately 36 degrees, thus presenting a much poorer resolution than the LRF, as illustrated in Fig. 7a. In the case of Fig. 7b, the Hokuyo LRF was used to perform the same test. The overture of the laser was set to 180 degrees with a rate of 512 samples per reading. It is possible to observe some discrepancy in some readings especially at the end of the movement due the odometry position error accumulated during motion.

In the second experiment, the main goal is to demonstrate the portability of the driver to different robots and sensors, which enables testing in our Arduino-based robots the existent algorithms in ROS. Hence, a mapping task with the incorporation and interaction of drivers for different sensors like LRF and a joystick controller was performed. Along these lines, this time the Traxbot v2 platform was equipped with an Hokuyo LRF and teleoperated with a *WiiMote* for a mapping task using Hector Mapping [16], which is available in the *hector\_slam* stack<sup>17</sup>.

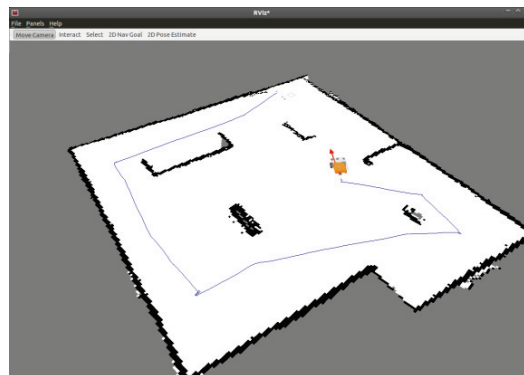


Fig. 8. Map generated by the Traxbot v2 with hector mapping.

<sup>16</sup> A video of the experiments is available at: <http://www.isr.uc.pt/~aaraujo/videos/Robotica2013>

<sup>17</sup> [http://www.ros.org/wiki/hector\\_slam](http://www.ros.org/wiki/hector_slam)

The teleoperation node runs on the eeePC netbook connected over the ROS network. The node subscribes to a topic which has the information of the *Wiimote* state and assigns functions for each pressed button, publishing then velocity commands, which are interpreted by the ROS driver, resulting then on motor commands. Additionally, the *hector\_mapping* node subscribes to the scans provided by the *hokuyo\_node* and publishes the estimate of the robot's pose within the map, while generating the map. Fig. 8 presents the resulting map in *rviz*, which was obtained with *hector\_mapping* on our experimental lab arena.

In the third and final experiment, we show not only the possibility to have coordinated behaviors with two physical robots, but also the possibility to include a third simulated robot running in stage which communicates with the other two forming a mixed team of real and virtual robots, as described in section III.B. In addition, we also integrate navigation capabilities in our robots, by running the *navigation stack*<sup>2</sup> with a known map, in this case, the map of our experimental lab arena (Fig.9).

The robots were commanded to navigate cyclically between a set of waypoints in the arena, as seen in the video of the experiment<sup>16</sup>. To further demonstrate their coordinating abilities, a common waypoint for all three robots was defined, and robots had to exchange messages through a shared ROS topic to avoid going to the common point at the same time. They would wait to go to the point at the center of the arena and priority was given to the robot who expressed firstly its intention to move to that point. All three robots were able to coordinate themselves in the environment without colliding to each other, due to the integration of the *navigation stack*<sup>2</sup>. Fig.10 presents a snapshot of *rviz*, illustrating the three robots moving in the arena.



Fig. 9. Experimental arena with a Traxbot v2 and a Stingbot cooperating with a virtual robot, running on stage.



Fig. 10. The three robots coordinating their behaviors by exchanging ROS messages (*rviz*).

## V. CONCLUSIONS AND FUTURE WORK

In this paper a solution for integrating Arduino-based robotic platforms in ROS, through the development of a ROS driver, was presented. It was shown the great advantages of integrating the platform with ROS middleware, enabling the usage of a wide range of tools and reducing the development time through code reuse. The robots, alongside with Arduino and ROS open-source development tools, present themselves as ideal platforms for educational robotics. Beyond providing access to all ROS tools, the driver also simplifies the robotic development by: *i*) supporting hardware abstraction to easily control the platform; *ii*) allowing for the extension and integration of all kinds of sensors; and *iii*) enabling multi-robot cooperation and coordination through the operation in a ROS network, both for real teams of homogeneous and heterogeneous robots, as well as hybrid teams of real and virtual agents, running the same code. Results from the experiments that were conducted demonstrate all these features and the insignificant overhead imposed by the driver was discussed.

## REFERENCES

- [1] Brooks, Rodney A., "New Approaches to Robotics", Science, vol. 253, pp. 1227- 1232, 13 September, 1991.
- [2] John-David Warren, Josh Adams and Harald Molle "Arduino Robotics", Springer Science and Business Media, 2011.
- [3] A. Araújo, D. Portugal, M. Couceiro, C. Figueiredo and R. Rocha, "TraxBot: Assembling and Programming of a Mobile Robotic Platform". In Proc. of the 4th International Conference on Agents and Artificial Intelligence (ICAART 2012), Vilamoura, Portugal, Feb 6-8, 2012.
- [4] M. Quigley, B. Gerkey, K. Conley, J. Faust, T. Foote, J. Leibs, E. Berger, R. Wheeler, and A. Y. Ng, "ROS: an open-source Robot Operating System," in Proc. Open-Source Software workshop of the International Conference on Robotics and Automation, Kobe, Japan, May, 2009.
- [5] B. Gerkey, R. Vaughan and A. Howard, "The Player/Stage Project: Tools for Multi-Robot and Distributed Sensor Systems", In Proc. of the Intl. Conf. on Advanced Robotics, pp. 317-323, Coimbra, Portugal, 2003.
- [6] G. Grisetti, C. Stachniss and W. Burgard, "Improved Techniques for Grid Mapping with Rao-Blackwellized Particle Filters", In IEEE Transactions on Robotics, 2006.
- [7] R. Rusu and S. Cousins, "3D is here: Point Cloud Library (PCL)", In Proc. of International Conference on Robotics and Automation (ICRA 2011), Shanghai, China, May 2011.
- [8] M. S. Couceiro, C. M. Figueiredo, J. M. Luz, N.M. F. Ferreira & R.P. Rocha. "A Low-Cost Educational Platform for Swarm Robotics", Int. Journal of Robots, Education and Art, Vol. 2(1), Feb., pp. 1-15, 2012.
- [9] Park, I. W. and Kim, J. O., "Philosophy and Strategy of Minimalism-based User Created Robots (UCRs) for Educational Robotics - Education, Technology and Business Viewpoint", International Journal of Robots, Education and Art, vol. 1, no. 1, 2011.
- [10] M. Kuipers, "Localization with the iRobot Create". In Proceedings of the 47th Annual Southeast Regional Conference ACM (ACM-SE 47), Clemson, South Carolina, USA, March 19-21, 2009.
- [11] B. Bagnall, "Maximum LEGO NXT: Building Robots with Java Brains". Variant Press, 2007.
- [12] Mondada, F. et al., "The e-puck, a Robot Designed for Education in Engineering". In Proc. of the 9<sup>th</sup> Conf. on Autonomous Robot Systems and Competitions, 1(1), pp. 59-65 2009.
- [13] Bonani, et al, "The MarXbot, "a Miniature Mobile Robot Opening new Perspectives for the Collective-Robotic Research" In Int. Conf. on Intelligent Robots and Systems, Oct. 18-22, 2010, Taipei, Taiwan, 2010.
- [14] Cummins J., Azhar, M.Q. and Sklar, E.: Using Surveyor SRV-1 Robots to Motivate CS1 Students. In: Proceedings of the AAAI 2008 Artificial Intelligence Education Colloquium, 2008.
- [15] S. Zaman, W. Slany and G. Steinbauer, "ROS-based Mapping, Localization and Autonomous Navigation using a Pioneer 3-DX Robot and their Relevant Issues", In Proc. of the IEEE Saudi International Electronics, Communications and Photonics Conference, Riad, Saudi-Arabia, 2011.
- [16] S. Kohlbrecher, J. Meyer, O. von Stryk and U. Klingauf, "A Flexible and Scalable SLAM System with Full 3D Motion Estimation", In Proc. of the IEEE International Symposium on Safety, Security, and Rescue Robotics (SSRR'2011), 50-55, Kyoto, Japan, Nov. 1-5, 2011.

# Image Processing Using Pearson's Correlation Coefficient: Applications on Autonomous Robotics

A. Miranda Neto, A. Correa Victorino, I. Fantoni, D. E. Zampieri, J. V. Ferreira and D. A. Lima

**Abstract**—Autonomous robots have motivated researchers from different groups due to the challenge that it represents. Many applications for control of autonomous platform are being developed and one important aspect is the excess of information, frequently redundant, that imposes a great computational cost in data processing. Taking into account the temporal coherence between consecutive frames, we have proposed a set of tools based on Pearson's Correlation Coefficient (PCC): (i) a Discarding Criteria methodology was proposed and applied as (ii) a Dynamic Power Management solution; (iii) an environment observer method based on PCC selects automatically only the Regions-Of-Interest; and taking place in the obstacle avoidance context, (iv) a method for Collision Risk Estimation was proposed for vehicles in dynamic and unknown environments. Applying the PCC to these tasks has not been done yet, making the concepts unique. All these solutions have been evaluated from real data obtained by experimental vehicles.

## I. INTRODUCTION

IN the last three decades, visual navigation for mobile robots or unmanned vehicles has become a source of countless research contributions. Some of these applications include: the development of Unmanned Aerial Vehicles (UAVs) that has been of interest for military applications. However, one limitation is their maximum flight time: they cannot carry large fuel payloads [3]. Future exploration of Mars requires long-endurance UAVs that use resources that are plentiful on Mars [4]. Finally, for military or civil purposes, vehicular applications have as objective the development of autonomous systems capable of driving a car autonomously in an urban environment and also to help the driver in its driver task [5], [6]. All these real-time platforms must provide the capability of perceiving and interacting with its neighbour environment, managing power consumption, CPU usage, etc.

The primary interest in this work, which is environment perception, is still in evolution. Part of this, machine vision, is an important tool that continuously monitors the way forward, proving appropriate road information in real time. Although extremely complex and highly demanding, thanks to the great

deal of information it can deliver, machine vision is a powerful means for sensing the environment and it has been widely employed to deal with a large number of tasks in the automotive field [7], but it can lead to some losses due to the processing time.

The problems of time-dependent and dynamic resource allocation have manifested themselves under different names, which include energy and memory consumption for the embedded systems [8]. It has been a topic of interest in the automotive industry [9].

In 1885, an empirical and theoretical development that defined regression and correlation as statistical topics were presented by Sir Francis Galton [10]. In 1895, Karl Pearson published the Pearson's Correlation Coefficient (PCC) [11]. The Pearson's method is widely used in statistical analysis, pattern recognition and image processing [12].

Based on Pearson's method, we have proposed a visual-perception system based on an automatic image discarding method as a simple solution to improve the performance of a real-time navigation system by exploiting the temporal coherence between consecutive frames [13]. This idea is also presented in the key-frame selection technique [14]. Further, we present the PCC as an environment observer method to save processor energy (power) consumption [15]. In the obstacle avoidance context for vehicles in dynamic and unknown environments, we have also proposed two others methods: a real-time collision risk estimation [16] and an extension of the environment observer method that selects automatically only the Regions-Of-Interest (ROI) [17].

To better understand these toolkit proposals, the Pearson's method is presented in Section II, followed by the Discarding Criteria method in Section III. Section IV introduces the Visual-Perception Layer based on Monocular Vision. Thereafter, the following sections are: Section V: Real-Time Dynamic Power Management, Section VI: Automatic Regions-Of-Interest Selection and Section VII: Collision Risk Estimation. Finally, the results are presented in Section VIII and the conclusions are given in Section IX.

## II. PEARSON'S CORRELATION COEFFICIENT (PCC)

The Pearson's method is widely used in statistical analysis, pattern recognition and image processing. Applications on the latter include comparing two images for image registration

Manuscript received Mars 24, 2013.

Arthur de Miranda Neto, Douglas Eduardo Zampieri and Janito Vaqueiro Ferreira are with the Autonomous Mobility Laboratory (LMA) at FEM/UNICAMP, Brazil.

Alessandro Correa Victorino, Isabelle Fantoni and Danilo Alves de Lima are with the Heudiasyc laboratory UMR 7253 CNRS/UTC, France.

purposes, disparity measurement, etc [12]. It is described in (1):

$$r_1 = \frac{\sum_i (x_i - x_m)(y_i - y_m)}{\sqrt{\sum_i (x_i - x_m)^2} \sqrt{\sum_i (y_i - y_m)^2}} \quad (1)$$

where  $x_i$  is the intensity of the  $i^{th}$  pixel in image 1,  $y_i$  is the intensity of the  $i^{th}$  pixel in image 2,  $x_m$  is the mean intensity of image 1, and  $y_m$  is the mean intensity of image 2.

### III. DISCARDING CRITERIA

The discarding criteria was presented as a simple solution to improve the performance of a real-time navigation system by choosing, in an automatic way, which images should be discarded and which ones should be treated at the visual perception system [13]. It was a new approach using the PCC.

In Fig. 1, basically, if the PCC indicates that there is a high correlation between a reference frame and another new frame acquired, the new frame is discarded without being processed (for example, the system can repeat a last valid command). Otherwise, the frame is processed and it is set as the new reference frame for the subsequent frame.

The inclusion of an automatic image discarding method leads in a reduction of the processing time. Although the system spends some milliseconds computing the PCC, it gains much more time, in some cases, discarding more than 90% of the images [18]. However, it is important to notice that this percentage is not dependent on the video sequence or image size, but on the obstacles / objects influence.

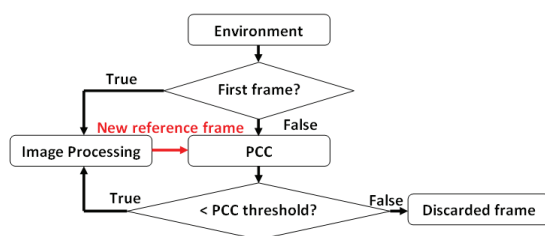


Fig. 1 – Discarding criteria [13].

### IV. VISUAL-PERCEPTION LAYER BASED ON MONOCULAR VISION

The perception of the environment is a major issue in autonomous vehicles. The perception layer uses many types of sensors [5]. The vision-based sensors are defined as passive sensors and the image scanning is performed fast enough for mobile robots. However, vision sensors are less robust than millimeter-wave radars in foggy, night, or direct sun-shine conditions [7]. All range-based obstacle detection systems have difficulty for detecting small or flat objects on the ground, and range sensors are also unable to distinguish between different types of ground surfaces [19]. However, the main problem with the use of active sensors is represented by interference among sensors of the same type, hence, foreseeing

a massive and widespread use of these sensing agents, the use of passive sensors obtains key advantages [7].

On the safety front, the progressive safety systems will be developed through the manufacturing of an “intelligent bumper” peripheral to the vehicle in answering new features as: blind spot detection, frontal and lateral pre-crash, etc. The objective in terms of cost to fill ADAS functions has to be very lower than the current Adaptive Cruise Control (500 €) [20].

Aware that in the majority of the autonomous systems, the machine-vision system is working together with other sensors, added to its low cost, this work uses a monocular vision-based sensor. Because it uses simple techniques and fast algorithms, the system is capable to achieve a good performance, where the compromise between processing time and images acquisition is fundamental.

### V. REAL-TIME DYNAMIC POWER MANAGEMENT

#### A. Related Work

Autonomous robots can perform desired tasks in unstructured environments without continuous human guidance. These systems have some degree of self-sufficiency. Self-configuring, self-optimizing and self-protecting are still an open question. For advances in the energy autonomy, robots will need to extract energy from the environment. In many ways robots will face the same problems as animals [9].

In this way, a system must therefore have knowledge of its available resources as well as its components, their desired performance characteristics and their current status. Dynamic Power Management (DPM) is a design methodology for dynamically reconfiguring systems to provide the requested services and performance levels with a minimum number of active components or a minimum load on such components. It encompasses a set of techniques that achieves energy-efficient computation by selectively turning off (or reducing the performance of) system components when they are idle (or partially unexploited) [21]. An autonomous robot planning tasks must be aware of power resources available [9]. Moreover, most electronic circuits and system designs are confronted with the problem of delivering high performance with a limited consumption of electric power, and for achieving highly energy-efficient computation is a major challenge in electronic design [21]. In this context, a DPM and Real-Time Scheduling techniques were presented in [22]. They were applied to reduce the power consumption of mobile robots. The DPM dynamically adjusts power states of components adaptive to the task’s need, reducing the power consumption without compromising system performance.

Finally, a case study of mobile robot’s energy consumption and conservation showed that motion accounts for less than 50% of the total power consumption [22]. This implies that other power consumers like computation have a big impact on power consumption [9]. These values were estimated by dividing the battery capacity by the time the computer can run with a fully charged battery when running different programs [22].

### B. Logical Dynamic Optimization

This section presents a logical dynamic optimization methodology. Based on the PCC variation and by exploiting the temporal coherence between consecutive frames, it is proposed a new environment observer method. This monocular-vision system observes if there are no significant changes in the environment, permitting that some logical components may be shut down to save processor energy consumption, and/or to make the CPU available for running concurrent processes.

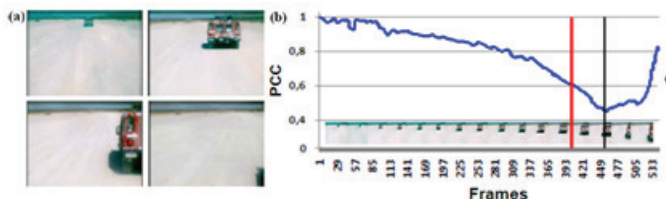


Fig. 2 – (a): The frames of the desert video [23]; (b) From a reference frame, its correlation with all others; Blue line: the Pearson's correlation in (1); The vertical black line: maximum point before collision; The vertical red line: Empirical Risk-of-Collision.

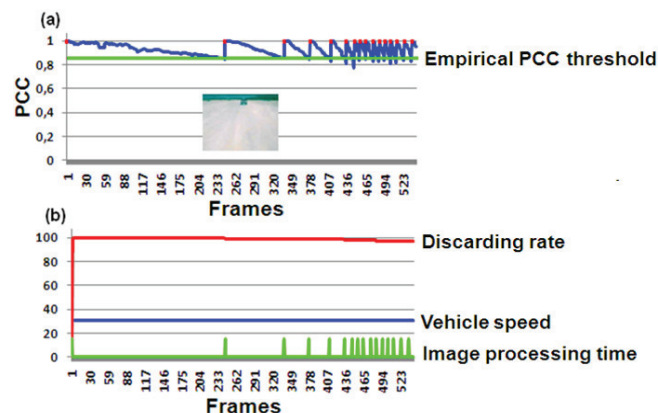


Fig. 3 – Desert video [23]: (a) Green line: empirical PCC threshold equal to 0.85; Above of the green line it presents the discarded images; Red points: reference frames; (b) Red line: discarding rate; Blue line: vehicle speed; Green line: hypothetical image processing time (15ms).

A robot can have many periodic tasks, such as motor and sensor control, sensing data reading, motion planning, and data processing. It may also have some aperiodic tasks, such as obstacle avoidance and communication. Moreover, for mobile robots, the tasks' deadlines are different at different traveling speeds. At a higher speed, the periodic tasks have shorter periods [22].

The Fig. 2 (a) shows an autonomous displacement through the Mojave Desert [23], where the robot Stanley has used an average speed of 30.7 km/h [24]. In Fig. 2 (b), due to PCC nature, taking a reference frame, in this case, the first frame of the Fig. 2 (a), a lower value of correlation is achieved when it is closer to the vehicle. That is, when the derivative approaches its maximum point, there is the obstacle detection.

The Fig. 3 (a) shows the same case from a different representation. From an empirical PCC threshold equal to 0.85 (green line), the reference frames (red points) are closer when it is near to an obstacle. Above of the green line all discarded

images.

Whereas the main problem that has to be faced when real-time imaging is concerned and which is intrinsic to the processing of images is the large amount of data [7], and as was presented in [15], the accumulated time of an image processing time (15ms) versus the gain obtained by using the discarding criteria could allow significant savings in CPU power consumption. In this case, the discarding rate remained over 80%.

### VI. AUTOMATIC REGIONS-OF-INTEREST SELECTION BASED ON PCC (ROI SELECTION)

According to the Pearson's correlation, in a certain analysis window (pair of frames), if the obstacle/object occupies a big portion of the scene, the PCC threshold tends to be low. Conversely, if obstacle/object occupies a small portion of the frame, it means that it is away from the vehicle and the system will have time enough to react. However, in real-time obstacle avoidance, for example, where are these interest points/pixels? Or, in a sequence analyzed, which pixels of the pair of images contributed most to the Pearson's coefficient computed? Which of them really need to be reprocessed?

Right after the Pearson's correlation in (1), it has  $x_m$  and  $y_m$ , respectively: the mean intensities of images 1 and 2. From these values, it begins again the process's correlation:

$$r_2 = \frac{\sum_i (x_i - r_{1Xm})(y_i - r_{1Ym})}{\sqrt{\sum_i (x_i - r_{1Xm})^2} \sqrt{\sum_i (y_i - r_{1Ym})^2}} = \begin{cases} -1 \\ or \\ +1 \end{cases} \quad (2)$$

where  $x_i$  is the intensity of the  $i^{th}$  pixel in image 1,  $y_i$  is the intensity of the  $i^{th}$  pixel in image 2,  $r_{1Xm}$  and  $r_{1Ym}$  were obtained in (1): i.e.:  $x_m$  and  $y_m$ .

For each pair of pixels analyzed in (2), the only possible result is: [-1 or +1]. That is, all pixels with intensities below these means will be candidates for interest points (ROI). Fig. 4 (c), (g) and (k) present this process, where the red pixels (interest points) represent  $r_2 = -1$ .

Taking as base an image resolution equal to image 96x72, by processing only when  $r_2 = -1$ , in desert video were processed about 205 thousand points, instead of 3.7 million points. In off-road context were processed about 10 million points, instead of 48 million points [17], [25].

### VII. COLLISION RISK ESTIMATION

#### A. Related work

In the obstacle avoidance context, the collision warning algorithms typically issue a warning when the current range to an object is less than the critical warning distance, where the safety can be measured in terms of the minimum time-to-collision (TTC) [26]. To calculate the TTC several techniques

are presented in the literature [27], [28]. Measuring distances is a non-native task for a monocular camera system [27]. However, TTC estimation is an approach to visual collision detection from an image sequence.

Optical flow may be used to TTC [29], [30]. However, the calculation of TTC from an optical flow has proven impractical for real applications in dynamic environment [28]. Additionally, gradient-based methods can be used with a certain degree of confidence in environments such as indoors where the lighting conditions can be controlled. It is computationally expensive [31]. On the other hand, Inverse Perspective Mapping allows to transform a front facing image to a top down bird's eye view [32]. However, those equations have parameters that depend on the camera's position and its viewing angle [33].

In this way, we have presented a novel approach to obtain Collision Risk Estimation (CRE) based on PCC from a monocular camera [16].

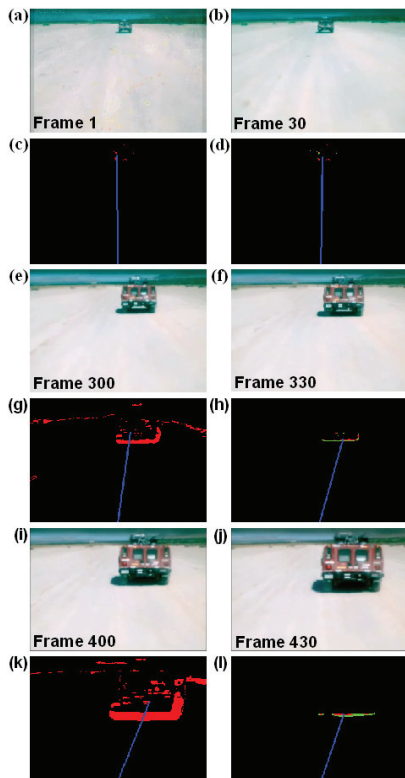


Fig. 4 – (a), (b), (e), (f), (i) and (j) are the frames of the desert video [23]; (c), (g) and (k) are the interest points from the process's correlation in (2); (d), (h) and (l) are the ITA results [17].

### B. Collision Risk Estimation (CRE)

By exploiting the temporal coherence between consecutive frames, this section presents an algorithm which estimates the CRE in dynamic and unknown environments.

The Fig. 4 (a) shows an autonomous displacement through the Mojave Desert [23], where the robot Stanley has used an average speed of 30.7 km/h [24]. In Fig. 2 (b), taking a reference frame, i.e. the first frame of the Fig. 4 (a), a lower value of correlation is achieved when it is closer to the vehicle, Fig. 2 (b): black line. That is, when the derivative approaches

its maximum point, there is the obstacle detection. Fig. 2 (b): red line presents an Empirical Risk-of-Collision,  $R_c = 1 - 0.6$ .

Taking into account  $R_c$ , the CRE is estimate in (3):

$$CRE_s = \frac{R_c}{(1 - r_1)} \quad (3)$$

where 1 (one) represents the reference frame and  $r_1$  was obtained in (1) and  $R_c = 1 - 0.6$ .

### C. Obstacle Direction: Interactive Thresholding Algorithm

From the interest points known in Section VI, this section presents the Interactive Thresholding Algorithm (ITA) [17] that reclassifies the background and foreground pixels based on Otsu Thresholding Method [34].

Taking as base an image resolution equal to image 96x72, the ITA process will be performed N-times until the result is invariably, or until the red points (foreground) are less than 100. For example, Fig. 4 (d), (h) and (l) present the final result of this process, where the green points were eliminated in the last iteration. Finally, the blue line indicates the object direction based on the center of area of the red points.

TABLE I  
 RELATIONSHIP BETWEEN FRAMES OF THE FIG. 4  
 AND COLLISION RISK ESTIMATION (CRE)  
 STANLEY AVERAGE SPEED: 30.7 KM/H [24]

Frames	$(1 - r_1)$	Variation in the Range	Risk of Collision	CRE in Seconds	Distance in Meters
1–30	(1-0.968)	0.032	$(R_c / 0.032)$	12.43s	106m
300–330	(1-0.907)	0.093	$(R_c / 0.093)$	4.31s	36.75m
400–430	(1-0.800)	0.200	$(R_c / 0.200)$	2.00s	17.08m

### D. Collision Risk Estimation: Case Study

The Table I presents the CRE from the Fig. 4:

- ✓ Frames column: it represents the pairs of frames [1–30], [300–330] and [400–430], respectively: Fig. 4: [(a), (b)], [(e), (f)] and [(i), (j)].
- ✓  $(1 - r_1)$  column: the Pearson's correlation obtained in (1).
- ✓ Variation in the Range column: the PCC variation between the first and last frames analyzed.
- ✓ CRE Second column: it estimates in (3).
- ✓ Distance Meters column: it presents an estimate in meters from the average speed of 30.7 Km/h [24].

## VIII. EXPERIMENTAL RESULTS

Besides the experimental DARPA test-banks [23], the results here were obtained using an experimental vehicle (Fig. 19) on real, dynamic and unknown environments. It was tested on a 2.5GHz Intel Core 2 Quad processor, 3.48 GB RAM, Microsoft Windows XP Professional SP3, Visual Studio C++ and OpenCV 2.1.0. In order to reduce the number of data, it also includes the resolution reduction of image (to 96x72). Following the same structure presented earlier:

- ✓ Subsection A: Real-Time Dynamic Power Management;
- ✓ Subsection B: Automatic Regions-Of-Interest Selection;
- ✓ Subsection C: Collision Risk Estimation.

A. Section V: Real-Time Dynamic Power Management

The Figures 15 and 16 show the performance of this method in real, dynamic and unknown environments. For all these cases, the discarding rate remains over 65%. Fig. 16 (a) presents the computational mean time of a horizon finding algorithm [35] in unknown and urban environment. In this way, from an empirical PCC threshold equal to 0.85, the red line shows that the computational mean time was 5.09 ms, against 15.62 ms without the discarding criteria. In Fig. 17 (b), above the green line, it presents the discarded images. A video showing the application of this method is available in [36].

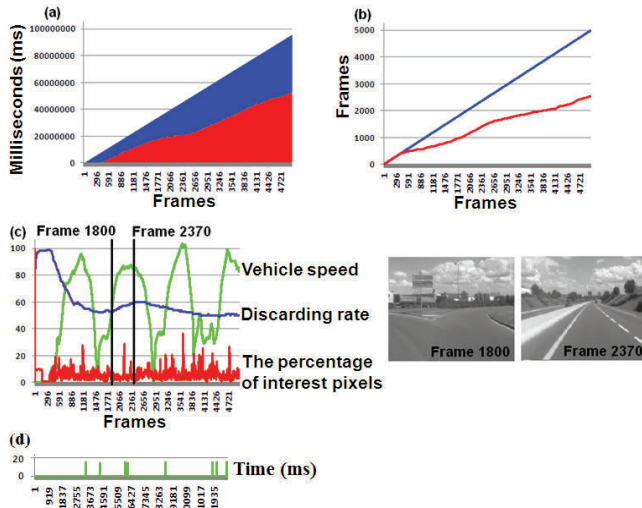


Fig. 15 – Real environment: Heudiasyc Laboratory in France, 2010: (a) In blue: the cumulative impact computations (ms); In red: the cumulative computations (ms) by using the discarding criteria. (b) In blue: the number of frames; In red: the number of discarded frames by using the discarding criteria. (c) In blue: discarding rate; In red: the percentage of interest pixels; In green: The vehicle speed; In the analysis window, represented by two black vertical lines, the performance evaluation of the discarding criteria in acceleration from 37 Km/h to 86 Km/h; (d) Green line: computational time.

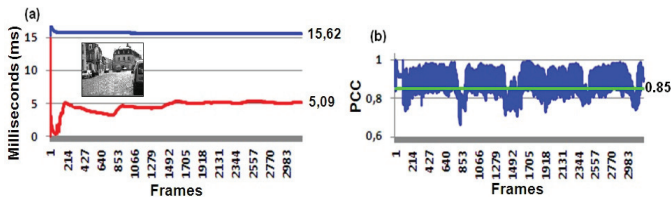


Fig. 16 – Real environment: Heudiasyc Laboratory in France, 2005: The computational mean time of a horizon finding algorithm [35] in unknown and urban environment; (a) The red line: the computational mean time was 5.09 ms with the discarding criteria; (a) The blue line: the computational mean time was 15.62 ms without the discarding criteria; (b) The green line: an empirical PCC threshold equal to 0.85; (b) In blue: DPM performance based on discarding criteria: above the green line, it presents all discarded images.

B. Section VI: Automatic Regions-of-Interest Selection

As has been shown in Section VI, at first stage of testing, in order to evaluate the proposed algorithm performance, it was used an urban and real experimental test-bank obtained using the vehicle shown in Fig. 19. Results for different types of image texture (road surfaces) were selected and its results are presented in [25]. For obstacle avoidance task, the Fig. 17 presents results at high speed on real-time conditions. A video showing the application of this method is available in [37].

C. Section VII: Collision Risk Estimation

Fig. 18 and Table II present the performance of the Collision Risk Estimation (CRE) in dynamic and unknown environment. These results were obtained in real conditions using the vehicle shown in Fig. 19.

Since in real conditions this monocular-vision system has been designed to investigate only a small portion of the road ahead of the vehicle, where the absence of other vehicles has been assumed [11], the Fig 18.a-(\*)a presents the fix analysis region (yellow line). As shown in [16], the computational mean time of the CRE process was equal to 7.8 ms. A video showing the application of this method is available in [38].

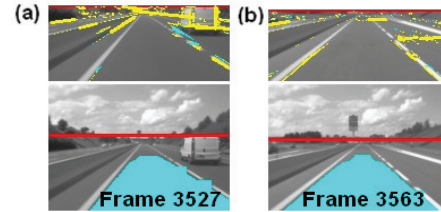


Fig. 17 – Real environment: Heudiasyc Laboratory in France, 2010: After the horizon finding algorithm performance [35], red line: (a) Speed 97.01 Km/h, the interest pixels represent 5% of the image; (b): Speed: 100.2 Km/h, the interest pixels represent 2% of the image.

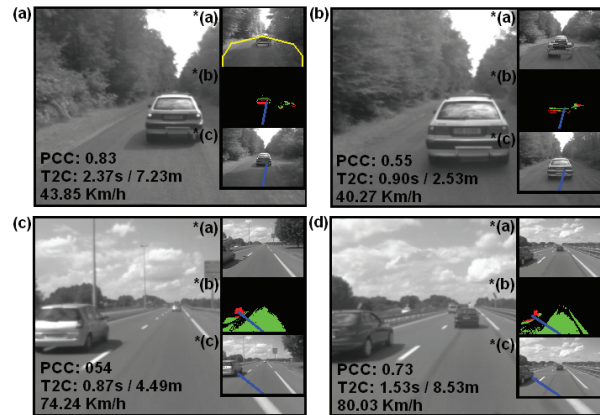


Fig. 18 – The results in real conditions: \*(a): the reference frame after the region-merging algorithm presented in [16]; \*(b) ITA results [17]; \*(c) Obstacle direction based on the center of area of the red points.

TABLE II  
 RELATIONSHIP BETWEEN FRAMES OF THE FIG. 18  
 AND COLLISION RISK ESTIMATION (CRE)

Frames	(1- $r_1$ )	Variation in the Range	Risk of Collision	CRE in Seconds	Distance in Meters
(a) 1001	(1-0.8315)	0.1685	( $R_c / 0.1685$ )	2.37s	7.23m
(b) 1024	(1-0.5584)	0.4416	( $R_c / 0.4416$ )	0.90s	2.53m
(c) 1139	(1-0.5411)	0.4589	( $R_c / 0.4589$ )	0.87s	4.49m
(d) 4654	(1-0.7394)	0.2606	( $R_c / 0.2606$ )	1.53s	8.53m

IX. CONCLUSION

This work presents a simple solution to improve the performance of a real-time perception system. The experiments showed that the inclusion of an automatic image discarding method based on PCC did result in a reduction of the processing time. This technique is also presented as an environment observer method (DPM) and futures work will

provide a real experimental test-bank to evaluate the real energy consumption economy in terms of electrical current used by the visual machine. Following, instead of processing all image pixels, an extension of the DPM that selects automatically only the ROI was proposed in order to perform an obstacle avoidance task in real time. Finally, a real-time algorithm which allows to calculate the risk of collision. In order to validate this proposal, futures work would be focused to provide ground truth measurements from a front mounted radar and/or LIDAR system. A remarkable characteristic of all methodologies presented here is its independence of the image acquiring system and of the robot itself. The same implementation can be uses in different mobile robots and may be extended to other sensors.



Fig. 19 – The experimental vehicle at Heudiasyc Laboratory in France.

#### ACKNOWLEDGMENT

The authors wish to thank Mr. Gerald Dherbomez for your support in data acquisition.

#### REFERENCES

- [1] F. Bonin-Font, A. Ortiz, G. Oliver, (2008), "Visual Navigation for Mobile Robots: A Survey", *Journal of Intelligent and Robotic Systems*.
- [2] B. Kim, P. Hubbard, D. Neculescu, (2003), "Swarming Unmanned Aerial Vehicles: Concept Development and Experimentation, A State of the Art Review on Flight and Mission Control", DRDC-OTTAWA-TM-2003-176; Technical Memorandum.
- [3] S. R. Anton, D.J. Inman, (2008), "Energy Harvesting for Unmanned Aerial Vehicles", In: *Proceeding of SPIE*.
- [4] R. Finkelstein, Robotic Technology Inc, (2009), "Energetically Autonomous Tactical Robot and Associated Methodology of Operation", Patent Application n°: 12/612,489, US 2010/0155156 A1.
- [5] S. Thrun, et al. (2006), "Stanley, the robot that won the DARPA Grand Challenge", *Journal of Robotic Systems*, Volume 23 , Issue 9, DARPA Grand Challenge, 661–692.
- [6] O. Gietelink, J. Ploeg, B. De Schutter, and M. Verhaegen, (2006) "Development of advanced driver assistance systems with vehicle hardware-in-the-loop simulations", *Vehicle System Dynamics*, vol. 44, no. 7, pp. 569–590.
- [7] M. Bertozzi, A. Broggi and A. Fascioli, (2000), "Vision-based intelligent vehicles: state of the art and perspectives". *Robotics and Autonomous systems* 32, 1–16.
- [8] P. Bouyer et al., (2010), "Quantitative analysis of real-time systems". *Journal Communications of the ACM*.
- [9] A. Deshmukh, P. A. Vargas, R. Aylett and K. Brown, (2010), "Towards Socially Constrained Power Management for Long-Term Operation of Mobile Robots", 11th Conference Towards Autonomous Robotic Systems, Plymouth, UK.
- [10] J. L. Rodgers and W. A. Nicewander, (1988), "Thirteen Ways to Look at the Correlation Coefficient", *The American Statistician*, 42.
- [11] K. Pearson, (1895), *Royal Society Proceedings*, 58, 241.
- [12] Y. K. Eugene and R.G. Johnston, "The Ineffectiveness of the Correlation Coefficient for Image Comparisons", Technical Report LA-UR-96-2474, Los Alamos, 1996.
- [13] A. Miranda Neto, L. Rittner, N. Leite, D. E. Zampieri, R. Lotufo and A. Mendeck, (2007), "Pearson's Correlation Coefficient for Discarding Redundant Information in Real Time Autonomous Navigation System", *IEEE Multi-conference on Systems and Control (MSC)*, Singapura.

- [14] W. Wolf, (1996), "Key frame selection by motion analysis," in *Proc. IEEE Int.Conf. Acoustics, Speech, and Signal Processing*.
- [15] A. Miranda Neto, A. C. Victorino, I. Fantoni and D. E. Zampieri, (2011), "Real-Time Dynamic Power Management based on Pearson's Correlation Coefficient", *IEEE International Conference On Advanced Robotics (ICAR 2011)*, Tallinn, Estonia.
- [16] A. Miranda Neto, A. C. Victorino, I. Fantoni and J. V. Ferreira, (2013), "Real-Time Collision Risk Estimation based on Pearson's Correlation Coefficient", *IEEE Workshop on Robot Vision (WoRV)*, Florida, US.
- [17] A. Miranda Neto, A. C. Victorino, I. Fantoni and D. E. Zampieri, (2011), "Automatic Regions-of-Interest Selection based on Pearson's Correlation Coefficient", *IEEE International Conference on Intelligent Robots and Systems (IROS), ViCoMoR*, California, US.
- [18] A. Miranda Neto, L. Rittner, N. Leite, D. E. Zampieri and A. C. Victorino, (2008), "Nondeterministic Criteria to Discard Redundant Information in Real Time Autonomous Navigation Systems based on Monocular Vision", *ISIC Invited Paper, IEEE Multi-conference on Systems and Control (MSC)*, San Antonio, Texas, US.
- [19] I. Ulrich and I. Nourbakhsh, (2000), "Appearance-Based Obstacle Detection with Monocular Color Vision", *Proceedings of the AAAI National Conference on Artificial Intelligence*, July/August 2000.
- [20] Radio Spectrum Committee, European Commission, Public Document, Brussels, RSCOM10–35, <http://ec.europa.eu/> [Dec. 02, 2010].
- [21] L. Benini, A. Bogliolo, and G. D. Micheli, (2000), "A Survey of Design Techniques for System-Level Dynamic Power Management", *IEEE Transactions on Very Large Scale Integration Systems*, 8(3):299-316.
- [22] H. Y. L. C. Yongguo Mei, Yung-Hsiang Lu, (2005), "A case study of mobile robot's energy consumption and conservation techniques", in *12th IEEE ICAR*, pp. 492--497.
- [23] DARPA 2005. "DARPA Grand Challenge", <http://www.darpa.mil/grandchallenge05/> [June 10, 2006]
- [24] Stanford Racing Team's Entry In The 2005 DARPA Grand Challenge, <http://www.stanfordracing.org/> [June 10, 2006]
- [25] A. Miranda Neto, (2011), "Embedded Visual Perception System applied to Safe Navigation of Vehicles", PhD Thesis, UNICAMP-Brazil/UTC-France.
- [26] O. J. Gietelink, J. Ploeg, B. Schutter, and M. Verhaegen, (2009), "Development of a driver information and warning system with vehicle hardware-in-the-loop simulations". *Mechatronics*, 19:1091–1104.
- [27] D. Müller, J. Pauli, C. Nunn, S. Görmer, S. Müller-Schneiders, (2009), "Time To Contact Estimation Using Interest Points", In: *IEEE Proceedings of the International Conference on Intelligent Transportation Systems (ITSC 2009)*, St.Louis, USA.
- [28] A. Negre, C. Braillon, J. Crowley and C. Laugier, (2006), "Real-time Time-To-Collision from variation of Intrinsic Scale", *INRIA base, Proc. of the Int. Symp. on Experimental Robotics*.
- [29] A. Beyeler, J. C. Zufferey, D. Floreano, (2009), "Vision-based control of near-obstacle flight", *Autonomous Robots*, 27(3): 201–219.
- [30] F. Ruffier and N. Franceschini, (2005), "Optic flow regulation: the key to aircraft automatic guidance", *Robotics Autonomous Systems* 50, pp. 177–194.
- [31] M. Mesbah, (1999), "Gradient-based optical flow: a critical review", *Proc. of the Fifth Int. Symp. on Signal Processing and Its Applications. ISSPA '99*, 1, (1999), 467–470.
- [32] H. A. Mallot, H. H. Bulthoff, J. J. Little, S. Bohrer, (1991), "Inverse perspective mapping simplifies optical flow computation and obstacle detection", *Biological Cybernetics* 64 (1991) 177–185.
- [33] S. Tan, J. Dale, A. Anderson, and A. Johnston, (2006), "Inverse perspective mapping and optic flow: A calibration method and a quantitative analysis," *Image and Vision Computing*, vol. 24, 153–165.
- [34] N. Otsu, (1978), "A threshold selection method from gray-level histogram". *IEEE Transactions on Systems, Man, and Cybernetics*.
- [35] A. Miranda Neto, A. C. Victorino, I. Fantoni and D. E. Zampieri, (2011), "Robust Horizon Finding Algorithm for Real Time Autonomous Navigation based on Monocular Vision", *IEEE International Conference on Intelligent Transportation Systems (ITSC 2011)*, Washinton DC, US.
- [36] <http://www.youtube.com/watch?v=XaZndmMaieE> [Jan. 31, 2013]
- [37] <http://www.youtube.com/watch?v=VcUQVC1F8Xw> [Jan. 31, 2013]
- [38] <http://youtu.be/J8YuZJFExk> [Jan. 31, 2013]

# Multi-Joint Gripper with Stiffness Adjuster

Koichi Koganezawa

Dep. of Mechanical Engineering  
Tokai University  
Hiratsuka, Kanagawa, Japan  
kogane@keyaki.cc.u-tokai.ac.jp

Takumi Tamamoto

Dep. of Mechanical Engineering  
Tokai University  
Hiratsuka, Kanagawa, Japan

**Abstract**— This paper proposes a multi-joint-gripper that achieves envelope grasping of unknown shape objects. Proposed mechanism is based on a chain of Planetary Gear Systems (PGS) controlled by only one motor. It also has a Variable Stiffness Mechanism (VSM) that controls joint stiffness to relieve interfering effects suffered from external or internal force/torque and to achieve a dexterous grasping. The experiments elucidate that the developed gripper achieves envelop grasping; the posture of the gripper automatically fits the shape of the object with no sensory feedback. And they also show that the VSM effectively works to relieve external interfering. This paper shows the detail of the mechanism and the experiments of its motion.

**Keywords**—Envelope Grasping; Multi-Joint-Gripper; Variable-Stiffness

## I. INTRODUCTION

The fatal disaster of the Fukushima nuclear plant being brought about by the earthquake and subsequently assaulting tsunami on March 11 in 2011 revealed the disability for the current robot technology to work around when it faced with such disastrous environments. The disaster also prompts to develop a new type of autonomous robot that should have tough and effective hand or gripper. The forthcoming robots used in an ultimate environment should satisfy the following requirements.

**Back-drivability (BD):** End-effectors always interact with external environment, of which effect should not be expected to be predictable. This fact requires the end-effector to have some “resiliency” to external interaction, which is interpreted as “back-drivability” of the joints in the technical point of view.

**Inherently safe design (ISD):** This property is much related to the BD in the sense that the end-effector is never harmful to external environment (especially to human). In addition to the BD, ISD requires some items as follows.

(a) Any electric/electronic devices or sensors should not be equipped on the portions that directly contact with external objects. Since the robots have to cope with expected severe environments, such as electromagnetic or radio-active fields.

(b) According to (a) the controller cannot much rely on the feedback from sensors such as tactile or pressure sensors.

ISD does not completely deny using sensory feedback, which might be helpful to accomplish some dexterous and precise motion of the end-effector if a measure against radio active noise is satisfactory. Therefore ISD requires that some primitive motions of the end-effector should be provided

without sensory feedback, in other words, mechanically, but it allows using the sensory feedback as subsidiary measures.

**Simple Control (SC):** The control should be as simple as possible. This requirement will be achieved along with pursuing the above BD and ISD requirements. BD will reduce the control burden to determine the end-effector’s motion when they interact with external objects. ISD also provides a simple control that does not much rely on the sensory feedback.

But most of all, the SC requirement prompts us to reduce the end-effector’s DOF as far as possible.

In this paper, we propose a multi-joint gripper that achieves envelope grasping for unknown-shape object under fulfilling the BD, ISD and SC requirements described above.

The pioneering work in this field will be the “soft gripper” developed by Hirose and Umetani[1]. Since then the wire driven series of joint became the most typical mechanical architecture that has been followed by a lot of subsequent studies[2-6]. The mechanisms proposed in these studies will satisfy the BD, ISD and SC requirements or a part of them, but the most crucial problem of these studies resides in using much number of wires for driving series of joints, which gives rise to the following troubles on actual assembling and controlling.

(a) Elasticity of the wire combined with the friction with pulleys sometimes causes unpredictable vibratory behavior of the gripper.

(b) There exists singular posture of the gripper, especially of those having much number of serial joints.

(c) Binding wires with appropriate tension is much cumbersome than one imagines and the tension is temperature dependent.

So this paper proposes a novel mechanism without using wire and pulley on its power transmission parts. It consists of a train of planetary gear system, of which fundamental function is the same as those of author’s another study [7]. We also propose a mechanism of adjusting stiffness of joints, which allows the gripper to vary the joint stiffness according to interactive conditions with grasping objects.

This paper is organized as follow. In the following section it shows a mechanism of the proposed gripper using planetary gear system, the principle of its motion and shape-fitting property to show it having the back-drivability. In the third section it shows the variable stiffness mechanism. The forth section is devoted to show the development of the machine

and its motion testing. The last section is devoted to some conclusive remarks.

## II. ONE DOF DRIVE MECHANISM

### A. Active/Passive amalgamation using planetary gears chain

We consider a planar multi-joint gripper of which driving torque is generated by only one motor and is transmitted to a distal end of the gripper via serially connected rotary joints. Fig.1 shows the outline of the driving mechanism of the proposed gripper. The planetary gear system (PGS) [Fig.1(a)] takes a crucial role for it, which is used as a “two inputs one output transmitter”. The rotation of the motor located at the proximal base is transmitted to the sun gear (SG) of the PGS that is located at the first joint by a timing belt. The carrier’s rotation is transmitted to the SG at the subsequent PGS by the timing belt. The link rotates together with the corresponding inner gear (IG). The carrier’s rotation is suppressed by the spring that is depicted as a simple tension spring in Fig.1(b) to explain the role on the fundamental motion of the gripper, but of which tension is controlled in the variable stiffness mechanism explained in the next section.

The mechanism, therefore, allows an amalgamation of the two inputs; one is an active torque input into the SG and the other is a passive torque input into the carrier with the spring. The beneficial points of this mechanism are as follows:

(a) Each joint is uncoupled with respect to torque transmission. By contrast, some mechanisms proposed in the past studies are coupled because all of the joints are remotely controlled from the base by using elongated wires[1][2], which will sometimes cause the gripper to take irreversible singular postures.

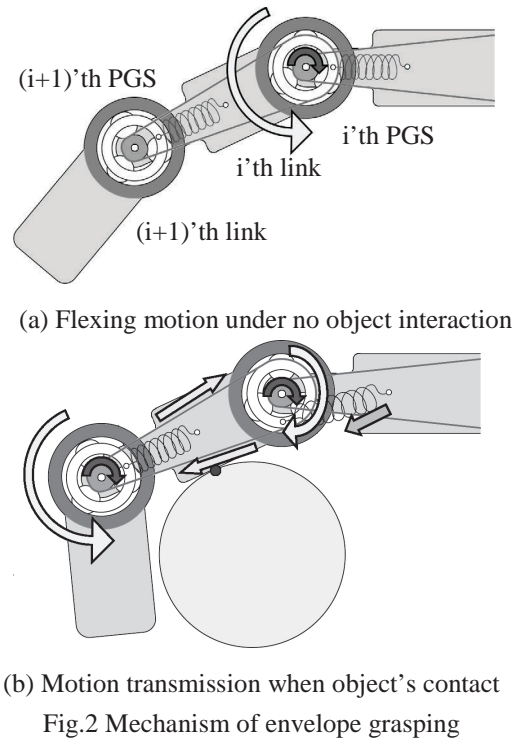
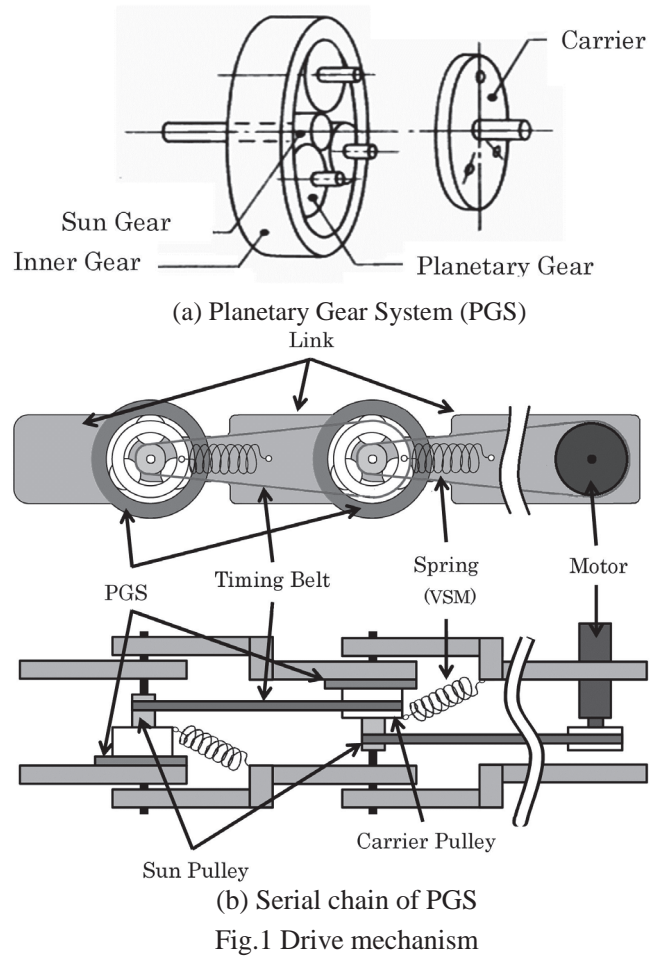
(b) It is recognized that elasticity of the system is concentrated on the springs, although the elasticity of timing belts exist but can be negligible. Moreover, the passive torque due to springs and the active torque due to the motor are separated. These facts make kinetic and dynamic analysis of the system very simple.

### B. Synergic rotation of all joints

Fig.2(a) explains the motion of the gripper when it suffers from no external interaction. The  $i$ 'th SG's clockwise rotation induces the  $i$ 'th IG's and the  $i$ 'th link's anticlockwise rotation, since the  $i$ 'th carrier is suspended of its rotation by the spring. But the  $(i+1)$ 'th SG's rotation happens because the timing belt is also rotated together with the  $i$ 'th link. The rotation angle of the  $(i+1)$ 'th SG is determined by the ratio between the diameter of the pulley attached at the  $(i+1)$ 'th SG and those of the  $i$ 'th carrier. So that the relative rotation of the  $(i+1)$ 'th IG with respect to the  $i$ 'th unit is also induced. As a result synergic rotation of all joints with one DOF is achieved. The relative angle of the  $i$ 'th joint  $\theta_i$  is determined as,

$$\theta_i = -\frac{S}{I}\theta_{Si} + \frac{S+I}{I}\theta_{Ci} \quad (1)$$

where  $\theta_{Si}$  and  $\theta_{Ci}$  is rotation angles of the  $i$ 'th SG and the  $i$ 'th carrier respectively, “S” and “I” are the teeth numbers of the



SG and the carrier respectively. Therefore, if  $\theta_{Ci} \cong 0$ ,  $\theta_i$  is almost determined by  $\theta_{Si}$  and since typically  $S / I \cong 1/3$ ,  $\theta_i$  takes speed-reduction with respect to the  $\theta_{Si}$  about 1/3. If  $\theta_i$  becomes zero due to the contact of the object,  $\theta_{Ci}$  is determined by  $\theta_{Ci} = S / (S + I) \theta_{Si}$  and this is transmitted to the next unit.

### C. Envelope grasping

Fig.2(b) describes how the gripper behaves when the  $i$ 'th link is hampered its flexing motion by a grasping object. It also prevents the  $i$ 'th IG's rotation. In this state the further clockwise rotation of the  $i$ 'th SG induces the clockwise rotation of the  $i$ 'th carrier with expanding the spring, which is transmitted to the  $(i+1)$ 'th SG to bring about further rotation of the  $(i+1)$ 'th IG and the  $(i+1)$ 'th link to wrap the object. As a result an envelope grasping is achieved as a continual motion of the gripper's synergic flexion with no additional switching operation. The rotation angles of the  $i$ 'th SG  $\theta_{Si}$  is determined by the  $(i-1)$ 'th joint and the carrier's angles as,

$$\theta_{Si} = -\frac{P_C}{P_S}(\theta_{Ci-1} - \theta_{i-1}) \quad (i = 2 \sim n) \quad (2)$$

with,  $P_C$  and  $P_S$ ; the teeth numbers of the pulleys attached to carrier and SG respectively.

## III. VARIABLE STIFFNESS MECHANISM (VSM)

The *soft gripper's* motion is affected by external force or torque including its own weight, inertia forces or another coupling force or torque. Therefore relatively high-stiffness is desirable under no contact with objects to assure almost precise synergic flexion. Once the gripper contacts an object and starts the envelope grasping, it should adjust its stiffness according to the object's elasticity. So we developed the variable stiffness mechanism (VSM) and employed it into the gripper.

### A. VSM

Fig.3 shows the VSM parts and Fig.4 is an appearance of assembling the VSM into the gripper. The rotation of the carrier pulls the wire that compresses the spring that is identical to the one symbolically depicted in Fig.1 and Fig.2. The cylinder that houses the spring to sustain its compressing motion is rotated by another motor to slide the trapezoid screw, which compress the spring to give it a pre-tension. The motor for the VSM is located at the base and the torque is transmitted to all of the VSMs via the gear train as shown in Fig.3. Two wires are used to pull the piston as shown in Fig.5. This is because that pulling by only one wire causes a torque zero state around  $\theta_c$  nearly/equal zero. On the other hand, by assigning two wires, a signum change of the carrier torque promptly occurs with a slight rotation of the carrier. Because the slight rotation of  $\theta_c$  brings about one wire's stretching and the other wire's loosening. So it assures pre-determined torque

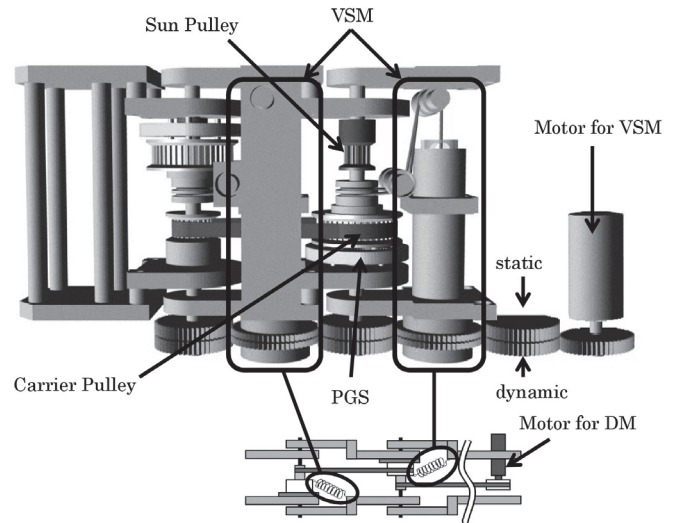


Fig.3 Structure of the experimental machine

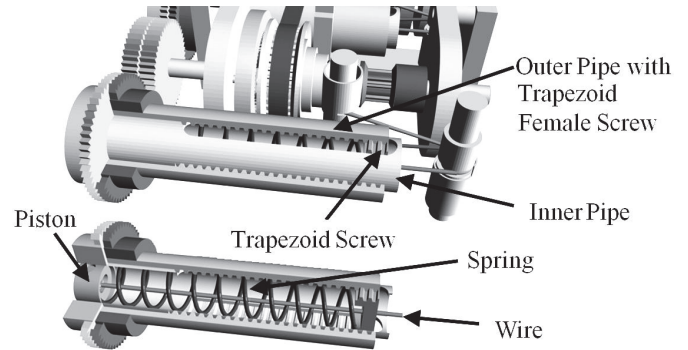
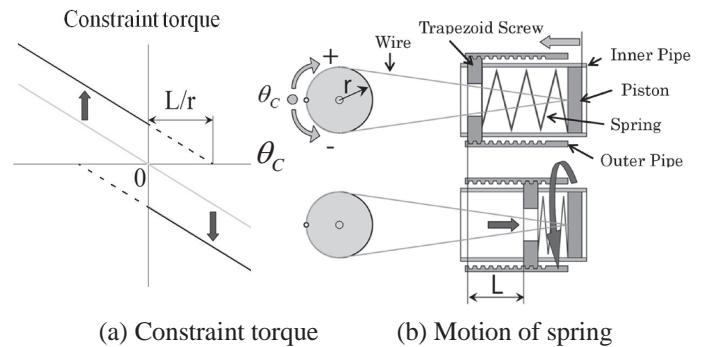


Fig.4 Structure of the variable stiffness mechanism



(a) Constraint torque (b) Motion of spring

Fig.5 Principle of variable stiffness mechanism of the carrier, of which value can be adjusted by the location of the trapezoid screw ("L" in Fig.5).

## IV. TEST MACHINES

We developed two test machines as shown in Fig.6. Test machine 1 (TM1) is simplified one without the VSM (Fig.6(a)). Both machines have five joints. The structure of the TM1 is depicted in Fig.7. Torsion springs are used for the spring that suppresses the carrier's rotation. The carrier's rotation is transmitted by two wires as same as the one shown in Fig.5 and the axis of the torsion spring is rotated always in

right screw direction regardless of the rotary direction of the carrier. The test machine 2 (TM2) is a full model employing the VSM (Fig.6(b)). Therefore the TM2 has 2 motors, one is for the active driving of all joints and the other is for driving the VSM. Table 1 shows some specifications of motor, gears and pulleys used in the TM1 and TM2.

Table 1 Design parameter of the experimental machine

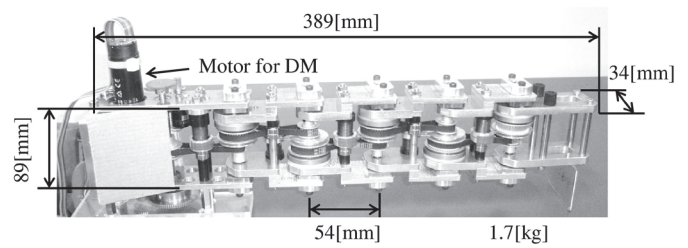
	Test machine 1	Test machine 2
Spring rate	$19.51 \times 8.5/8$ [Nmm/rad] 8.5/8:PulleyRadius Ratio	3.83[N/mm]
Radius of wire		4.5
Pulling pulley [mm]		4.5
S : z (Sun Gear)	40	40
I : z (Inner Gear)	80	80
Pc : z (Carrier Pulley)	42	42
Ps : z (Sun Pulley)	21	21
Length between the axis [mm]	54	54
Actuator	Maxon EC22 Blushless 50W, Gear head 370:1	Maxon EC22 Blushless 50W $\times$ 2 Gear head 370:1

A. Envelope grasping

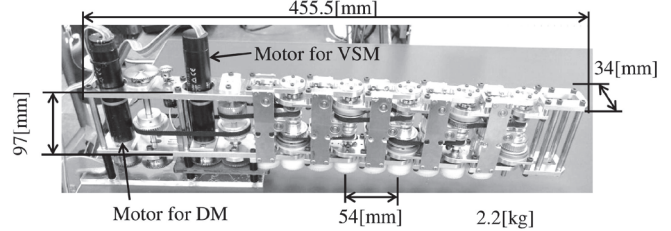
Fig.8 shows the experiment of the envelope grasping using the TM1 with two different allocation of the grasping object. As can be seen, the TM1 can achieve the envelope grasping even the object is allocated nearby the gripper's tip by pulling it to the place nearby the base.

Fig.9 shows the allocation points of the grasping object (paper cup) with which the gripper succeeded or did not succeed the envelope grasping. As shown the gripper can cover a wide range of area within the locus of the finger tip. Since the gripper can flex in the left and right hand sides (Fig.8 shows the right hand side flexion), the successful area will be expanded in both sides.

Fig.10 shows the envelope grasping of the TM1 with various shape objects. We observed that the TM2 achieved the



(a) Test machine 1



(b) Test machine 2

Fig.6 Appearance of the test machines

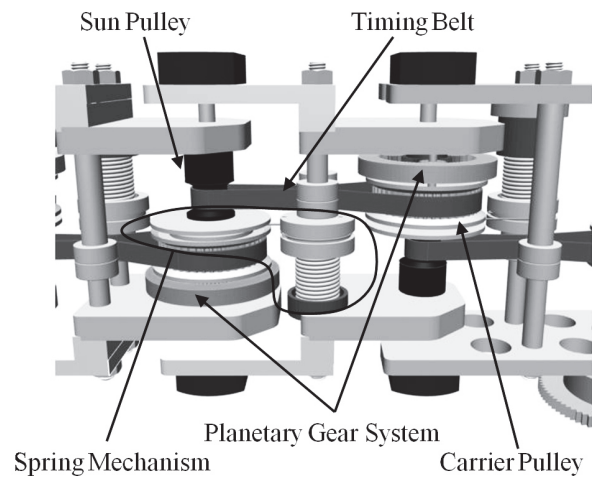
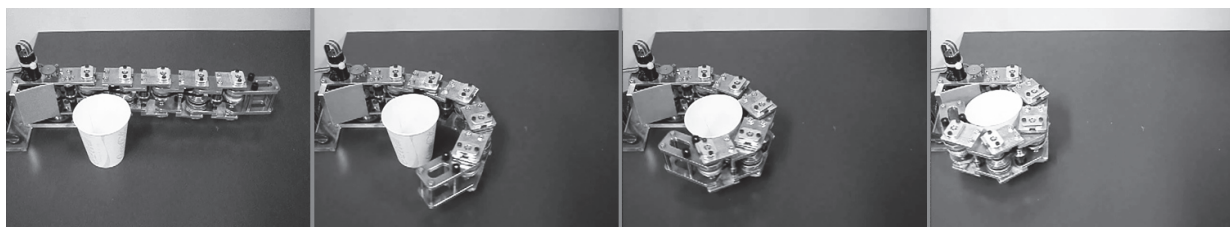
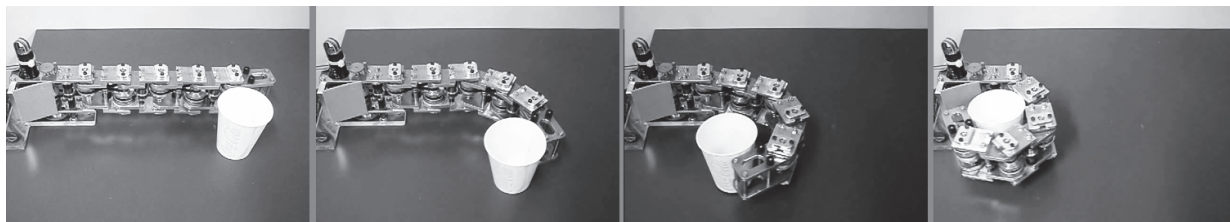


Fig.7 Structure of the test machine 1



(a) The case of locating the object nearby the base



(b) The case of locating the object nearby the tip

Fig.8 Envelope grasping of the paper cup (the test machine 1)

identical envelope grasping. It is noteworthy that all of the motions are achieved by the identical constant velocity driving of the motor with no sensory feedback.

**B. Effect of the VSM**

The effect of the VSM employed in the TM2 is evaluated by the following experiments. The TM2 takes flexing motion, of which the first and the last postures are shown in Fig.11. Two typical pre-determined torque of the carrier are tested. Fig.12 shows the time course of the every carriers' angle when the SG of the first joint rotates 46 deg by the PD controller as shown in the figure. To change the pre-determined torque of the carrier, the location of the trapezoidal screw in the VSM ("L" in Fig.5) is set as 2.25 mm and 6 mm. All of the carriers rotate at the onset of motion mainly because of the inertia force and torque. This carrier rotation should be vanished as the time elapses, but we observe some non-vanished deviation in the case of low pre-determined carrier torque (Fig.12(a)). This is mainly due to the friction of the mechanism. On the other hand, high pre-determined torque of the carrier assures the prompt recovering of the carriers' angle to be zero (Fig.12(b)).

Fig.13 is the time course of the every joint angle in the same experiment as shown in Fig.12. All of the joint angle should converge to -40 deg, however the low pre-determined torque of the carrier does not assure to converge to the desired angle (Fig.13(a)), which is also due to friction torque. On the other hand, setting the pre-determined torque high allows favorable convergence as shown in Fig.13(b).

**V. CONCLUSIONS**

A novel mechanism of the multi-joint gripper is proposed and the test machines were developed. The planetary gear system train takes the most important role in the mechanism. It allows the active/passive torque amalgamation with no torque coupling between the joints. The experiments of the test machines elucidated the proposed mechanism achieves one DOF synergic flexion and envelope grasping of various shape objects. The variable stiffness mechanism is also proposed and implemented into the test machine. The experiments showed the VSM effectively improves the motion of the gripper. It can be concluded the proposed gripper satisfies the BD, ISC and SC requirements that are defined in the introduction.

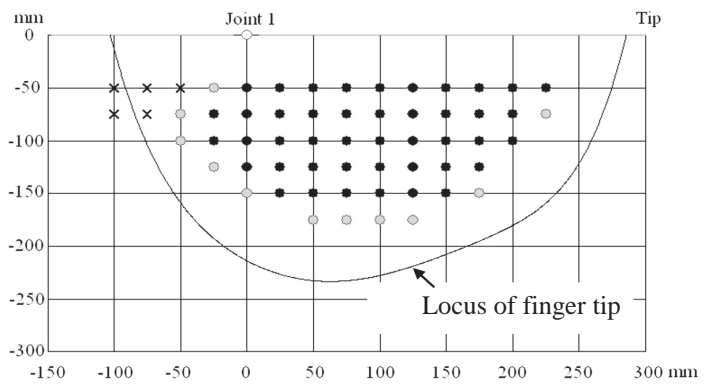


Fig.9 Object placing points where the gripper successfully or unsuccessfully takes envelope grasping  
 Black dot: successful point, Gray and Cross dot: unsuccessful point

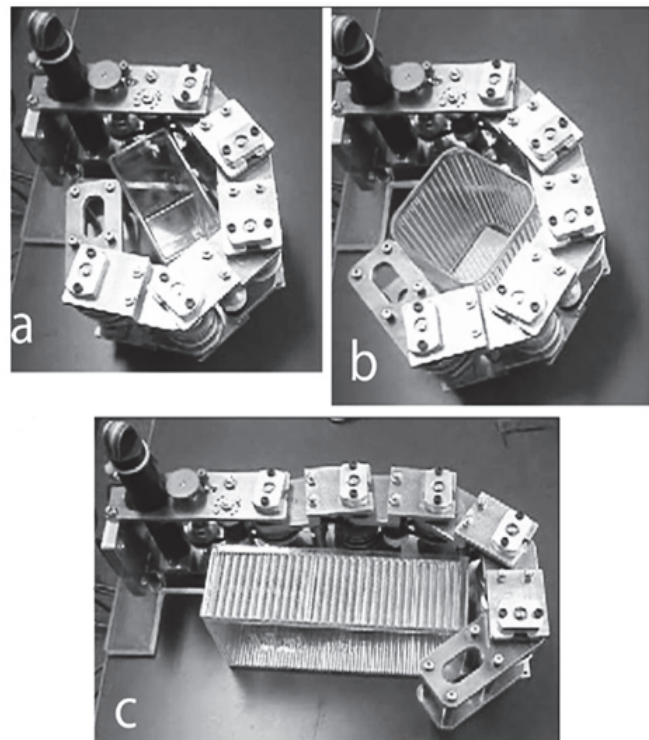


Fig.10 Envelope grasping of various shape objects

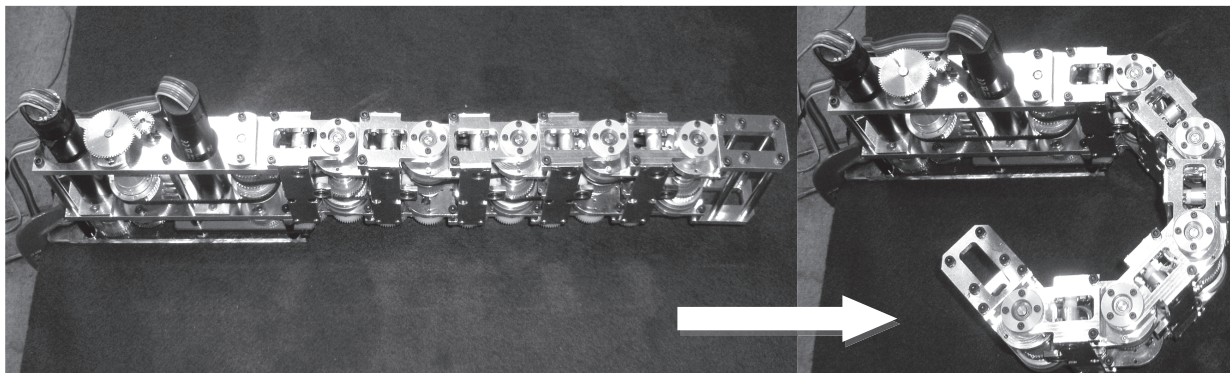


Fig.11 Initial and final postures of the TM2 motion

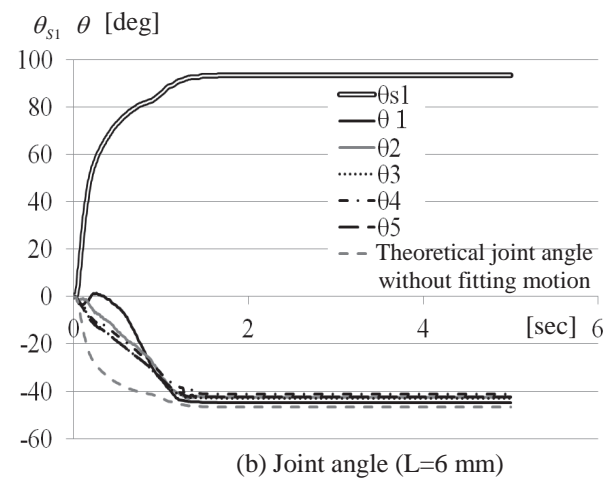
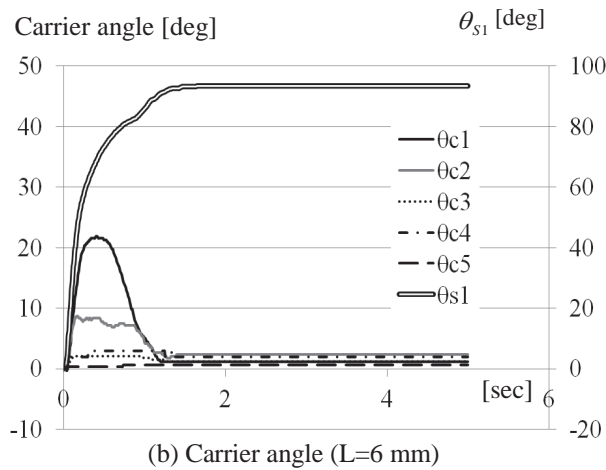
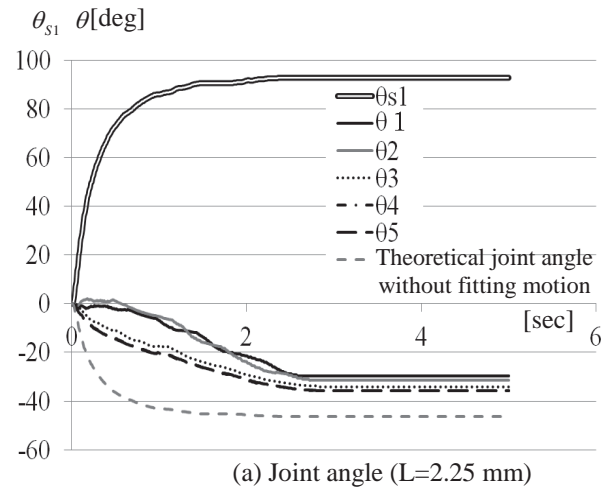
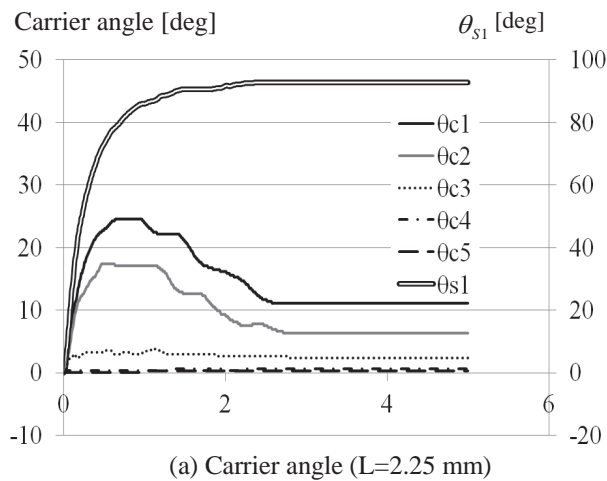


Fig.12 Carrier angle trajectory when driving the gripper with different pretention of the VSM

Fig.13 Joint angle when driving the gripper with different pretention of the VSM

### References

- [1] S. Hirose and Y. Umetani, "The Development of Soft Gripper for the Versatile Robot Hand," Mechanism and Machine Theory, Pergamon Press, 13, pp.351-359 (1978)
- [2] S. Hirose and S. Ma, "Coupled tendon-driven multijoint manipulator," IEEE Intern. Conf. on Robotics and Automation, pp. 1268-1275, 1991.
- [3] S. Hirose, "Biologically Inspired Robots (Snake-like Locomotor and Manipulator)," Oxford University Press, 1993.
- [4] N. Dechev, W. L. Clegghorn and S. Naumann, "Multiple Finger, Passive Adaptive Grasp Prosthesis Hand," Mechanism Machine Theory, Vol.36, No.10, pp.1157-1173, 2001.
- [5] B. Massa, S. Roccella, M. C. Carrozza and P. Dario, "Design and Development of an Underactuated Prosthetic Hand," Proc. Of the 2002 IEEE Intern., Conf. on Robotics & Autom., pp.3374-3379, 2002.
- [6] M. Wassink, R. Carloni and S. Stramigioli, "Port-Hamiltonian Analysis of a Novel Robotic Finger Concept for Minimal Actuation Variable Impedance Grasping," IEEE Intern. Conf. on Robotics and Automation, pp. 771-776, 2010.
- [7] Koganezawa, K. and Y. Ishizuka, Novel Mechanism of Artificial Finger using Double Planetary Gear System, Proc. of the IEEE/RSJ Intern. Conf. on Intelligent Robots and Systems, pp. 3184-3191, 2008.

# Manual, Automatic and Shared Methods for Controlling an Intelligent Wheelchair

Adaptation to Cerebral Palsy Users

Brigida Monica Faria

DETI/UA – Dep. Electrónica,  
Telecomunicações e Informática/UA  
and ESTSP/IPP – Escola Superior de  
Tecnologia da Saúde do Porto /  
Instituto Politécnico do Porto  
Aveiro and Porto, Portugal  
btf@estsp.ipp.pt

Luis Paulo Reis

EEUM – Escola de Engenharia da  
Universidade do Minho,  
Departamento de Sistemas de  
Informação and LIACC –  
Laboratório de Inteligência Artificial  
e Ciência de Computadores, Univ.  
do Porto  
Guimaraes and Porto  
lpreis@dsi.uminho.pt

Nuno Lau

DETI/UA – Dep. de Electrónica,  
Telecomunicações e Informática /  
Universidade de Aveiro and IEETA  
– Instituto de Engenharia  
Electrónica e Telemática de Aveiro  
Aveiro  
nunolau@ua.pt

**Abstract** — The development of an intelligent wheelchair (IW) platform that may be easily adapted to any commercial wheelchair and aid any person with special mobility needs is the main objective of this project. To be able to achieve this main objective, three distinct control methods were implemented in the IW: manual, shared and automatic. Several manual, shared and automatic control algorithms were developed for this task. This paper presents three of the most significant of those algorithms with emphasis on the shared control method. Experiments were performed, using a realistic simulator, with real users suffering from cerebral palsy in order to validate the approach. These experiments enabled to conclude which were the best shared control methods to implement on the IW. The experiments also revealed the importance of using shared (aided) controls for users with severe disabilities. The patients still felt having complete control over the wheelchair movement when using a shared control at a 50% level and thus this control type was very well accepted and should be used in intelligent wheelchairs since it is able to correct the direction in case of involuntary movements of the user but still gives him a sense of complete control over the IW movement.

**Keywords**—*intelligent wheelchair; automatic control; shared control; manual control; cerebral palsy*

## I. INTRODUCTION

Scientific research allowed the evolution and development of many technologies that are nowadays used in everyday life. In particular, innovations in the field of assistive technologies enabled increased autonomy and independence for human beings that, for some reason, have some kind of disability. Intelligent wheelchairs are an obvious application of the scientific work developed in the last decades on this area. Moreover, these assistive technologies still are object of research and the interaction between them and the user it is still an open research problem. The interaction between the Human and the IW is an important component to take in consideration.

The users' opinions should also be integrated in the development process of the instruments which are to serve and fulfill a human necessity. An electric wheelchair is typically driven by two individually powered wheels which rotate around a horizontal axis, and another two non-powered caster wheels, which besides rotating around a horizontal axis, also have the ability to rotate around a vertical axis [1]. The mapping of joystick positions to individual wheel speeds can be performed in many ways and it is this mapping that will determine the manual control behavior. For that reason, several of these mappings were implemented tested with real users in a simulated environment and based on the users' feedback some interesting conclusions about mappings were achieved [1]. Nevertheless, an IW can also have a completely high level manner of control, for example an action such as "go to bedroom" can be performed autonomously by the IW. In shared control, the navigation process is divided between patient and machine. In this case, it is the machine which takes control when the navigation of the patient endangers its own safety, in situations such as potential collisions with objects [2].

This paper is organized in 5 sections. The first section is composed by this introduction. The second section reports the related work about Intelligent Wheelchairs including a briefly description about the IntellWheels project. The implementations of the proposed methods for manual, shared and automatic control are described in third section. Next, the experimental work and results are presented. Finally some conclusions and directions for future work conclude the paper.

## II. INTELLIGENT WHEELCHAIRS

In the last years several prototypes of IW have been developed and many scientific works have been published [3-5] in this area. Next it is presented the state of art related to intelligent wheelchairs with special attention to the work developed in the IntellWheels project.

A. Intelligent Wheelchairs' Developments

Nowadays, science allows having intelligent wheelchairs, very similar in shape to traditional wheelchairs, with high maneuverability and navigational intelligence, with units that can be attached and/or removed and with high power independence [5]. A simple definition of Intelligent Wheelchair is a locomotion device used to assist a user having some kind of physical disability, where an artificial control system augments or replaces the user control [6-7]. The main objective is to reduce or eliminate the user's task of having to drive a motorized wheelchair. Usually, an IW is controlled by a computer, has a set of sensors and applies techniques derived from mobile robotics research in order to process the sensor information and generate the motors commands in an automatically way or with a shared control. The interface may consist of a conventional wheelchair joystick, voice based control, facial expressions or even gaze control, among others. The developments since 1986 with the Madarasz project [8] evolved all over the world. Several new projects were presented. Table I presents a list of some IW prototypes and describes some of their characteristics.

TABLE I. INTELLIGENT WHEELCHAIRS' PROJECTS

<p><b>Madarasz</b></p>  <p>Project of an autonomous wheelchair presented in 1986. Wheelchair with a micro-computer, a digital camera and an ultra-sound scanner.</p>	<p><b>Omnidireccional IW</b></p>  <p>Hoyer and Holper [9] presented in 1993 an omnidirectional IW.</p>
<p><b>Two legs' IW</b></p>  <p>In 1994 Wellman [10] presented a hybrid wheelchair which was equipped with two extra legs.</p>	<p><b>NavChair</b></p>  <p>The NavChair [11] was presented in 1996. It is equipped with 12 ultrasonic sensors and an on-board computer.</p>
<p><b>Tin Man I</b></p>  <p>Tin Man I [12] at 1995</p>	<p><b>Tin Man II</b></p>  <p>Tin Man II [13] at 1998</p>

presented three operation modes: individual conducting a wheelchair with automatic obstacles deviation; moving throughout a track; moving to a point.

presented more advanced characteristics: store travel information; return to the starting point; follow walls; through doors; recharge battery.

**FRIEND's Project**



Robot presented in 1999 which consists of a motorized wheelchair and a MANUS manipulator [14].

**LURCH**



In 2007 started the LURCH (Let Unleashed Robots Crawl the House) project [15] which aims at developing an autonomous wheelchair.

**RoboChair**



In 2009 Robochair [16] aims to be an open framework for future assistive applications. Design modular and based in open standards for easy extension and low cost.

**VAHM**



In 2010 the VAHM project [17] presented a new prototype of an intelligent wheelchair with a deictic interface.

**ARTY**



In 2012 was published and presented the Assistive Robot Transport for Youngsters (ARTY) [18]. This is an intelligent paediatric wheelchair.

**Smart Driving Assistance**



In 2012 was presented the results of the smart driving assistance from the University of Bremen [19].

It is possible to observe several solutions with complex ergonomics, however there are also some projects that try to consider the users' opinions about the modifications to their wheelchairs. The project presented in the next section tries following the principle of introducing in a conventional wheelchair a simple platform that can transform it into an intelligent wheelchair.

### B. IntellWheelsProject

The IntellWheels project aims developing an intelligent wheelchair platform that may be easily adapted to any commercial wheelchair and aid any person with special mobility needs [20]. The project main focus is the research and design of a multi-agent platform, enabling easy integration of different sensors, actuators, devices for extended interaction with the user, navigation methods and planning techniques and methodologies for intelligent cooperation to solve problems associated with intelligent wheelchairs [21].

A real prototype (Fig. 1) was created by adapting a typical electric wheelchair. Two side bars with a total of 16 sonars, a laser range finder and two encoders were incorporated.



Fig. 1. Real prototype of the IW.

In the IntellWheels project it was also developed a simulator called *IntellSim*. The objective of this simulator is essentially to support the test of algorithms, analyze and test the modules of the platform and safely train users of the IW in a simulated environment [5] [22].

A multimodal interface was also developed that allows driving the wheelchair with several inputs such as joystick, head movements or more high level commands such as voice commands, facial expressions, and gamepad or even with a combination among them. For example it is possible to blink an eye and say “go” for the wheelchair to follow a right wall [23]. Therefore it is possible to drive the IW with a completely automatically way, with a shared or using the usual manual control.

### III. MANUAL, AUTOMATIC AND SHARED CONTROLS

One initial objective of the IntellWheels project was to be able to control the wheelchair using three distinct methods: manual, shared and automatic. During the course of the project several manual and shared algorithms have been developed, but their comparative evaluation had never been performed. In the course of this work several experiments were performed, experiments to provide the best manual control, shared or automatic control adapted for the patients.

### A. Manual Control

The mapping of joystick positions to individual wheel speed can be done in an infinite number of combinations, and it is this mapping that will determine the response behavior to manual control.

Considering that the joystick handle position is represented in a Cartesian coordinate system, with two axis,  $x$  and  $y$ , which vary between -1 and 1. These  $(x, y)$  coordinates can be used to determine the distance of the handle to the central (resting) position of the joystick  $(0, 0)$  and an angle relating to a reference vector (which is usually  $(0, 1)$ ). The desired speed of the left wheel ( $L$ ) or the right wheel ( $R$ ) is represented by normalized values (between -1 and 1). With positive values the wheels rotate forward and with negative values the wheels rotate backward.

An intuitive mapping was implemented and the equations for  $R$  and  $L$  are:

$$\begin{cases} R = y - nx \\ L = y + nx \end{cases} \quad (1)$$

the value  $nx$  follows the Equation:

$$nx = \begin{cases} u_1 c_{point} + (x - c_{point}) \times u_2 & \text{if } x > c_{point} \\ -u_1 c_{point} + (x + c_{point}) \times u_2 & \text{if } x < -c_{point} \\ u_1 x & \text{if } -c_{point} \leq x \leq c_{point} \end{cases} \quad (2)$$

where  $c_{point} \in [0,1]$ ;  $u_1 \in [0,1]$  and  $u_2 \in [0,1]$ . The tested values were  $c_{point} = 0.2$ ;  $u_1 = 0.5$  and  $u_2 = 0.25$ . The first slope  $u_1$  allows a fast curve and the next slope  $u_2$  after the cut point ( $c_{point}$ ) should allow a slower curve.

### B. Automatic Control

The developed automatic control has as main objective following a predefined circuit without the need of user intervention. The automatic control assumes full control over the navigation of the wheelchair and executes the navigating task following the circuit points without any user’s intervention. A predefined circuit can be specified by defining the relevant circuit points and the wheelchair can autonomously drive to the specified points.

The main reason to create an automatic control was concerned with the methodology used to achieve a shared driving algorithm for the intelligent wheelchair. The users in the study performed predetermined tasks such as collecting objects along a circuit. This automatic control assumes the self-localization problem solved and hence the IW always knows its position in the environment. Before this work, the IntellWheels IW was already capable of some forms of automatic control that did not rely on localization, such as “follow wall” or other high level actions like “go forward” [23]. However, it still missed an automatic driving algorithm based on the current position and orientation and the desired position and orientation.

Fig. 2 shows the idea of the algorithm implemented. If the IW would move directly from target to target, it would have to stop and turn on the spot at each target. This is a very unnatural way of driving the IW. In order to have a smoother path, The IW should consider not only the following target, but also the target that follows. The position of the wheelchair in the world referential ( $x, y$ ) combined along with the position of the target (T) and the next target (NT) in order to determine a corrected target (CT) of the trajectory.

$$CT = T + d_{[CT,T]} \times \frac{\overrightarrow{NTT}}{\|\overrightarrow{NTT}\|} \quad (3)$$

With the introduction of the corrected target it is possible to have a smoother trajectory of the wheelchair.

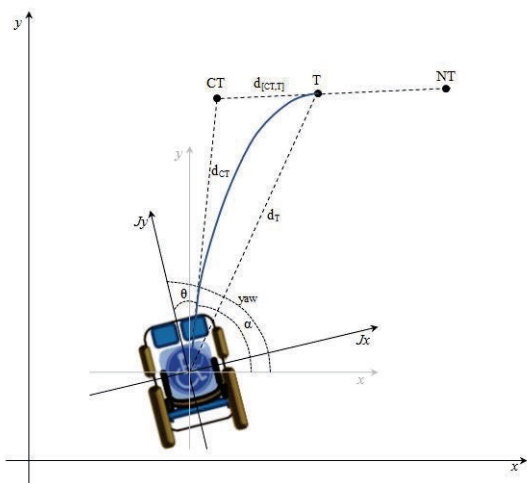


Fig. 2. Automatic action of following circuit.

The corrected target is calculated using a ramp function as shown in Fig. 3 and has the same direction as the target (T) to the next target (NT).

$$d_{[CT,T]} = \begin{cases} 0 & \text{if } 0 < d_T < a \\ \frac{d_{max}}{b-a} d_T - \frac{a \times d_{max}}{b-a} & \text{if } a \leq d_T < b \\ d_{max} & \text{if } b \leq d_T < +\infty \end{cases} \quad (3)$$

A maximum distance  $d_{[CT,T]}$  ( $d_{max}$ ) could be chosen, considering for example the surrounding obstacles, in the Fig. 3 it has a value of 0.5 units and  $a$  has the value 0.5 and  $b$  has the value 1.5.

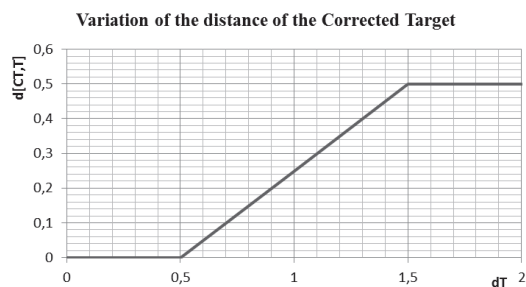


Fig. 3. Variation of the distance of the corrected target

The distance of the target to the corrected target is determined by the value of the ramp function using the distance of the wheelchair to the target ( $d_T$ ) as input. Knowing this distance, the position of the corrected target may be determined by projecting the point along the next target to target line at this distance from the target. Using this information and the difference between yaw and angle  $\alpha$  it is possible to calculate the direction of the joystick relatively to the corrected point ( $\theta$ ).

### C. Shared Control

The concept behind the shared control implemented is to understand the intention of the user while providing an easier and safer navigation. This means that, for example, if a user has a high level of difficulty in driving the IW but his intentions can be recognized, the shared control helps the navigation of the wheelchair. Additionally the wheelchair takes control when the navigation of the patient endangers its own safety, in situations such as potential collisions with objects. The computer momentarily takes control and acts on the wheelchair, taking into account the information from sensors and the commands from the user.

A more concrete example is given in Fig. 4. If the position of the joystick is at a higher distance than a given threshold from the automatic control command then it uses the user command otherwise it uses a weighted average of the automatic control and manual control. The weights used in the weighted average determine the aid level that is provided to the user.

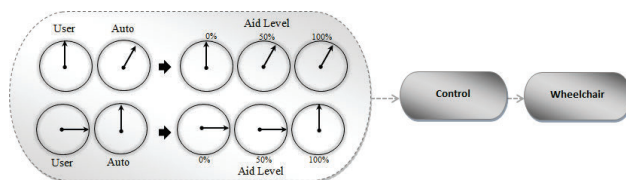


Fig. 4. Aided control relatively to the user and to the automatic control.

The implementation of the shared control also considered the obstacle avoidance procedure with the information of the sensors present in the IW. With this tool a more confident way of driving the IW is executed by the users with severe disabilities.

## IV. EXPERIMENTS AND RESULTS

The experiments using the simulator *IntellSim* allowed testing the users' ability in driving the wheelchair with several

input devices. After that it was possible to verify if an extra help should be provided to the user. It is possible to provide the users with the shared control with distinct aided levels. In fact, the experiments with the shared control aimed at testing how the users with cerebral palsy would react when having a control that helps them in the task of driving wheelchair. The usability level was determined based on users' feedback after testing the different shared controls without previously knowing the control characteristics: aided control at a 100%, aided control at a 50% and manual with obstacle avoidance. The experiments were conducted using the *IntellSim* and the order of tests with the shared controls was set randomly. A circuit was defined and several objects to be collected (passing near them) were put along the way. These objects (blue balls in Fig. 5) determine the path that the wheelchair should follow.

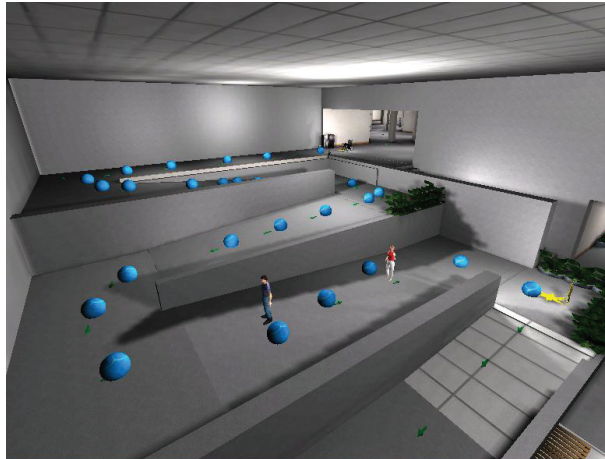


Fig. 5. Circuit for testing the shared controls.

The patients tested the shared controls using the joystick as input device and, in different rounds, using head movements detected using a wiimote. After each round the patients answered to a questionnaire composed of four parts: user identification; experience with videogames and joysticks; questions adapted from the Computer System Usability Questionnaire (CSUQ) [24] for each tested option and a final question about the preference order of the tested options.

The sample was a group of 8 cerebral palsy patients with the level IV and V of the Gross Motor Function Measure [25]. This sample is characterized by having six males and two females, with a mean of age of 31 years old. All had experience with the joystick of their electric wheelchair although the experience with video games was low, except in one case that answered always play videogames. Table II shows the summary of statistics measures about the final score for all the mapping options. The obtained results from the final score of the CSUQ show a tendency to consider the aided control at a 50% the best way to drive the wheelchair with the joystick and the wiimote. In general, the opinions considered all options very useful except in the case of the head movements with obstacle avoidance which had the worst result. Nevertheless it is possible to affirm that the cerebral palsy patients would react favorably when having a control that helps the driving of the wheelchair.

TABLE II. SUMMARY OF STATISTICAL MEASURES OF THE ADAPTED CSUQ SCORE

Adapted CSUQ – Final Score						
Statistics	Joystick			Wiimote		
	Aid Cont. 100%	Aid Cont. 50%	Obs. Avoid.	Aid Cont. 100%	Aid Cont. 50%	Obs. Avoid.
Mean	82.7	<b>87.1</b>	84.1	76.0	<b>76.4</b>	50.6
Median	88.9	<b>99.2</b>	88.9	84.9	<b>91.3</b>	41.3
Std. Dev.	21.0	22.3	19.4	24.7	33.1	30.8
Min	39.68	36.5	44.4	31.8	15.9	14.3
Max	100	100	100	100	100	96.83

In order to confirm the differences between the shared controls using joystick and wiimote, the Friedman test (related samples Friedman's test two way analysis of variance by ranks) was applied to the final scores. The p values were 0.484 and 0.004, and for that reason there are not statistical evidences to affirm that the distributions of the scores are significantly different for the joystick shared controls and there are statistical evidences to affirm that the distributions of the scores are significantly different for the wiimote (head movements) shared control at a level of 0.05.

Table III shows the p values of the multiple comparisons, using the Fisher's least significant difference (LSD) in the case of the head movements shared controls.

TABLE III. MULTIPLE COMPARISONS OF THE HEAD MOVEMENTS SHARED CONTROLS

Multiple Comparisons LSD		
Head movements shared controls(p values)		
	Aid. Control 100%	Aid. Control 50%
Aided control 50%	1	--
Obstacle Avoidance	<b>0.001</b>	<b>0.001</b>

The results of the CSUQ score also confirm the tendency to the order of preference as can be observed in Table IV.

TABLE IV. SUMMARY STATISTICS ABOUT THE ORDER OF PREFERENCE OF THE SHARED CONTROLS

Order of preference (1- Best to 6- Worst)						
Statistics	Joystick			Wiimote		
	Aid Cont. 100%	Aid Cont. 50%	Obst. Avoid.	Aid Cont. 100%	Aid Cont. 50%	Obst. Avoid.
Median	2	2	3	1	2	3
Min	1	1	1	1	2	1
Max	2	3	3	2	3	3

The aided control was chosen as the best way of driving the wheelchair in the case of using the joystick and the wiimote for the head movements. It was interesting to verify that all the patients found the experience of the aided control very pleasant. The careful observation of the experiments executed by the patients was also done by the occupational therapists and some interesting notes are important to register. All the users think that they had control of the wheelchair even when they were using the aided control at a level of 100%, except one case that had involuntary movements. He found strange

that the wheelchair had such as smooth behavior and stopped a few times to check if the wheelchair corresponded to his action. Another situation was a case of a patient that had cognitive deficits; the level of motivation was very high when using the shared control at a level 100% and this could be identified by his non-verbal language.

## V. CONCLUSIONS AND FUTURE WORK

The shared control experiments revealed the importance of using aided controls for users with severe disabilities. The patients still felt having complete control over the wheelchair movement when using a shared control at a 50% level and thus this control type was very well accepted and should be used as the main control method for the IW prototype. Overall the responses were very positive to this kind of control in terms of usability. In this study, the shared control was only used in the simulated environment. However, the future evolution of the project will enable to have the localization issue of the real wheelchair solved in order to allow the aided control also in the real environment.

Future work will be concerned with conducting a deeper study of the control methods by testing different configuration parameters for each control type and by testing the control methods with a broader sample of wheelchair users. Another experiment will be concerned with the use of machine learning algorithms to create user driving models and using them to create automatic control methods based on real user behavior.

## ACKNOWLEDGMENTS

This work was funded by the ERDF – European Regional Development Fund through the COMPETE Programme (operational programme for competitiveness) and by National Funds through FCT - Portuguese Foundation for Science and Technology within project «INTELLWHEELS - Intelligent Wheelchair with Flexible Multimodal Interface, RIPD/ADA/109636/2009». B. M. Faria thanks to FCT for the PhD Scholarship FCT/SFRH/BD/44541/2008.

## REFERENCES

- [1] B. M. Faria, L. Ferreira, L. P. Reis, N. Lau, M. Petry, and J. C. Soares, "Manual Control for Driving an Intelligent Wheelchair: A Comparative Study of Joystick Mapping Methods", IROS 2012, Progress, challenges and future perspectives in navigation and manipulation assistance for robotic wheelchairs workshop, IEEE/RSJ International Conference on Intelligent Robots and Systems 2012, Vila Moura, Algarve, pp. 7-12 October 2012, ISBN: 978-972-8822-26-2.
- [2] M. Petry, A. P. Moreira, R. Braga and L. P. Reis, "Shared control for obstacle avoidance in intelligent wheelchairs," in IEEE Conference on Robotics, Automation and Mechatronics, Singapore, 2010., pp. 182-187.
- [3] R. Simpson, "Smart wheelchairs: A literature review," *Journal of Rehabilitation Research & Development*, July/August 2005, pp. 423-435.
- [4] B. Woods and N. Watson, "The social and technological history of wheelchairs," *International Journal of Therapy and Rehabilitation*, vol. 11, no. 9, pp. 407-410, 2004.
- [5] B. M. Faria, S. Vasconcelos, L. P. Reis, and N. Lau, Evaluation of Distinct Input Methods of an Intelligent Wheelchair in Simulated and Real Environments: A Performance and Usability Study. *Assistive Technology: The Official Journal of RESNA (Rehabilitation Engineering and Assistive Technology Society of North America)*, USA, DOI: 10.1080/10400435.2012.723297, in press.
- [6] R. Simpson, E. LoPresti, S. Hayashi, I. Nourbakhsh and D. Miller, "The Smart Wheelchair Component System," *Journal of Rehabilitation Research & Development*, vol. 41, no. 3B, May/June 2004, pp. 429-442.
- [7] R. Braga, M. Petry, A. P. Moreira and L. P. Reis, "Concept and Design of the Intellwheels Platform for Developing Intelligent Wheelchairs," in *LNEE/ Informatics in Control, Automation and Robotics*, 2009.
- [8] R. L. Madarasz, L. C. Heiny, R. F. Crompt and N. M. Mazur, "The design of an autonomous vehicle for the disabled," *IEEE Journal of Robotics and Automation*, vol. 2, no. 3, September 1986, pp. 117-126.
- [9] H. Hoyer and R. Hölper, "Open control architecture for an intelligent omnidirectional wheelchair," in *Proc.1st TIDE Congress*, Brussels, 1993.
- [10] P. Wellman, V. Krovi and V. Kumar, "An adaptive mobility system for the disabled," in *Proc. IEEE Int. Conf. on Robotics and Automation*, 1994.
- [11] R. Simpson, "NavChair: An Assistive Wheelchair Navigation System with Automatic Adaptation," in *Assistive Technology and Artificial Intelligence*, Berlin, Springer-Verlag Berlin Heidelberg, 1998, p. 235.
- [12] D. Miller and M. Slack, "Design and testing of a low-cost robotic wheelchair," in *Autonomous Robots*, 1995.
- [13] Miller, "Assistive Robotics: An Overview," in *Assistive Technology and AI*, 1998.
- [14] B. Borgerding, O. Ivlev, C. Martens, N. Ruchel and A. Gräser, "FRIEND: Functional robot arm with user friendly interface for disabled people," in *5th European Conf. for the Advancement of Assistive Technology*, 1999.
- [15] L. Project, "LURCH – the autonomous wheelchair," [Online]. Available: [http://airwiki.ws.dei.polimi.it/index.php/LURCH\\_The\\_autonomous\\_wheelchair](http://airwiki.ws.dei.polimi.it/index.php/LURCH_The_autonomous_wheelchair). [Accessed May 2011].
- [16] B. Bonail, J. Abascal, and L. Gardeazabal, "Wheelchair-based open robotic platform and its performance within the ambienet project," in *Proceedings 2nd International Conference on Pervasive Technologies Related to Assistive Environments*, ACM: Corfu, Greece, 2009, pp. 1-6.
- [17] A. Pruski, M. Ennaji and Y. Morere, "VAHM: A user adapted intelligent wheelchair," in *Proceedings of the 2002 IEEE International Conference on Control Applications*, Glasgow, 2002.
- [18] H. Soh and Y. Demiris, "Towards Early Mobility Independence: An Intelligent Paediatric Wheelchair with Case Studies," in *IROS 2012 Workshop on Progress, Challenges and Future Perspectives in Navigation and Manipulation Assistance for Robotic Wheelchairs*, Vila Moura, 2012.
- [19] C. Mandel, T. Rofer and I. Lohmuller, "On the Clinical Evaluation of Smart Driving Assistance for Power Wheelchairs," in *IROS 2012 Workshop on Progress, Challenges and Future Perspectives in Navigation and Manipulation Assistance for Robotic Wheelchairs*, Vila Moura, 2012.
- [20] R. Braga, M. Petry, L. L. Reis, A. P. Moreira, *IntellWheels: Modular development platform for intelligent wheelchairs*, *Journal of Rehabilitation Research & Development*, 48, 9, 2011, pp. 1061-1076.
- [21] R. Braga, M. Petry, A. P. Moreira, L. P. Reis. *Intellwheels: A Development Platform for Intelligent Wheelchairs for Disabled People*. Proceeding of the 5th International Conference on Informatics in Control, Automation and Robotics. Vol I. Funchal, Madeira, Portugal, 2008, pp.115-121.
- [22] M. Petry, A. P. Moreira, L. P. Reis, R. Rossetti, *Intelligent Wheelchair Simulation: Requirements and Architectural Issues*, in *11th International Conference on Mobile Robotics and Competitions*, Lisbon, 2011.
- [23] B. M. Faria, S. Vasconcelos, L. P. Reis, N. Lau, *A Methodology for Creating Intelligent Wheelchair Users' Profiles*, *ICAART 2012 - 4th International Conference and Artificial Intelligence*, Algarve, 2012, pp 171-179.
- [24] J. R. Lewis, "IBM Computer Usability Satisfaction Questionnaires: Psychometric Evaluation and Instructions for Use," *International Journal of Human-Computer Interaction*, vol. 7, no. 1, 1995, pp. 57-78.
- [25] P. R. J., R. P., B. D. and L. M. H., "Content validity of the expanded and revised Gross Motor Function Classification System," *Development Medicine and Child Neurology*, vol. 50, no. 10, pp. 744-750, 2008.

# Complete Analytical Inverse Kinematics for NAO

Nikos Kofinas, Emmanouil Orfanoudakis, and Michail G. Lagoudakis  
Intelligent Systems Laboratory, Department of Electronic and Computer Engineering  
Technical University of Crete, Chania, Crete 73100, Greece  
Email: {nikofinas, vosk, lagoudakis}@intelligence.tuc.gr

**Abstract**—The design of complex dynamic motions for humanoid robots is achievable only through the use of robot kinematics. In this paper, we study the problems of forward and inverse kinematics for the Aldebaran NAO humanoid robot and present a complete, exact, analytical solution to both problems, including a software library implementation for real-time onboard execution. The forward kinematics allow NAO developers to map any configuration of the robot from its own joint space to the three-dimensional physical space, whereas the inverse kinematics provide closed-form solutions to finding joint configurations that drive the end effectors of the robot to desired target positions in the three-dimensional physical space. The proposed solution was made feasible through a decomposition into five independent problems (head, two arms, two legs), the use of the Denavit-Hartenberg method, and the analytical solution of a non-linear system of equations. The main advantage of the proposed inverse kinematics solution compared to existing approaches is its accuracy, its efficiency, and the elimination of singularities. In addition, we suggest a generic guideline for solving the inverse kinematics problem for other humanoid robots. The implemented, freely-available, NAO kinematics library, which additionally offers center-of-mass calculations, is demonstrated in two motion design tasks: basic center-of-mass balancing and pointing to the ball.

## I. INTRODUCTION

Articulated robots with multiple degrees of freedom, such as humanoid robots, have become popular research platforms in robotics and artificial intelligence. Our work focuses on autonomous humanoid platforms with multiple manipulators capable of performing complex motions, such as balancing, walking, and kicking. These skills are required in the Standard Platform League of the RoboCup robot soccer competition [1], in which all teams compete using the Aldebaran NAO humanoid robot [2], which is our target robot platform.

The design of complex dynamic motions is achievable only through the use of robot kinematics, which is an application of geometry to the study of arbitrary robotic chains. However, past work [3]–[5] has not fully solved the inverse kinematics problem for the NAO robot, since it focuses exclusively on the robot legs. Furthermore, the widely-known analytical solution [3] for the inverse kinematics of the legs is purely geometric and cannot be generalized to other kinematic chains. Also, existing numerical solutions [5] are inherently prone to singularities and, therefore, lack in robustness.

In this paper, we present a complete and exact analytical forward and inverse kinematics solution for all limbs of the Aldebaran NAO humanoid robot, using the established Denavit–Hartenberg convention [6], [7] for revolute joints. The main advantage of the proposed solution is its accuracy, its

efficiency, and the elimination of singularities. In addition, we contribute an implementation of the proposed NAO kinematics as a freely-available software library<sup>1</sup> for real-time execution on the robot. This work enables NAO software developers to make transformations between configurations in the joint space and points in the three-dimensional physical space and vice-versa, on-board in just microseconds, as the library is designed for high-performance real-time execution on the limited embedded platform of the robot. The implemented NAO kinematics library, which additionally offers center-of-mass calculations, is demonstrated in two tasks<sup>2</sup>: basic center-of-mass balancing and pointing to the ball. The library has been integrated into the software architecture of our RoboCup team *Kouretes* [www.kouretes.gr] and is currently being used in various motion design problems, such as dynamic balancing, trajectory following, dynamic kicking, and omnidirectional walking. Extrapolating from our work on the NAO, we also present some guidelines for finding analytical solutions to the inverse kinematics problem for any humanoid with revolute joints of up to 6 degrees of freedom (DOF) per manipulator.

## II. BACKGROUND

### A. The Aldebaran NAO Humanoid Robot

NAO (v3.3) is a 58cm, 5kg humanoid robot (Figure 1). The NAO robot carries a fully capable computer on-board with an x86 AMD Geode processor at 500 MHz, 256 MB SDRAM, and 2 GB flash memory running an Embedded Linux distribution. It is powered by a 6-cell Lithium-Ion battery which provides about 30 minutes of continuous operation and communicates with remote computers via an IEEE 802.11g wireless or a wired Ethernet link. NAO RoboCup edition has 21 degrees of freedom; 2 in the head, 4 in each arm, 5 in each leg and 1 in the pelvis (there are two pelvis joints which are coupled together on one servo and cannot move independently). All joints are position-controlled, using closed-loop PID controllers and encoders. It also features a variety of sensors: an Inertial Measurement Unit (IMU) in the torso, Force Sensitive Resistors (FSR) on each foot, ultrasonic range sensors on the chest, and two VGA cameras on the head.

### B. Transformation Formalism

The translation and orientation of a joint  $j$  with respect to an adjacent joint  $i$  in the three-dimensional space can be fully

<sup>1</sup>Library download link: [www.github.com/kouretes/NAOKinematics](http://www.github.com/kouretes/NAOKinematics)

<sup>2</sup>Video download link: [www.intelligence.tuc.gr/kouretes/NAOKinematics](http://www.intelligence.tuc.gr/kouretes/NAOKinematics)

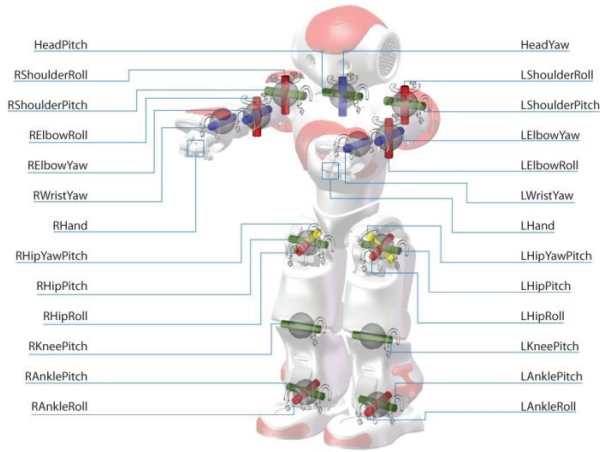


Fig. 1. NAO v3.3 kinematic chains and joints (Academics Edition, 25 DOF) described using a  $4 \times 4$  (affine) transformation matrix  $\mathbf{T}_i^j$ :

$$\mathbf{T}_i^j = \begin{bmatrix} \mathbf{X} & \bar{\mathbf{y}} \\ [0 \ \dots \ 0] & 1 \end{bmatrix} \quad (1)$$

where  $\mathbf{X} \in \mathbb{R}^{3 \times 3}$  and  $\bar{\mathbf{y}} \in \mathbb{R}^3$ . A transformation matrix  $\mathbf{T}_i^j$  provides the translation ( $\bar{\mathbf{y}}$ ) and orientation (contained in  $\mathbf{X}$ ) of a coordinate system  $j$  with respect to coordinate system  $i$ . A transformation matrix is invertible, if and only if  $\mathbf{X}$  is invertible, and is formed as:

$$\mathbf{T}^{-1} = \begin{bmatrix} \mathbf{X}^{-1} & -\mathbf{X}^{-1}\bar{\mathbf{y}} \\ [0 \ \dots \ 0] & 1 \end{bmatrix}$$

Given a robotic manipulator of  $N$  joints, an equal number of left-handed Cartesian coordinate systems (frames) are established, each affixed to the previous one, and the one-to-one transformation between them forms a transformation matrix.

For convenience, we enumerate joint frames starting from an established base frame, typically a fixed point on the robot's body. A point  $\bar{\mathbf{p}}_j = [p_x \ p_y \ p_z \ 1]^\top$  described in frame  $j$  can be transformed to a point  $\bar{\mathbf{p}}_i$  in another frame  $i$  by cascading the transformations for all intermediate frames:

$$\mathbf{T}_i^j = \mathbf{T}_i^{i+1} \mathbf{T}_{i+1}^{i+2} \dots \mathbf{T}_{j-1}^j \quad \text{and} \quad \bar{\mathbf{p}}_i = \mathbf{T}_i^j \bar{\mathbf{p}}_j$$

For the needs of forward and inverse kinematics, we utilize translations and rotations. A *translation transformation* has  $\mathbf{X} = \mathbf{I}_3$  (the identity matrix) and the desired offset as  $\bar{\mathbf{y}}$  in Eq. 1. We denote a parametric translation matrix for  $\bar{\mathbf{y}} = \bar{\mathbf{t}}$  as  $\mathbf{A}(\bar{\mathbf{t}})$ . It can be trivially shown that  $\mathbf{A}^{-1}(\bar{\mathbf{t}}) = \mathbf{A}(-\bar{\mathbf{t}})$  and  $\mathbf{A}(\bar{\mathbf{w}} + \bar{\mathbf{z}}) = \mathbf{A}(\bar{\mathbf{w}})\mathbf{A}(\bar{\mathbf{z}})$ . A *rotation transformation* has  $\bar{\mathbf{y}} = \bar{\mathbf{0}}$  (no translation) and  $\mathbf{X}$  in Eq. 1 is an arbitrary rotation matrix  $\mathbf{R}$  ( $\mathbf{R}^{-1} = \mathbf{R}^\top$  and  $\det(\mathbf{R}) = 1$ ). We denote the elementary rotation matrices about the  $x, y, z$  axes as  $\mathbf{R}_{\text{axis}}(\text{angle})$ . All rigid body transformations related to kinematics consist of cascaded elementary transformations (translations and rotations) and, therefore, are always invertible.

### C. Denavit–Hartenberg Convention

The established formalism for describing transformations between two frames adjacent to a joint is the Denavit–Hartenberg (DH) parameters:  $\mathbf{a}$ ,  $\alpha$ ,  $d$ , and  $\theta$ . For the NAO,

these parameters are provided by the manufacturer. The current angle (state) of the joint is  $\theta$ . Given the parameters of some joint  $j$ , the DH transformation that describes the translation and orientation of the reference frame of joint  $j$  with respect to the reference frame of the previous joint  $j - 1$  is:

$$\mathbf{T}_{j-1}^j = \mathbf{R}_x(\alpha_j) \mathbf{A}([a_j \ 0 \ 0]^\top) \mathbf{R}_z(\theta_j) \mathbf{A}([0 \ 0 \ d_j]^\top)$$

Being a product of invertible matrices, a DH transformation matrix is always invertible.

### D. Transformation Decomposition

An arbitrary transformation matrix can be decomposed as a “translation after rotation” pair:

$$\mathbf{T} = \begin{bmatrix} \mathbf{R} & \bar{\mathbf{y}} \\ \bar{\mathbf{0}}^\top & 1 \end{bmatrix} = \begin{bmatrix} \mathbf{I}_3 & \bar{\mathbf{y}} \\ \bar{\mathbf{0}}^\top & 1 \end{bmatrix} \begin{bmatrix} \mathbf{R} & \bar{\mathbf{0}} \\ \bar{\mathbf{0}}^\top & 1 \end{bmatrix}$$

Using the *Yaw–Pitch–Roll* convention, any rotation matrix  $\mathbf{R}$  decomposes into a product of the three elementary rotations:

$$\mathbf{R} = \mathbf{R}_z(a_z) \mathbf{R}_y(a_y) \mathbf{R}_x(a_x)$$

The orientation vector  $[a_x \ a_y \ a_z]^\top$  can be extracted analytically from any rotation matrix. Therefore, any *position* in the three-dimensional space, described by the six values of a translation vector  $[p_x \ p_y \ p_z]^\top$  and an orientation vector  $[a_x \ a_y \ a_z]^\top$ , defines a unique transformation matrix.

### III. NAO FORWARD KINEMATICS SOLUTION

Taking the torso frame of the NAO robot as the base frame, the forward kinematic equations for the five kinematic chains of NAO (RoboCup Edition) are the following:

$$\mathbf{T}_{\text{Base}}^{\text{Head}} = \mathbf{A}_{\text{Base}}^0 \mathbf{T}_0^1 \mathbf{T}_1^2 \mathbf{R}_x(\frac{\pi}{2}) \mathbf{R}_y(\frac{\pi}{2}) \mathbf{A}_2^{\text{Head}} \quad (2)$$

$$\mathbf{T}_{\text{Base}}^{\text{LHand}} = \mathbf{A}_{\text{Base}}^0 \mathbf{T}_0^1 \mathbf{T}_1^2 \mathbf{T}_2^3 \mathbf{T}_3^4 \mathbf{R}_z(\frac{\pi}{2}) \mathbf{A}_4^{\text{LHand}} \quad (3)$$

$$\mathbf{T}_{\text{Base}}^{\text{RHand}} = \mathbf{A}_{\text{Base}}^0 \mathbf{T}_0^1 \mathbf{T}_1^2 \mathbf{T}_2^3 \mathbf{T}_3^4 \mathbf{R}_z(\frac{\pi}{2}) \mathbf{A}_4^{\text{RHand}} \mathbf{R}_z(-\pi) \quad (4)$$

$$\mathbf{T}_{\text{Base}}^{\text{LFoot}} = \mathbf{A}_{\text{Base}}^0 \mathbf{T}_0^1 \mathbf{T}_1^2 \mathbf{T}_2^3 \mathbf{T}_3^4 \mathbf{T}_4^5 \mathbf{T}_5^6 \mathbf{R}_z(\pi) \mathbf{R}_y(-\frac{\pi}{2}) \mathbf{A}_6^{\text{LFoot}} \quad (5)$$

$$\mathbf{T}_{\text{Base}}^{\text{RFoot}} = \mathbf{A}_{\text{Base}}^0 \mathbf{T}_0^1 \mathbf{T}_1^2 \mathbf{T}_2^3 \mathbf{T}_3^4 \mathbf{T}_4^5 \mathbf{T}_5^6 \mathbf{R}_z(\pi) \mathbf{R}_y(-\frac{\pi}{2}) \mathbf{A}_6^{\text{RFoot}} \quad (6)$$

where each  $\mathbf{T}_i^j$  in the equations above is the DH transformation matrix between joints  $i$  and  $j$  in the corresponding chain and the  $\mathbf{A}$ 's are translation matrices defined by the specifications of the robot (lengths of limbs) [5].

Should we need to extract the position of some manipulator  $b$  with respect to another  $a$  (e.g. head with respect to left leg), we can construct two such chains  $\mathbf{T}_c^a$ ,  $\mathbf{T}_c^b$  from a common point  $c$  (e.g. Base) and combine them as  $\mathbf{T}_a^b = (\mathbf{T}_c^a)^{-1} \mathbf{T}_c^b$ .

### IV. SOLVING THE INVERSE KINEMATICS PROBLEM

Precise control of manipulators and effectors can be achieved by solving the inverse kinematics problem, whereby the values  $\theta_i$  of the angles of various joints must be determined to place the manipulator at a specific target position (translation and/or orientation). The solution of the inverse problem is robot-specific and generally under/over-determined kinematic chains exist. Iterative numerical solutions may converge to a solution, but, in general, suffer from singularities and poor performance [8]. On the other hand, analytical solutions are fast and exact, but require significant effort in extracting them.

### A. Inverse Kinematics Methodology

The following seven steps were taken in order to find a complete solution for the inverse kinematics problem for all the kinematic chains of the NAO humanoid robot.

1) *Construct the numeric transformation:* Given a desired target position, denoted by an orientation vector  $\bar{a} = [a_x \ a_y \ a_z]^T$  and a translation vector  $\bar{p} = [p_x \ p_y \ p_z]^T$ , it is easy to reconstruct the target transformation matrix:

$$\mathbf{T} = \mathbf{A}(\bar{p})\mathbf{R}_z(a_z)\mathbf{R}_y(a_y)\mathbf{R}_x(a_x)$$

2) *Construct the symbolic transformation:* Setting all  $\theta$  parameters as unknowns in the forward kinematics solution of the target kinematic chain yields a symbolic matrix:

$$\mathbf{T}_{\text{base}}^0 \mathbf{T}_0^j(\theta_0, \dots, \theta_j) \mathbf{T}_j^{\text{end}}$$

3) *Form a non-linear system:* By equating the above matrices, a non-linear system is formed, since the unknown  $\theta$ 's appear in transcendental trigonometric forms. Now, the problem is to find values for the  $\theta$ 's from 12 equations (the upper  $3 \times 4$  block) of which only up to six are independent.

$$\mathbf{T} = \mathbf{T}_{\text{base}}^0 \mathbf{T}_0^j(\theta_0, \dots, \theta_j) \mathbf{T}_j^{\text{end}}$$

4) *Manipulate both sides:* The chain can be simplified by eliminating known terms. Such terms (e.g. the base and the end transformations) can be removed by multiplying both sides of the system with the appropriate inverse matrix:

$$(\mathbf{T}_{\text{base}}^0)^{-1} \mathbf{T} (\mathbf{T}_j^{\text{end}})^{-1} = \mathbf{T}_0^j(\theta_0, \dots, \theta_j)$$

As soon as we find a solution for some  $\theta_i$ , we can remove in a similar way the corresponding joint  $i$  from the chain, because the corresponding DH transformation matrix is now known; this can occur if and only if this joint is the first or the last in the kinematic chain.

Another way to manipulate the chain is to induce arbitrary (known) constant transformations at the beginning or the end of the chain, aiming at simplifying the non-linear system.

$$\mathbf{T}_c (\mathbf{T}_{\text{base}}^0)^{-1} \mathbf{T} (\mathbf{T}_j^{\text{end}})^{-1} = \mathbf{T}_c \mathbf{T}_0^j(\theta_0, \dots, \theta_j)$$

In some kinematic chains we can decouple the orientation and translation sub-problems. Quite often the target translation vector can be expressed as a function of fewer joints in the analytical equation of the kinematic chain or in the analytical equation of the reverse kinematic chain.

5) *Use geometry and trigonometry:* It is possible to form a closed-form solution for some  $\theta_j$  using a geometric model of the chain. For chains with up to two links (non-zero  $a$  and  $d$  parameters) or “arm and wrist” chains commonly found in humanoids, a geometric approach can easily determine the values for the joints that lie between the links. These joints can be modeled as an angle of the triangle formed by the links, so the value of the joint can be obtained using trigonometry.

The kinematic arm chain of the NAO robot, for example, has such a joint. Figure 2 shows the triangle formed by the upper arm, the lower arm, and the line that connects the base with the target point. Upper and lower arm lengths are known

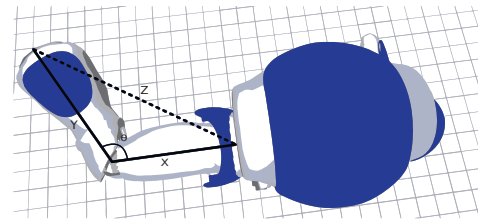


Fig. 2. Triangle formed by the robot arm

and the third side of the triangle can be computed using the Euclidean distance between the base of the chain and the end of the chain. The law of cosines, yields a set of complementary closed-form solutions for the angle  $\theta$ .

6) *Solve the non-linear system:* The resulting equations are combinations of  $\sin \theta_i$  and  $\cos \theta_i$ , thus, the closed-form solution of these equations must utilize the inverse trigonometric functions ( $\text{acos}$ ,  $\text{asin}$ ). The transcendental nature of the  $\text{acos}$  and  $\text{asin}$  trigonometric functions has the inherent problem of producing multiple solutions in  $[-\pi, \pi]$ . Without any restrictions on the valid range of a joint, we must examine all candidate solutions for each joint and their combinations for validity. To avoid this multiplicity, solutions that rely on  $\text{atan}$  and  $\text{acot}$  are preferred, but forming them might not be possible for a particular chain.

7) *Validate through forward kinematics:* Generally, there are multiple candidate solutions for the joint values, due to the existence of complementary and/or supplementary angles. A validation step is taken to discard invalid candidates. This validation is performed by feeding each candidate solution to the forward kinematics of the chain and checking whether the resulting position matches precisely the target position. Choosing among the valid solutions, if more than one, can be addressed independently of kinematics.

### B. Applicability

The methodology presented above offers a generic guideline for solving the inverse kinematics problem on typical humanoid robot kinematic chains that have the generic two-link configuration (found in both the arms and legs). More specifically, the kinematic chains must have up to five joints or six joints with three consecutive ones having intersecting axes [9], [10] to expect a possible solution.

## V. NAO INVERSE KINEMATICS SOLUTION

Using the methodology presented above, we find the inverse kinematics solution for all five kinematic chains of NAO (RoboCup Edition): head (2 joints), left arm (4 joints), right arm, left leg (6 joints), and right leg. The left chains are almost identical to the right ones, thus the solutions are similar. Due to space restrictions, the solutions for the the left part are presented in detail, whereas the ones for the right part are abbreviated. Full details may be found in a longer technical report [11].

### A. Inverse Kinematics for the Head Chain

The head chain consists of only two joints (HeadYaw, HeadPitch—in this order), therefore we can solve for either

$$\begin{aligned}\theta_2 &= \text{asin} \left( \frac{-p_z + l_3}{\sqrt{l_1^2 + l_2^2}} \right) - \text{atan} \left( \frac{l_1}{l_2} \right) + \frac{\pi}{2} \\ \theta_2 &= \pi - \text{asin} \left( \frac{-p_z + l_3}{\sqrt{l_1^2 + l_2^2}} \right) - \text{atan} \left( \frac{l_1}{l_2} \right) + \frac{\pi}{2} \\ \theta_1 &= \pm \text{acos} \left( \frac{p_x}{l_2 \cos \left( \theta_2 - \frac{\pi}{2} \right) - l_1 \sin \left( \theta_2 - \frac{\pi}{2} \right)} \right) \\ &\quad \text{provided a target translation } (p_x, p_y, p_z), \text{ or} \\ \theta_1 &= a_z \quad \theta_2 = a_y \\ &\quad \text{provided a target orientation } (a_x, a_y, a_z)\end{aligned}$$

Fig. 3. Head Inverse Kinematics Solution

the translation ( $\bar{p}$ ) or the orientation ( $\bar{a}$ ) of the target position to obtain a solution. In the latter case, we can achieve the desired target orientation simply by setting the HeadYaw and HeadPitch joints to  $a_z$  and  $a_y$  respectively, and assume  $a_x = 0$ . In the former case, we construct the symbolic matrix through the forward kinematics solution (Eq. 2). Now, we can equate the translation part from the symbolic matrix with  $\bar{p}$  and from these equations we can easily find the desired  $\theta$  values. Figure 3 shows the resulting analytical solution, in which  $l_1$  and  $l_2$  are the  $x$  and the  $y$  part of the end translation and  $l_3$  is the  $z$  part of the base translation.

### B. Inverse Kinematics for the Left Arm Chain

The left arm chain consists of four joints (LShoulderPitch, LShoulderRoll, LEIbrowYaw, LEIbrowRoll—in this order). Following our methodology, the first three steps are straightforward given the forward kinematics solution (Eq. 3). The fourth step is not required, because the problem is not too complicated. Using trigonometry, we find the value of  $\theta_4$ , as shown in Figure 2. Next, the remaining three joint values are easily extracted by solving the equations of the non-linear system. Finally, we validate all candidate solutions through the forward kinematics validation step. Figure 4 shows the resulting analytical solution, in which  $\bar{s}$  is the base translation vector,  $l_1$  is the  $y$  part of the base translation,  $l_3$  is the length of the upper arm,  $l_4$  is the length of the lower arm, and  $\mathbf{T}_{(i,j)}$  is the  $(i, j)$  element of matrix  $\mathbf{T}$ .

### C. Inverse Kinematics for the Right Arm Chain

The right arm chain is almost identical to the left arm chain. The only difference is in the forward kinematics solution, since there is one more rotation at the end of the chain (Eq. 4). This last rotation can be easily removed following the fourth step of our methodology, by multiplying both sides of the equations from the right with  $(\mathbf{R}_z(-\pi))^{-1}$ . Besides this difference, all other steps have similar results. The analytical solution is the one shown in Figure 4 with the following differences: (a) matrix  $\mathbf{T}$  must be multiplied upfront by  $(\mathbf{R}_z(-\pi))^{-1}$  from the right, (b) there is no minus sign in the equation for  $\theta_4$ , (c) there is a minus sign before  $\mathbf{T}_{(2,4)}$  in the equation for  $\theta_2$ , and (d) all instances of  $(\theta_2 - \frac{\pi}{2})$  in the equations for  $\theta_3$  and  $\theta_1$  are changed to  $(\theta_2 + \frac{\pi}{2})$ .

$$\begin{aligned}\theta_4 &= - \left( \pi - \text{acos} \left( \frac{l_3^2 + l_4^2 - \|\bar{s} - \bar{p}\|_2}{2l_3l_4} \right) \right) \\ \theta_2 &= \pm \text{acos} \left( \frac{\mathbf{T}_{(2,4)} - l_1 - \left( \frac{l_4 \sin \theta_4 \mathbf{T}_{(2,2)}}{\cos \theta_4} \right)}{l_3 + l_4 \cos \theta_4 + l_4 \frac{\sin^2 \theta_4}{\cos \theta_4}} \right) + \frac{\pi}{2} \\ \theta_3 &= \text{asin} \left( \frac{\mathbf{T}_{(2,3)}}{\sin \left( \theta_2 - \frac{\pi}{2} \right)} \right) \quad \theta_3 = \pi - \text{asin} \left( \frac{\mathbf{T}_{(2,3)}}{\sin \left( \theta_2 - \frac{\pi}{2} \right)} \right) \\ \theta_1 &= \begin{cases} \pm \text{acos} \left( \frac{\mathbf{T}_{(3,3)} + \frac{\mathbf{T}_{(1,3)} \sin \theta_3 \cos \left( \theta_2 - \frac{\pi}{2} \right)}{\cos \theta_3}}{\cos \theta_3 + \frac{\cos^2 \left( \theta_2 - \frac{\pi}{2} \right) \sin^2 \theta_3}{\cos \theta_3}} \right) & \text{if } \theta_3 \neq \frac{\pi}{2} \\ \pm \text{acos} \left( \frac{\mathbf{T}_{(1,3)}}{\cos \left( \theta_2 - \frac{\pi}{2} \right) \sin \theta_3} \right) & \text{if } \theta_3 = \frac{\pi}{2} \end{cases}\end{aligned}$$

Fig. 4. Left Arm Inverse Kinematics Solution

$$\begin{aligned}\mathbf{T}' &= \left( \mathbf{R}_x \left( \frac{\pi}{4} \right) \left( (\mathbf{A}_{\text{Base}}^0)^{-1} \mathbf{T} (\mathbf{A}_6^{\text{End}})^{-1} \right) \right)^{-1} \\ \theta_4 &= \pm \left( \pi - \text{acos} \left( \frac{l_1^2 + l_2^2 - \|\bar{0} - \bar{p}\|_2}{2l_1l_2} \right) \right) \\ \theta_6 &= \begin{cases} \text{atan} \left( \frac{\mathbf{T}'_{(2,4)}}{\mathbf{T}'_{(3,4)}} \right) & \text{if } (l_2 \cos \theta_5 + l_1 \cos (\theta_4 + \theta_5)) \neq 0 \\ \text{undefined} & \text{if } (l_2 \cos \theta_5 + l_1 \cos (\theta_4 + \theta_5)) = 0 \end{cases} \\ \mathbf{T}'' &= \left( (\mathbf{T}')^{-1} (\mathbf{T}_5^6 \mathbf{R}_z(\pi) \mathbf{R}_y(-\frac{\pi}{2}))^{-1} \right)^{-1} \\ \theta_5 &= \text{asin} \left( - \frac{\mathbf{T}''_{(2,4)} (l_2 + l_1 \cos \theta_4) + l_1 \mathbf{T}''_{(1,4)} \sin \theta_4}{l_1^2 \sin^2 \theta_4 + (l_2 + l_1 \cos \theta_4)^2} \right) \\ \theta_5 &= \pi - \text{asin} \left( - \frac{\mathbf{T}''_{(2,4)} (l_2 + l_1 \cos \theta_4) + l_1 \mathbf{T}''_{(1,4)} \sin \theta_4}{l_1^2 \sin^2 \theta_4 + (l_2 + l_1 \cos \theta_4)^2} \right) \\ \mathbf{T}''' &= (\mathbf{T}'')^{-1} (\mathbf{T}_3^4 \mathbf{T}_4^5)^{-1} \\ \theta_2 &= \pm \text{acos} (\mathbf{T}'''_{(2,3)}) - \frac{\pi}{4} \\ \theta_3 &= \text{asin} \left( \frac{\mathbf{T}'''_{(2,2)}}{\sin \left( \theta_2 + \frac{\pi}{4} \right)} \right) \quad \theta_3 = \pi - \text{asin} \left( \frac{\mathbf{T}'''_{(2,2)}}{\sin \left( \theta_2 + \frac{\pi}{4} \right)} \right) \\ \theta_1 &= \pm \text{acos} \left( \frac{\mathbf{T}'''_{(1,3)}}{\sin \left( \theta_2 + \frac{\pi}{4} \right)} \right) + \frac{\pi}{2}\end{aligned}$$

Fig. 5. Left Leg Inverse Kinematics Solution

### D. Inverse Kinematics for the Left Leg Chain

The kinematic chain of the left leg has six joints (LHipYawPitch, LHipRoll, LHipPitch, LKneePitch, LAnklePitch, LAnkleRoll—in this order), but since the first three joints have intersecting axes, the problem is possibly solvable [9], [10]. We construct both the numerical and symbolic parts of the system with the help of forward kinematics (Eq. 5). Following the fourth step, to make the problem easier, we remove the known translations from the kinematic chain. Then, to simplify the solution we induce a  $\mathbf{R}_x(\frac{\pi}{4})$  transformation at the start of the chain. In effect, we transform the first joint from a yaw-pitch joint to a yaw joint, which is simpler to handle. Close examination of the resulting kinematic chain reveals that

the first four joints are responsible for the translation part and all six joints are responsible for the orientation part. It would be convenient, if only three joints were affecting the translation of the end effector, because in that case we could extract these joints just from the translation part. Thus, we invert the transformation matrix to form the reverse chain. Now, only three joints (LAnkleRoll, LAnklePitch, LKneePitch) affect the translation. We can now find  $\theta_4$  the same way we found  $\theta_4$  for the arms. We focus on the triangle formed by the UpperLeg, LowerLeg, and the line connecting the base to the target point. Next, the  $\theta_5$  and  $\theta_6$  angles can be extracted from the translation part. The solution we found for  $\theta_6$  has some undefined points, because the denominator of the result may become zero. These undefined points are discussed in Section VI.

After we calculate  $\theta_4$ ,  $\theta_6$ , and  $\theta_5$  from the translation part, we can go back to step four and remove the, now, known DH transformation matrices from the chain. The resulting kinematic chain consists of only three joints, which control only the orientation. It is easy to extract the remaining joint values from the nine equations of the rotation block. Figure 5 shows the resulting analytical solution, in which  $l_1$  is the length of the upper leg and  $l_2$  is the length of the lower leg.

#### E. Inverse Kinematics for the Right Leg Chain

The right leg chain is identical to the left leg chain. The only difference is the DH parameter  $\alpha$  of the first joint. Thus, we must multiply instead with  $\mathbf{R}_x(-\frac{\pi}{4})$ . Otherwise, the solution is exactly the same as the solution shown in Figure 5 with all instances of  $(\theta_2 + \frac{\pi}{4})$  changed to  $(\theta_2 - \frac{\pi}{4})$ .

### VI. IMPLEMENTATION

Having completed all kinematics in analytical form, we created `NAOKinematics`, a software library for real-time, onboard execution of NAO kinematics in C++. Given that C++ offers no library for optimized real-time matrix operations, we relied on our linear algebra framework `KMat` [12] for such operations. A Matlab version of the library is also available for other applications. Our library includes five functions for calculating the forward kinematics for each chain, given the corresponding joint values. It also includes five functions, whose input is the desired target position and output is a set of solutions, for all the joints of a specified chain. The library also includes a function for calculating the center of mass of the robot given a set of values for all joints.

As mentioned before, there are a few target positions for the legs which lead to an infinity of solutions for the AnkleRoll joint, when the KneePitch and AnklePitch joints take specific values and essentially cancel the effect of AnkleRoll on the translation of the reverse chain. Figure 6 shows one of these problematic configurations. The locus of these configurations is a line in the configuration space (Figure 7). To verify that in practice the robot never reaches any of these configurations, we let the robot perform the entire range of motions available to it during operation in a RoboCup field (walk, kicks, stand-up, etc.) and plotted these motions alongside the problematic locus. The results are shown in Figure 7. It is clear that no



Fig. 6. An instance of the problematic leg configurations

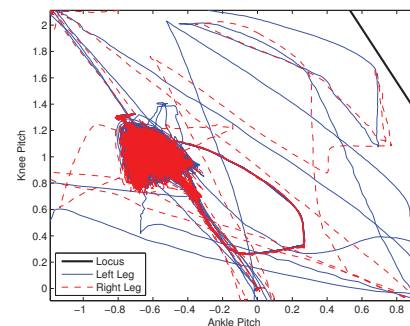


Fig. 7. Trajectories of motion in a subspace of the leg joints

motion brought the robot to these configurations. In practice, it is rather unlikely that anyone will consistently give target positions that drive the joints in that area, during regular use.

### VII. RESULTS

#### A. Real-Time Performance

One of the goals of this work was to implement a software library for real-time kinematics computations on the robot. We measured the performance of our implementation for each of the functions we offer. Table I shows average execution times.

#### B. Demonstration I: Basic CoM Balancing

In this demonstration, we seek to implement a very basic balancing method. In particular, we want to make NAO move one of its feet to the point of the projection of the Center of Mass (CoM) on the floor. First, we calculate the translation of the CoM relatively to the torso frame using forward kinematics. The problem is that the  $x$ - $y$  plane of the torso frame is rarely parallel to the floor. Thus, we read off the inertial unit of the robot the current rotation (angleX and angleY) of the

TABLE I  
 ON-BOARD EXECUTION TIMES OF THE NAOKINEMATICS LIBRARY

Kinematics Function	Time ( $\mu$ s)
Forward Kinematics for Head	54.28
Forward Kinematics for Arm	66.72
Forward Kinematics for Leg	80.88
Inverse Kinematics for Head	70.79
Inverse Kinematics for Arm	170.55
Inverse Kinematics for Leg	185.29
Calculation of the Center of Mass	394.55

torso plane. Now, we can calculate the translation of the CoM relatively to the rotated torso:

$$\mathbf{T}_{\text{rotated}} = \mathbf{R}_y(\text{angleY})\mathbf{R}_x(\text{angleX})\mathbf{A}(\text{CoM})$$

Then, we assign a custom value to  $p_z$  in  $\mathbf{T}_{(4,3)}$ , which represents the desired torso height from the floor and that yields  $\mathbf{T}'_{\text{rotated}}$ . Now we must rotate back to the torso frame:

$$\mathbf{T}_{\text{final}} = (\mathbf{R}_y(\text{angleY})\mathbf{R}_x(\text{angleX}))^{-1}\mathbf{T}'_{\text{rotated}}$$

Finally, we extract  $p_x$ ,  $p_y$ , and  $p_z$  from  $\mathbf{T}_{\text{final}}$  and we set  $[p_x \ p_y \ p_z]^T$  as the target translation for inverse kinematics. The target orientation is set to  $[a_x \ a_y \ a_z]^T = [-\text{angleX} \ -\text{angleY} \ 0]^T$ , because we do not care about the rotation about the  $z$ -axis. Note that the foot is always parallel to the floor, excluding any hardware precision errors.

### C. Demonstration II: Pointing to the Ball

In this demonstration, our goal is to make the NAO point to the ball with its stretched arms. Apart from the kinematics, to realize this task we employed our vision module [12] for ball recognition, along with the module that filters the belief of the robot about the ball location. Initially, NAO scans for the ball. When found, it points to it with the left, the right, or both arms, depending on where the ball is located (left, right, or front). The ball observation can be described as a two-dimensional translation  $(p_x, p_y)$  on the floor. We add the height of the torso (found through forward kinematics) as the third coordinate  $p_z$  to form the ball translation  $(p_x, p_y, p_z)$  in the three-dimensional space. We also set  $a_x$  to zero, because we are only rotating about the  $y$ -axis (up/down) and the  $z$ -axis (right/left). To find the other two orientations, we focus on the straight line that connects the location of the ball and the point of the ShoulderPitch joint relatively to the torso frame. The orientations  $a_y, a_z$  are the angles between this line and the corresponding axes. Additionally, the target point lies on this line at a distance equal to the length of the stretched arm from the ShoulderPitch joint. We run this procedure for both arms and obtain the solution(s) from inverse kinematics. If both solutions are returned, the robot raises both arms pointing to the ball. If only one solution is returned, the robot raises only one arm; the other arm cannot physically point to the ball.

## VIII. CONCLUSION

In this paper, we presented a complete, exact, analytical solution for the problems of forward and inverse kinematics of the NAO robot. The main advantage of our solution is its accuracy, its efficiency, and the elimination of singularities. In addition, we contributed an implementation of the proposed NAO kinematics as a freely-available software library for real-time execution on the robot or for simulations.

Our approach to NAO kinematics is based on standard principled methods for studying robot kinematic chains. No complete analytical solution with full implementation for the NAO robot has been published before. The currently widely-known solution of team B-Human [3] applies only to the legs,

is purely geometric, and cannot be generalized to other kinematic chains. In addition, their work has not studied the effect of the existing potentially problematic configurations. We have tried to implement the other published analytical solution for the legs by team MRL [4], but we were not able to reproduce their results. Finally, the numerical solution [5] offered by the manufacturer of the robot, Aldebaran Robotics, is a proprietary implementation, which unfortunately is inherently prone to singularities and, therefore, lacks in robustness. It should be noted that none of the two demonstrations we presented in this paper could be realized with the existing solutions and implementations of NAO kinematics.

Since kinematics is the base for several applications related to robot motion, we expect that our work will be useful not only to RoboCup SPL teams, but also to any NAO software developer. We believe that NAO developers can take advantage of our off-the-shelf NAO kinematics library to work on omnidirectional walk algorithms, dynamic balancing methods, dynamic kick engines, etc. Our library can offer the basis for following dynamic trajectories in real time for walking and kicking or calculating the center of mass dynamically in real time for balancing.

Finally, our methodology offers a generic guideline for addressing the problem of inverse kinematics in humanoid robots. Apart from extending our work to the Academic Edition of NAO, which has four additional joints, one of our future goals is to apply the same methodology to robots similar to NAO, such as the Darwin-OP humanoid robot, which has a maximum of six degrees of freedom per kinematic chain.

## REFERENCES

- [1] H. Kitano, M. Asada, Y. Kuniyoshi, I. Noda, E. Osawa, and H. Matsubara, "Robocup: A challenge problem for AI," *AI Magazine*, vol. 18, no. 1, pp. 73–85, 1997.
- [2] D. Gouaillier and P. Blazevic, "A mechatronic platform, the Aldebaran Robotics humanoid robot," in *Proceedings of the 32nd IEEE Annual Conference on Industrial Electronics (IECON)*, 2006, pp. 4049–4053.
- [3] C. Graf, A. Härtl, T. Röfer, and T. Laue, "A robust closed-loop gait for the Standard Platform League humanoid," in *Proceedings of the Fourth Workshop on Humanoid Soccer Robots*, 2009, pp. 30–37.
- [4] M. G. Jadidi, E. Hashemi, M. A. Z. Harandi, and H. Sadjadian, "Kinematic modeling improvement and trajectory planning of the NAO biped robot," in *Proceedings of the 1st Joint International Conference on Multibody System Dynamics*, 2010.
- [5] Aldebaran Robotics, "Nao documentation," 2012, only available online: [www.aldebaran-robotics.com/documentation](http://www.aldebaran-robotics.com/documentation).
- [6] J. Denavit and R. S. Hartenberg, "A kinematic notation for lower-pair mechanisms based on matrices," *ASME Journal of Applied Mechanics*, vol. 22, pp. 215–221, 1955.
- [7] R. S. Hartenberg and J. Denavit, *Kinematic Synthesis of Linkages*. New York: McGraw-Hill, 1964.
- [8] S. R. Buss, "Introduction to inverse kinematics with Jacobian transpose, pseudoinverse and damped least-squares methods," 2009, available at: [www.math.ucsd.edu/~sbuss/ResearchWeb/ikmethods/iksurvey.pdf](http://www.math.ucsd.edu/~sbuss/ResearchWeb/ikmethods/iksurvey.pdf).
- [9] D. Pieper and B. Roth, "The kinematics of manipulators under computer control," in *Proceedings of the 2nd International Congress on Theory of Machines and Mechanisms*, vol. 2, 1969, pp. 159–169.
- [10] D. Pieper, "The kinematics of manipulators under computer control," Ph.D. dissertation, Stanford University, U.S.A., 1968.
- [11] N. Kofinas, "Forward and inverse kinematics for the NAO humanoid robot," Diploma Thesis, Technical University of Crete, Greece, 2012, available at: [www.intelligence.tuc.gr/lib/downloadfile.php?id=430](http://www.intelligence.tuc.gr/lib/downloadfile.php?id=430).
- [12] E. Orfanoudakis, "Reliable object recognition for the RoboCup domain," Diploma Thesis, Technical University of Crete, Greece, 2011.

# On the development and simulation of a Robotic Ultrasound Guided System for Orthopedic Surgical Procedures

P.J.S. Gonçalves, P.M.B. Torres  
Polytechnic Institute of Castelo  
Branco, Univ Tecn Lisboa,  
IDMEC, LAETA, Portugal  
paulo.goncalves@ipcb.pt

F. Santos, R. António, N. Catarino  
Polytechnic Institute of Castelo  
Branco, Av Empresário, 600-767  
Castelo Branco, Portugal  
pedrotorres@ipcb.pt

J.M.M. Martins  
Instituto Superior Técnico,  
Univ Tecn Lisboa, IDMEC,  
LAETA, Lisbon, Portugal  
jorgemartins@ist.utl.pt

**Abstract**—Surgical navigation is a crucial concept in computer assisted surgery. The use of robots in the surgery room largely benefits from this concept recent developments, namely with the use of non-invasive and radiation free imaging systems, like ultrasound (US). This paper presents the algorithms and software tools developed for US based orthopedic surgery navigation. In the second part of the paper are presented the algorithms and software tools developed for controlling a robotic manipulator, that can be used both in simulation and in a real scenario. The paper also presents the developed simulation scenario, for a surgical procedure in Hip Resurfacing, e.g., the first drill of the femur head. For navigation, the system, during surgery, acquires a 3D US bone surface from a sequence of US images. This bone surface will then be registered to the pre-operative bone model, for a precise knowledge of the bone position and orientation. The measured bone movement is used by the simulation tool to control the robot manipulator drilling trajectory.

## I. INTRODUCTION

Image-guided surgical navigation is on the rise in many different areas of medicine, with strong growth in orthopedic surgery. In computer assisted orthopedic surgery procedures, the surgeon has to locate and identify specific anatomical structures in order to improve surgical accuracy. Currently the navigation systems applied to the orthopedic surgery use invasive methods to locate the bones in surgical space. Acrobot [1] or Robodoc [2], are examples of such systems, used in knee or hip replacement surgeries. With the system proposed in this paper is possible to reduce or eliminate the use of fiducial markers, decreasing patient recovery time and consequences after surgery. Work with a surgical robot demands substantial training and continual practice, since surgeons are not used to working with robots. To overcome the fear and help the surgeons in adapting, surgical procedures simulation is very important, so it is strongly emphasized in this paper.

This article focuses on orthopedic surgery, namely in Hip Resurfacing surgery, where obtaining the position and orientation of the bones and surgical instruments is very important. The first drill of the femur head is of special importance for the surgical procedure success, in terms of accuracy. The main objective is to obtain the intra-operative pose of the femur related to the pre-operative scenario. For that, in this paper, are proposed algorithms for bone contour

segmentation, tracking and registration, using specific equipment like: Ultrasound (US) images; NDI Polaris Spectra tracker, and a specially designed US probe holder.

Simulators gain everyday more importance, providing essential knowledge about systems behaviour (in this paper, the surgical environment) before being placed in the real working scenarios. The purpose of the paper is also to create a simulated surgery room environment and a constant flow of data between the simulator and other equipment and softwares that allows to test the performance of Ultrasound Guided Robotic Surgery Systems, designed to orthopedic surgery.

## II. ULTRASOUND BASED BONE TRACKING

In this section is proposed a ultrasound bone tracking module, as part of a navigation system for orthopedic surgery. This module is based on the Image Guided Surgery Toolkit, IGSTK (<http://www.igstk.org/>). It is a free open source C++ toolkit, and provides a framework for rapid prototyping of customized image-guided surgical applications. The toolkit provides a set of components common to general purpose navigation systems, such as interface with tracking systems, image registration and visualization through the ITK and VTK toolkits, (<http://www.itk.org/>) and (<http://www.vtk.org/>). For the navigation system proposed in this paper the integration of the Open Computer Vision library, OpenCV (<http://opencv.willowgarage.com/>), was also done to allow ultrasound image acquisition and processing from the US probe, through a USB video capture. Next sub-sections describe the hardware setup, the contour bone extraction and tracking from US images, and how to obtain a point cloud from a sequence of captured images.

### A. Hardware setup

In Figure 1 is depicted an overview of the Navigation system and the surgical robot, in terms of the coordinate frames and the relationships between them. Note that the preoperative and intra-operative scenarios are clearly split. In the lower part of the figure appears two NDI Polaris targets that are usually attached to the US probe and to the robot frame. The first for tracking the bone and the second to calibrate the frame robot pose in the intra-operative scenario. The 3D CT femur bone model, acquired in the preoperative

scenario is the origin of the overall setup, because of the model itself is more accurate, i.e., the data obtained from US images is less accurate. All points in the model are referenced to the CT. The relation between the 3D US points acquired in the intraoperative scenario and 3D CT points from the bone model is obtained from point cloud registration using the methods later presented in section III. See the transformation  ${}^{CT}T_{NDI}$ , in figure 1. The pose of the robot end-effector also has to be referenced by the Navigation system to inform the robot controller of its location. The relationship between the Robot frame and the CT frame ( ${}^{CT}T_R$ ), is determined during the hardware setup, in the intra-operative scenario and once obtained remains fixed, as long the robot base does not move from its initial position.

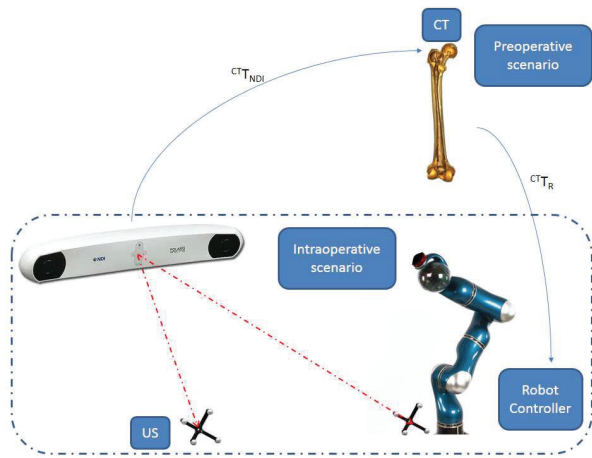


Fig. 1. Overview of the hardware setup and frames transformations.

### B. US based bone extraction and tracking

In this sub-section is proposed a method to extract and track the femur bone in a sequence of US images. This work appears in sequence of previous work of the authors [3], where a comparative study for segmenting bones in US images was performed. The *Threshold Level Set Segmentation* (TLSS) [4] obtained the best results and will further tested in this paper.

The algorithm is depicted in Figure 2 and comprises the next steps:

- 1) *Initialization* - where the US probe, with the NDI Polaris target, is correctly placed in the field of view of the NDI Polaris cameras. Also the segmentation process is initialised here, as seen below in the text.
- 2) *Image Acquisition* - where the US image is acquired using the methods implemented in OpenCV.
- 3) *NDI trigger* - where a point within the bone in the US image is chosen to start the NDI Polaris acquisition, and synchronizes the tracking process. After, the same point is used as the seed of the segmentation algorithm.
- 4) *Segmentation and Tracking* - where the bone surface in the US image is extracted.
- 5) *3D points extraction* - where the 3D points in the bone surface are calculated, using the 2D data obtained in

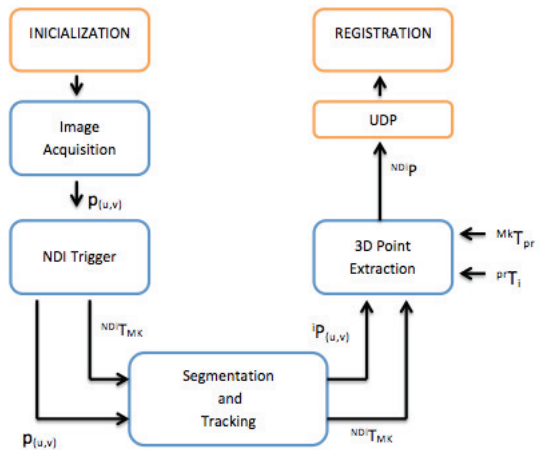


Fig. 2. Ultrasound based Bone Tracking process.

the previous step.

- 6) *UDP* - where the 3D US point cloud for an image (slice) is sent to the registration module.

This process is continuously repeated overtime to extract a suitable number of slices to then obtain a 3D US bone surface for registration, see Section III. The 4th step of the algorithm, *Segmentation and Tracking*, is of special relevance because of the image processing issues related to US images, i.e., its high level of noise. Further, since the bone is a rigidly anatomically structure, only the top surface of the bone appears in US images as can be seen in figure 3, in the red square. The main challenge of the segmentation method is to identify where the bone is, in US images. To aid the segmentation algorithm, i.e., to improve accuracy and also to speed up the segmentation, a region of interest (ROI) is defined in the first image, also in the first step of the algorithm. The ROI is marked with a square around the bone, as seen in figure 3. After this initialization, all images that arrive through the video card are segmented using the TLSS algorithm. Its goal is to define a range of intensity values that classify the bone of interest and then base the propagation term on the level set equation for that intensity range. Using the level set approach [5], the smoothness of the evolving surface can be constrained to prevent some of the leaking that is common in connected-component schemes [4]. The next iterations of the segmentation use the centroid of the bone contour, extracted in the current step, that is also responsible for the ROI update. The contour obtained in each slice, properly referenced in the NDI frame is sent in packs of 3D points by UDP to the registration process.

### C. Point Cloud Extraction

The bone contours points extracted from US images,  ${}^i P(u, v)$ , using the US probe are converted to 3D points, using the NDI Polaris Spectra pose measurement system. This sensor measures the pose of the NDI Polaris target  $M_k$  related to its reference frame  $NDI$ , i.e., the transformation

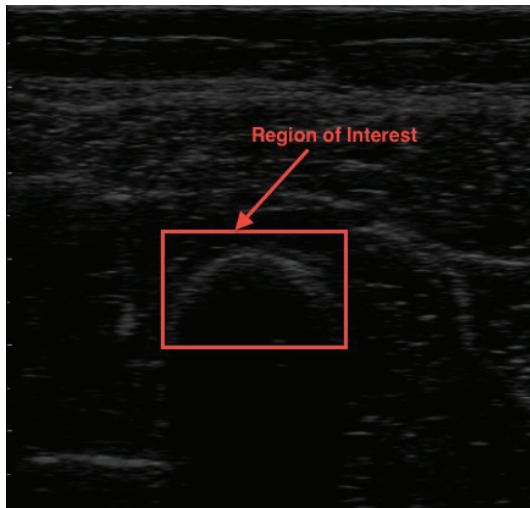


Fig. 3. Region of interest in an US image of the femur.

${}^{NDI}T_{Mk}$ . From (1) are obtained the 3D points of the bone, in the NDI frame.

$${}^{NDI}P = {}^{NDI}T_{Mk} \times {}^{Mk}T_{pr} \times {}^{pr}T_i \times {}^iP(u, v) \quad (1)$$

where,  ${}^{NDI}T_{Mk}$ , represent the relationship between passive markers and the NDI Polaris,  ${}^{Mk}T_{pr}$ , represent the relationship between US probe extremity and Marker,  ${}^{pr}T_i$  corresponds to the relationship between the image plane and US probe, and finally,  ${}^iP(u, v)$  represent a point in the image.  $S_x$  and  $S_y$  are the scale factors for the  $(u, v)$  pixel coordinates. The transformations  ${}^{Mk}T_{pr}$  and  ${}^{pr}T_i$ , depicted in Figure 4, are previously calibrated off-line.  $(u_0, v_0)$  are the image coordinate offsets.

$${}^iP(u, v) = \begin{pmatrix} u_i - u_0 \\ v_i - v_0 \\ 0 \\ 1 \end{pmatrix} \quad (2)$$

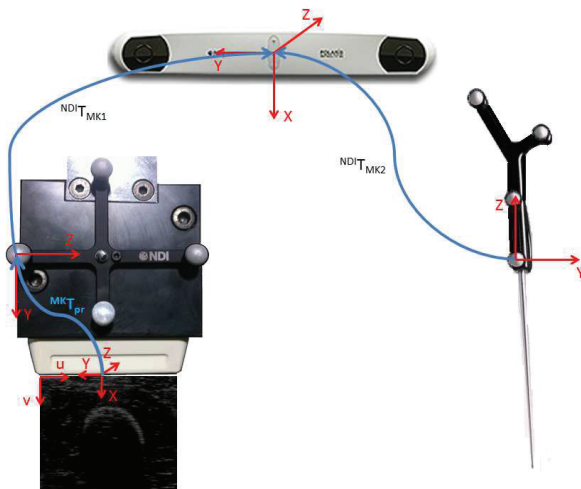


Fig. 4. NDI and ultrasound coordinate frames.

### III. REGISTRATION

In this section are presented the visualisation and registration modules of the US based navigation system.

#### A. Visualization

The Navigation system, in the preoperative part, incorporates a 3D visualization component, useful in surgical planning. It is also used in the intra-operative scenario to identify features and areas of intervention. With this functionality, the surgeon can reconstruct the total size of the bone or some regions of interest, have the possibility of rotate the bone and analyse the interior and exterior. 3D image reconstruction is implemented using the Visualization Toolkit (VTK) for Surface Rendering [6] and Volume Rendering [7].

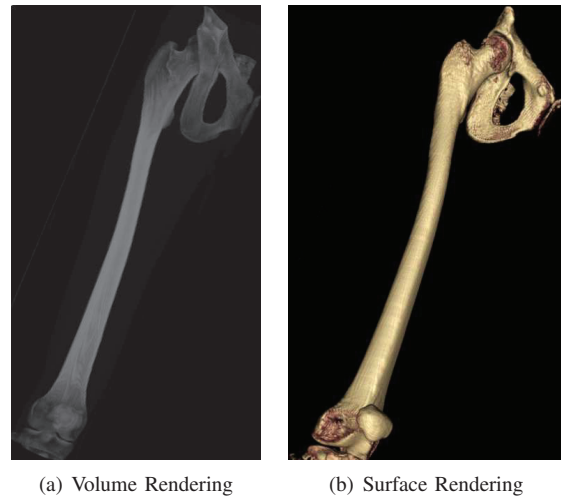


Fig. 5. Results of Visualization a human femur.

#### B. Iterative Closest Point Method

The Iterative Closest Point Method (ICP) method [8] is the standard method used to perform registration between two set of 3D points. It transforms two sets of points to a common coordinate frame. If the exact correspondences of the two data sets could be known, then the exact translation  $t$  and rotation  $R$  can be found. The main issue of the method is to find the corresponding points between the two data sets,  $Y = (y_1, \dots, y_M)^T$  and  $X = (x_1, \dots, x_N)^T$ . To obtain the closest point of  $Y$  to a point in  $X$ , the Euclidean distance is applied. When all points of the data set  $Y$  are associated to the point in  $X$  the transformation is estimated by minimizing a mean square cost function:

$$E_{ICP} = \sum_i \|R \cdot x_i + t - y_i\|^2 \quad (3)$$

#### C. The Registration Process

One of the main goals of a surgical navigation tool is to have a fast and precise update of the target position and orientation, in our case, the femur. To achieve these goals and since in the surgery procedure the femur does not change its position drastically, a *local registration*, i.e., when the two points clouds to register are "not far from each

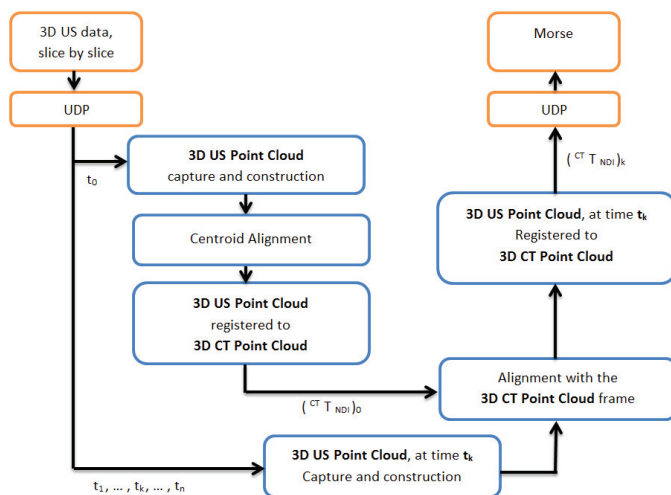


Fig. 6. The Registration Process.

other”, is performed on-line. In the presented work, when the femur, in each update, translates or rotates more than 10[mm] / 3[degrees] in each axis, a *calibration* procedure is performed.

The registration process, depicted in Fig. 6 is divided in two sub-processes. First a *calibration* procedure must take place and afterwards a *local registration* sub-process will take place during the US based navigation.

The *calibration* sub-process, takes place at time  $t_0$ , after receiving a 3D US point cloud that represents the femur US surface, obtained from the Bone tracking process. This sub-process will calculate the transformation,  $({}^{CT}T_{NDI})_0$ , to be used in the *local registration* sub-process. Its main goal is to place, i.e., register, the 3D US surface in the correct position to the pre-operative 3D CT femur model. It comprises two steps. First, is obtained the difference between the centroids, of the 3D US and the 3D CT point clouds. This difference will define the distance separating the two clouds, and is used to move the US cloud close to the CT cloud. In the second step, is applied the ICP method to register the two point clouds and obtain a precise registration.

The *local registration* sub-process registers a 3D US point cloud sent by *Bone Tracking* module. This point cloud have 50[mm] length, value that revealed accurate results for the local registration procedure, after numerous trials. The calibration transformation  $({}^{CT}T_{NDI})_0$  is then used to align the US point cloud to the CT point cloud, to fasten the registration computational time, by reducing the search radius of the ICP method. At each sample time  $t_k$  the *local registration* outputs to the *simulation* the transformation matrix  $({}^{CT}T_{NDI})_k$ . This matrix quantifies the motion, both translation and rotation, of the femur bone.

#### IV. SURGICAL NAVIGATION SIMULATION

##### A. Robotic Simulation

The use of a simulators can ease the development and validation processes, allowing to verify the component integration and to evaluate their behaviour under different

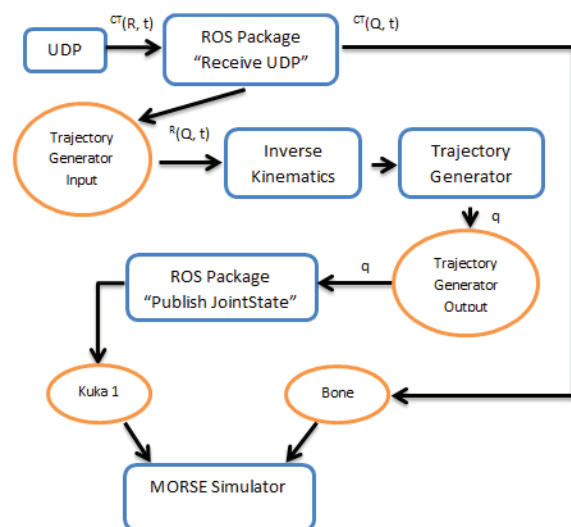


Fig. 7. The Simulation Process. Circles are the ROS nodes and squares are the developed functions/packages.

controlled circumstances. Simulation is cheaper in terms of time and human resources than experiments with real robots and medical imaging equipment. Another advantage is that a simulated environment can be significantly more complex and larger than a lab environment, and meanwhile ensure a perfect repeatability. Nowadays there are several robotic simulators like USARSim [9], MORSE [10], and more recently Gazebo (<http://gazebo.org/>), just to name the most used open-source tools. After analysing those software’s we concluded that MORSE was our best choice because it can be easy to use, have a active developing community, can be used in different contexts for testing and verification of robotics systems as a whole, at a medium to high level of abstraction. One of the main interests of the simulator is that it can be reusable by researchers, engineers and is being upgraded as part of multiple projects. Another important issue is that the simulator can interact with any middleware used in robotics, e.g., ROS [11] or OROCOS [12], and not just impose a format that others must adapt to.

##### B. The Simulation Environment

This section presents the simulation environment developed for testing the robot behaviour when performing a surgical procedure, e.g., drilling the head of the femur. Since the patient, and consequently his femur, can move during surgery, that movement is measured by the *bone tracking* and *registration* modules. This measurement,  $({}^{CT}T_{NDI})_k$ , is then used by the robot to adapt its trajectory to compensate the bone movement, when drilling.

In Figure 7 are depicted the ROS nodes and packages developed, as well the OROCOS functions for the KUKA LWR inverse kinematics and trajectory planning. This process receives from the registration process the bone movement,  $({}^{CT}T_{NDI})_k$ , at each sample time. From this input, it is generated the robot end-effector (with drill) trajectory taking into account the bone movement. It is also visualised the

bone movement at each sample time. To receive  $({}^{CT}T_{NDI})_k$ , a (ROS) package *Receive UDP* was created to set up the UDP server code for Unix environments. This package converts the rotation matrix, into a quaternion, commonly used in ROS pose, in both CT and robot frames. The first pose  ${}^{CT}(Q, t)$  is then published directly in the MORSE simulation, and is responsible for the bone movement. The second pose  ${}^R(Q, t)$  goes to a specific node, that reads the input to the Orocos Trajectory Generator [13]. Afterwards, Orocos reads  ${}^R(Q, t)$ , and calculates the Inverse Kinematics and generates the trajectory to reach the bone, for the seven joint coordinates,  $q$ . Since the Orocos Trajectory Generator publishes in a specific ROS node, another ROS package, *Publish JointState*, was created to redirect the information to the MORSE simulation. This package subscribes the node with the Orocos output and publishes it directly to the Morse simulation, updating the rotation of the drilling robot.

It is also present in Figure 10 a second KUKA LWR robot equipped with an Ultrasound probe, that send the 3D US bone surface to the NDI Polaris. At this stage it is statically positioned above the bone, measuring bone movements, but in future works we plan to also generate trajectories for automatically retrieve data from the bone surface.



Fig. 8. Threshold Level Set Segmentation Results.

## V. EXPERIMENTAL RESULTS

### A. Segmentation Results

In this sub-section is proposed a method to extract and track the femur bone in a sequence of US images. This work appears in sequence of previous work of the authors [3], where a comparative study for segmenting bones in US images was performed. The *Threshold Level Set Segmentation* (TLSS) [4] obtained the best results and will be further tested in this paper. The TLSS segmentation algorithm was applied at 201 US images of a human femur, verifying once again the results obtained in [3], as depicted in Figure 8. In Table I are presented the mean and the standard deviation (std) of the Mahalanobis distance [3]. The distances calculated are between the 201 segmented contours and the correspondent contours manually extracted by a medical expert. After segmentation is necessary to extract only the upper surface of the femur (open contour). The points extracted from the contour are related with calibration equations, presented in section II-B, to give the position in the CT/world coordinates.

	Mean $M_{dist}[mm]$	Std $M_{dist}[mm]$	Time [s]
TLSS	1.4070	0.0526	1.1

TABLE I  
 RESULTS FOR THE TLSS SEGMENTATION.

	Before Registration $H_{dist}[mm]$	After Registration $H_{dist}[mm]$	Time [s]
Calibration	6.3821	1.2703	1.56
Registration	6.5945	1.6372	0.39

TABLE II  
 RESULTS BEFORE AND AFTER THE REGISTRATION PROCESS.

### B. Registration results

All the methods presented in section III were implemented in a standalone PC, using the Point Cloud Library (PCL) [14], under an Ubuntu environment. This PC communicates with the PCs running the *Bone Tracking* and *Simulation* modules using the UDP protocol. Following previous work from the authors [15], where it was demonstrated that the bone registration procedure is dependent in the initial relative position of the clouds, the *local registration* sub-process improved the results, as presented in Table II. Dozens of registrations were performed to obtain the mean values presented in Table II for the both the experiments performed. The performance metric for point cloud registration assessment is used the modified Hausdorff distance as proposed by Dubuisson and Jain [16], because it is robust to outliers and the distance increases monotonically with the difference between the two point clouds. In figure 9 is depicted the results obtained for *calibration* and *local registration* using ICP, where can be seen a perfect match between the CT and US registered clouds.

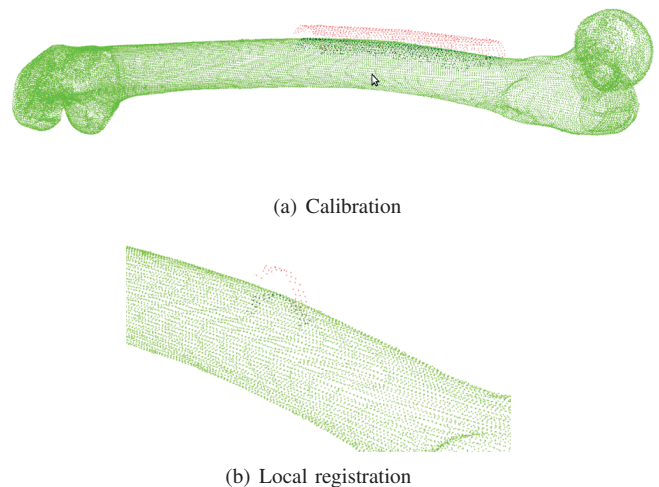


Fig. 9. Results for Calibration and Registration. 3D CT point cloud (green). 3D US point cloud before registration (red). 3D CT point cloud after registration (black).

### C. Simulation results

This section presents the results obtained at the current developing stage of the simulations. At this point and regarding Figure 10, the MORSE environment have a stable link with the registration module. In the MORSE environment, its global frame was chosen to be same as the  $CT$  frame, making the  $CT$  frame the "world frame". According to this, the transformation ( ${}^{CT}T_R$ ) was defined when placing the robots in the environment.

## VI. CONCLUSIONS AND FUTURE WORK

In this paper were tackled several issues on the development and simulation of a Robotic Ultrasound Guided System for Orthopedic Surgical Procedures. The example surgical procedure was the first drill of the femur head, where the Ultrasound based system can measure and track bone movements during the task. In the first part, the intra-operative 3D US bone surface was successfully obtained, from the algorithm proposed by the authors that includes Threshold Level Set Segmentation, using the US probe and the NDI Polaris Spectra. The 3D US surface was then registered to the preoperative scenario, from the algorithm proposed by the authors that includes the ICP method, with success. With this procedure the bone position and orientation is known referenced to the  $CT$  frame, where the surgery is planned. Finally, the previous two parts of the paper were validated in the simulator. The sequence of bone positions were obtained directly from the registration process and the robot manipulator end-effector (drill) trajectories were obtained from a trajectory planner that includes the robot inverse kinematics. The preoperative planned trajectories are corrected in this tool using the known bone movement. Future research will be focused in increase accuracy and speed of the procedures presented in this paper, for bone segmentation, tracking and registration.

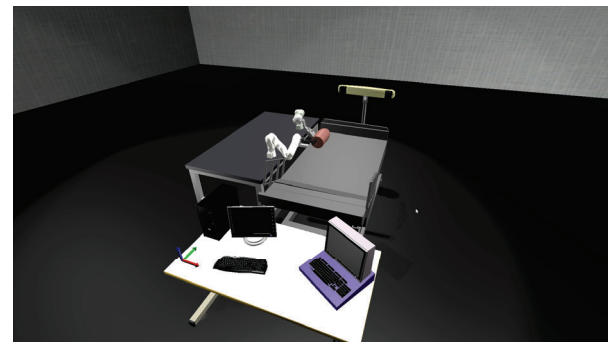
## ACKNOWLEDGMENT

This work was partly supported by FCT project PTDC/EME-CRO/099333/2008 and EU-FP7-ICT-231143, project ECHORD.

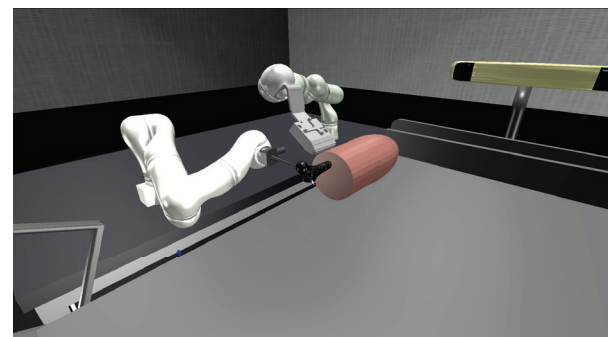
## REFERENCES

- [1] M. Jakopec, F. Rodriguez y Baena, S. Harris, P. Gomes, J. Cobb, and B. Davies, "The hands-on orthopaedic robot "acrobot": Early clinical trials of total knee replacement surgery," *Robotics and Automation, IEEE Transactions on*, vol. 19, pp. 902 – 911, oct. 2003.
- [2] P. Kazanzides, B. Mittelstadt, B. Musits, W. Bargar, J. Zuhars, B. Williamson, P. Cain, and E. Carbone, "An integrated system for cementless hip replacement," *Engineering in Medicine and Biology Magazine, IEEE*, vol. 14, pp. 307 –313, may/jun 1995.
- [3] N. M. M. Catarino, P. J. S. Gonçalves, and P. M. B. Torres, "Bone contour segmentation from us images a comparative study," in *Proceedings of the 18th Portuguese Conference on Pattern Recognition*, (Coimbra, Portugal), October 26 2012.
- [4] L. Ibanez, W. Schroeder, and J. Cates, *The ITK Software Guide*. Kitware, 2005.
- [5] J. Sethian, *Level Set Methods and Fast Marching Methods*. Cambridge University Press, 1996.
- [6] Y. Huang, Z. Qiu, and Z. Song, "3d reconstruction and visualization from 2d ct images," in *IT in Medicine and Education (ITME), 2011 International Symposium on*, vol. 2, pp. 153 –157, dec. 2011.

- [7] Z. Li and J. Zhang, "Study on volume rendering of ct slices based on ray casting," in *Computer Science and Information Technology (ICCSIT), 2010 3rd IEEE International Conference on*, vol. 7, pp. 157 –160, july 2010.
- [8] P. J. Besl and N. D. McKay, "A method for registration of 3-d shapes," *Pattern Analysis and Machine Intelligence*, vol. 14(2), pp. 239 – 256, 1992.
- [9] S. Carpin, M. Lewis, J. Wang, S. Balakirsky, and C. Scrapper, "Usarsim: a robot simulator for research and education," in *Robotics and Automation, 2007 IEEE International Conference on*, pp. 1400 –1405, april 2007.
- [10] G. Echeverria, N. Lassabe, A. Degroote, and S. Lemaignan, "Modular open robots simulation engine: Morse," in *Robotics and Automation (ICRA), 2011 IEEE International Conference on*, pp. 46 –51, may 2011.
- [11] M. Quigley, K. Conley, B. P. Gerkey, J. Faust, T. Foote, J. Leibs, R. Wheeler, and A. Y. Ng, "Ros: an open-source robot operating system," in *ICRA Workshop on Open Source Software*, 2009.
- [12] H. Bruyninckx, "Open robot control software: the orocos project," in *Robotics and Automation, 2001. Proceedings 2001 ICRA. IEEE International Conference on*, vol. 3, pp. 2523 – 2528 vol.3, 2001.
- [13] N. H. Francisco Ramos, Mohanarajah Gajamohan and R. DAndrea, "Time-optimal online trajectory generator for robotic manipulators," in *Robot Earth Technical Report*, feb 2013.
- [14] R. B. Rusu and S. Cousins, "3D is here: Point Cloud Library (PCL)," in *IEEE International Conference on Robotics and Automation (ICRA)*, (Shanghai, China), May 9-13 2011.
- [15] F. Santos, P. J. S. Gonçalves, and P. M. B. Torres, "3d point cloud registration of the femoral bone, using the point cloud library," in *Proceedings of the 18th Portuguese Conference on Pattern Recognition*, (Coimbra, Portugal), October 26 2012.
- [16] M.-P. Dubuisson and A. Jain, "A modified hausdorff distance for object matching," in *Pattern Recognition, 1994. Vol. 1 - Conference A: Computer Vision and Image Processing., Proceedings of the 12th IAPR International Conference on*, vol. 1, pp. 566 –568 vol.1, oct 1994.



(a) Full surgical scenario



(b) Zooming the robots and the femur

Fig. 10. The developed MORSE surgical environment.

# An Evaluation of Local Feature Combiners for Robot Visual Localization

Francisco M. Campos

LabMAG and the Mechanical Engineering Department  
Instituto Superior de Engenharia de Lisboa  
Lisbon, Portugal  
fcampos@dem.isel.pt

Luís Correia

LabMAG, Computer Science Department  
Universidade de Lisboa  
Lisbon, Portugal  
Luis.Correia@di.fc.ul.pt

João M. F. Calado

IDMEC and the Mechanical Engineering Department  
Instituto Superior de Engenharia de Lisboa  
Lisbon, Portugal  
jcalado@dem.isel.pt

**Abstract**—In the last decade, local image features have been widely used in robot visual localization. To assess image similarity, a strategy exploiting these features compares raw descriptors extracted from the current image to those in the models of places. This paper addresses the ensuing step in this process, where a combining function must be used to aggregate results and assign each place a score. Casting the problem in the multiple classifier systems framework, we compare several candidate combiners with respect to their performance in the visual localization task. A deeper insight into the potential of the sum and product combiners is provided by testing two extensions of these algebraic rules: threshold and weighted modifications. In addition, a voting method, previously used in robot visual localization, is assessed. All combiners are tested on a visual localization task, carried out on a public dataset. It is experimentally demonstrated that the sum rule extensions globally achieve the best performance. The voting method, whilst competitive to the algebraic rules in their standard form, is shown to be outperformed by both their modified versions.

**Keywords**— robot visual localization; information fusion; multiple classifier systems.

## I. INTRODUCTION

Currently, the most successful approach to vision-based robot localization relies on local image features, extracted from interest points detected in the image. The construction of appearance representations building on local features has followed two main paradigms: on the one hand, the descriptors are quantized onto a predefined visual vocabulary, being assigned corresponding visual words. Although this representation, denoted bag-of-words, is interesting due to the fast appearance comparison it offers, some limits to its descriptive power have been identified [1][2]. An alternative strategy is the exploitation of raw feature descriptors, thus avoiding approximations resulting from quantization. This approach involves direct comparison of the descriptors, extracted from the test image, to those comprising the models

of places in the environment. A central issue in using this method to compare appearances is the fusion of information obtained from multiple features. In [3][4] this issue is resolved through a voting scheme, which relies on a hard level comparison of features. An alternative approach is pursued in [5], where the continuous values resulting from the comparison are accumulated in a score function. In spite of the success of the two approaches, to the best of our knowledge no evaluation of information fusion methods, applied to raw feature descriptors, has ever been performed. In this paper, we perform such an evaluation, addressing the information fusion issue within the framework of multiple classifier systems. The choice of this framework arises naturally, given the similarities between local feature based recognition and multiple classifier systems. Yet, the specificities of the visual localization problem determine the type of tools, from multiple classifier systems, that are applicable here. At the localization stage it is not possible to predict either the quantity or the appearance of the features that will be extracted. This implies that one should not train classifiers to treat specific visual features, but should instead rely on a general classifier, suitable for any feature available to the recognizer. Hence, in this paper we consider a probabilistic model for local features that leads to a generic probabilistic base classifier. The aim of the paper is to provide an evaluation of classifier combiners, thus the two most popular non-trained combination methods are considered: the product and sum rules. Furthermore, two extensions of these rules, as well as a voting method previously used in robot localization, are assessed. In addition to addressing a localization task based on local features only, we assess performance in the situation where additional information is integrated, through Bayes fusion. For this purpose, we chose a global image feature, gist [6], since it is also extracted from image data, and provides information complementary to local features.

This paper is organized as follows: after reviewing related work in section 2, we outline the concepts used in our approach

to local feature based robot localization, in section 3; section 4 introduces the combination rules and their extensions, as well as the reliability estimation methods; results of our experiments are detailed in section 5 and, finally, section 6 draws the conclusions of the paper.

## II. RELATED WORK

There is a wide range of well studied methods for the fusion of real-valued classifier outputs, including algebraic and statistical rules as well as trained combiners [7]. Among these methods, the sum rule and product rule have received considerable attention, due to their simplicity and good results. In practice, the sum rule has often been the preferred choice, due to its robustness. In spite of a solid theoretical foundation, it has been observed that the product rule is more sensitive to noise and to poor probability estimates of the base classifiers [8]. This drawback is addressed in [9], where the authors introduce a thresholding method that was shown to improve performance. Even though the sum rule behaves more reliably, in some cases there is room for improvement, by modulating the contributions of base classifiers. This approach has been successful in applications such as audio speech recognition [10] and person authentication [11], suggesting that weight adaptation is a viable solution to deal with noise, which may differently affect, at each time instance, the various information sources or, more generally, the various base classifiers. In studies where classifier contribution to the final decision is computed dynamically, the weighting of this contribution is usually associated to a reliability measure. In audio-based applications, researchers have derived the reliability measure from estimates of noise level in the input signal [11][12]. A more general approach, which is not limited to audio signals, relies on the analysis of base classifier scores for the extraction of the reliability measure. Along these lines, methods using the difference between the best two likelihood ratios [13], the dispersion of the class posterior probabilities [13] and maximum class posteriors [14] have been investigated. In the same category, another method that has gained considerable attention over the last years relies on the entropy of the posterior distribution [10]. This measure is adopted in this work, as it is claimed to be more powerful, for using all the information available in the posterior distribution [15]. Furthermore, in a study on audio-visual speech recognition [12], the entropy measure is shown to outperform the dispersion of posterior probabilities.

The traditional approach to mapping entropy to weights is to take the inverse entropy value, which reflects our intuition that low entropy distributions originate from reliable classifiers, which should receive greater weights, while classifiers producing close to flat distributions, with high entropy, should be weighted lower. In spite of agreement with these primary conditions, the inverse relation may not yield an optimal mapping, hence recently a number of studies proposed and assessed alternative functions [15][10]. In [10] a variation of the inverse entropy method is proposed, aiming at greatly reducing the contribution of higher entropy classifiers. This is achieved by computing the average entropy of classifiers and assigning a fixed small weight to classifiers with entropy above that value. In [15] the authors introduce an alternative mapping

function, defining the weights to be proportional to the negative entropy, and this outperformed the standard inverse relationship. In spite of the considerable attention feature combination has received in other research areas, an evaluation of combiners for visual robot localization has not been performed before.

Within the category of voting schemes, a few methods have been proposed for local feature based localization. In [3] the scale-invariant feature transform (SIFT) features extracted from the test image are matched against the descriptors from training images, through the matching rule proposed by Lowe [16]. Through this matching rule, a hard level decision is taken, simply indicating the presence or absence of the feature in a training image. A similar approach is provided in [4], where a dissimilarity measure is derived from the number of matches, the total number of features in the test and training images as well as a geometric alignment distance. Despite the success of the aforementioned voting schemes, these methods have not been assessed against the potentially more accurate approach that relies on continuous valued scores obtained from descriptor comparison.

## III. ROBOT VISUAL LOCALIZATION

Robot localization can be addressed as a recognition problem, where the current sensor data is ascribed to a place from a map of the environment. When appearance representations rely on local image features, each feature may produce opinions for places, later to be aggregated in a final score. Within the framework of multiple classifier systems, fusion of opinions may be addressed by associating each feature with a base classifier. In this section we define the base classifiers of our approach, by describing how posterior estimates are obtained from a local feature. As one of the goals of this work is to assess the performance of combiners when their outcome is fused with additional visual information, in this section we also introduce a global image feature, gist, and describe how it is integrated with combiner outputs.

### A. Base Classifiers

Let the current appearance  $I$  be described by a set of  $n_f$  visual feature descriptors  $\{d_1, d_2, \dots, d_{n_f}\}$  and  $L$  denote the robot location, defined over a map comprising  $n_p$  places:  $\{l_1, l_2, \dots, l_{n_p}\}$ . Models of places are constructed by dividing a training image sequence into subsequences so that each corresponds to a distinct place. The model of a place  $l_j$  is therefore defined by the collection of  $n_l$  descriptors,  $d_1^j, d_2^j, \dots, d_{n_l}^j$ , extracted during the training stage. In order to evaluate appearance similarity, the likelihood of a descriptor  $d_i$  may be estimated using a kernel density estimator:

$$P(d_i | l_j) = \frac{1}{n_l} \sum_{m=1}^{n_l} K(\text{dist}(d_i, d_m^j)), \quad (1)$$

where  $K(\cdot)$  is the Gaussian Kernel function, with standard deviation  $\sigma$ , and  $\text{dist}$  is an appropriate distance function. The posterior distribution of the base classifier associated with feature  $d_i$  is obtained through Bayes rule, yielding

$$P(l_j | d_i) = \frac{P(d_i | l_j)P(l_j)}{P(d_i)} \quad (2)$$

Here a uniform prior for place distribution is applied, as we are considering the situation of having no previous knowledge about the robot location.

#### B. Fusion with Gist

For the purpose of our experiments in the fusion of local features with gist, this feature is extracted in all test and model images. Thus, descriptor  $g$  is obtained for the current image, while the model of a place  $j$  includes  $ng_j$  descriptors,  $g_1^j, g_2^j, \dots, g_{ng_j}^j$ , each extracted from a training image of that place. In the computation of likelihood  $P(g|l_j)$ ,  $g$  is compared to all gist descriptors in the model of  $l_j$ , through the Euclidean distance, and the minimum value is found. The likelihood of  $g$  is obtained by evaluating the zero-centered Gaussian function (standard deviation  $\sigma_g$ ) at the minimum distance.

In order to perform localization exploiting both gist and local features, distribution  $P(l_j|I, g)$  is estimated. Under the assumption of conditional independence of local features and gist, this estimate may be computed through Bayes rule as

$$P(l_j | I, g) = \frac{P(I, g | l_j)P(l_j)}{P(I, g)} = \frac{P(I | l_j)P(g | l_j)P(l_j)}{P(I, g)}. \quad (3)$$

However, the combiners we are considering output posterior distributions, rather than likelihoods. Hence, we expand the previous expression as

$$P(l_j | I, g) = \frac{P(l_j | I)P(I)}{P(l_j)} \times \frac{P(g | l_j)P(l_j)}{P(I, g)}, \quad (4)$$

which may be rewritten in the form

$$P(l_j | I, g) \propto P(l_j | I)P(g | l_j). \quad (5)$$

### IV. LOCAL FEATURE FUSION THROUGH CLASSIFIER COMBINATION

#### A. Classifier Combination Methods

In local feature based localization, the ultimate goal is to arrive at an estimate of  $P(l_j|I)$  derived from the outputs of individual base classifiers,  $P(l_j|d_i)$ . Below, we briefly review the two algebraic combination rules as well as the voting method to be assessed in this paper. Additionally, the extensions of the algebraic rules are outlined.

**Sum rule** - The sum rule may be expressed by the generalized form

$$P(l_j | d_1, \dots, d_{nf}) = \sum_{i=1}^{nf} w_i P(l_j | d_i), \quad (6)$$

where  $w_i$  is the weight that reflects reliability of classifier  $i$ . These weights are constrained to sum up to one and, in the standard form of the sum rule, are equally set to  $1/nf$ .

**Product rule** - According to this rule, support for location  $l_j$  is obtained by multiplying the outputs of base classifiers raised to the corresponding weights:

$$P(l_j | d_1, \dots, d_{nf}) = \frac{1}{Z} \prod_{i=1}^{nf} P(l_j | d_i)^{w_i}. \quad (7)$$

In this expression,  $Z$  is a normalizing constant. As before, the standard rule is obtained by setting all weights to be equal, in this case with the value of 1.

**Threshold rule** - In [9] the authors introduce a modified product rule devised to alleviate the dominating effect of close to zero probabilities in this fusion method. This is accomplished by a mechanism that modifies classifiers outputs that fall below a predefined threshold. Thus, before applying the product rule, the probability estimate from each base classifier is modified according to

$$\begin{cases} P(l_j | d_i) = Th, & P(l_j | d_i)_o < Th \\ P(l_j | d_i) = P(l_j | d_i)_o, & P(l_j | d_i)_o \geq Th \end{cases} \quad (8)$$

where the index  $o$  refers to the original probability estimates from the base classifiers and  $Th$  denotes the threshold value.

**Voting method** - Contrasting to the aforementioned methods, the voting scheme used in [3] performs an image-to-image rather than an image-to-model comparison. In effect, this method relies on the matching criterion of [16], which establishes feature correspondences between two images. In [3] the voting method is applied to visual localization by first finding, for each place, the training image with the highest number of matches with respect to the test image. Final scores assigned to places are the number of matches of the corresponding winning images. In this paper we use this implementation of the voting method and, where posterior probabilities are needed as the outcome of the combiner, the score distribution is converted to a probability distribution by normalization.

#### B. Reliability Estimation Methods

In this paper we evaluate the weighted combination rules with weights being derived from the posterior distribution entropy. To this end, the entropy of the posterior distribution output of a base classifier is computed, by

$$H_i = - \sum_{j=1}^{np} P(l_j | d_i) \log P(l_j | d_i) \quad (9)$$

In order to use this measure in a weighted combination scheme, the entropy is mapped onto weights by a suitable transformation. We consider four methods to perform this mapping: inverse entropy (IE) [10][15], negative entropy (NE)

[15], inverse entropy with average threshold (IEAT) [11], and negative entropy with average threshold (NEAT).

IE - In the inverse entropy method, each classifier weight is proportional to the inverse of the respective entropy:

$$w_i = 1/H_i \quad (10)$$

NE - In the negative entropy method, weights are proportional to the negative entropy, being computed as

$$w_i = H_{max} - H_i \quad (11)$$

In this expression  $H_{max}$  is the maximum value the entropy can take. For a problem with  $np$  candidate locations it takes the value of  $\log(np)$ .

IEAT - The IEAT method [10] computes preliminary weights  $w'_i$  in the same way as the IE method. Then, weights that fall below the mean of  $w'_i$  are assigned a low value ( $10^{-4}$ ), while the remaining weights are kept unchanged. In practice this procedure corresponds to eliminating the contribution of higher entropy features.

NEAT - This method, which has not been tested in previous works, results from computing preliminary weights  $w'_i$  as in NE and then applying the same rule as IEAT.

## V. RESULTS

In this section we compare the classifier combination rules as well as the reliability estimation methods outlined in section 4, on an outdoor place recognition task. To this end, we resorted to the public FDF park dataset, used in past visual localization investigations [17][18]. This dataset describes the Frederick D. Fagg Park of the University of Southern California as a 9-location map, providing several video sequences for each location, gathered using a 8mm handheld camcorder carried by a person. The videos are organized in 8 sets used for testing and 7 sets used in training, each containing about 11000 frames. Strong lighting variation is the main source of variability in the data, since the videos were collected at different days and times of day. Considering the available test and training sets, several experimental conditions can be established. Our experiments showed that the difficulty of the localization task varies significantly with the differences in training and test lighting conditions, but the relative performance of the classifiers being tested is generally consistent. Hence, results for two representative training conditions, sets A and C, will be presented in the following analysis of results. These sets were chosen for posing challenging, yet distinctive scenarios to the place recognizer. The video sequences in the datasets are provided with the label of the corresponding place where they were captured. Thus, the localization task we consider aims at identifying the correct label for each image in a test set. Results presented in the next sections refer to the recognition rate obtained in this classification task.

For the purpose of our experiments, all images are processed for extraction of local features, as well as gist. Local

features are identified through the scale-space extrema detector and encoded in SIFT descriptors [16]. In gist extraction, steerable filters at 2 scales and 8 orientations are applied. Then, mean filter responses are averaged on a 4-by-4 grid, yielding gist descriptors of length 256. The parameters used in the experiments were empirically set for best performance, taking the values  $\sigma=100$ ,  $\sigma_g=0.22$ , and  $Th=0.2$ .

### A. Performance of the Combination Methods

Results for all combination methods are shown in tables 1 and 2, respectively obtained with training sets A and C. Results for the sum and the product rules are provided using the standard rules as well as the threshold and weighted (NEAT) versions. As we can see, the sum rule is clearly superior to the product rule, when the standard versions are considered. This was an expected outcome, as the product rule is more sensitive to noisy data, which is prevalent in difficult test scenarios. In the most discrepant situations, the difference in performance of the two rules is larger than 10%. In its threshold version, the product rule exhibits a substantial improvement, achieving levels of performance closer to the sum rule. Average recognition rate differences are now less than 1%. It is interesting to notice that the sum rule is also favoured by the threshold operation, which was originally developed to increase the product rule accuracy. By comparing the weighted with the standard rules, we can conclude that the weighting scheme also contributes to improve the recognition rate of both rules. The performance gains observed are similar to the threshold method; nevertheless, in this respect the weighting scheme is on average slightly more efficient with the sum rule.

Despite using a hard-level decision outcome of base classifiers, the voting method performs reasonably well. In particular, the comparison with the standard algebraic rules is favourable to voting, in the case of training set C. However, all the modifications of the standard rules are superior to the voting method, in the two training sets.

### B. Evaluation of the Reliability Measures

In order to evaluate the reliability estimation methods, localization experiments were carried out with the schemes detailed in section 4. The corresponding results are shown in table 3 by the mean recognition rates obtained over all test sets. We observe that, with the product rule, the methods IEAT and NEAT generally surpass their non-eliminating feature counterparts, respectively IE and NE. This should be explained by the fact that high entropy features result in poor posterior distribution estimates, which are especially detrimental to the product rule. Thus, by strongly reducing the contribution of these features, the IEAT and NEAT methods achieve a performance gain. Smaller differences are observed when the same comparison is performed with respect to the sum rule. Yet, on average, IEAT and NEAT also perform better than IE and NE respectively. The comparison of methods using the inverse entropy function (IE and IEAT) with those using negative entropy function (NE and NEAT) shows consistent superiority of the latter in training set A. However, this relation is not observed in training set C, suggesting that none of these mappings is optimal.

TABLE 1. RECOGNITION RATE [%] OBTAINED WITH THE VARIOUS COMBINATIONS RULES ON TRAINING SET 'A'.

Test set	Voting	Standard rule		Threshold		Weighting (NEAT)	
		Sum	Product	Sum	Product	Sum	Product
1	95.1	99.7	95.5	99.9	99.8	99.9	99.4
2	80.9	93.7	83.3	95.7	94.8	96.3	94.4
3	93.5	97.9	96.9	97.8	97.8	97.8	97.7
4	95.4	97.4	97.0	97.3	97.2	97.7	98.1
5	85.5	94.0	84.8	97.1	96.0	97.7	94.6
6	82.6	89.7	81.9	93.2	92.4	94.0	91.1
7	92.6	96.6	95.8	96.8	96.8	96.9	96.4
8	92.0	97.6	93.2	99.3	99.1	98.4	96.5
mean	89.7±5.4	95.8±3.0	91.1±6.1	97.1±2.0	96.7±2.2	97.3±1.6	96.0±2.4

TABLE 2. RECOGNITION RATE [%] OBTAINED WITH THE VARIOUS COMBINATIONS RULES ON TRAINING SET 'C'.

Test set	Voting	Standard rule		Threshold		Weighting (NEAT)	
		Sum	Product	Sum	Product	Sum	Product
1	97.6	90.5	82.0	99.2	98.4	99.7	98.0
2	94.8	97.4	84.2	99.3	98.9	99.2	98.3
3	100.0	100.0	100.0	100.0	100.0	100.0	100.0
4	100.0	100.0	100.0	100.0	100.0	100.0	100.0
5	94.6	95.1	81.5	96.9	96.0	98.1	97.3
6	99.7	99.3	88.9	100.0	100.0	100.0	99.7
7	99.9	99.9	96.5	100.0	100.0	100.0	100.0
8	98.0	93.2	83.6	98.1	98.2	97.0	96.0
mean	98.1±2.1	96.9±3.4	89.6±7.5	99.2±1.1	98.9±1.3	99.3±1.1	98.7±1.4

### C. Fusion with Gist

Previously, we analyzed localization results based solely on base combiner outcomes. Here we focus on the behaviour of these rules when their outcome is combined, through Bayes fusion (5), with gist. It should be noted that the use of Bayes fusion, together with the product rule for local feature combination, implies gist having the same role as a local feature, since the product operation is implicit in Bayes rule. In contrast, through the sum rule, local features are aggregated by an averaging operation, that filters their individual contribution. In this case, Bayes fusion with gist allows this feature to have a stronger impact. Comparing the mean recognition rate results in table 4 with those in tables 1 and 2, for the standard sum rule, it is noticeable that the influence of gist negatively impacts performance. In the worse case (training set A) a reduction in average recognition rate of about 5% is observed. This can be attributed to the low discriminativity of gist, which in this case implied a global performance reduction. Nonetheless, when the sum rule is used in its threshold and weighted versions and gist has a positive impact. This is due to the higher accuracy of posterior estimates provided by these modifications, which compensates for the low discriminativity of gist. Results for the product rule suggest that fusion with gist is not detrimental to the standard rule, and gains can be achieved, in the enhanced versions of the rule. But, where this feature is most beneficial (training set C), the gain is less pronounced than that observed with the sum rule.

Since the voting method computes a score by accumulating votes from base classifiers, some similarities to the sum rule

are expected. Results for the combination of voting estimates with gist show that fusion also has a strong influence here. However, while the standard sum rule was negatively impacted, the voting method exhibits performance improvements. Yet, when the sum rule modifications are considered, it still compares favourably against the voting method.

## VI. CONCLUSIONS

The goal of this paper was to study the relative merits of different local feature combination methods, for the purpose of robot visual localization. Our experiments have demonstrated that the algebraic rules show significant limitations, in their standard versions. The product rule, being more sensitive to noise, does not offer competitive performance. On the other hand, the fusion of combiner outputs with gist, through Bayes rule, proved the standard sum rule to be limited in compensating for the low discriminativity of gist.

Both the sum and the product rules can be substantially enhanced by suitable modifications. In this regard, two adaptations were assessed, the first applying a threshold on base classifier outcomes, whereas the second weights base classifiers contribution. An interesting finding was that the threshold method, originally developed to attenuate the product rule limitations, also improves the sum rule performance. Our comparison of the threshold method with the weighting method showed similar performance gains over the standard rules. The voting method proved competitive to the algebraic rules in their standard form, however, it was outperformed by all the

TABLE 3. MEAN RECOGNITION RATE [%] OBTAINED WITH THE FOUR RELIABILITY ESTIMATION METHODS. RESULTS FOR TRAINING SETS ‘A’ AND ‘C’.

Training set	Sum				Product			
	<i>IE</i>	<i>NE</i>	<i>IEAT</i>	<i>NEAT</i>	<i>IE</i>	<i>NE</i>	<i>IEAT</i>	<i>NEAT</i>
A	96.9±2.2	97.2±1.9	97.2±1.7	97.3±1.6	94.7±3.2	95.5±2.8	95.9±2.5	96.0±2.4
C	99.2±0.9	99.2±1.1	99.4±1.0	99.3±1.1	97.5±2.9	97.6±2.4	98.9±1.1	98.7±1.4

TABLE 4. MEAN RECOGNITION RATE [%] OBTAINED BY FUSING LOCAL FEATURE BASED ESTIMATES WITH GIST. RESULTS FOR TRAINING SETS ‘A’ AND ‘C’.

Training set	Voting	Standard rule		Threshold		Weighting (NEAT)	
		<i>Sum</i>	<i>Product</i>	<i>Sum</i>	<i>Product</i>	<i>Sum</i>	<i>Product</i>
A	94.7±3.3	91.7±6.0	91.1±6.1	97.3±2.1	96.9±2.2	97.6±1.6	96.1±2.4
C	99.7±0.4	94.8±5.2	89.6±7.5	99.9±0.2	99.1±1.2	99.9±0.2	98.7±1.4

enhanced versions.

In our evaluation of the weighting method, reliability of base classifiers is derived from their entropy. Several candidate functions for the mapping from entropy to weights were tested. While the inverse entropy and negative entropy functions did not show consistent differences in results, the severe reduction of high entropy features contribution showed a systematic improvement in the product rule.

Our experiments on Bayes fusion with gist have shown the voting and sum rules to be more susceptible to this combination. In particular, the standard sum rule exhibited substantial performance reduction after fusion, which was nevertheless compensated in the enhanced versions of the rule. When Bayes fusion is used together with the product rule, gist contributes to the posterior estimates in the same way as the local features. This implies a smaller influence of gist, confirmed in our experiments, which showed a slight but consistent performance gain.

Overall, it is notable that the extensions of the sum rule are very consistent in outperforming the other methods, indicating that these should be the preferred choices to local feature combination. Future work will extend this evaluation to a larger number of datasets, including indoor environments, and will address the integration of multiple frame information through a temporal filter.

#### REFERENCES

[1] F. Jurie and B. Triggs, “Creating efficient codebooks for visual recognition,” in *IEEE Int. Conf. on Computer Vision*, 2005, vol. 1, pp. 604–610.

[2] O. Boiman, E. Shechtman, and M. Irani, “In defense of Nearest-Neighbor based image classification,” in *IEEE Conf. on Computer Vision and Pattern Recognition*, 2008, pp. 1–8.

[3] F. Li, X. Yang, and J. Kosecka, “Global Localization and Relative Positioning Based on Scale-Invariant Keypoints,” *Robotics and Autonomous Systems*, vol. 52, no. 1, pp. 27–38, 2005.

[4] T. Goedemé, M. Nuttin, T. Tuytelaars, and L. Van Gool, “Omnidirectional Vision Based Topological Navigation,” *Int. Journal of Computer Vision*, vol. 74, no. 3, pp. 219–236, Jan. 2007.

[5] F. M. Campos, L. Correia, and J. M. F. Calado, “Global Localization with Non-Quantized Local Image Features,” *Robotics and Autonomous Systems*, vol. 60, no. 8, pp. 1011–1020, 2012.

[6] A. Oliva and A. Torralba, “Modeling the shape of the scene: a holistic representation of the spatial envelope,” *Int. Journal of Computer Vision*, vol. 42, no. 3, pp. 145–175, 2001.

[7] L. Kuncheva, *Combining Pattern Classifiers: Methods and Algorithms*, John Wiley & Sons, 2004.

[8] D. Tax, M. V. Breukelen, R. Duin, and J. Kittler, “Combining multiple classifiers by averaging or by multiplying?,” *Pattern Recognition*, vol. 33, pp. 1475–1485, 2000.

[9] F. M. Alkoot and J. Kittler, “Modified product fusion,” *Pattern Recognition Letters*, vol. 23, no. 8, pp. 957–965, Jun. 2002.

[10] H. Misra, H. Bourlard, and V. Tyagi, “New entropy based combination rules in HMM/ANN multi-stream ASR,” in *Acoustics, Speech, and Signal Processing*, 2003, pp. 741–744.

[11] C. Sanderson and K. Paliwal, “Noise compensation in a person verification system using face and multiple speech features,” *Pattern Recognition*, vol. 36, pp. 293–302, 2003.

[12] M. Heckmann, F. Berthommier, and K. Kroschel, “Noise adaptive stream weighting in audio-visual speech recognition,” *Journal on Applied Signal Processing*, no. 11, pp. 1260–1273, 2002.

[13] T. Wark and S. Sridharan, “Adaptive fusion of speech and lip information for robust speaker identification,” *Digital Signal Process.*, vol. 11, no. 3, pp. 169–186, 2001.

[14] R. Seymour, D. Stewart, and J. Ming, “Audio-visual integration for robust speech recognition using maximum weighted stream posteriors,” in *INTERSPEECH*, 2007, pp. 654–657.

[15] M. Gurban and J. Thiran, “Dynamic modality weighting for multi-stream hmms in audio-visual speech recognition,” in *Proc. of the 10th conf. on Multimodal Interfaces*, 2008, pp. 237–240.

[16] D. Lowe, “Distinctive Image Features from Scale-Invariant Keypoints,” *Int. J. of Comp. Vision*, vol. 60, no. 2, pp. 91–110, 2004.

[17] C. Siagian and L. Itti, “Rapid biologically-inspired scene classification using features shared with visual attention,” *IEEE Trans. on Pattern Analysis and Machine Intelligence*, vol. 29, no. 2, pp. 300–312, Feb. 2007.

[18] C. Siagian and L. Itti, “Biologically Inspired Mobile Robot Vision Localization,” *IEEE Trans. on Robotics*, vol. 25, no. 4, pp. 861–873, Oct. 2009.

# Combining sparse and dense methods in 6D visual odometry

Hugo Silva, Eduardo Silva  
INESC TEC Robotics Unit  
School of Engineering, Polytechnic Institute of Porto  
Email:hsilva, eaps@lsa.isep.ipp.pt

Alexandre Bernardino  
Institute of Systems and Robotics  
IST Lisbon, Portugal  
Email: alex@isr.ist.utl.pt

**Abstract**—Visual Odometry is one of the most powerful, yet challenging, means of estimating robot ego-motion. By grounding perception to the static features in the environment, vision is able, in principle, to prevent the estimation bias rather common in other sensory modalities such as inertial measurement units or wheel odometers. We present a novel approach to ego-motion estimation of a mobile robot by using a 6D Visual Odometry Probabilistic Approach. Our approach exploits the complementarity of dense optical flow methods and sparse feature based methods to achieve 6D estimation of vehicle motion. A dense probabilistic method is used to robustly estimate the epipolar geometry between two consecutive stereo pairs; a sparse feature stereo approach to estimate feature depth; and an Absolute Orientation method like the Procrustes to estimate the global scale factor.

We tested our proposed method on a known dataset and compared our 6D Visual Odometry Probabilistic Approach without filtering techniques against a implementation that uses the well known 5-point RANSAC algorithm. Moreover, comparison with an Inertial Measurement Unit (RTK-GPS) is also performed, for providing a more detailed evaluation of the method against ground-truth information.

## I. INTRODUCTION

Visual Navigation Systems have been increasingly used to help improve robot's ability to perceive and navigate through out their environment. These systems are mainly built by one or more low-cost sensors(cameras), and are becoming ubiquitous, together with Inertial Measurement Units(IMU), in modern mobile robots.

An important component of such systems is the ability to estimate the robot velocity. When vision cameras are used as sensors, this capability is generically denoted as Visual Odometry(VO). Usually such systems are based on computer vision techniques such as deterministic optical-flow techniques and/or appearance based matching.

One of the main advantages of using VO techniques is their ability to provide short term estimates of robot velocity to feed higher levels of the robot navigation system, instead of relying solely in constant angular and linear velocity motion models. Constant velocity models are unable to cope with camera/robot sudden movements and often conduct to tracking failures. Some related work, performed by Alcantarilla et al [1], used this method as prior for the prediction step of a robust EKF-SLAM algorithm.

VO has been a continuous topic of research over the past years. These systems suffered a major outbreak due to the

outstanding work of [2] on NASA Mars Rover Program. Nister et al ([3],[4]) developed a Visual Odometry system, based on a 5-point algorithm, that became the standard algorithm for comparison of Visual Odometry techniques. This algorithm can be used either in stereo or monocular vision approaches and consists on the use of several visual processing techniques, namely: feature detection and matching, tracking, stereo triangulation and RANSAC [5] for pose estimation with iterative refinement.

Others, like Ni et al[6], use sparse flow separation of features based on disparity together with two-point RANSAC to recover rotation, while for the translation a one-point RANSAC algorithm is used.

In [7] it is proposed a visual odometry estimation method using stereo cameras. A closed form solution is derived for the incremental movement of the cameras and combines distinctive features (SIFT) [8] with sparse optical flow.

Notwithstanding the amount of research in Visual Odometry during the past few years, almost all approaches employ feature based methods. These methods have the advantage of being fast, since only a subset of the image points is processed, but depend critically on the features to track between consecutive pairs of frames and are often sensitive to noise. On the contrary, dense methods combined with probabilistic approaches have demonstrated higher robustness to noise and outliers. In Domke et al [9], a method for estimating the epipolar geometry describing the motion of a camera is proposed using dense probabilistic methods. Instead of deterministically choosing matches between two images, a probability distribution is computed over all possible correspondences. By exploiting a larger amount of data, a better performance is achieved under noisy measurements. However, that method is more computationally expensive and does not recover translational scale factor.

In our work, we propose the use of a dense probabilistic method such as Domke et al [9] but with two important additions: (i) a sparse feature based method is used to estimate the translational scale factor and (ii) a fast correspondence method using a recursive ZNCC(Zero Normalized Cross Correlation) implementation is provided for computational efficiency.

Our method, here on denoted (6DP) combines sparse feature detection and tracking for stereo-based depth estimation, using the well-known Harris corner detector[10] and a variant of the

dense probabilistic ego-motion method developed by Domke et al [9] to propagate the sparse features along time. Upon obtaining two registered point sets in consecutive time frames, an Absolute Orientation method, defined as an orthogonal Procrustes problem (AO) is used to recover motion scale.

To evaluate our system versus current state-of-the-art techniques, we utilized Kitt et al [11] dataset. Our focus is on the raw estimation of robot velocity, so no filtering was performed. We compared the results obtained by our method against our implementation of a 5-point RANSAC method with highly distinctive SIFT [8] features, in order to provide a valid comparison between different approaches for angular and linear velocity camera motion estimation.

Furthermore, we compared our results against IMU measurements [11], which have already accurate position measurements from fusing INS data with GPS information, thus providing ground-truth information.

This paper is organized as follows: In section II, our algorithm and implementation is discussed, in section III experimental results are presented and finally in section IV conclusions and future work plans are presented.

## II. 6D VISUAL ODOMETRY USING PROBABILISTIC EGOMOTION

Our solution is based on the probabilistic method of ego-motion estimation using the epipolar constraint developed by Domke et al [9]. This is a dense image pixel correlation method, that due to its probabilistic nature, does not commit the match correlation of image point  $P_k(x,y)$  in  $I_{T_k}^L$  to other image point  $P_k(x,y)$  in  $I_{T_{k+1}}^L$ . Instead, it copes with several hypothesis of matching for image point  $P_k(x,y)$  in  $I_{T_{k+1}}^L$ , thus making the estimation of the fundamental matrix  $E_s$  more robust to image feature matching errors and hence providing a more accurate camera motion estimation  $[R,t]$  between  $I_{T_k}$  and  $I_{T_{k+1}}$ . However, the method from [9] is unable to estimate motion scale, so we added a stereo vision sparse feature based approach that takes Harris corner features from  $I_{T_k}$ , and use knowledge of  $E_s$  to search along the epipolar lines the correspondences between  $I_{T_k}^L$  and  $I_{T_{k+1}}^L$ .

$$F_{I_{T_k}^L, I_{T_{k+1}}^L} = K_L'^T E_s K_L^T \quad (1)$$

This sparse and dense feature based approach, allows to narrow the search for correspondences between  $I_{T_k}^L$  and  $I_{T_{k+1}}^L$  to feature points that lie on the epipolar line, making this method less time consuming, as well as more robust to errors in feature matching correlation between image frames. An architecture of our proposal is shown in figure 1. In summary, it is composed by the following main steps:

- 1) First, image feature points are detected in the current pair of stereo frames  $(I_{T_k}^L, I_{T_k}^R)$ , using a known feature detector. These image feature points are then correlated between left and right image to obtain 3D point depth information. It is assumed a calibrated and rectified stereo system, thus search for matches is done along horizontal epipolar lines.

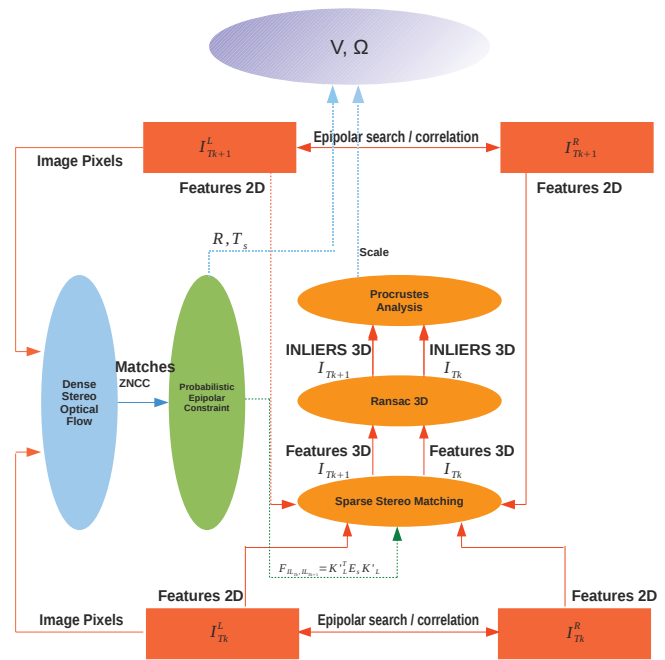


Fig. 1. 6D Visual Odometry System Architecture

- 2) Second, dense likelihood correspondence maps are computed based on ZNCC[12] correlation. These maps are used to recover the fundamental matrix between two consecutive left image pairs  $I_{T_k}^L$  and  $I_{T_{k+1}}^L$ , through likelihood maximization of fundamental matrix hypotheses supported on the computed dense correspondence maps.
- 3) Third, due to the need to determine the motion scale between  $I_{T_k}$  and  $I_{T_{k+1}}$ , a Procrustes absolute orientation method(AO) is utilized. The AO method uses 3D image feature points obtained by triangulation from stereo image pairs  $(I_{T_k}^L, I_{T_k}^R)$  and  $(I_{T_{k+1}}^L, I_{T_{k+1}}^R)$  combined with robust techniques like RANSAC[5], thus obtaining only good candidates (inliers) for Procrustes based motion scale determination.
- 4) Finally, vehicle linear and angular velocity  $(V, \Omega)$  between  $I_{T_k}$  and  $I_{T_{k+1}}$  is determined.

### A. Probabilistic Correspondence

The key to the proposed method relies in the consideration of probabilistic rather than deterministic matches. Usual methods for motion estimation consider a match function  $M$  that associates coordinates of points  $\mathbf{m} = (x,y)$  in image 1 to points  $\mathbf{m}' = (x',y')$  in image 2 :

$$M(\mathbf{m}) = \mathbf{x}' \quad (2)$$

Instead, the probabilistic correspondence method defines a probability distribution over the points in image 2 for all points in image 1:

$$P_{\mathbf{m}}(\mathbf{m}') = P(\mathbf{m}'|\mathbf{m}) \quad (3)$$

Thus, all points  $\mathbf{m}'$  in image 2 are candidates for matching with point  $\mathbf{m}$  in image 1 with *a priori* likelihoods proportional to

$P_{\mathbf{m}}(\mathbf{m}')$ . One can consider  $P_x$  as images (one per each pixel in image 1) whose value in  $\mathbf{m}'$  is proportional to the likelihood of  $\mathbf{m}'$  matching with  $\mathbf{m}_x$ . For the sake of computational cost, likelihoods are not computed for the whole range in image 2 but just to windows around  $\mathbf{m}$  (or suitable predictions given prior information). In [9] this value was computed via the normalized product, over a filter bank of Gabor filters with different orientation and scales, of the exponential of the negative differences between the angle of the Gabor filter responses in  $\mathbf{m}$  and  $\mathbf{m}'$ . The motivation for using a Gabor filter bank was the robustness of their responses to changes in the brightness and contrast of the image. However, the computations demand a significant computational effort, thus we propose to perform the computations with the well known ZNCC method, displayed in equation 4.

$$C_{x,y}(u,v) = \frac{\sum_{x,y \in W} (f(x,y) - \bar{f})(g(x+u,y+v) - \bar{g})}{\sqrt{\sum_{x,y \in W} (f(x,y) - \bar{f})^2} \sqrt{\sum_{x,y \in W} (g(x+u,y+v) - \bar{g})^2}} \quad (4)$$

This function is also known to be robust to brightness and contrast changes and recent efficient recursive schemes developed by Huang et al[12] render it suitable to real-time implementations. That method is faster to compute and yields the same quality as the method of Domke.

1) *Recursive ZNCC*: The global objective of the ZNCC method is to compare a reference subset (the correlation window sampled in the reference image) to a corresponding template in another image. The method developed by Huang et al[12] uses a recursive scheme for calculating the numerator of (5) and a global sum-table approach for the denominator, thus saving significant computation time.

In summary, the method has two distinctive parts one for calculating ZNCC numerator and other for the denominator calculation. The ZNCC equation 4 can be described in the following form.

$$C_{x,y}(u,v) = \frac{P(x,y;u,v) - Q(x,y;u,v)}{\sqrt{F(x,y)}\sqrt{G(x,y;u,v)}} \quad (5)$$

On the other hand, although  $Q(x,y;u,v)$  can be calculated using a sum-table approach, the term  $P(x,y;u,v)$  involves cross correlation terms between both images and cannot be calculated recurring to a sum-table approach, since  $(u,v)$  are sliding window parameters.

We selected a window size  $N_x, N_y = 20$ , thus the number of calculations of  $P$  would be  $[(2N_x + 1) \times (2N_y + 1)]$  addition operations. Yet, due to a fast recursive approach we can extend calculations made for a given point  $P(x,y)$  to  $P(x+L_x, y+L_y)$  in the camera reference image  $I_{T_k}^L$  (see more details in [12]).

2) *Probabilistic Egomotion*: From two images of the same camera, one can recover its motion up to the translation scale factor. This can be represented by the epipolar constraint which, in homogeneous normalized coordinates can be written as:

$$(\mathbf{s}')^T E \mathbf{s} = 0 \quad (6)$$

where  $E$  is the so called Essential Matrix [13], a  $3 \times 3$  matrix with rank 2 and 5 degrees-of-freedom. Intuitively, this matrix expresses the directions in image 2 that should be searched for matches of points in image 1. It can be factored by:

$$E = R[t]_{\times} \quad (7)$$

where  $R$  and  $t$  are, respectively, the rotation and translation of the camera between the two frames.

To obtain the Essential matrix from the probabilistic correspondences, [9] proposes the computation of a probability distribution over the (5-dimensional) space of essential matrices. Each dimension of the space is discretized in 10 bins, thus leading to 100000 hypotheses  $E_i$ . For each point  $\mathbf{s}$  the likelihood of these hypotheses are evaluated by:

$$P(E_i|\mathbf{s}) \propto \mathbf{s}' : (\mathbf{s}')^T E_i \mathbf{s} = 0 P_{\mathbf{s}}(\mathbf{s}') \quad (8)$$

Intuitively, for a single point  $\mathbf{s}$  in image 1, the likelihood of a motion hypothesis is proportional to the best match obtained along the epipolar line generated by the essential matrix. Assuming independence, the overall likelihood of a motion hypothesis is proportional to the product of the likelihoods for all points:

$$P(E_i) \propto \prod_{\mathbf{s}} P(E_i|\mathbf{s}) \quad (9)$$

After a dense correspondence probability distribution has been computed for all points, the method [9] computes a probability distribution over motion hypotheses represented by the epipolar constraint. Finally, given the top ranked motion hypotheses, a Nelder-Mead simplex method is used to refine the motion estimate.

Once the essential matrix between images  $I_{T_k}^L$  and  $I_{T_{k+1}}^L$  has been computed by the method described in the previous section, we search along the epipolar lines for matches in  $I_{T_{k+1}}^L$  to the features computed  $I_{T_k}^L$ , as displayed in figure 2.

Finally, the matches in  $I_{T_{k+1}}^L$  are propagated to  $I_{T_{k+1}}^R$  by searching along the horizontal stereo epipolar lines. From this step we compute the 3D cloud of points at time  $T_{k+1}$  corresponding to the ones obtained for  $T_k$ . Points whose matches were not found or unreliable are discarded from the point clouds.

Furthermore, by finding the correspondence between all points ( $I_{T_k}^L$  and  $I_{T_{k+1}}^L$ ) using the epipolar constraint, motion estimation up to a scale factor  $(R, T_s)$  between images  $I_{T_k}^L$  and  $I_{T_{k+1}}^L$  can be computed.

$$E = [T_s]_{\times} R \quad (10)$$

However, since the current method does not allow motion scale recovery, translation  $T_s$  component does not contain translation scale information. This type of information, is calculated by an alternative absolute orientation method like the Procrustes method.

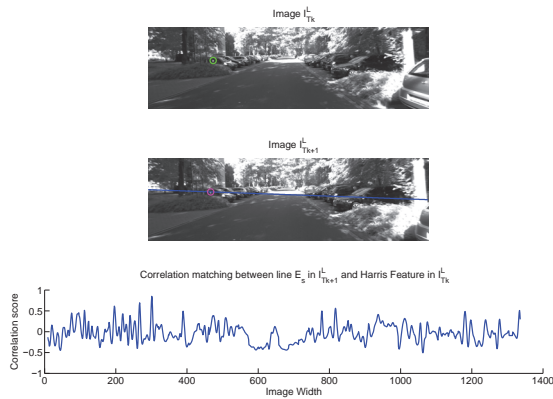


Fig. 2. Image feature Point that lie in the epipolar line estimated between  $I_{T_k}$  to  $I_{T_{k+1}}$

### B. Procrustes Analysis and Scale Factor Recovery

The Procrustes method allows to recover rigid body motion between frames, through the use of 3D point matches. We assume a set of 3D features (computed by triangulation of Harris corners in our implementation) in instant  $t_{T_k}$  be described by  $\{X'_i\}_{T_k}$ , move to a new position and orientation in  $t_{T_{k+1}}$ , described by  $\{Y'_i\}_{T_{k+1}}$ . This transformation can be represented as:

$$Y'_i = RX'_i + T \quad (11)$$

where  $Y'_i$  points, are 3D feature points in  $I_{T_{k+1}}$ .

These points were detected using probabilistic matched points between  $I_{T_k}^L$  and  $I_{T_{k+1}}^L$ , that were triangulated to their stereo corresponding matches in  $I_{T_{k+1}}^R$ . These two sets of points are the ones that are used by Procrustes method to estimate motion scale.

In order to estimate motion  $[R, T]$ , a cost function that measures the sum of squared distances between corresponding points is used.

$$c^2 = \sum_i^n \|Y'_i - (RX'_i + T)\|^2 \quad (12)$$

Performing minimization of equation 12, gives estimates of  $[R, T]$ . Although conceptually simple, some aspects regarding the practical implementation of the Procrustes method must be taken into consideration. Namely, since this method is very sensible to data noise, obtained results tend to vary in the presence of outliers. To overcome this difficulty, RANSAC [5] is used to discard possible outliers within the set of matching points.

1) *Bucketing*: For a correct motion scale estimation, it is necessary to have a proper spatial feature distribution through out the image. For instance, if the Procrustes method uses all obtained image feature points without having their image spatial position into consideration, the obtained motion estimation  $[R, T]$  between two consecutive images could turn out biased.

Given these facts, to avoid having biased samples in the RANSAC phase of the algorithm, a bucketing technique [14] is implemented to assure a unbiased image feature distribution sample.

### C. Linear and Angular Velocity Estimation

To sum up the foregoing, we determine camera motion estimation up to a scale factor using a probabilistic method, and by adding stereo vision combined with Procrustes estimation method, we are able to determine missing motion scale, thus being able to easily obtain both linear and angular camera velocities  $(V, \Omega)$ .

## III. RESULTS

In this section, some results illustrating the performance of our proposed solution for 6D Visual Odometry estimation are presented.

### A. Setup

We utilized Kitt et al [11] dataset sequence. This dataset contains stereo vision information (2 cameras) separated by a 40 cm baseline, frame-rate at 10 fps and  $391 \times 1344$  image resolution. Moreover, regarding ground-truth data, the dataset also contains fused GPS and IMU information consistent with vehicle pose(x,y,z) and orientation (roll,pitch,yaw) information. We aligned the vehicle reference frame with the camera reference frame for comparison purposes.

We compared the performance of our approach against ground-truth IMU (RTK-GPS) information and also versus our 5-point RANSAC algorithm using SIFT features [8]. Our objective is to compare our sparse and dense feature based solution with non-preserving scale feature detectors, as opposing to a more direct approach using SIFT and Nearest Neighbour strategy to correlate features between  $I_{T_k}^L$  and  $I_{T_{k+1}}^L$ .

To validate our results, we used the AO method for motion scale estimation in both approaches, even though there is no need to do so for the 5-point RANSAC implementation.

### B. Results Comparison

In this section, one can observe results comparing our approach versus IMU ground-information and also with our implementation of the 5-point RANSAC algorithm. We present results of 6D velocities estimation (Linear and Angular) in the camera reference frame, which is defined as: X axis contains pitch information, Y axis yaw information and Z axis roll information according to the right hand rule, Z points towards the front.

Our method (6DP) contains a hybrid approach (dense and sparse) correlation method. Results were obtained using only 1000 ZNCC correlation points between  $I_{T_k}^L$  and  $I_{T_{k+1}}^L$ .

In figure 3, one can observe the performance for angular velocity estimation between our 6DP method versus IMU and 5-point RANSAC information. The displayed results demonstrate a high degree of similarity between performance obtained using 6DP and IMU ground-truth information results. Additionally, results obtained by 6DP were performed without

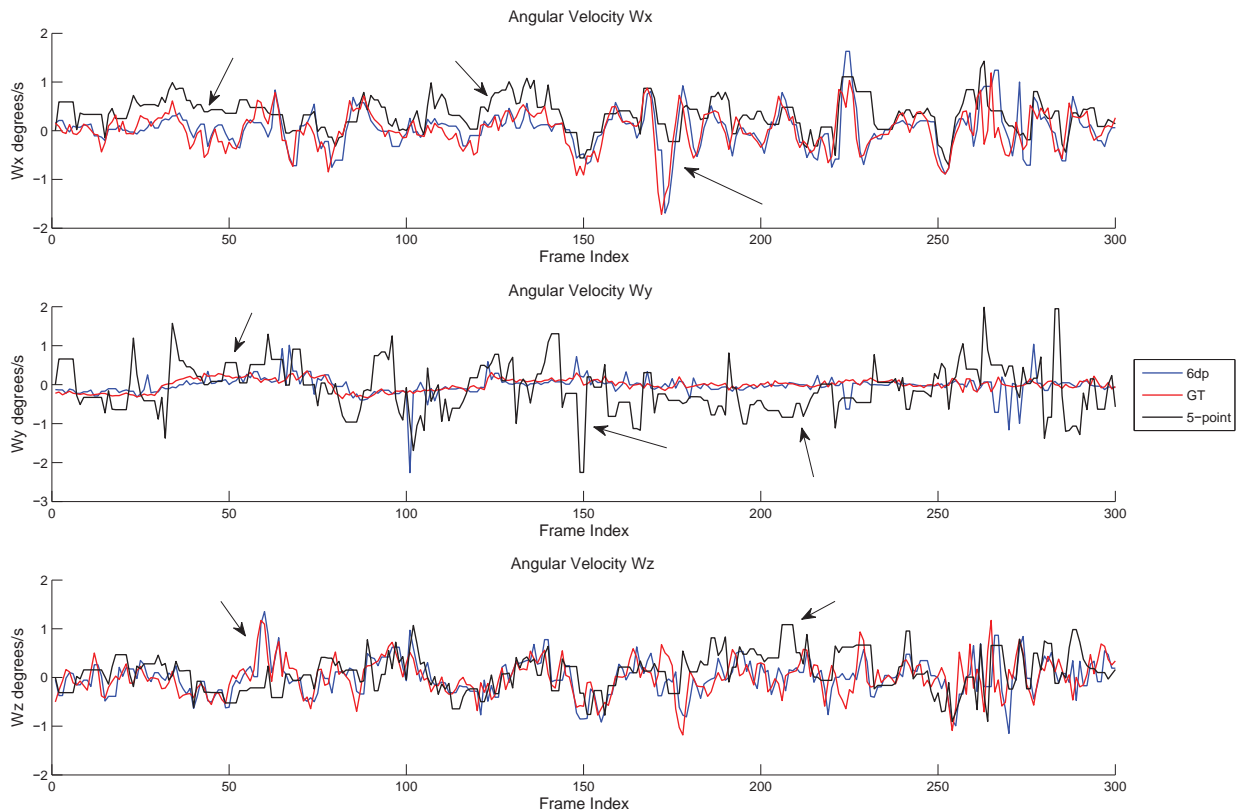


Fig. 3. Comparison of Angular velocities Estimation Results

using any type of filtering technique, thus the display of one or two clear outliers (see figure arrows), that do not influence overall results when compared to IMU filtered information. Most importantly, when it comes to angular velocities estimation 6DP method performance is better than the performance exhibited by the 5-point RANSAC algorithm.

However, for linear velocities as displayed in figure 4, the 5-point RANSAC algorithm implementation performance is smoother than our 6DP approach, especially in Z axis  $T_z$ . This may be due to the use of more reliable features (SIFT)[8] in the 5 point algorithm than the Harris corners used in 6DP.

The results here displayed demonstrate a compatible performance of both algorithms, one more suitable for linear motion estimation and the other more suitable for angular motion estimation.

What concerns methods run-time operations, 6DP by using recursive ZNCC approaches allows to reduce Domke Gabor Filter processing time by 20 percent. Even so, 6DP it is not yet suitable for real-time applications.

#### IV. CONCLUSIONS AND FUTURE WORK

In this paper, we presented a novel 6D Visual Odometry algorithm based on sparse and dense feature based mixture of Probabilistic Egomotion methods with stereo vision. We

tested our algorithm performance against other known methods for visual odometry estimation, namely against the 5-point RANSAC algorithm.

The obtained results demonstrated that probabilistic methods are a viable way to conduct visual odometry estimation, especially by providing additional evidence that this type of approach performs particularly well on estimating camera rotation movement and translation up to a scale factor.

However, results presented also show that for obtaining motion scale estimation, the performance of using Harris corners propagated through  $E$  from sequential time frame images are not as accurate as the one obtained using highly distinctive features such as SIFT. Following this further, this occurs due to low correlation values between  $I_{T_k}^L$  and  $I_{T_{k+1}}^L$  points.

In future work, one can overcome such events by extending our probabilistic approach to other types of multiple view geometry parametrization scheme. Moreover one that is able to cope with camera motion estimation with motion scale without the use of stereo vision. Other approach, can be adding IMU mechanization to the visual odometry estimation (Inertial Priors), to help select the more appropriate features for use with Absolute Orientation method.

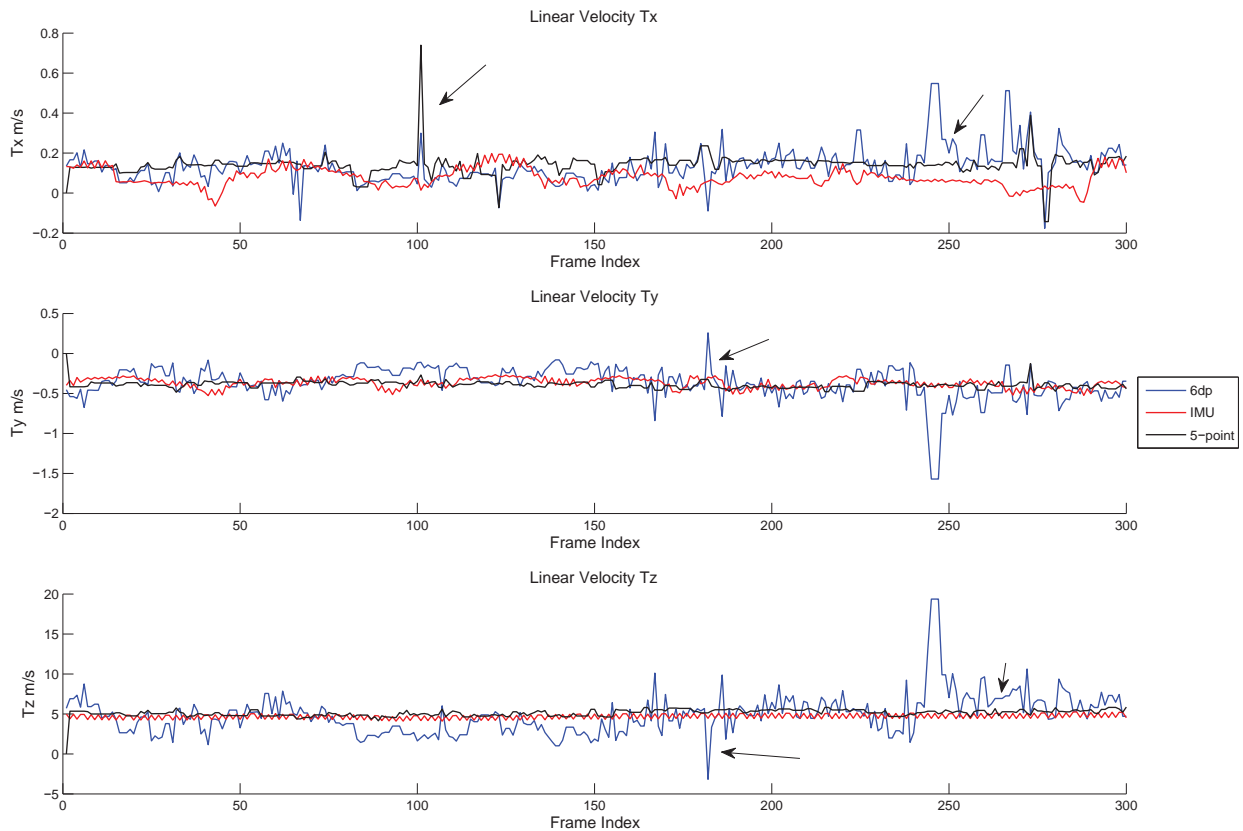


Fig. 4. Comparison of Linear Velocities Estimation Results

#### ACKNOWLEDGMENTS

This work is financed by the ERDF European Regional Development Fund through the COMPETE Programme (operational programme for competitiveness) and by National Funds through the FCT Fundacao para a Ciencia e a Tecnologia (Portuguese Foundation for Science and Technology) within project FCOMP - 01-0124-FEDER-022701 and under grant SFRH / BD / 47468 / 2008

#### REFERENCES

- [1] P. Alcantarilla, L. Bergasa, and F. Dellaert, "Visual odometry priors for robust EKF-SLAM," in *IEEE International Conference on Robotics and Automation, ICRA 2010*. IEEE, 2010, pp. 3501–3506.
- [2] M. Maimone and L. Matthies, "Visual Odometry on the Mars Exploration Rovers," in *IEEE International Conference on Systems, Man and Cybernetics*. Ieee, 2005, pp. 903–910.
- [3] D. Nistér, O. Naroditsky, and J. Bergen, "Visual odometry for ground vehicle applications," *Journal of Field Robotics*, vol. 23, no. 1, pp. 3–20, 2006.
- [4] D. Nistér, "An efficient solution to the five-point relative pose problem," *IEEE Trans. Pattern Anal. Mach. Intell.*, vol. 26, pp. 756–777, June 2004.
- [5] M. A. Fischler and R. C. Bolles, "Random sample consensus: A paradigm for model fitting with applications to image analysis and automated cartography," *Communications of the ACM*, vol. 24, no. 6, pp. 381–395, 1981.
- [6] K. Ni, F. Dellaert, and M. Kaess, "Flow separation for fast and robust stereo odometry," in *IEEE International Conference on Robotics and Automation ICRA 2009*, vol. 1, 2009, pp. 3539–3544.
- [7] F. Moreno, J. Blanco, and J. González, "An efficient closed-form solution to probabilistic 6D visual odometry for a stereo camera," in *Proceedings of the 9th international conference on Advanced concepts for intelligent vision systems*. Springer-Verlag, 2007, pp. 932–942.
- [8] D. Lowe, "Distinctive image features from scale-invariant keypoints," *International journal of computer vision*, vol. 60, no. 2, pp. 91–110, 2004.
- [9] J. Domke and Y. Aloimonos, "A Probabilistic Notion of Correspondence and the Epipolar Constraint," in *Third International Symposium on 3D Data Processing, Visualization, and Transmission (3DPVT'06)*. IEEE, Jun. 2006, pp. 41–48.
- [10] C. Harris and M. Stephens, "A combined corner and edge detection," in *Proceedings of The Fourth Alvey Vision Conference*, 1988, pp. 147–151.
- [11] B. Kitt, A. Geiger, and H. Lategahn, "Visual odometry based on stereo image sequences with ransac-based outlier rejection scheme," in *IEEE Intelligent Vehicles Symposium (IV), 2010*. IEEE, 2010, pp. 486–492.
- [12] J. Huang, T. Zhu, X. Pan, L. Qin, X. Peng, C. Xiong, and J. Fang, "A high-efficiency digital image correlation method based on a fast recursive scheme," *Measurement Science and Technology*, vol. 21, no. 3, 2011.
- [13] R. I. Hartley and A. Zisserman, *Multiple View Geometry in Computer Vision*, 2nd ed. Cambridge University Press, ISBN: 0521540518, 2004.
- [14] Z. Zhang, R. Deriche, O. Faugeras, and Q.-T. Luong, "A robust technique for matching two uncalibrated images through the recovery of the unknown epipolar geometry," *Artificial Intelligence Special Volume on Computer Vision*, vol. 78, no. 2, pp. 87 – 119, 1995.

# Enhanced PCA-Based Localization Using Depth Maps with Missing Data

Fernando Carreira and João M. F. Calado  
IDMEC-IST - Technical University of Lisbon  
and ADEM-ISEL - Polytechnic Institute of Lisbon  
1959-007 Lisboa, Portugal  
Email: {fcarreira,jcalado}@dem.isel.ipl.pt

Carlos Cardeira  
IDMEC-IST  
Technical University of Lisbon  
1049-001 Lisboa, Portugal  
Email: carlos.cardeira@ist.utl.pt

Paulo Oliveira  
ISR-IST and IDMEC-IST  
Technical University of Lisbon  
1049-001 Lisboa, Portugal  
Email: p.oliveira@dem.ist.utl.pt

**Abstract**—In this paper a new method for a global self-localization of mobile robots based on a PCA positioning sensor to operate in unstructured environments is proposed and experimentally validated. Unlike many existing systems that use RGB signals to capture information from the environment, in this work a 2D depth sensor is used, allowing the self-localization to be performed under different illumination conditions. However, depth sensors provide measurements corrupted with missing data, due to limitations on the support physic principles exploited (e.g. light that illuminates surfaces with diffuse reflection or wave fading), which severely degrades the performance of the estimation techniques and limits its use. The main goal of this paper is to present a self-localization system for mobile robots based on a PCA positioning sensor that relies on corrupted depth measurements and the corresponding experimental validation. The proposed method allows for the implementation of a global self-localization system for indoor environments with higher accuracy, that provide a Gaussian estimated position error and work in any illumination conditions.

## I. INTRODUCTION

The problem of mobile robots localization with only onboard sensors in indoors environments has been a great challenge to researches in mobile robotics, see [8], [3] and the references therein. To perform this task, usually, mobile robots are equipped with different types of sensors like compasses, accelerometers, gyros, cameras, time of flight cameras and encoders, providing enough information to the measuring system to determine its global pose, i.e., position and orientation in a mapped environment.

Vision is one of the most popular sensors in mobile robotics to provide measurements to solve the localization, due to the large amount of information provided on the environment, extracted from the RGB image [23], [22], [16], [11]. However, in vision systems remains a general limitation related to different environment illumination conditions that decreases the localization systems robustness.

To avoid the above mentioned problem, some localization systems are based on time-of-flight sensors [17]. The use of time-to-flight sensors allows to obtain depth information about the environment and presents a more robust system able to cope with different light conditions. Moreover, the time-of-flight cameras allows the capture of depth images, where the sensor is able to receive a grid with depth information from all field of view [1]. However, it is expensive to implement this type of cameras in many mobile robotic platforms.

Recently, the companies PrimeSense and Microsoft developed a device primarily for video games, called Kinect, that combines a RGB and a depth camera. Due to its low price and a straightforward way to be connected with a computer, the

Kinect device became popular in mobile robotics community creating several different applications of mobile robots [25], [12], [13].

A very common problem in depth sensors, including the Kinect depth sensor, is the existence of missing data in signals, caused by IR beams that are not well reflected, not returning to the depth sensor receiver. In [19], [20], a method using the Principal Component Analysis (PCA) methodology is presented to avoid the problem of missing data in signals and its performance is compared with other state-of-the-art algorithms. The PCA [14] is an efficient algorithm that converts the database into an orthogonal space creating a database with a high compression ratio, when compared with the amount of captured data. Moreover, the PCA allows to develop localization systems that do not depend on any predefined structure [15], [2], i.e. does not need to detect any specific features about the environment. In [21], PCA is used for terrain reference navigation of underwater vehicles.

There are different approaches in installing cameras to develop localization systems. The most common solution is to allow placement of cameras to look around to obtain its position [24], [11], while some mobile robots use a single camera looking upward [9], [26]. The use of vision from the ceiling has the advantage that images can be considered without scaling and are static.

While many localization systems uses the information of extraction features to the localization of the mobile robot in a structured environment [18], the use of PCA allows the creation of a localization system with a great compression ratio and without the need of feature extracting.

In this work, the main purpose is the experimental validation of [19], [20] avoiding the missing data existing in a ceiling vision localization system performed by a Kinect depth sensor.

This paper is organized as follows: Section II presents the mobile robot platform and the motivation for the use of Kinect in the proposed localization system; in the Section III, the principal component analysis for signals with missing data is detailed. For performance analysis purposes, Section IV presents experimental results of the proposed method, compared with the results achieved using the classical PCA algorithm along a straight line (1D localization); in Section V the results of the proposed method are presented and validated in a 2D localization approach. Finally, Section VI presents some conclusions and unveils future work.

## II. MODEL PLATFORM

The experimental validation of the positioning system proposed in this paper is performed resorting to a low cost mobile

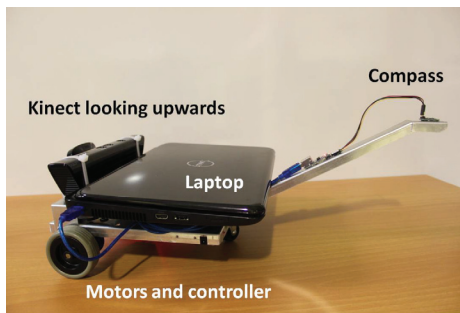


Fig. 1. Mobile platform equipped with kinect sensor and compass

robotic platform [4], with the configuration of a Dubins car. A Microsoft Kinect is installed on the platform, pointing upwards to the ceiling, and a digital compass, located on the extension arm (robot rear part) to avoid the magnetic interference from the motors (see Fig. 1)

The Kinect includes a RGB camera with a VGA resolution ( $640 \times 480$  pixels) using 8 bits and a 2D depth sensor ( $640 \times 480$  pixels) with 11 bits of resolution. The use of this sensor for mobile robots localization could combine the capture of a RGB image and a depth map about the environment, obtaining RGB-D images, as shown in Fig. 2. This image depicts the ceiling view captured by the Kinect installed onboard the mobile robot. Note that it is possible to observe both the 3D shape of the existing technical installations in the ceiling and its color.

The robot moves in an environment indoors in buildings with some information (e.g. building-related systems such as HVAC, electrical and security systems, etc.). It is possible to use the signals captured by a Kinect looking upward (RGB image, depth map or both) by an algorithm that can provide mobile robot global position in the environment.

Due to limitations found in image-based mobile robot localization approaches, regarding illumination changes, and aiming the development of an efficient self-localization solution that can work in places with variation on the level of illumination, only the Kinect depth signal is used, resorting to an adaptation to the method proposed in [21], [6], [7], [5] to the problem at hand.

However, as it is possible to observe in Fig. 2, due to geometry and properties of some objects, several waves are

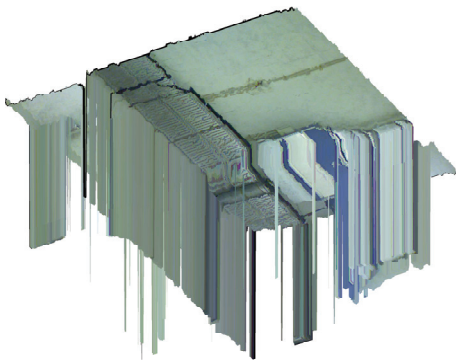


Fig. 2. RGB-D image of the ceiling view obtained by the kinect installed onboard the mobile robot

not well reflected and, thus, can not be understood by the depth sensor receiver. In the case of Kinect, such a problem results in the appearance of points with null distance ( $0mm$ ) inside the data array with the depth values (distances to various points in the plane), that may lead to erroneous results in the localization system. In this paper an extension of a PCA-based position approach will be presented aiming to cope with the illumination variability problem common to usual vision systems, in both cases to be validated experimentally.

### III. PCA FOR SIGNALS WITH MISSING DATA

PCA [14] is a methodology based on the Karhunen-Loève (KL) transformation that is often used in applications that need data compression, like image and voice processing, data mining, exploratory data analysis and pattern recognition. The data reduction is obtained through the use of a database eigenspace approximation by the best fit eigenvectors. This technique makes the PCA an algorithm that has a high compression ratio and requires reduced computational resources. The PCA algorithm is used as the mobile robot position sensor in [6], [7].

The PCA eigenspace is created based on a set of  $M$  stochastic signals  $\mathbf{x}_i \in \mathbb{R}^N$ ,  $i = 1, \dots, M$  acquired by a Kinect depth sensor installed onboard the mobile robot, considering an area with  $N$  mosaics in two dimensional space,  $N = N_x N_y$ , where  $N_x$  and  $N_y$  are the number of mosaics in  $x$  and  $y$  axis, respectively.

In the common PCA-based approaches, the eigenspace of the set of acquired data is characterized by the corresponding mean  $\mathbf{m}_x = \frac{1}{M} \sum_{i=1}^M \mathbf{x}_i$ . However, usually these signals obtained by sensors are corrupted with missing data. In the case of the depth map provided by Kinect, the points where failures occurred in the depth data reception are marked with a null distance ( $0mm$ ). Therefore, the existence of missing data in signal  $\mathbf{x}_i$  corrupts the PCA mean value computation creating an orthogonal space with erroneous data.

To solve the position estimation problem when data with missing data is used, a mean substitution method is applied to the PCA position sensor, as described below. Thus, a vector  $\mathbf{l}$  with length  $N$  consisting of boolean values is used to mark the real and missed data of a signal  $\mathbf{x}_i$ . Then, considering the  $j^{th}$  component of acquired signal  $\mathbf{x}_i$ , the index  $\mathbf{l}_i(j)$  is set to 1 if the signal  $\mathbf{x}_i(j)$  is available and it is set to 0 if there is a missing data.

Hence, to avoid the negative impact of the sensor signals missing data in PCA-based approaches performance, an extension to this methodology is proposed in this paper, where instead of considering all values of the  $M$  stochastic signals to compute the previously mentioned mean value  $\mathbf{m}_x$ , only the correct data is used and the value corresponding to missing data is neglected. Thus, the mean data is computed as follows:

$$\mathbf{m}_x(j) = \frac{1}{c(j)} \sum_{i=1}^M \mathbf{l}_i(j) \mathbf{x}_i(j), \quad j = 1, \dots, N \quad (1)$$

where  $c(j)$  is the number of  $j^{th}$  components for a set of  $M$  signals  $\mathbf{x}_i \in \mathbb{R}^N$ ,  $i = 1, \dots, M$  without missing data. The counter  $\mathbf{c}$  is a vector with length  $N$  defined by:

$$\mathbf{c} = \sum_{i=1}^M \mathbf{l}_i \quad (2)$$

In order to apply the mean substitution method to the PCA algorithm, all missing data presented in the acquired database is replaced by the mean value of the corresponding component, i.e., if there is a missing data in the  $j^{th}$  component of the  $i^{th}$  signal, the missing value  $x_i(j)$  is replaced with the value of  $\mathbf{m}_x(j)$ . After this substitution, the decomposition of the  $x_i(j)$  into the orthogonal space follows the PCA algorithm classical approach, i.e.  $\mathbf{v} = \mathbf{U}^T(\mathbf{x} - \mathbf{m}_x)$ . Matrix  $\mathbf{U} = [\mathbf{u}_1 \mathbf{u}_2 \dots \mathbf{u}_N]$  should be composed by the  $N$  orthogonal column vectors of the basis, verifying the eigenvalue problem

$$\mathbf{R}_{xx}\mathbf{u}_j = \lambda_j\mathbf{u}_j, \quad j = 1, \dots, N, \quad (3)$$

Assuming that the eigenvalues are ordered, i.e.  $\lambda_1 \geq \lambda_2 \geq \dots \geq \lambda_N$ , the choice of the first  $n \ll N$  principal components leads to stochastic signals approximation given by the ratio on the covariances associated with the components, i.e.  $\sum_n \lambda_n / \sum_N \lambda_N$ .

During the mission, before the projection of the depth image into the orthogonal space, the mean substitution should be followed in order to eliminate the problem caused by missing data in the signal  $\mathbf{x}$ , i.e., all  $j^{th}$  component of the signal  $x_i$  should be replaced by the corresponding mean value  $\mathbf{m}_x(j)$ .

The robot position  $\hat{x}$  and  $\hat{y}$  is obtained by finding a given neighborhood  $\delta$ , the mosaic whose eigenvector is nearest to the acquired signal decomposed into the orthogonal space:

$$\forall_i \|\hat{x} \hat{y}^T - [x_i \ y_i]^T\|_2 < \delta, \quad r_{\text{PCA}} = \min_i \|\mathbf{v} - \mathbf{v}_i\|_2; \quad (4)$$

Given the mosaic  $i$  that verifies this condition, its center coordinates  $[x_i \ y_i]^T$  are selected as the robot position obtained by the PCA-based sensor.

Then, the mean substitution approach is used when there is missing data in the depth signals coming from the Kinect sensor. Just like during the creation of the PCA eigenspace, it must be done before the application of the PCA algorithm, i.e., all  $j^{th}$  component of the signal  $x_i$  should be replaced by the corresponding mean value  $\mathbf{m}_x(j)$ .

#### IV. EXPERIMENTAL RESULTS ALONG A STRAIGHT LINE (1D LOCALIZATION)

As concept validation, the proposed self-localization method is initially developed considering a straight line (1D), based on the model proposed in [6] and detailed in the appendix A. Thus, to create the PCA eigenspace, a set of 31 depth images are captured along a straight line with 3 m of length (sampling ratio of 0.1 m). Considering that the Kinect depth sensor has a resolution of 640 by 480 points, and with the purpose of reducing the amount of data stored in PCA eigenspace, the depth images are compressed with a ratio of 100 : 1, and transformed into vectors  $\mathbf{x}_i \in \mathbb{R}^{3072}$ ,  $i = 1, \dots, 31$ .

The mobile robot follows along a straight line with constant velocity and the position estimation is obtained using the model proposed in [6], see Appendix A for details. The position estimates are based on data obtained from the onboard sensors and the commands to the actuators, assuming constant values between sampling times (zero order hold assumption).

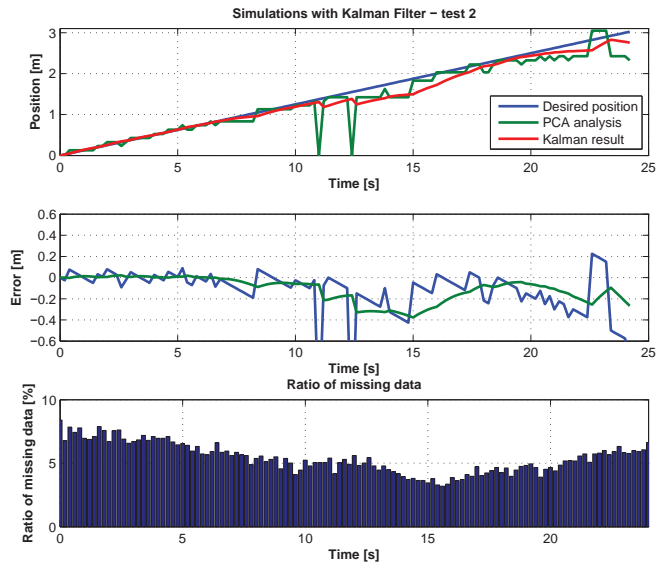


Fig. 3. Results of PCA-based positioning sensor and localization estimates from Kalman filter

#### A. Monte Carlo Performance Tests

To assess the mobile robot self-localization methodology proposed in this paper, a Monte Carlo test composed of 10 experiments as described above is repeated. Images are captured with a frequency of 5 Hz to be processed by the PCA-based positioning sensor; Fig. 3 gives the localization results obtained in one of those experiments. The results show that the PCA algorithm provides a reasonable approximation to the real robot localization. However, due to the existence of missing data, the position obtained by the PCA algorithm often gives incorrect results.

Analyzing Fig. 3, it is possible to see that the obtained position often reaches errors greater than 0.1 m (distance at which the images are acquired to the eigenspace). Figure 4 shows the results of three tests, where it is possible to see the existence of large perturbations in the results of the PCA-based position sensor. Even the fusion of this results with the odometry, through a Kalman filter (KF), detailed

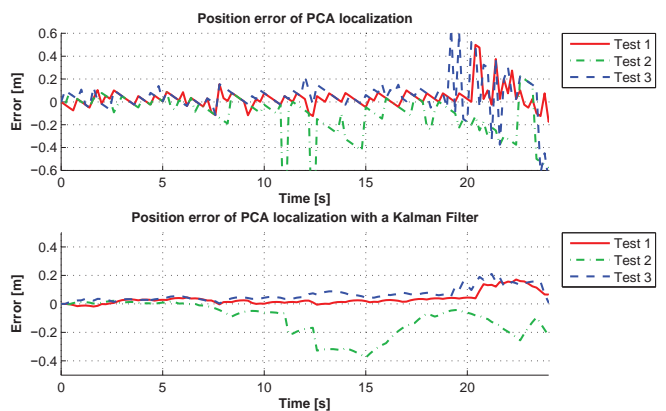


Fig. 4. Localization errors of tests along a straight line

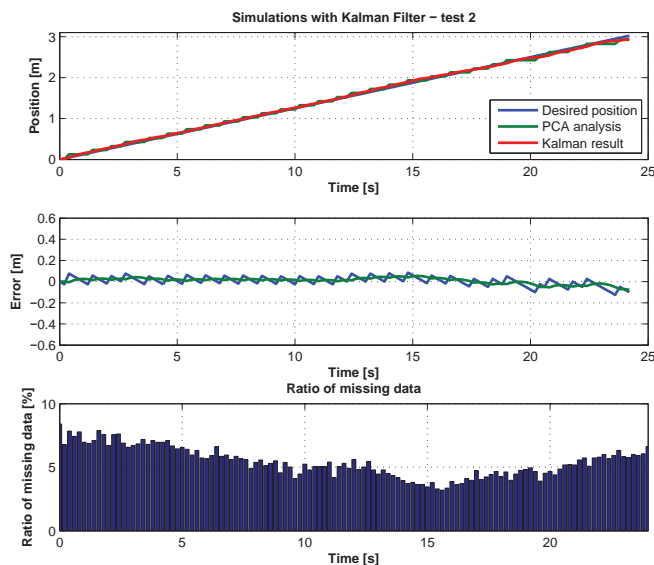


Fig. 5. Results of PCA-based positioning sensor and localization estimates from Kalman filter - new method

in Appendix A, do not always is able to estimate the robot position with accuracy because the PCA position sensor often provides results with large error. As it is possible to see, the position error obtained by the PCA-based position sensor often exceeds 0.1 m.

### B. Monte Carlo Performance Tests with Missing Data Correction

Following the methodology proposed in Section III, successful tests are made to check the enhanced performance of the localization system in presence of missing data. Thus, to validate this extension to the PCA-based approach, the same acquired depth data has been considered.

Comparing Fig. 5 with Fig. 3, it is possible to observe that the proposed method is able to eliminate the existing missing data and provide a position value with better accuracy. Analyzing the results presented in Fig. 6, it is possible to see that the results now obtained present position errors smaller

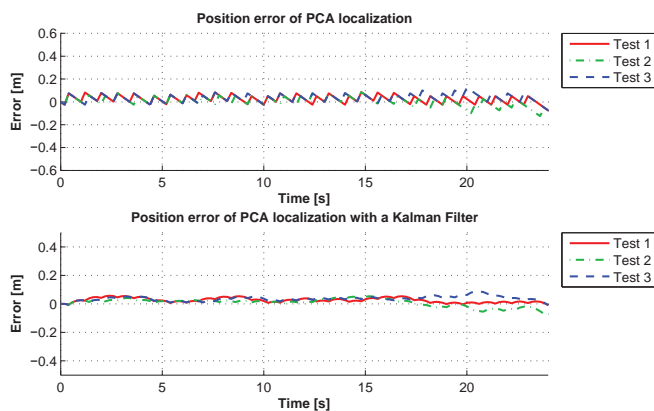


Fig. 6. Localization errors of tests along a straight line - new method

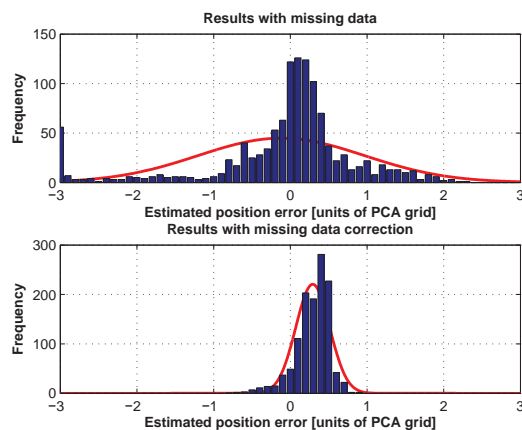


Fig. 7. Distribution of the estimated position error for both methods, considering a PCA grid with 0.1 m

than 0.1 m. Once the proposed method is able to compute the robot position with a better accuracy, its fusion with the odometry, through a KF, always provides smoothly results and near of the real robot localization.

Finally, analyzing the histogram of the position error obtained by the PCA-based position sensor after the 10 performed tests (see Fig. 7), it is possible to see that the error of both methods is approximately Gaussian with a mean error close to zero.

Considering that the data to create the PCA eigenspace are acquired with 0.1 m of distance, it is possible to observe that all estimated position errors are less than the sampling distance of PCA eigenspace, while that considering signals with missing data, only about 68 % of results (1 standard deviation) are inside of this distance.

## V. CONCEPT VALIDATION IN 2D LOCALIZATION

In order to solve the problem of 2D localization, a new PCA eigenspace is created with a set of captured depth images along a grid map with a distance of 0.3m (in  $x$  and  $y$  axis) in an area of  $5m \times 4.5m$  (Fig. 8). The captured depth images are cropped with a circular mark allowing the rotation and comparison of captured depth images when the robot is in the same position, but with different attitude, during a mission. In

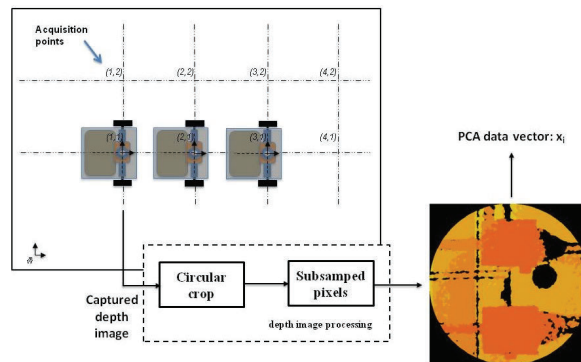


Fig. 8. Grid map and depth image processing to create a PCA eigenspace

order to compress the amount of data, the depth images are sampled with a compression ratio of 100 : 1 and converted into a vector that will be added to PCA eigenspace. In [7], [5], the authors followed a similar approach using a RGB camera but the method revealed to be sensitive to illumination conditions.

During an experiment, it is possible to estimate the robot attitude and position, as well as the angular motion speed and the robot angular slippage, using only the signals obtained by the onboard sensors (Kinect, compass and encoders), through a self-localization sensor based in two KF and one PCA algorithm, with an architecture as detailed in Fig. 9.

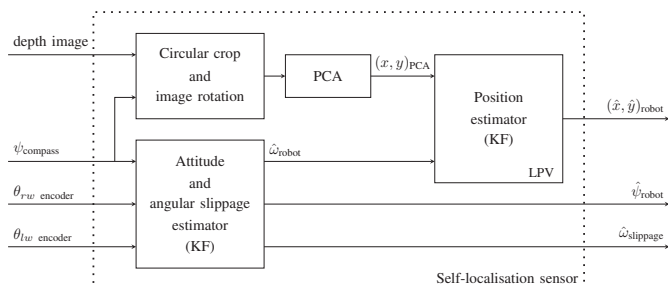


Fig. 9. Architecture of the self-localization sensor

The following notation is used in Fig. 9:

- $\psi_{compass}$  - orientation angle given by the compass;
- $\theta_{rwencoder}$  - angle given by the encoder of the right wheel;
- $\theta_{lwencoder}$  - angle given by the encoder of the left wheel;
- $(x, y)_{PCA}$  - coordinates given by the PCA sensor;
- $(\hat{x}, \hat{y})_{robot}$  - estimated robot coordinates in the world referential;
- $\hat{\omega}_{robot}$  - estimated angular speed;
- $\hat{\omega}_{slippage}$  - estimated differential slippage.

Detailing the architecture of the self-localization sensor presented in Fig. 9, the KF depicted on the left of the figure implements the attitude optimal estimator model that is responsible to estimate the mobile robot attitude and the angular slippage (see Appendix C). Once all acquired depth images for the PCA database are taken with the same orientation and compressed with a circular crop (Fig. 8), then during a mission, the acquired depth images must be rotated to zero degrees of attitude, using the compass angle, and compressed with the same circular crop. The position estimator (on the right of the figure) implements a Linear Parameter-Varying (LPV) model as a function of the estimated angular speed in a KF, fusing it with the position obtained by the PCA algorithm (see Appendix B).

Resorting to this architecture, it is possible to estimate the position, attitude and angular slippage of the mobile robot with a global stable error dynamic. For more details about this self-localization architecture see technical report [7].

#### A. Results for 2D localization

To test the mobile robot self-localization performance of the proposed approach in a environment (considering 2D

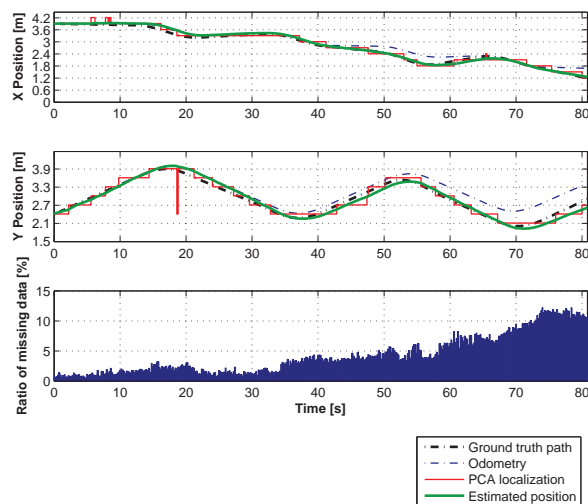


Fig. 10. Estimated position along time

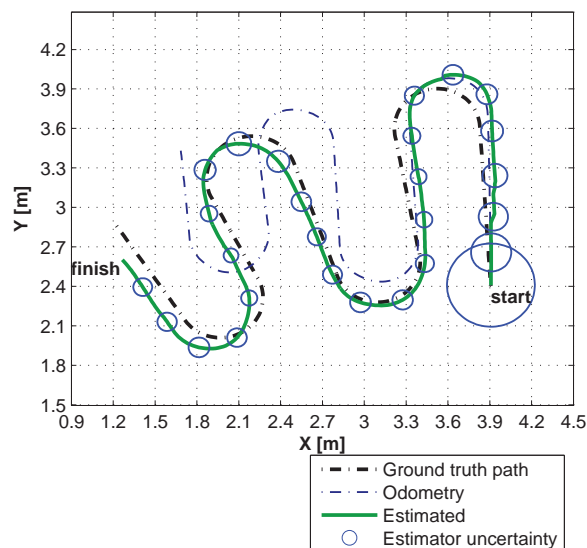


Fig. 11. Map with estimated position considering a ground truth path.

localization), several tests are performed with the classical lawnmower type trajectory, combining both straight lines and curves, with a  $0.1 \text{ m} \cdot \text{s}^{-1}$  robot speed and 5 Hz of sampling frequency. During the robot motion the real mobile robot trajectory is measured allowing the comparison of the estimated position with the real one (ground truth test) and the corresponding position errors analyzed.

As it is possible to see in Fig. 10, that the position results obtained by the PCA algorithm is very close to the ground truth trajectory. Therefore, fusing the kinematic model of the robot with the position obtained by the PCA in the KF allows estimating position values with a very good accuracy (see Appendix B for details).

Figure 11 shows the position estimated with the ground truth trajectory and the position obtained by the odometry. Comparing the results of the odometry with the estimated

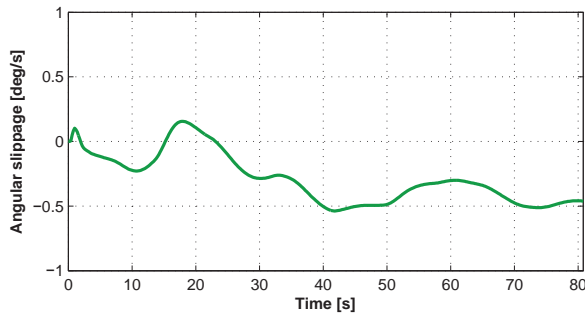


Fig. 12. Angular slippage estimated

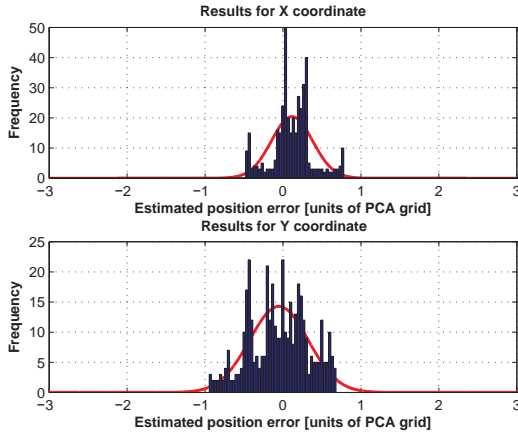


Fig. 13. Distribution of the estimated position error for both axis, considering a PCA grid with 0.3 m

position it is possible to see an angular slippage in motion, that is increasing the difference between the estimated attitude and the one obtained by the odometry along time. This angular slippage is caused by systematic errors, such as uncertainties in the dimensions of the wheels, eccentric shaft problems, misalignment of the shafts, etc. It is possible to observe that in the initial part of the trajectory the estimator obtains a result close to the odometry. However, the localization system can approximate the estimated position with the ground truth trajectory.

Furthermore, analyzing Fig. 12, it is possible to observe the existence of an angular slippage of  $-0.5 \text{ rad} \cdot \text{s}^{-1}$  (positive for slippage in clockwise direction), that is detected at 40 s by the attitude estimator. Looking at Fig. 10 after 40 s (instant which is detected angular slippage), the results of the position estimator are closer to the ground truth path than the odometry.

Finally, analyzing the histograms of Fig. 13 it is possible to conclude that the statistical distribution of the estimated position errors is approximately Gaussian with a mean close to zero. Moreover, comparing the variation of the distribution with the distance of the grid map acquired to create the PCA eigenspace, it is possible to see that, the proposed self-localization system is able to estimate the position with an error less than the distance between the acquired depth images, as happened with the localization in 1D.

## VI. CONCLUSIONS

The existence of missing data in image is sometimes inevitable and it can induce a positioning system to an erroneous localization. In this paper an extension of a PCA methodology aiming to avoid the negative impact of missing data in signals is developed and experimentally validated. The proposed localization system is based only on a Kinect sensor installed onboard, looking upwards to the ceiling, where the depth sensor often provides signals with missing data, caused by IR beams that not were reflected.

All tests were successfully performed, allowing to conclude that the proposed approach can be useful in a number of mobile robotics applications where the existence of missing data is inevitable and causes a localization systems performance degradation. Moreover, the proposed method allows to validate the application of the Kinect depth sensor, in a mobile robot localization system based on an extension of a classical PCA algorithm to operating in unstructured environments. The propose localization system is optimal and globally stable, under the Gaussian approaches resorting to classical Kalman filtering techniques.

The method was successfully validated in a self-localization system, using only onboard sensors and estimates the position with a global stable error dynamics.

In the future, the proposed localization method will be implemented in a path following control approach, where the self-localization system will be integrated in a control close loop. Later, in order to increase the self-knowledge about the place, the proposed PCA algorithm will be updated to create a dynamic PCA database. This development will allow an architecture able to perform different tasks like obstacle avoidance, robot-human interaction, rescue activities or integration in a multi-robots platform for collaborative work.

## APPENDIX

For the sake of readability of this paper, this appendix shows the models and estimators used for the 1D and 2D validation experiments. These models and estimators may be found, with more detail, in [7].

### A. Model for position estimation in 1D localization

The mobile robot kinematic model that describes the movement in a straight line (1D) is

$$\dot{x} = u + b + \mu_1 \quad (5)$$

$$\dot{b} = 0 + \mu_2 \quad (6)$$

considering the following assumptions:

- the slippage velocity is constant or slowly varying (i.e.  $\dot{b} = 0$ );
- the noise in the actuation (motors are in closed loop) and the slippage velocity are assumed as zero-mean uncorrelated white Gaussian noise,  $\mu_i \sim N(0, \sigma_i^2)$ .

Expressing the model dynamics in a state-space system with  $\mathbf{x} = [x \ b]^T$ ,

$$\dot{\mathbf{x}} = \begin{bmatrix} 0 & 1 \\ 0 & 0 \end{bmatrix} \mathbf{x} + \begin{bmatrix} 1 \\ 0 \end{bmatrix} u + \begin{bmatrix} 1 & 0 \\ 0 & 1 \end{bmatrix} \begin{bmatrix} \mu_1 \\ \mu_2 \end{bmatrix} \quad (7)$$

$$y = [1 \ 0] \mathbf{x} + \gamma \quad (8)$$

The output of this system  $y$  is the positioning sensor measurement described Section III. Since the position estimator is processed in a digital processor, the discrete model is obtained assuming that the vehicle velocity  $u$  is constant (zero order hold assumption) between two consecutive processing times, resulting

$$\mathbf{x}(k+1) = \begin{bmatrix} 1 & T \\ 0 & 1 \end{bmatrix} \mathbf{x}(k) + \begin{bmatrix} T \\ 0 \end{bmatrix} u(k) + \begin{bmatrix} T & T^2/2 \\ 0 & T \end{bmatrix} \mu(k) \quad (9)$$

$$y(k) = [1 \ 0] \mathbf{x}(k) + \gamma(k) \quad (10)$$

The design of a linear time-invariant Kalman filter for the underlying model described above is by now classic and the reader is referred to [10].

### B. Model for position estimation in 2D localization

The classic differential drive mobile robot model is given by

$$\dot{x} = u \cos \theta \quad (11)$$

$$\dot{y} = u \sin \theta \quad (12)$$

$$\dot{\theta} = \omega \quad (13)$$

where  $u$  is the common mode speed,  $x$  and  $y$  are the robot coordinates in the world referential,  $\theta$  is the orientation angle of the robot in the world referential and  $\omega$  is the angular speed.

However, the classic non-linear model for differential drive mobile robots can be rewritten for a new state variables, becoming in a Linear Parameter Varying (LPV) model. Thus, differentiating: (11)–(13):

$$\ddot{x} = -u\omega \sin \theta = -\omega \dot{y} \quad (14)$$

$$\ddot{y} = u\omega \cos \theta = \omega \dot{x} \quad (15)$$

$$\ddot{\theta} = \dot{\omega} \quad (16)$$

and choosing as state vector  $\mathbf{x} = [x \ \dot{x} \ y \ \dot{y}]^T$ , a new LPV model for differential drive mobile robot is obtained:

$$\dot{\mathbf{x}} = \overbrace{\begin{bmatrix} 0 & 1 & 0 & 0 \\ 0 & 0 & 0 & -\omega \\ 0 & 0 & 0 & 1 \\ 0 & \omega & 0 & 0 \end{bmatrix}}^{\mathbf{A}} \mathbf{x} \quad (17)$$

$$\dot{\theta} = \omega \quad (18)$$

Considering the LPV model (17)–(18) and assuming that  $\omega$  is constant between two sampling times (zero order hold assumption), the follow discrete model can be obtained (see [7] for more details):

$$\mathbf{x}(k+1) = \overbrace{\begin{bmatrix} 1 & \frac{\sin \omega T}{\omega} & 0 & \frac{1 + \cos \omega T}{\omega} \\ 0 & \cos \omega T & 0 & -\sin \omega T \\ 0 & \frac{1 - \cos \omega T}{\omega} & 1 & \frac{\sin \omega T}{\omega} \\ 0 & \sin \omega T & 0 & \cos \omega T \end{bmatrix}}^{\mathbf{A}(\omega)} \mathbf{x}(k) + \overbrace{\begin{bmatrix} T & \frac{1 - \cos \omega T}{\omega^2} & 0 & -\frac{\omega T - \sin \omega T}{\omega^2} \\ 0 & \frac{\sin \omega T}{\omega} & 0 & -\frac{1 - \cos \omega T}{\omega} \\ 0 & \frac{\omega T - \sin \omega T}{\omega^2} & T & \frac{1 - \cos \omega T}{\omega} \\ 0 & \frac{1 - \cos \omega T}{\omega} & 0 & \frac{\sin \omega T}{\omega} \end{bmatrix}}^{\mathbf{G}(\omega)} \mathbf{v}(k) \quad (19)$$

$$\mathbf{y}(k) = \underbrace{\begin{bmatrix} 1 & 0 & 0 & 0 \\ 0 & 0 & 1 & 0 \end{bmatrix}}_{\mathbf{C}} \mathbf{x}(k) \quad (20)$$

Finally, in order to estimate the mobile robot position, the Linear Parameter Varying (LPV) model (19)–(20) is fused with the position obtained by the PCA-based position sensor, through the KF presented in Fig. 14, where  $x(k)$  and  $y(k)$  are the position obtained by the PCA sensor in instant  $k$  and  $\hat{x}(k)$  and  $\hat{y}(k)$  are the estimated position in the same instant.

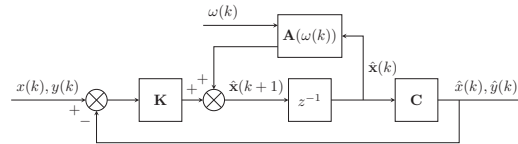


Fig. 14. Block diagram of the position estimator

### C. Model for attitude and angular slippage estimation in 2D localization

The model that describes the angular motion of the differential drive mobile robot is

$$\dot{\psi} = \omega + s \quad (21)$$

$$\dot{s} = 0 \quad (22)$$

where  $\omega$  is the angular speed,  $\psi$  is the attitude of the robot and  $s$  is the angular slippage in differential motion.

Considering the state vector  $\boldsymbol{\theta} = [\psi \ s]^T$ , the kinematic model in state space can be defined by:

$$\dot{\boldsymbol{\theta}} = \begin{bmatrix} 0 & 1 \\ 0 & 0 \end{bmatrix} \boldsymbol{\theta} + \begin{bmatrix} 1 \\ 0 \end{bmatrix} \omega \quad (23)$$

Assuming that signals processing is performed by a digital processor,  $\omega$  and  $\psi$  are constant between sampling times (zero order hold assumption), allowing to obtain the discrete model of attitude:

$$\boldsymbol{\theta}(k+1) = \overbrace{\begin{bmatrix} 1 & T \\ 0 & 1 \end{bmatrix}}^{\mathbf{A}} \boldsymbol{\theta}(k) + \overbrace{\begin{bmatrix} T \\ 0 \end{bmatrix}}^{\mathbf{B}} \omega(k) \quad (24)$$

$$y(k) = \underbrace{\begin{bmatrix} 1 & 0 \end{bmatrix}}_{\mathbf{C}} \boldsymbol{\theta}(k) \quad (25)$$

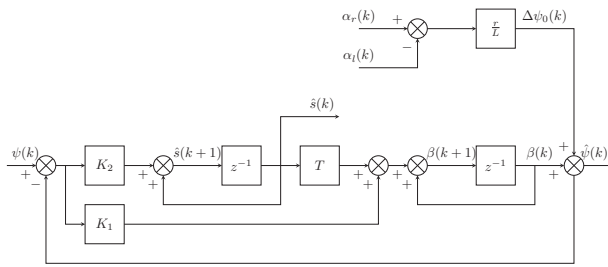


Fig. 15. Block diagram of the attitude and angular slippage estimator

Applying a KF to the discrete model (24–25), following the steps described in [7], the optimal attitude and angular slippage estimator presented in Fig. 15 is obtained, where  $\psi(k)$  is the angle of compass captured in instant  $k$ ,  $r$  is the radius of the wheels,  $l$  is the distance between wheels,  $\alpha_r(k)$  and  $\alpha_l(k)$  are the lengths of the paths of left and right wheels (that can be read directly from the encoders onboard) and  $\hat{\psi}(k)$  and  $\hat{s}(k)$  are the estimated attitude and angular slippage of the robot, respectively.

Finally, the angular speed of the robot applied in LPV (20) is obtained through a numerical difference of the estimated attitude of the robot:

$$\hat{\omega}(k) = \frac{\hat{\psi}(k) - \hat{\psi}(k-1)}{T} \quad (26)$$

#### ACKNOWLEDGMENTS

The authors thank the valuable assistance of João Rodrigues in the development of the work reported in this paper.

This work was partially supported by Fundação para a Ciência e a Tecnologia, through IDMEC under LAETA.

#### REFERENCES

- [1] Sergio Almansa-Valverde, Jos Carlos Castillo, and Antonio Fernandez-Caballero. Mobile robot map building from time-of-flight camera. *Expert Systems with Applications*, 39(10):8835 – 8843, 2012.
- [2] Matej Artač, Matjaž Jogan, and Aleš Leonardis. Mobile robot localization using an incremental eigenspace model. In *IEEE International Conference on Robotics and Automation*, pages 1025–1030, Washington, DC, USA, May 2002.
- [3] T. Bailey and H. Durrant-Whyte. Simultaneous localization and mapping (SLAM): part II. *Robotics Automation Magazine, IEEE*, 13(3):108 – 117, September 2006.
- [4] C. Cardeira and J. Sá da Costa. A low cost mobile robot for engineering education. In *Industrial Electronics Society, 2005. IECON 2005. 31st Annual Conference of IEEE*, pages 2162–2167, Raleigh, USA, 2005.
- [5] F. Carreira, C. Christo, D. Valério, M. Ramalho, C. Carreira, J. M. F. Calado, and P. Oliveira. 2d pca-based localization for mobile robots in unstructured environments. In *IEEE/RSJ International Conference on Intelligent Robots and Systems (IROS 2012)*, pages 3767–3868, Vilamoura, Portugal, October 2012.
- [6] F. Carreira, C. Christo, D. Valério, M. Ramalho, C. Carreira, J. M. F. Calado, and P. Oliveira. Experimental validation of a PCA-based localization system for mobile robots in unstructured environments. In *Robotica - 12th International Conference on Autonomous Robot Systems and Competitions*, pages 69–74, Guimarães, Portugal, April 2012.
- [7] F. Carreira, C. Christo, D. Valério, M. Ramalho, C. Carreira, J. M. F. Calado, and P. Oliveira. Experimental validation of a PCA-based localization system for mobile robots in unstructured environments. IDMEC/CSI Internal Report, <http://www1.dem.ist.utl.pt/carreira/Mesh/Ca12b.pdf>, June 2012.
- [8] H. Durrant-Whyte and T. Bailey. Simultaneous localization and mapping: part I. *Robotics Automation Magazine, IEEE*, 13(2):99 –110, June 2006.

- [9] Yasuaki Fukutani, Tomoyuki Takahashi, Masahiro Iwahashi, Tetsuya Kimura, Samsudin Siti Salbiah, and Norrima Binti Mokhtar. Robot vision network based on ceiling map sharing. In *11th IEEE International Workshop on Advanced Motion Control (AMC 2010)*, pages 164–169, Nagaoka, Niigata, March 2010.
- [10] A. Gelb. *Applied optimal estimation*. MIT Press, 1974.
- [11] Arturo Gil, Oscar Mozos, Monica Ballesta, and Oscar Reinoso. A comparative evaluation of interest point detectors and local descriptors for visual slam. *Machine Vision and Applications*, 21:905–920, 2010.
- [12] A.S. Huang, A. Bachrach, P. Henry, M. Krainin, D. Maturana, D. Fox, and N. Roy. Visual odometry and mapping for autonomous flight using an rgb-d camera. In *15th International Symposium on Robotics Research (ISRR)*, Flagstaff, Arizona, USA, August 2011.
- [13] W.T. Huang, C.L. Tsai, and H.Y. Lin. Mobile robot localization using ceiling landmarks and images captured from an rgb-d camera. In *IEEE/ASME International Conference on Advanced Intelligent Mechatronics (AIM 2012)*, pages 855–860, Kachsiung, Taiwan, July 2012.
- [14] I. Jolliffe. *Principal Component Analysis*. Springer-Verlag, 2002.
- [15] Ben Kröse, Roland Bunschoten, Stephan Ten Hagen, Bas Terwijn, and Nikos Vlassis. Household robots look and learn: environment modeling and localization from an omnidirectional vision system. *IEEE Robotics & Automation Magazine*, 11:45–52, December 2004.
- [16] Bor-Woei Kuo, Hsun-Hao Chang, Yung-Chang Chen, and Shi-Yu Huang. A light-and-fast slam algorithm for robots in indoor environments using line segment map. *Journal of Robotics*, 2011:12, 2011.
- [17] U. Larsson, J. Forsberg, and A. Wernersson. Mobile robot localization: integrating measurements from a time-of-flight laser. *IEEE Transactions on Industrial Electronics*, 43(3):422–431, June 1996.
- [18] Martin Lauer, Sascha Lange, and Martin Riedmiller. Calculating the perfect match: an efficient and accurate approach for robot self-localization. In *Robocup 2005: Robot soccer world cup IX*, pages 142–153. Springer, 2006.
- [19] P. Oliveira. Interpolation of signals with missing data using pca. In *IEEE International Conference on Acoustics, Speech and Signal Processing (ICASSP 2006)*, volume 3, page III, Toulouse, France, May 2006.
- [20] P. Oliveira and L. Gomes. Interpolation of signals with missing data using principal component analysis. *Multidimensional Syst. Signal Process.*, 21(1):25–43, March 2010.
- [21] Paulo Oliveira. MMAE terrain reference navigation for underwater vehicles using PCA. *International Journal of Control*, 80(7):1008–1017, July 2007.
- [22] Davide Scaramuzza, Friedrich Fraundorfer, and Roland Siegwart. Real-time monocular visual odometry for on-road vehicles with 1-point ransac. In *IEEE International Conference on Robotics and Automation (ICRA2009)*, pages 4293–4299, Kobe, Japan, May 2009.
- [23] Wolfram Burgard Sebastian Thrun and Dieter Fox. *Probabilistic Robotics*. Intelligent Robotics and Autonomous Agents. MIT Press, August 2005.
- [24] C. Siagian and L. Itti. Biologically inspired mobile robot vision localization. *IEEE Transactions on Robotics*, 25(4):861–873, August 2009.
- [25] J. Stowers, M. Hayes, and A. Bainbridge-Smith. Altitude control of a quadrotor helicopter using depth map from microsoft kinect sensor. In *IEEE International Conference on Mechatronics (ICM 2011)*, pages 358–362, Istanbul, Turkish, April 2011. IEEE.
- [26] De Xu, Liwei Han, Min Tan, and You Fu Li. Ceiling-based visual positioning for an indoor mobile robot with monocular vision. *IEEE Transactions on Industrial Electronics*, 56(5):1617–1628, May 2009.

# TIGRE - An autonomous ground robot for outdoor exploration

Alfredo Martins, Guilherme Amaral, André Dias, Carlos Almeida, José Almeida, Eduardo Silva  
INESC TEC Robotics Unit

ISEP - School of Engineering Polytechnic Institute of Porto  
Email: aom, gsilva, adias, c.almeida, jma, eaps@lsa.isep.ipp.pt

**Abstract**—In this paper we present an autonomous ground robot developed for outdoor applications in unstructured scenarios. The robot was developed as a versatile robotics platform for development, test and validation of research in navigation, control, perception and multiple robot coordination on all terrain scenarios. The hybrid systems approach to the control architecture is discussed in the context of multiple robot coordination. The robot modular hardware and software architecture allows for a wide range of mission applications. A precise navigation system based on high accuracy GPS is used for accurate 3D environment mapping tasks. The vision system is also presented along with some example results from stereo target tracking in operational environment.

## I. INTRODUCTION

In this work we present an autonomous ground vehicle for outdoor exploration. The robot was designed in order to provide a versatile platform for multiple application robotics research in outdoor land scenarios.

A large volume of research has addressed the applications of unmanned ground vehicles in outdoor scenarios and the problems posed are as diverse as motion control, localization, mapping, planning, perception or decision making or artificial intelligence oriented ones [1]. Outdoor land robots can be useful in safety and security applications (both civilian and military), in surveillance and patrolling tasks, in reconnaissance, agriculture, exploration and mapping, for cargo, human transport and logistics support, in establishing communication links or in search and rescue operations.

These applications have different sets of requirements leading to the existence of multiple robotic dedicated solutions. Many mobile research platforms ranging from commercial solutions [2] to custom research lab developed ones [3], [4], [5] are available.

One area of active research and with strong impact is search and rescue applications [6]. Multiple robot approaches with heterogeneous capabilities [7] have been proposed, leading to developments in multi-robot coordination.

In the outdoor field robotics scenario, the European Land Robot Competition (ELROB) [8] has been fostering the development of outdoor mobile robots mainly for security in surveillance and patrol tasks and for transport support.

For (ELROB) scenarios (outdoor natural environments) UGVs are developed based on medium or full sized all terrain vehicles [3], [7], [4] in order to operate in the relatively large operation areas and be able to carry a suitable set of sensors.

The TIGRE (Terrestrial Intelligent General purpose Robotic Explorer) robot is a vehicle of this class. It is also based on an all terrain vehicle and combines autonomous drive robot

capabilities, such as GPS based navigation, road and terrain classification for motion planning, vision and laser rangefinder obstacle avoidance with outdoor manoeuvrability and specific surveillance sensors such as infra-red vision. Three main guidelines structured the development: capability of operation in medium size areas, to act as research platform in multi-robot coordination in outdoor environments and to support robotic research in particular areas of field robotics such as underground navigation or precise 3D environment modelling.

The navigation system uses high precision GPS for outdoor localization, with particular relevance in missions for precise 3D modelling and the system has also the possibility of using additional higher quality INS sensors for operation in GPS deprived areas. A high precision 3D LIDAR can also be incorporated for modelling tasks allowing the test and development of new modelling and navigation solutions.

In the following sections the TIGRE hardware is described followed by the software architecture. Guidance and control aspects are addressed in section IV. Next, the localization system is described followed by the vision system architecture. Some results from missions in target detection and localization are presented in section VI followed by concluding remarks and future works.

## II. HARDWARE

This system is based on a electric propulsion all-terrain vehicle equipped onboard processing (Intel i5 based single board computer, ), wireless communications (IEEE 802.11a Ubiquiti Bullet 5GHz access point), infra-red pan&tilt thermographic camera (L3 ThermoEye 5000), laser rangefinder (SICK LMS-200), a visible spectrum camera pair (Basler aca1300-30gc), precision GPS receivers (Septentrio PolaRx2e and Novatel Smart Antenna) and inertial sensors (Microstrain 3DM).



Fig. 1. TIGRE UGV

Traction is achieved through a brushless DC motor physically connected to the rear axle. The direction is also electri-

cally actuated and uses the Ackerman trapezium geometry. A magnetic encoder provides the absolute direction angle.

Four LiFePO4 batteries are used providing a minimum 4hours of autonomy time assuming a continuous usage at  $1ms^{-1}$  vehicle speed. The vehicle is depicted in figure 1. An aluminium frame with a tower was fixed in the vehicle to support all the sensors. The color GigE cameras were positioned at the tower's top in order to provide a stereo vision (with external synchronized trigger control). The thermographic pan & tilt unit is also fixed on top between the stereo pair along with the IMU. Both the GPS and wireless communication antennas are located at the rear of the tower. At the front of the robot was set the laser range finder unit. The main system electronics is located in a watertight enclosure.

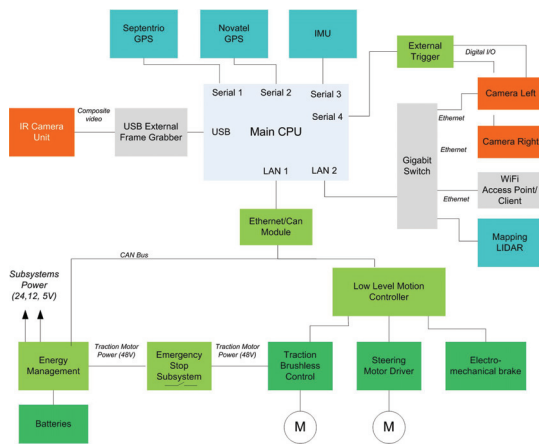


Fig. 2. System architecture

A set of custom made low level vehicle control subsystems (power system control, direction control and traction controller) are connected in a CAN bus. A custom developed Ethernet/CAN interface is used in one of the CPU ethernet ports to provide access to the vehicle CAN bus (see figure 2). In addition, a separate emergency module with a dedicated RF remote is used to cut the traction motors power remotely and/or actuate the mechanical brakes with a small electric actuator.

### III. SOFTWARE ARCHITECTURE

The vehicle software architecture follows a modular and hierarchic structure (see Fig. 3).

Lower level modules provide interface with the sensors and actuators (on top of the various Linux device drivers). The image processing is performed in a pipeline structure with increased abstraction and reduced information [9] at the later stages. In *Multi-camera target detection* identified image targets are combined to produce 3D target candidates. The *Target Selection* phase performs tracking and selection of relevant targets. These are then, either used in the *Guidance control* (for ex: in target following) and/or published to other robots in the team for multi-robot operations.

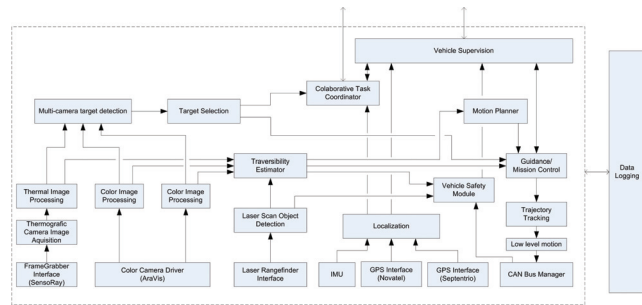


Fig. 3. Software architecture

Image information (color based classification) is combined with detected obstacles with the laser rangefinder to determine the terrain traversability in front of the vehicle. This information is used both in the guidance control implementing the current motion maneuver and in the *Vehicle Safety Module* for emergency stops.

The localization produces a current estimate of the vehicle pose in the world reference frame, from the navigation sensors, namely the IMU and the GPS. This information is used in all the motion control levels (both in *Trajectory Tracking* and *Mission control*) and also sent to other robots in a cooperating scenario. Data logging and remote telemetry can be performed in all the hierarchic levels and software modules.

Motion control is performed by an hybrid system executor (*Mission control*) responsible for generating vehicle trajectories for the *Trajectory tracking*. This module produces vehicle low level velocity and position (steering angle) references sent to the hardware low level motion control through the CANbus.

The software is implemented in multiple processes and runs on the GNU/Linux operating system.

The ROS framework [10] is used, providing both inter-process communications, adding modularity and maintainability and providing set of useful development and implementation tools. There is no direct 1 to 1 mapping in the architecture represented in Figure 3 and the ROS node graph implementation since some modules in figure 3 are implemented in multiple nodes (such as image processing or localization) and parts of the software are not implemented directly in ROS.

The ROS framework still has large restrictions for multi-robot scenarios and also some limitations on the communications latency and overhead. Some solutions have been provided in order to alleviate the problem posed by the need of existence of a centralized ROS master node. These solutions establish some form of communication between the masters running on each robot. But, the intermittent robot connections (usual large areas of operation with robots entering and leaving the team) are not well supported. To solve this problem for multi-robot communications we use the LCM communication middleware [11] in order to publish/subscribe in another robot the topics of the other robots.

Also taking in mind both the multi-robot applications and the need for accurate time synchronization of data, the Linux

Chrony clock-synchronization daemon is used with PPS (pulse per second) information from GPS. This process allows to synchronize the system clock to GPS time and in addition provides multiple robot clock synchronization.

Additionally video streaming (from any of the cameras) is performed by the VLC streamer with MPEG4v codec.

#### IV. NAVIGATION GUIDANCE AND CONTROL

##### A. Control

The vehicle control architecture follows an hybrid systems approach [12] allowing both continuous time control with discrete state evolution. The basic vehicle control maneuvers can be defined as hybrid automata [13]. More complex motion control maneuvers can be obtained by the hierarchical composition of simpler ones. Lower level reactive control can be combined with higher level deliberative planning both in continuous time and by the discrete state transition events occurring (or generated) at the various levels of hierarchy in the maneuvers.

The path tracking used in the basic path following maneuvers (continuous time part) is a simple line of sight controller and is the same used in [14]. The method is a nonlinear feedback function of the cross track error  $e_p$  measured from the center of the front axle to the nearest path point  $(c_x, c_y)$ .

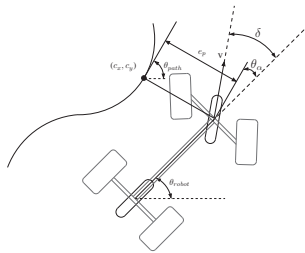


Fig. 4. Path tracking

The first term of the control law simply keeps the wheels aligned with the given path by setting the steering angle  $\delta$  equal to the heading error.

$$e_\alpha = \theta_{robot} - \theta_{path} \quad (1)$$

where  $\theta_{robot}$  is the heading of the vehicle and  $\theta_{path}$  is the heading of the path at  $(c_x, c_y)$ . In the presence of error  $e_p$  a second term adjusts  $\delta$  such that the intended trajectory intersects the path tangent from  $(c_x, c_y)$  at  $k v(t)$  units from the front axle. The resulting of the steering control law is given as

$$\delta(t) = \theta_e + \tan^{-1} \left( \frac{k e_p(t)}{v_x(t)} \right) \quad (2)$$

where  $k$  is a gain parameter.

Rollover is a important concern in the vehicle locomotion due to the vehicle characteristics and possible rough terrain. The robot rollover detection is based on roll angle estimation and on velocity and is prevented by limiting the velocity / steering angle relation).

##### B. Cooperative mission control

In a multi vehicle cooperative setup each vehicle usually provides a high level interface to the team coordination [15]. This can be done in a centralized [15] or distributed [16] ways. Currently there is a strong effort in the research community towards distributed approaches due to advantages in reliability and scalability. In hierarchical coordination approaches [15] higher layers of the vehicle sensing and control infrastructure provide higher level of abstraction information for coordinating purposes. These can be vehicle positions and discrete vehicle states and high level commands.

In TIGRE architecture, multiple vehicle coordination can occur at different levels of hierarchy. Explicit discrete event coordination can occur in a multi-robot setup (such as with other land based robots or with aerial robots) by exchange of coordinating events. These events can be generated at all vehicle control levels and by external entities as other robots. In addition continuous variables (for ex: a particular sensor reading) can be shared between multiple robots leading to tighter multiple vehicle control loops.

Our architecture for multirobot coordination uses an hierarchical approach similar to [15] considering 2 layers, one representing local vehicle control and a multirobot controller. We consider also a coordinating variable  $\xi_i = [\xi_c \ \xi_\sigma]$  and a performance output for each vehicle  $z_i = [z_{i_c} \ z_{i_\sigma}]$  but for these variables we consider not only a continuous part ( $\xi_c$  and  $z_{i_c}$ ) but also an additional discrete part ( $\xi_\sigma$  and  $z_{i_\sigma}$ ). In contrast to the two controllers solution proposed by Beard with a discrete event system supervisor and a team formation continuous controller, our architecture has both the multiple robot coordination and the local vehicle controller as hybrid systems allowing discrete and continuous control both locally and for the robot team.

Each robotic vehicle is described in general as a non linear dynamic system  $S_i$  with states  $x_i$ , inputs  $u_i$  and outputs  $y_i$ .

The local vehicle controller eq.(3) can be viewed as an hybrid system [12] with a set of continuous time flows for each discrete state  $q_i$  and generating the robot control inputs  $u_i$ .

$$C_i : \begin{cases} \dot{x}_{q_i} = f_{q_i}(x_{q_i}, y_i, \xi_c) \\ u_i = b_{q_i}(x_{q_i}, y_i, \xi_c) \\ z_{i_c} = h_{q_i}(x_{q_i}, y_i, \xi_c) \\ q_i = \phi_i(q_i^-, x_{q_i}, y_i, \sigma_i, \xi) \\ z_{i_\sigma} = \varphi_i(q_i, x_{q_i}, y_i, \sigma_i) \end{cases} \quad (3)$$

The discrete state update function  $\phi_i$  depends not only on the states, but also on the vehicle output  $y_i$ , on local set of events  $\sigma_i$  and on the coordinating variable  $\xi$ . The local set of events are produced by guard conditions on discrete state transitions and external events (such as user generated events).

$$M : \begin{cases} \dot{x}_{q_M} = f_{q_M}(x_{q_M}, z_1 \dots z_N) \\ \xi_c = g_{q_M}(x_{q_M}, \sigma_M, z_1 \dots z_N) \\ q_M = \phi_M(q_M^-, x_{q_M}, \sigma_M, z_1 \dots z_N) \\ \xi_\sigma = \varphi_M(q_M, x_{q_M}, \sigma_M) \end{cases} \quad (4)$$

The global team coordination controller  $M$  eq.(4) can also be considered as an hybrid system with both continuous and discrete evolution depending on the performance variables for the  $N$  vehicles and generating the coordination variable.

This approach does not impose any particular multi robot coordination topology allowing both centralized approaches (for instance in mixed initiative missions linked human based Command and Control "C2C" systems) and distributed coordination mechanisms.

From the implementation point of view, the characteristics of the ROS framework [10] allow a large versatility in terms of multi robot cooperation. Without considering the multiple robot scenario ROS limitations referred earlier (currently resolved through the use of additional communication middleware), the software design based on loosely coupled components (such as the ROS computational nodes) allows for information exchange to occur at different vehicle hierarchic levels, and of varying degrees of abstraction (since in the same ROS network, nodes in different robots can publish and subscribe to topics in the same or different robots, whose abstraction level depends on the content and purpose of the publishing nodes).

### C. Localization

The primary navigation sensors are GPS and IMU. The vehicle has two GPS receivers being one of them a precision double frequency (RTK capable) receiver. GPS accuracy is augmented with Precise Point Positioning (PPP) when satellite orbit and timing information is available. PPP [17] uses precise satellite orbits and clock data to reduce errors in single GPS receiver. The satellite orbit information (available in the IGS-International GPS Service) can be used in real time when the vehicle operates with internet access (information updated 4 times per day).

Other method for improving the GPS solution precision, is the use of DGPS- RTK (Differential GPS Realtime Kinematic). This method requires the existence of a known base station whose corrections are sent to the vehicle ("rover"). The vehicle is equipped with a dual-frequency (L1/L2) receiver with RTK corrections achieving high positioning accuracy (in order of few cm). GPS logged raw data can also be post-processed with ultra-precise orbit information achieving subcentimeter accuracy for static positioning.

The vehicle localization state (position and attitude) is given (in most situations) by two separate blocks. The position is obtained directly from the GPS since the vehicle dynamics is relatively slow and the GPS receiver provides high precision at 10Hz rate. The attitude is obtained by the IMU mecanization filtering and magnetic compass readings in order to provide an Attitude Heading Reference System (AHRS). This two blocks can when needed (for instance in higher dynamic situations) be combined in a loosely coupled GPS-INS extended kalman filter to obtain full 6DOF vehicle state.

For navigation in areas where GPS is unavailable, a monocular visual odometry SLAM (Simultaneous Localization And Mapping) navigation method is used [18]. In addition, the

vehicle can use the navigation sensors described in [18] with a tactical grade INS (iMAR iNAV-FMS-E) replacing the MicroStrain 3DM IMU providing much higher quality IMU data.

## V. VISION SYSTEM

The robot vision system is based in a pair of color cameras and an infrared one. The system is used in two types of functions, for situational awareness directly in human super-vised tasks (such as basic video streaming to a remote operator), or in target detection and scene analysis image processing tasks such as intrusion detection and for navigation purposes.

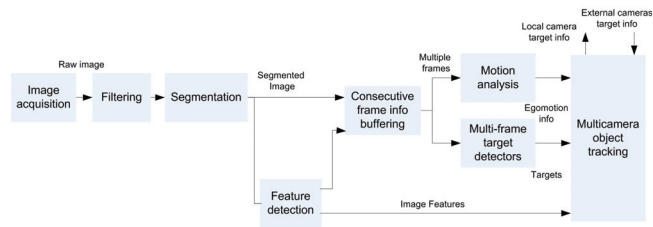


Fig. 5. Vision system

Image acquisition for the color cameras is performed with an external synchronized trigger (in sync with the system clock). This is set at a fixed rate ensuring both the simultaneity of images on the left and right images required for stereo processing and also the frame timestamping needed for other multi-camera processing and for feature based navigation purposes.

The infrared camera 320x240 pixel image is acquired at 30 fps through the USB framegrabber (without external trigger). Currently both color images are captured at maximum resolution (1278x958) and also at 30fps. Each vehicle camera can be used independently or in a multiple camera setup such as conventional stereo arrangement (both color cameras) or in conjunction with the IR one.

Figure 5 presents an overall overview on the vision system architecture. A pipeline structure similar to the architecture presented in [9] is used. For each camera upon acquisition, global filtering can be operated on the image to affect its properties. This type of operation, depending on the particular application can consist in possible multiple options such as sharpening, color adjustments or denoising as examples. In addition for streaming purposes the original raw image can be either logged (this can occur in all pipeline stages) or encoded and transmitted. The possibly processed image is then segmented according to suitable methods (such as color based segmentation, edge detectors or other morphological operators). Region of interest or feature detectors are then applied to the segmented image in order to identify relevant features or targets. Image processing is applied either in a single frame pipeline basis or in a consecutive frame analysis framework. The later type of processing uses multiple

consecutive frames to extract information. Examples of this type of processing are visual odometry computations where the motion information is extracted, consecutive frame stereo calculations or multiframe based target detectors. Target 3D positioning can be determined from multi-camera information. In our case, this can be done with images from the stereo color pair or with one from the infrared camera and other from the color (this can be extended to other cameras). Using the standard pinhole camera model, the image points (for an undistorted image) in homogeneous coordinates are given by:

$$\mathbf{x} = \mathbf{K}[\mathbf{R}|\mathbf{t}]\mathbf{X} \quad (5)$$

where  $\mathbf{K}$  are the intrinsic parameters,  $[\mathbf{R}|\mathbf{t}]$  are the camera extrinsic parameters and  $\mathbf{X}$  is the 3D point in the world frame (usually this is the vehicle body fixed frame). Each camera provides a set of  $\mathbf{x}_i$  points. These, when corresponding to the same real world point can be combined in a multi view geometry to provide  $\mathbf{X}_i$ . To determine the full 3D position it is necessary to make the correspondence between same target points in the different camera images. In classic dense stereo all the image points are possible candidates and computationally efficient methods like RANSAC [19] are applied to determine point position in the epipolar line. The TIGRE vision system assumes a sparse framework. In this case only the relevant points in the image (for ex: target detected points) are processed (also only for these is the distortion removed). For each corresponding pair of target image points ( $\mathbf{x}_1, \mathbf{x}_2$ ) on different cameras (for the same target) the relative 3D positioning is determined by triangulation or by solving the overdetermined system:

$$\begin{cases} \mathbf{x}_1 = \mathbf{K}_1[\mathbf{R}_1|\mathbf{t}_1]\mathbf{X} \\ \mathbf{x}_2 = \mathbf{K}_2[\mathbf{R}_2|\mathbf{t}_2]\mathbf{X} \end{cases} \quad (6)$$

The 3D target detection implementation in the ROS framework is depicted in Figure 6. The offline extrinsic camera parameter calibration is also included.

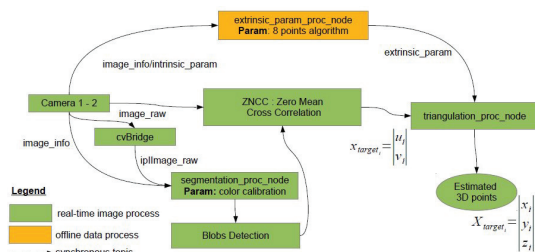


Fig. 6. Vision target detection implementation

## VI. RESULTS

Field tests were performed with the robot in the Oporto City Park. These tests were conducted in relatively easy terrain (grass and earth) due to limitations in the allowed area of operation. Human target tracking and following missions were performed using the stereo color camera pair. The target

position was logged with a precision GPS receiver (identical to the Septentrio one used on the robot).

In addition, a cooperative mission was performed with an aerial autonomous robot (Ashtec's Pelican UAV) where the UAV detected the target and informed the ground vehicle to follow it (for more information see [20]).



Fig. 7. Two frames from the color cameras with the detected target marked

In Figure 7 two images from the color camera taken during the target tracking maneuver, are presented with the detected target marked. Three images from the IR camera during the same maneuver (but not at the same times) are also shown in figure 8. The human target was wearing a red vest to facilitate detection on the low powered UAV onboard processor. Although this is not a realistic assumption, the detection on the UGV can be performed by more advanced methods and also on the thermographic camera [21], and for the UAV further developments must be pursued in the implementation on the limited resources of realistic vision human target detectors.

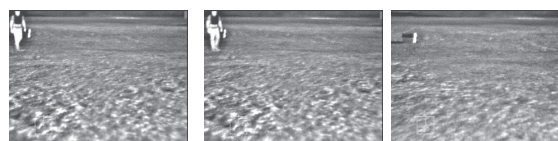


Fig. 8. Thermographic camera snapshots

In figure 9 the detected target positions (using the color camera stereo pair), robot trajectory and real target trajectory are indicated for a segment of the tracking maneuver when the robot is approaching the target and stopping afterwards.

## VII. CONCLUSIONS

In this work is presented the TIGRE autonomous ground vehicle. The robot was developed for outdoor exploration and to be a versatile robotics research platform. Applications scenarios envision security tasks, precise mapping, cooperative missions with other autonomous robots, and operation in unstructured environments such as underground. The vehicle hardware solutions are described along with the comprehensive set of sensors. A hybrid systems approach was followed in the vehicle control architecture. Basic motion control is performed by hybrid (discrete and continuous) maneuvers. These are composed in hierarchical finite (for the discrete state) automata providing more complex motion functionalities. The software implementation aspects were also addressed. An overall overview for the vision system is presented along with a particular use for stereo target tracking. The robot

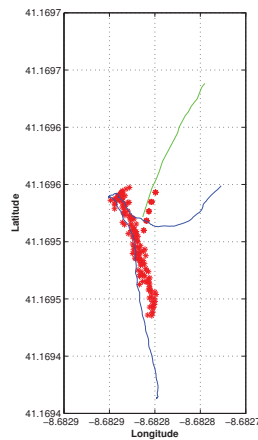


Fig. 9. Target tracked positions (blue-target position, green-robot trajectory, red- vision based target localization)

has already performed missions in operational environment both alone and also in cooperation with an unmanned aerial robot. Some demonstrative results from missions performed in outdoor scenario are also presented.

An extensive future work is envisioned for further development. Applications of visual odometry and visual features navigation are to be tested in multiple scenarios. The multi-robot cooperative framework is to be validated in missions with additional multiple heterogeneous robots, and issues like hybrid systems stability properties in the coordination should be analysed. Integration of new sensors is also to be pursued, namely fast 3D Lidar for obstacle avoidance. These developments are to be considered in a overall goal of achieving long term autonomy in hostile and unstructured outdoor environments. In the immediate future this vehicle will participate in this year Euroathlon trials (an European Union funded initiative for field robotics trials and competitions), were new results under development in navigation and perception are to be validated.

#### ACKNOWLEDGMENTS

The authors acknowledge the support given by the ISEP-IPP and INESC TEC to this project. This work is financed by the ERDF - European Regional Development Fund through the COMPETE Programme and by National Funds through the FCT - Portuguese Foundation for Science and Technology within project FCOMP-01-0124-FEDER-022701 and under Perception-Driven Coordinated Multi-Robot Motion Control Project with reference PTDC/EEA-CRO/100692/2008.

#### REFERENCES

[1] K. Berns, K.-D. Kuhnert, and C. Armbrust, "Off-road Robotics: An Overview," *KI - Künstliche Intelligenz*, vol. 25, no. 2, pp. 109–116, Mar. 2011.  
 [2] S. Ioannou, K. Dalamagkidis, K. P. Valavanis, E. K. Stefanakos, and P. H. Wiley, "On Improving Endurance of Unmanned Ground Vehicles: The ATRV-Jr Case Study," in *2006 14th Mediterranean Conference on Control and Automation*. IEEE, Jun. 2006, pp. 1–6.

[3] C. Armbrust, M. Proetzsch, and K. Berns, "Behaviour-Based Off-Road Robot Navigation," *KI - Künstliche Intelligenz*, vol. 25, no. 2, pp. 155–160, Feb. 2011.  
 [4] L. Bascetta, D. Cucci, G. Magnani, and M. Matteucci, "Towards the implementation of a MPC-based planner on an autonomous All-Terrain Vehicle," in *2012 IEEE/RSJ International Conference on Intelligent Robots and Systems, IROS 2012 - Workshop on Robot Motion Planning: Online, Reactive, and in Real-time*, Vilamoura, Portugal, Oct. 2012.  
 [5] M. Sapharishi, C. Spence Oliver, C. Diehl, K. Bhat, J. Dolan, A. Trebi-Ollennu, and P. Khosla, "Distributed surveillance and reconnaissance using multiple autonomous ATVs: CyberScout," *IEEE Transactions on Robotics and Automation*, vol. 18, no. 5, pp. 826–836, Oct. 2002.  
 [6] R. R. Murphy, "Findings from NSF-JST-NIST Workshop on Rescue Robotics," in *2010 IEEE Safety Security and Rescue Robotics*. IEEE, Jul. 2010, pp. 1–4.  
 [7] L. Kuhnert, M. Ax, M. Langer, D. N. Van, and K.-d. Kuhnert, "Absolute high-precision localisation of an unmanned ground vehicle by using real-time aerial video imagery for geo-referenced orthophoto registration," *Autonome Mobile Systeme 2009, Informatik Aktuell*, pp. 145–152, 2009.  
 [8] F. E. Schneider, D. Wildermuth, and I. Processing, "European Land Robot Trial ( ELROB ) Towards a Realistic Benchmark for Outdoor Robotics," in *Proceedings of the 1st international conference on Robotics in Education, RiE2010*. FEI STU, Slovakia, 2007, pp. 65–70.  
 [9] H. Silva, J. M. Almeida, L. Lima, A. Martins, and E. Silva, "A Real Time Vision System for Autonomous Systems: Characterization during a Middle Size Match," in *RoboCup 2007: Robot Soccer World Cup XI*, ser. Lecture Notes in Computer Science, U. Visser, F. Ribeiro, T. Ohashi, and F. Dellaert, Eds. Berlin, Heidelberg: Springer Berlin Heidelberg, 2008, vol. 5001, pp. 504–511.  
 [10] M. Quigley, K. Conley, B. P. Gerkey, J. Faust, T. Foote, J. Leibs, R. Wheeler, and A. Y. Ng, "ROS: an open-source Robot Operating System," in *ICRA Workshop on Open Source Software*, 2009.  
 [11] A. Huang, E. Olson, and D. Moore, "Lightweight Communications and Marshalling for Low-Latency Interprocess Communication," MIT, Tech. Rep., 2009.  
 [12] J. Ding, J. Gillula, H. Huang, M. Vitus, W. Zhang, and C. Tomlin, "Hybrid Systems in Robotics," *IEEE Robotics & Automation Magazine*, vol. 18, no. 3, pp. 33–43, Sep. 2011.  
 [13] R. Alur, C. Courcoubetis, T. A. Henzinger, and P.-H. Ho, "Hybrid Automata: An Algorithmic Approach to the Specification and Verification of Hybrid Systems," in *Hybrid Systems*, R. L. Grossman, A. Nerode, A. P. Ravn, and H. Rishel, Eds. Springer-Verlag, 1993, vol. 736, pp. 209–229.  
 [14] S. Thrun, M. Montemerlo, H. Dahlkamp, D. Stavens, A. Aron, J. Diebel, P. Fong, J. Gale, M. Halpenny, G. Hoffmann, K. Lau, C. Oakley, M. Palatucci, V. Pratt, P. Stang, S. Strohband, C. Dupont, L.-e. Jendrosseck, C. Koelen, C. Markey, C. Rummel, J. V. Niekerk, E. Jensen, P. Alessandrini, G. Bradski, B. Davies, S. Ettinger, A. Kaehler, A. Nefian, and P. Mahoney, "Stanley : The Robot that Won the DARPA Grand Challenge," *Journal of Field Robotics*, vol. 23, no. April, pp. 661–692, 2006.  
 [15] R. Beard, J. Lawton, and F. Hadaegh, "A coordination architecture for spacecraft formation control," *IEEE Transactions on Control Systems Technology*, vol. 9, no. 6, pp. 777–790, 2001.  
 [16] H. Li, F. Karray, and O. Basir, "A Framework for Coordinated Control of Multiagent Systems and Its Applications," *IEEE Transactions on Systems, Man, and Cybernetics - Part A: Systems and Humans*, vol. 38, no. 3, pp. 534–548, May 2008.  
 [17] K. Chen and Y. Gao, "Real-Time Precise Point Positioning Using Single Frequency Data," in *Proceedings of the ION GNSS 18th International Technical Meeting of the Satellite Division*, Long Beach, USA, 2005, pp. 13–16.  
 [18] A. Ferreira, J. M. Almeida, and E. Silva, "Application of Visual-Inertial SLAM for 3D Mapping of Underground Environments," in *2012 IEEE/RSJ International Conference on Intelligent Robots and Systems - Workshop on Planning, Perception and Navigation for Intelligent Vehicles*, Vilamoura, Portugal, 2012.  
 [19] R. Hartley and A. Zisserman, *Multiple View Geometry in Computer Vision*. Cambridge: Cambridge University Press, 2003.  
 [20] "PCMMC Multi-Robot Coordinated Outdoor Experiments video." [Online]. Available: <http://www.youtube.com/watch?v=McDQ6S5Qxc>  
 [21] J. Han and B. Bhanu, "Fusion of color and infrared video for moving human detection," *Pattern Recognition*, vol. 40, no. 6, pp. 1771–1784, Jun. 2007.

# Robot@Factory: Localization Method Based on Map-Matching and Particle Swarm Optimization

Andry Maykol G. Pinto, A. Paulo Moreira and Paulo G. Costa  
INESC TEC - INESC Technology and Science,  
Faculty of Engineering, University of Porto, Portugal  
Email: andry.pinto@fe.up.pt, amoreira@fe.up.pt and paco@fe.up.pt

**Abstract**—This paper presents a novel localization method for small mobile robots. The proposed technique is especially designed for the Robot@Factory which is a new robotic competition presented in Lisbon 2011. The real-time localization technique resorts to low-cost infra-red sensors, a map-matching method and an Extended Kalman Filter (EKF) to create a *pose tracking* system that is well-behaved. The sensor information is continuously updated in time and space through the expected motion of the robot. Then, the information is incorporated into the map-matching optimization in order to increase the amount of sensor information that is available at each moment. In addition, a particle filter based on Particle Swarm Optimization (PSO) relocates the robot when the map-matching error is high. Meaning that the map-matching is unreliable and robot is lost. The experiments conducted in this paper prove the ability and accuracy of the presented technique to localize small mobile robots for this competition. Therefore, extensive results show that the proposed method have an interesting localization capability for robots equipped with a limited amount of sensors.

## I. INTRODUCTION

The localization is perhaps the most critical aspect for robot navigation because the robot must be aware of its *pose* (position and orientation) to accomplishing all the tasks with safety. The localization method proposed in this article resorts to low-cost sensors whose information is temporary and spatially updated using the dead-reckoning (odometry). This creates a local map of the robot's surrounding environment. Therefore, the localization is accomplished by correlating the local and the global map (the map of the entire environment). The correlation of both maps is made by a map-matching procedure. An extended kalman filter (EKF) combines the dead-reckoning and map-matching estimations, leading to a reliable *pose tracking*. A particle filter based on particle swarm optimization (PSO) is also used by the localization technique to increase their robustness. The PSO performs the *global localization* if the map-matching algorithm is unable to correctly estimate the robot's pose, for instance, when the matching error is high.

Contributions of this articles include:

- An innovative and suitable localization technique for small robotics competitions since it allows a reliable and accurate pose estimation with cost effective sensors;
- Updating the sensor information (temporal and spatial) using the dead-reckoning. This increases the performance of map-matching procedure and, by consequence, the accuracy of the pose tracking;

- Particle filter based on PSO formulation allows to recover the robot from wrong pose estimations (global localization);
- Extensive evaluation of the proposed technique.

The experimental results include the performance and accuracy characterization for the proposed technique, using one autonomous guided vehicle (AGV) equipped with only four infra-red distance sensors in the official Robot@Factory environment<sup>1</sup>. The article is organized as follows. Section II presents the related works and section III explains the proposed localization technique. The section IV presents an extensive set of experiments and the results for several parameter configurations. Finally, section V shows the main conclusions about the proposed method.

## II. RELATED WORK

The literature about indoor localization of mobile robots is long and rich because there are several localization techniques to handle the localization problem: *pose tracking*, *global localization* and *kidnapped*. Probabilistic methods based on Bayes Filters are the most common approaches to deal with the localization. Bayes Filter use the recursive property to obtain the conditional probability distribution of the state space. Several Bayesian methods can be found, namely: kalman filter [11] [8], Markov [3] [2] and particle filters [4] [9] [17]. Localization methods based on map-matching are intuitive to Humans because they usually rely on maps to plan their navigation. Although, these methods require high level cognitive processes to interpret maps and, commonly, a large amount of sensor information creates a well defined local map [14]. The simultaneous localization and mapping (SLAM) is often used to solve the localization problem in unknown environments since it is based on two related steps: map modeling and localization. The work presented by Ethan Eade and Tom Drummond et al. (2009) [5] uses artificial vision systems to map the environment. The extraction and identification of visual features from monocular images, for instance, edges and borders, creates the map by an association process. A SLAM technique for navigation of a robot team (cooperation tasks) is presented in [15]. The SLAM method is based on artificial vision for feature extraction of 3D landmarks (global position). In addition, a "Rao-Blackwellized" particle filter is used for fusing landmark measurements. They claim that mapping-based approaches for autonomous mobile robots

<sup>1</sup>The Robot@Factory was presented in the 11th International Conference on Mobile Robots and Competitions, ROBOTICA 2011, Lisbon.

are rewarding techniques since the map can also be used for high-level tasks. SLAM approaches are, usually, applied to static environments during the inference process (mapping) because it is more difficult to correlate features that represent moving objects. An updating approach is proposed by [6]. The approach is based on several steps to detect when the map changes (based on a weighted averaging). Consequently, it creates a local map that is used to update the global map, after a proper consistent analysis and alignment process. Two localization methods that resort to laser range finders can be found in [7] and [18]. In the last research, the vertexes obtained from the laser data are considered as features and compared against the vertexes available in the global map. The major problem of this approach is related to their performance since it is affected by the inaccuracy of the extracted vertexes.

### III. APPROACH

The localization method proposed by this paper relies on a fully-known metric map of a robotic competition. The indoor localization method uses an improved version of a map-matching algorithm whose original concept is based on [12]. The original algorithm was developed for the RoboCup competition and it resorts to an omni-directional camera to detect the transition points between white lines and the green field. Thus, the matching procedure uses the robot's distance to those points. The approach proposed in [12] have some limitations related with the amount and quality of the sensor information since small or poor data leads to an unsatisfactory convergence between local and global map [13]. Relevant improvements are proposed to increase the localization's robustness of robots with few low-cost sensors, namely: A temporal approach that updates the past information of sensors based on dead-reckoning which increases the amount of data that is available for matching; A particle filter based on particle swarm optimization generates pose estimations whenever the matching error is large. Therefore, the algorithm updates the sensors values using the odometry in order to improve the convergence of matching. The pose estimation that is obtained by the map-matching or the PSO is fused with the dead-reckoning using an EKF (based on the covariance since it measures the confidence of each pose estimative). When the map-matching error is high, meaning a low confidence in the current estimative, the PSO starts with the goal of re-localize the robot. Therefore, a set of particles are released over the global map to search the space in order to find a result with high confidence. A general overview of the localization technique is presented in figure 1. The map-matching with the temporal updating and the EKF creates a reliable *pose tracking*. In addition, the particle swarm optimization allows the robot to recover from an erroneous pose estimation.

#### A. Pose tracking

An improved version of the map-matching technique [12] does not use an omni-directional camera to detect transition points in a soccer field like in [12] however the information is provided by infra-red sensors and converted to the navigation (Cartesian) coordinates. The developed algorithm is computationally efficient because it keeps available all the necessary information about the environment. It uses complex matrices to represent the distance and gradient maps. The pose estimation

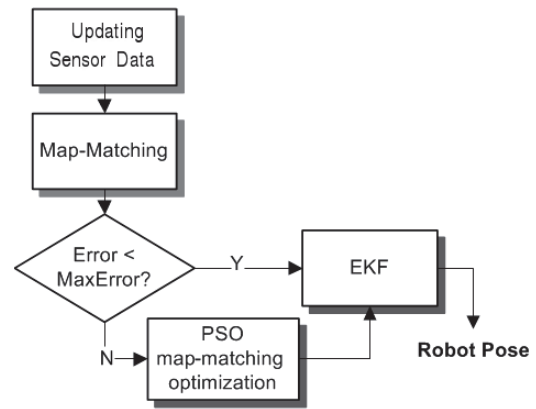


Fig. 1. Schematic of the localization algorithm.

is accomplished by a minimization of an error function using the RPROP (*Resilient Propagation*). The optimization method requires the knowledge of the first derivatives (gradient maps) relative to the robot position and orientation, for instance, distance and gradient matrices. Briefly, the environment where the robot travels must be known and discretized. Thus, a distance map (distance from each cell to the nearest wall or obstacle) is obtained by common distance algorithms, see figure 2. The black pixel represents obstacles and lighter gray pixel means higher distance. The minimization of a cost function [12] gives the robot's pose that best fits in the current sensor data. Therefore, the cost is an error function based on the distance between each sensor point and the nearest natural markers.

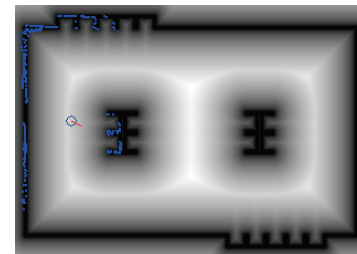


Fig. 2. Example of a distance map with a representation of the proposed localization technique (spatial and temporal updating process). The robot's position and orientation are depicted in the image (blue circle with a red line to indicate the front).

Additionally, two more maps must be calculated (the gradient maps). They reflect the changes of distance relative to each Cartesian axis. The maps are calculated only once which makes the computation of the cost function (map distance) and first derivatives (gradient maps), needed by the minimization technique, very fast and efficient. Therefore, the steps for map-matching are: calculation of the cost error function by using the current sensors points and the distance map. The first order derivatives of the error function (gradient maps) are then used by the RPROP to obtain the pose estimation.

There are cases when the minimization is unreliable, namely, when the cost function is flat (the sensor information is insufficient to characterize the environment) and when the cost function displays a minimum around the saddle (the localization component in one direction is well defined however, the

sensor information does not characterize well the orthogonal component). Therefore, an unambiguously description of the robot's surrounding environment is essential for an accurate pose estimation. This can be achieved only with a reasonable quantity and quality of sensor data, for example, using laser range finders. However, expensive sensors limits the localization of small robots in our context since the goal of the Robot@Factory competition is to introduce robotic concepts to younger teams and, therefore, simple and cheap solutions are preferred.

### B. Updating sensor data

This article proposes updating in time and space the sensor information by using the dead-reckoning. In this way, the amount of sensor information increases, even if an insufficient number of sensors are available. Updating the sensor information improve the minimization of the cost function and, thus, has a great applicability because it reduces the number of sensors that must be used (or a laser range finder solution).

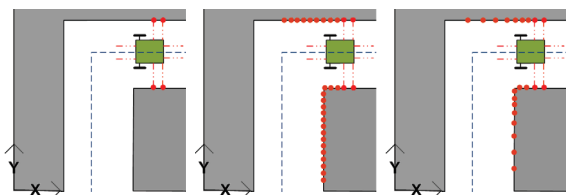


Fig. 3. Schematic of the robot without and with the sensor data updating, left and center images respectively. The right image presents the dynamic data that is obtained in a similar way to the center image however, the concentration is less for older sensor points.

Figure 3 (on left) presents the current sensor information (red points) where the number of sensors is insufficient to characterize the surrounding environment, as can be noticed. Figures 3 (center) and (right) show two local maps (the set of orange and red points) that are created by the same number of sensors however considering spatial and temporal updating. In both figures, the amount of sensor information available at each moment is sufficient to characterize the local environment. Figure 3 (center) depicts the spatial updating and figure 3 (right) the spatial and temporal updating. Considering only spatial updating, older points have the same contribution than newer points. Temporal updating reduces the temporal concentration for older points, decreasing the influence of the dead-reckoning's error in the matching process and, therefore, newer sensor positions are continuously updated while older points are removed.

The number of sensor points that is used to characterize the local map must be limited to avoid an excessive complexity of the minimization procedure. In addition, the data concentration must be adjusted according to the environment to make possible a concentration of data that is higher for recent points and lower for more older points. This focuses the map-matching on the recent points and, consequently, the estimation process is more accurate. The updating algorithm, see figure 1, converts each sensor distance to the XY coordinates (by knowing the relative position and orientation of each sensor). Thus, the linear and angular velocity of the robot are fundamental to determine the new sensor position. The longest distance between robot and sensor point must be

defined and the updating process individually applied to the sensor information of each robot's side in order to ensure an equilibrium of information. The concentration of data is defined by configuring the range between consecutive sensor points, in other words, sensor points are selected as function of relative distance and until a maximum number of points is reached.

### C. Estimate Fusion: EKF

The dead-reckoning is accurate for small robot's displacements and, hence, the EKF is a commonly used to combines the map-matching and the odometry in order to obtain a reliable pose estimation. Due to the lack of space, only the relevant aspects of the EKF are defined. Equation 1 presents the kinematic nonlinear model of the differential robot which is used by the EKF:

$$\begin{bmatrix} x_{k+1} \\ y_{k+1} \\ \theta_{k+1} \end{bmatrix} = \begin{bmatrix} x_k + v_k \times \Delta_T \times \cos\left(\theta_k + \frac{w_k \times \Delta_T}{2}\right) \\ y_k + v_k \times \Delta_T \times \sin\left(\theta_k + \frac{w_k \times \Delta_T}{2}\right) \\ \theta_k + w_k \times \Delta_T \end{bmatrix} \quad (1)$$

were the state vector is the robot's pose ( $x_k, y_k$  and  $\theta_k$  are the position in Cartesian coordinates and orientation, respectively). The  $v_k$  and  $w_k$  are the control inputs (linear and angular velocity, respectively) and  $\Delta_T$  is the time between consecutive calculations. At time  $k$ , the observation is  $z_k = [x_k^z, y_k^z, \theta_k^z]^T$  and it is obtained from the map-matching localization. The covariance matrix of the state error is defined by  $Q_k$  and affects the position and orientation of the robot. Considering that the state noise are independent [16] then the covariance matrix that models the odometry's error is diagonal and defined in [16]. The observation covariance matrix,  $R_k$ , is defined similar to [16]. Its diagonal elements are obtained by the confidence of the map-matching procedure. In each cycle, the second derivative of the cost function related to  $x$ ,  $y$  and  $\theta$  and the precomputed gradient maps are used to obtain the  $var(err_x)$ ,  $var(err_y)$  and  $var(err_\theta)$ . Thus, the  $R_k$  is non-constant and reflects a reliability measure of the matching.

$$R_k = \begin{bmatrix} var(err_x) & 0 & 0 \\ 0 & var(err_y) & 0 \\ 0 & 0 & var(err_\theta) \end{bmatrix} \quad (2)$$

The robot's kinematic model is used to predict the state based on the linear and angular velocity. The correction of the priori estimative is performed with the map-matching estimations. This decreases of the state covariance if the map-matching estimative is reliable.

### D. Particle Swarm Optimization

The PSO technique uses particles (with pose and velocity) to search the environment space looking for better solutions [10]. Each particle adjusts their speed according to its personal solution and current best solution considering the entire swarm, i.e., a neighborhood relationship is defined. On a single iteration ( $i$ ), each particle is attracted to its best solution (personal best,  $pBest$ ) and the better solution of their neighborhood (global best,  $gBest$ ). Thereby, the speed  $V$  and

pose  $p = (x, y, \theta)$  of each particle is dynamically adjusted according to its current pose, velocity and distances between its current pose,  $pBest$  and  $gBest$  (see the particle evolution in equations 3 and 4).

$$V_i = \phi_1 V_{i-1} + \phi_2 r_1 (pBest - p_{i-1}) + \phi_3 r_2 (gBest - p_{i-1}) \quad (3)$$

$$p_i = p_{i-1} + V_i \quad (4)$$

were  $V_i = [v_x, v_y, w]^T$  is the linear velocity in both Cartesian axes and angular velocity at iteration  $i$ . The parameter  $\phi_1 = [\phi_{1x}, \phi_{1y}, \phi_{1\theta}]^T$  controls the inertia factor (is usually set to  $< 1$  for convergence),  $\phi_2 = [\phi_{2x}, \phi_{2y}, \phi_{2\theta}]^T$  the personal influence weights and  $\phi_3 = [\phi_{3x}, \phi_{3y}, \phi_{3\theta}]^T$  the social influence weights. Usually, the  $\phi_2 + \phi_3 = 4$  [10]. The orientation difference must be normalized to maintains the orientation in the range  $(-\pi, +\pi)$ . Each scalar  $r_i$  is a uniform random number between (0,1) and gives a stochastic characteristic to the PSO.

The PSO model allows the robot to re-localize itself in anomalous situations because a high matching error triggers the global localization mechanism. In more detail, the algorithm starts by initializing each particle pose and velocity. The particles search for solutions around the last well known pose in order to increase the convergence rate. Initially, particle velocities are considered to be random and under no circumstances the particle's pose can leave the map. After the initialization, the objective function is calculated for each particle (since it gives a solution) and  $pBest$  and  $gBest$  are both updated. Finally, the linear and angular velocities ( $v_x$ ,  $v_y$  and  $w$ ) of each particle are calculated and then, the pose of the particle is updated. The algorithm ends when a reasonable solution is found, for instance, a solution with low matching error.

#### IV. PRACTICAL RESULTS

##### A. Robot@Factory

Robot@Factory is a new competition introduced during the 11th Portuguese Robotics Open and it focuses on manufacturing management for one or several AGV's (Automated Guided Vehicles). Their main goals are: produce a specific number of different parts, control the robot navigation and scheduling operation sequences [1]. The factory ( $3 \times 1.88m$ ) consists of an input warehouse with a maximum capacity of five parts, one output warehouse (to store the produced parts), eight production machines where the parts have to be processed according to their operation sequence and one or more AGV's responsible for transporting the parts. There are three different types of parts, each one with a different operation sequence in these machines (at center of the environment). It is important to notice that, each machine can only process one part at time and it has different operation times according to the type of part being processed [1]. For helping participants to prepare the competition, an official Robot@Factory environment based on SimTwo<sup>2</sup> which is a powerful simulation environment

that resorts to well established libraries, for instance, Open Dynamic Engine (ODE) for simulating rigid body dynamics and GLScene which is a 3D library based on OpenGL (Open Graphics Library). This simulation platform faithfully represents the real competition environment since the driving systems, the sensors, the mechanical and physical properties of bodies are precisely modeled, figure 4. The simulation platform has also several advantages because it allows to conduct realistic navigation procedures and the real localization information (ground truth) of the robot can be obtained and compared against the performance of the proposed localization technique.

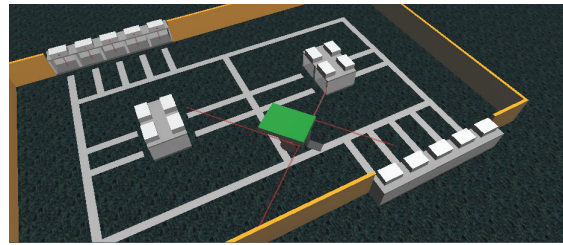


Fig. 4. Official Simulation Environment for the Robot@Factory competition.

A differential robot ( $0.30 \times 0.22m$ ) with four infra-red sensors located in the front, both sides and, finally, on the back, is used during the conducted experiments (see figure 4). For modeling the infra-red error, a real sensor SHARP - GP2Y0A21 is considered whose effective range is between 0.10m and 0.80m. After performing precise experiments about the behavior of this sensor during its full range, it is possible to conclude that the error model can be reliably represented by a zero mean Gaussian distribution,  $N(0, \sigma_{IR}^2)$ . Nevertheless, the variance  $\sigma_{IR}^2$  is a function of the measured distance ( $dist$ ) and can be approximated by a third order polynomial function, for instance,  $\sigma_{IR}^2(dist) = |1.01e^{-6}dist^3 - 1.80e^{-5}dist^2 + 1.01e^{-4}dist - 1.47e^{-3}|$  meters. To modeling the dead-reckoning, the  $Q_k$  of the EKF, it was followed the chapter 5 of [16]. The characterization of  $Q_k$  and  $R_k$  is extremely important because it allows a realistic representation of the most important aspects that affects the performance of the proposed localization method. Future experiments will be conducted using a real environment of the Robot@Factory in order to compare the expected performance, presented by this research, with the performance that is obtained by a true robot.

##### B. Performance Analysis

Extensive experiments are conducted with realistic infra-red and odometry errors (previously modeled) in order to evaluate the accuracy and computational cost of the proposed technique. The influence of three localization parameters is analyzed, for instance, the maximum number of sensor points, maximum distance of points to the robot and the concentration distribution of data along space and time. In addition, the performance of the localization is studied for two different navigation paths.

An especial notation allows to follow more easily the conducted experiments. Each trial has one number and one letter. The number  $\{0, 1, 2, 3\}$  represents the maximum number of points  $\{200, 300, 400, 500\}$ , respectively. The letters  $\{A, B, C, D\}$  mean different configurations of data concentration. "A" is the control trial where maximum distance allowed

<sup>2</sup><http://paginas.fe.up.pt/paco/wiki/index.php?n=Main.SimTwo>

is 1m and it has equal concentration of data for older and younger points. "B" represents the same than "A" however, the maximum distance for the points is 1.5m. Experiments "C" and "D" show the performance for different data concentrations. Both represent higher concentration of younger sensor points than "A" and "B" however, the letter "D" represents a trial with lower concentration for older data when compared to "C".

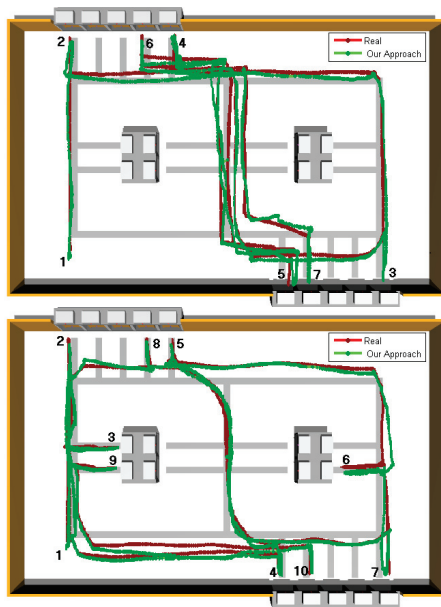


Fig. 5. Experiment 2-C: Path 1 - direct movement between the top and bottom warehouses (top image). Path 2 - indirect movement (bottom image). The localization of the robot obtained by the proposed technique is represented in green and the ground truth in red.

Figure 5 shows the localization of the robot for two navigation paths using the proposed technique with a 2-C configuration. Visually, the pose estimation (green) overrides the ground truth (red) in almost the entire paths. Figure 2 depicts the map-matching process using the updating process (sensor points are represented in blue). The robot is reaching the third step according to the second path of the figure 5 (bottom image). The updating procedure is extremely important for the map-matching because it allows a good characterization of the surrounding environment with only four infra-red sensors.

Figure 6 shows quantitative results that were obtained in both paths and for different configurations. The trial 3-B represents the worst case since the mean error is 0.07m and 4.8° with a standard deviation of 0.06m and 9°. As expected, there are differences between "A", "B", "C" and "D" configurations. Experiments based on "A" and "B" usually have position errors higher than "C" and "D". This is shown in the graph of the position error. The reason for the higher performance of configurations with less concentration of older points is related to the dead-reckoning data that is used by the updating process since more recent points are less affected by the accumulation error. Large number of points or large maximum distance lead to a higher accumulation of errors because the estimation is highly influenced by distant and by older points. This affects minimization process and decreases the matching accuracy. Thereby, parameters must be adjusted according to the environment topology.

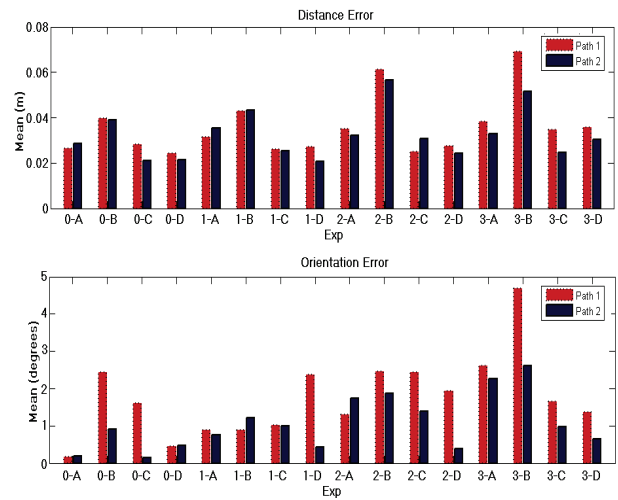


Fig. 6. Graphical representation of the absolute mean (position and orientation) error for several configurations and considering both paths.

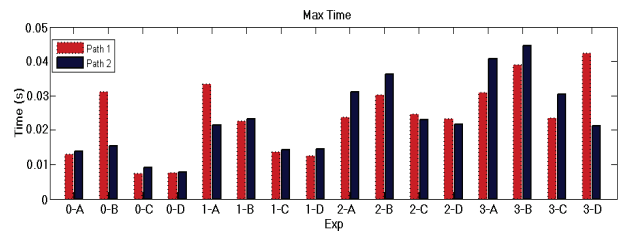


Fig. 7. Longest cycle time for both paths and considering different trials (using a CPU Intel I3 M350, 2.75GHz).

The computational time in each conducted experiment is shown in figure 7. The localization of the robot is usually accomplished in less than 40 milliseconds. Thus, the proposed localization technique reaches a real-time performance however, the amount of sensor data used by the map-matching increases the time spent by the technique to estimate the localization of the robot. By increasing the concentration of younger and closer sensor points the processing time decreases without a negative impact on the overall localization accuracy. Actually, the figure 6 shows lower errors in these situations ("C" and "D").

### C. Particle Swarm Optimization

The PSO was not used in any circumstance during the previous experiments and even for an additional free-path navigation experiment that was conducted for a large period of time (2 hours). Therefore, a pose tracking error is simulated in order to activate the re-localization mechanism. The error consists by adding 0.5m to the x-component, 0.8m to y-component and 90 degrees to the orientation of the current pose. The symmetry of the Robot@Factory environment is a major problem for the PSO formulation since there are at least two possible matching solutions at each time. To avoid this problem, the particles' searching space is initialized to an area around the last pose estimation with a low matching error. The stopping criteria of the PSO is the number of iterations or the map-matching error being lower than a threshold.

The map-matching error is 1m and 90° around the second

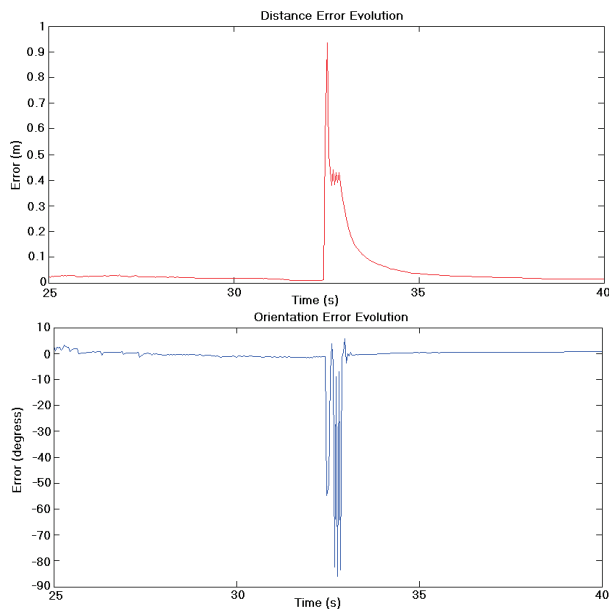


Fig. 8. Distance error evolution (on the top) and orientation error evolution (on the bottom) of the map-matching in a kidnap situation. PSO configured with 15 particles, 30 iterations,  $\phi_1 = 1.2$ ,  $\phi_2 = 1.5$  and  $\phi_3 = 2.5$ .

33, see figure 8. This large error triggers the PSO which in less than 2 seconds reacquires one good pose estimation (the matching error decreases and the robot is relocated again). This two seconds demonstrates the remarkable ability of the PSO to solve the *global localization problem*.

## V. CONCLUSION

A real-time localization technique for the Robot@Factory competition is presented in this paper. It differs from other methods since it combines a map-matching algorithm, spatial and temporal updating procedure and a particle filter based on particle swarm optimization. The spatial and temporal updating procedure increases the amount of sensor information that is available and is used by the map-matching, avoiding the need for many sensors or a laser range finder. The EKF combines the dead-reckoning with the map-matching pose estimation, leading to a reliable *pose tracking*. In addition, the PSO allows to re-locate the robot when the map-matching returns an unreliable pose estimation (the matching error is high) and, thereby, it is an important mechanism that searches the environment looking for a possible solution when the robot is completely lost. The conducted experiments prove the accuracy, flexibility and robustness of the proposed technique since it achieves an error, usually, lower than 0.04m and 2degrees. Extensive experiments also prove the PSO capability to re-locate the robot in anomalous situations. Therefore, several important improvements are proposed in this article to increase the performance of an efficient map-matching algorithm.

## ACKNOWLEDGMENT

This work is partly funded by the Portuguese Government through FCT - Foundation for Science and Technology, SFRH-BD-70752-2010 and by the PRODUTECH PTI Project (no. 13851) - New Processes and Innovative Technologies for the Production Technologies Industry which is funded by the

Incentive System for Technology Research and Development in Companies, under the Competitive Factors Thematic Operational Program of the Portuguese National Strategic Reference Framework and by the EU's European Regional Development Fund.

## REFERENCES

- [1] Andry Maykol Pinto and Luis F. Rocha and Antonio Paulo Moreira and Paulo G. Costa. Shop Floor Scheduling in a Mobile Robotic Environment, In: EPIA 2011 - LNAI 7026 proceedings: Progress in Artificial Intelligence, Springer, 377-391, 2011
- [2] Dieter Fox and Wolfram Burgard and Sebastian Thrun. Active Markov Localization for mobile robots. In: Robotics and Autonomous Systems, 25:195-207, 1998.
- [3] Dieter Fox and Sebastian Thrun and Wolfram Burgard. Markov Localization for Mobile Robots in Dynamic Environments. In: Elsevier Science: Journal of Artificial Intelligent Research, 11:391-427, 1999.
- [4] Dieter Fox and Wolfram Burgard and Frank Dellaert e Sebastian Thrun. Monte carlo localization: Efficient position estimation for mobile robots. In: Sixteenth National Conference on Artificial Intelligence, 25:195-207, 1999.
- [5] Ethan Eade and Tom Drummond. Edge landmarks in monocular SLAM. In: Image and Vision Computing, 27:588-596, 2009.
- [6] Fabrizio Abrate and Basilio Bona and Marina Indri and Stefano Rosa and F. Tibaldi. Map updating in dynamic environments. In: 41st International Symposium on Robotics (ISR), 1-8, 2010.
- [7] Fredy Tungadi, Wen L. Dennis Lui, Lindsay Kleeman and Ray Jarvis. Robust online map merging system using laser scan matching and omnidirectional vision. In: IEEE/RSJ International Conference on Intelligent Robots and Systems (IROS), 7-14, 2010.
- [8] J.J.Leonard and H.F. Durrant-White. A mobile robot localization by tracking geometric beacons. In: IEEE transactions on Robotics and Automation, 3:376-382,1991.
- [9] Jeong Woo and Young-Joong Kim and Jeong Lee and Myo-Taeg Lim. Localization of mobile robot using particle filter. In: SICEICASE International Joint Conference, 10:3031 - 3034, 2009.
- [10] Kronfeld, Marcel and Weiss, Christian and Zell, Andreas. A Dynamic Swarm for Visual Location Tracking. In: 6th International Conference on Ant Colony Optimization and Swarm Intelligence, 203-210, 2008
- [11] L.Jetto and S.Longhi and D.Vitali. Localization of a wheeled mobile robot by sensor data fusion based on a fuzzy logic adapted kalman filter. In: Elsevier Science: Control Engineering Practice, 7:763 - 771, 1999.
- [12] M. Lauer, S. Lange and M. Riedmiller. Calculating the perfect match: an efficient and accurate approach for robot self-localization; Robot Soccer World, In RoboCup 2005, Cup IX , LNCS., Springer, 27:142153, 2005.
- [13] Manuel Gouveia, A. Paulo Moreira, Paulo Costa, Luis P. Reis and Marcos Ferreira. Robustness and precision analysis in map-matching based mobile robot self-localization. IRobot - 14th Portuguese Conference on Artificial Intelligent, EPIA 2009, Aveiro, 4:243-253, 2009
- [14] Mohammed A. Quddus and Washington Y. Ochieng and Robert B. Noland. Current map-matching algorithms for transport applications: State-of-the art and future research directions. In: Elsevier Science: Transportation Research Part C: Emerging Technologies, 15:312-328, 2007
- [15] Monica Ballesta, Miguel Julia, Arturo Gil and Oscar Reinoso. Multi-robot visual slam using a Rao-blackwellized particle filter. In: Elsevier Science: Robotics and Autonomous Systems, 92:68-80, 2010.
- [16] Sebastian Thrun and Wolfram Burgard and Dieter Fox. Probabilistic Robotics, Cambridge (Mass.): MIT Press, first edition, 2005
- [17] Sebastian Thrun and Dieter Fox and Wolfram Burgard and Frank Dellaert. Robust Monte Carlo localization for mobile robots. In: Elsevier Science : Artificial Intelligent, 128:99-141, 2001
- [18] Shung Han Cho and Sangjin Hong. Map Based Indoor Robot Navigation and Localization Using Laser Range Finder. In: International Conference on Control Automation, Robotics and Vision (ICARCV), 1559 - 1564, 2010.

# Multi-Robot Cooperative Stereo for Outdoor Scenarios

A. Dias, J. Almeida, E. Silva

INESC TEC Robotics Unit  
School of Engineering Polytechnic Institute of Porto  
Email: adias, jma, eaps@lsa.isep.ipp.pt

P. Lima

Institute for Systems and Robotics  
Instituto Superior Técnico (IST), Lisbon Portugal  
Email: pal@isr.ist.utl.pt

**Abstract**—In this paper, we propose a cooperative perception framework for multi-robot real-time 3D high dynamic target estimation in outdoor scenarios based on monocular camera available on each robot. The relative position and orientation between robots establishes a flexible and dynamic stereo baseline. Overlap views subject to geometric constraints emerged from the stereo formulation, which allowed us to obtain a decentralized cooperative perception layer. Epipolar constraints related to the global frame are applied both in image feature matching and to feature searching and detection optimization in the image processing of robots with low computational capabilities. In contrast to classic stereo, the proposed framework considers all sources of uncertainty (in localization, attitude and image detection from both robots) in the determination of the objects best 3D localization and its uncertainty. The proposed framework can be later integrated in a decentralized data fusion (DDF) multi-target tracking approach where it can contribute to reduce *rumor propagation* data association and track initialization issues. We demonstrate the advantages of this approach in real outdoor scenario. This is done by comparing a stereo rigid baseline standalone target tracking with the proposed multi-robot cooperative stereo between a micro aerial vehicle (MAV) and an autonomous ground vehicle (AGV).

## I. INTRODUCTION

In recent years, we have seen a growing research effort on novel multi-robot cooperative tasks for heterogeneous mobile robotics applications. This ongoing development is driven by a significant number of potential end-user applications, where is necessary to reduce the human in the loop interaction which includes large-scale sensing operations[12], cooperative search and rescue tasks[5], surveillance[7], recognition reconnaissance and border control[8]. Currently, mobile robots employed on these high-end user applications are equipped with state-of-the art sensing equipment allowing them to navigate and perceive their surrounding environment. One of the most common and versatile means of perception in mobile robotics applications is visual sensing with one or more cameras which are able to acquire visual information[13] based on cooperative approaches. Taking this a step further, here we address an outdoor multi-robot scenario without localization issues, with the surveillance task goal of detecting and estimating 3D high dynamic targets positions behavior in a cooperative vision flexible and dynamic stereo baseline framework.

State of art approaches to enumerated end-user applications can be organized according to cooperative tasks emerged from local or cooperative perception.

In local perception approach, each robot is capable of detecting and locating targets, sharing that information over some communication middleware that can be later used to some cooperative mechanism for task allocations[10].

Considering the proposal scenario, those approaches present several limitations in any possible vision setups: monocular or stereo rig baseline. In monocular vision, we have the intrinsic difficulty in estimating depth and absolute scale[1], so 3D target estimation without target known size is a research challenge. Techniques like SFM(structure-from-motion) or SLAM(Simultaneous localization and mapping) are able to estimate depth from a monocular camera[6][3], but the scene must have a large field of view and motion must not occur along the optical axis and preferably parallax motion to allow a fast uncertainty map convergence[1]. SLAM techniques are able to obtain good results in depth estimation for indoor and even in outdoor map building scenarios although with constraints such as high computational requirements (not available in most of the robots with low payload), lower camera dynamic, preferably with features loop closing and large field of view, but unable to track targets with high dynamic behavior. Still with monocular vision and for a particularly case of aerial vehicles depth estimation can be obtained based on flat earth assumption[2]. Although it is simple, its application is limited to tracking objects on the ground with low accuracy and not applied to our addresses scenario. Regarding stereo rig baseline, 3D target estimation is a well known solution due to its relatively simple image scale and depth estimation although with limited application when the goal is to track targets whose depth distance greatly exceeds the available stereo rig baseline, therefore reducing the stereo setup to a bearing-only sensor[15]. The estimation error grows quadratically with the depth[15][4], becoming even more relevant this limitation when the robot majority tends to decrease its scale factor and consequently smaller rig baseline. The enumerated limitations strengthens our proposal by having a multi-robot monocular approach with a flexible and dynamic baseline between robots able estimate 3D information from correlated detected targets.

Focusing now in cooperative perception approaches, characterized by each robot, available at the multi-robot formation, builds its own local partial representation of the world, described by the belief state and share in order to improve

their knowledge. Some of this methods are: Decentralized Data Fusion(DDF)[11] by incorporating 2D measures possible to be represented by Gaussian Mixture Model(GMM)[9], Cooperative SLAM[14] and for the special case of indoor scenarios a decentralized EKF monocular camera inertial sensor fusion method[1] to recover the relative configuration between monocular cameras. Common to all enumerated methods is the requirement translation of the information received from other robots to the same local representation. This step is critical in order to avoid *rumor propagation* that could lead to overoptimistic estimations. In Cooperative SLAM[14] this problem was considered and solved through the epipolar geometric constraint between cameras. This is part of your proposal in which we detail in section II-C.

### A. The Aim of this Work

We propose a method to estimate the 3D target information based on multi-robot vision bearing-only measurements in outdoor scenarios.

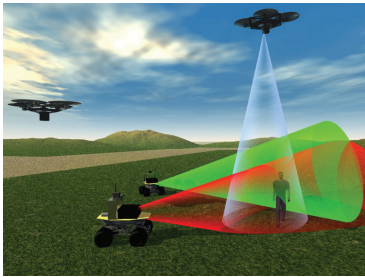


Fig. 1. Multi-Robot Cooperative Stereo

The relative positions and orientations between monocular cameras are allowed to change over time, which means that we are able to form a flexible stereo baseline and establish overlap views based on geometric constraints emerged from the multi-robot collaborative stereo formulation and provide a 3D outdoor localization for multi-targets with high dynamic behavior (see figure 1). The envisioned multi-robot cooperative stereo framework can combine monocular vision information from heterogeneous vision sensors included, but is not limited to, infrared thermographic camera, visible camera and multi-spectral cameras which means that we can have multiple robots cooperating in the same environment and combining the information provided by each vision sensor. As regards DDF target tracking approaches the framework can be applied as layer able to support data association and avoid *rumor propagation* between robots and in the initialization process of new targets.

The paper is organized as follows: in section II we present the multi-robot cooperative stereo framework and detail the developed blocks. Section III describes the outdoor scenario and the vehicles used to obtain the results detailed in section IV, followed by conclusions and future work in Section V.

## II. MULTI-ROBOT COOPERATIVE STEREO FRAMEWORK

The general scheme for the multi-robot cooperative stereo framework is presented and detail in this section.

### A. Notation

Considering the fact that the proposal framework is applied to multiple robots  $n$  with different coordinates frames and during the formulation we will require coordinate transformation matrix from one coordinate (designated by *from*) to another coordinate frame (designated by *to*), we use the following notation:  ${}_{from}^{to}S_n$ . To represent the coordinate transformation, we label  $\{C\}$  for camera frame,  $\{B\}$  for body frame,  $\{N\}$  for navigation expressed in *ENU* (earth-fixed east-north-up) and  $\{W\}$  for global frame expressed in *ECEF* (earth-centered, earth-fixed) coordinate. The upper bold case notation represent matrix, lower bold case vectors and lower case scalar variables.

### B. System Overview

The proposed cooperative stereo framework architecture is outlined in figure 2.

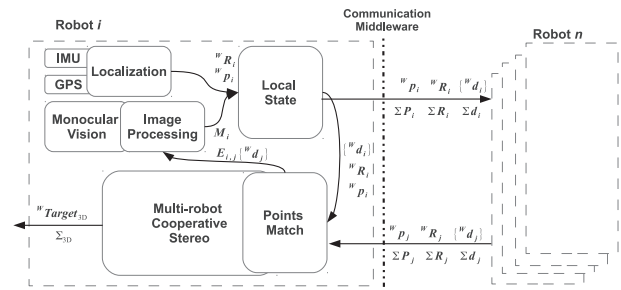


Fig. 2. Multi-Robot Cooperative Stereo Architecture

The architecture is composed by a localization layer responsible for providing to the local state layer the attitude and global frame position of the robot. Although in the current implementation this information came from INS/GPS fusion but could be in the future come from any other localization system. For each camera available in the robot, a image processing block provide the  $\{M_i\}$  with the detected target measurement and the correspond uncertainty. For each image processed the robot share over a middleware communication, with the robot that is sharing the same overlap view, the position  ${}^W p_i$  and orientation of camera  ${}^W R_i$  as well as a list of possible targets measurements  $\{{}^W d_i\}$ . The information provided from other robots is then used by a features correspond block (section II-C). The position and attitude of both robots cameras will establish the essential matrix  $E_{i,j}$  that will define epipolar restrictions between targets pairs. Finally the target pairs are applied to obtain the 3D target measurement  ${}^W \mathbf{Target}_{3D}$  and uncertainty  $\Sigma_{3D}$  as detailed in algorithm 1. Before present the proposed algorithm we will describe for robot  $i$  the variables and inputs depicted in figure 3.

The camera position in the global frame is obtained:

$${}^W p_i = {}^W T_i \cdot {}^N T_i \cdot {}^B p_i \quad (1)$$

where  ${}^B p_i$  is the camera position in body frame as:

$${}^B p_i = {}^B R_i \cdot (-t_i) \quad (2)$$

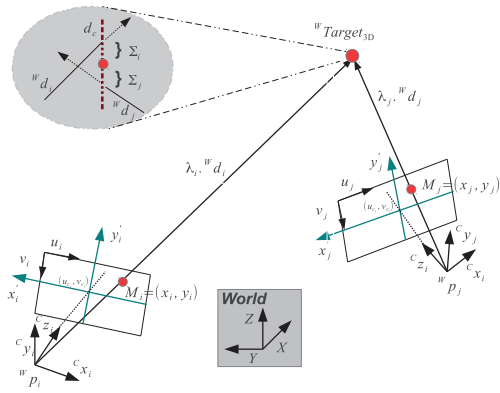


Fig. 3. System setup between robot  $i$  and  $j$

being  ${}^B_C \mathbf{R}_i$  and  $\mathbf{t}_i$  achieved from the camera extrinsic calibration and where the  ${}^W_N \mathbf{T}_i = \begin{bmatrix} {}^N_B \mathbf{R} & {}^W_{robot} \mathbf{P} \\ {}^N_B \mathbf{0} & 0 \end{bmatrix}$  and  ${}^N_B \mathbf{T}_i = \begin{bmatrix} {}^N_B \mathbf{R} & 0 \\ 0 & 0 \end{bmatrix}$  are respectively the transformation matrix from body to navigation and navigation to world.

The direction vector to the target in world frame is:

$${}^W \mathbf{d}_i = {}^W_N \mathbf{R}_i \cdot {}^N_B \mathbf{R}_i \cdot {}^B \mathbf{d}_i \quad (3)$$

where  ${}^B \mathbf{d}_i$  is the same vector in body frame equal to  ${}^B_C \mathbf{R}_i \cdot \left[ \frac{x_i - u_c}{f_x}, \frac{y_i - v_c}{f_y}, 1 \right]^T$ ,  $(u_c, v_c)$  principal point (that is usually at the image center), focal lengths  $(f_x, f_y)$  and  $\{M_i\} = (x_i, y_i)$  are the detected target measurement.

### C. Multi-Robot Stereo Correspondence

The features match between different cameras  $i, j$  is performed through the epipolar geometric line information. To avoid ambiguous matches, the corresponding points are searched over the epipolar line in a narrow band within  $2\sigma$  distance. In order to obtain the epipolar line, each robot will share the rotation matrix (4) and the candidate feature position (1), both related to the global frame.

$${}^W_C \mathbf{R}_i = {}^W_N \mathbf{R}_i \cdot {}^N_B \mathbf{R}_i \cdot {}^B_C \mathbf{R}_i \quad (4)$$

With this information we estimate the stereo rotation  $R$  matrix and translation  $t$  vector 5 and consequently the essential matrix  $E_{i,j} = \hat{t} \cdot R$ .

$$\begin{cases} t = ({}^W_C \mathbf{R}_i)^T \cdot ({}^W \mathbf{p}_i - {}^W \mathbf{p}_j) \\ \mathbf{R} = ({}^W_C \mathbf{R}_j)^T \cdot {}^W_C \mathbf{R}_i \end{cases} \quad (5)$$

### D. Stereo Measurement Uncertainty

In order to define uncertainty in 3D target we will first define the uncertainty associated to each intersection point  $P_{int_i}$  and  $P_{int_j}$ . To achieve the  $P_{int_i}$  covariance called  $\Sigma_{P_{int_i}}$ , we need to obtain the jacobian matrix of  $P_{int_i}$  in order to input variables  $\nu_{i,j}$ .

$$\begin{aligned} J_i &= \nabla_{\nu_{i,j}} P_{int_i}(\nu_{i,j}) \\ J_j &= \nabla_{\nu_{i,j}} P_{int_j}(\nu_{i,j}) \end{aligned} \quad (6)$$

### Algorithm 1 Multi-Robot Cooperative Stereo

Assuming that each robot share a 3-tuple  $({}^W \mathbf{p}_i, {}^W_C \mathbf{R}_i, \{{}^W \mathbf{d}_i\})$  for robot  $i$  and  $({}^W \mathbf{p}_j, {}^W_C \mathbf{R}_j, \{{}^W \mathbf{d}_j\})$  for robot  $j$ . For each pair of points received from robots  $i, j$  we will perform the following steps:

**Step 1:** Evaluate the correspondence between points detected in each camera considering the epipolar constraint (details in section II-C). If the points are without correspond with the epipolar constraint, the algorithm proceed to the next steps otherwise the tuples are label as being targets.

**Step 2:** Obtain perpendicular vector to  ${}^W \mathbf{d}_i$  and  ${}^W \mathbf{d}_j$  (see figure 4).

$$\mathbf{d}_c = \perp ({}^W \mathbf{d}_i, {}^W \mathbf{d}_j)$$

**Step 3:** Estimate the value of the  $\lambda_i$  where the ray  $({}^W \mathbf{p}_i + \lambda_i \cdot {}^W \mathbf{d}_i)$  intersects the plane  $\pi_j$  defined by the other monocular robot camera  $j$  optical center in world frame  ${}^W \mathbf{p}_j$  and the direction vector  $({}^W \mathbf{d}_j, \mathbf{d}_c)$  being the intersection point  $\mathbf{P}_{int_i} = {}^W \mathbf{p}_j + \lambda_j \cdot {}^W \mathbf{d}_j$ . The same approach for  $\lambda_j$ .

$$\begin{cases} \lambda_i = \frac{({}^W \mathbf{p}_j - {}^W \mathbf{p}_i)^T \cdot (\mathbf{d}_c \wedge {}^W \mathbf{d}_j)}{{}^W \mathbf{d}_i^T \cdot (\mathbf{d}_c \wedge {}^W \mathbf{d}_j)} \\ \lambda_j = \frac{({}^W \mathbf{p}_i - {}^W \mathbf{p}_j)^T \cdot (\mathbf{d}_c \wedge {}^W \mathbf{d}_i)}{{}^W \mathbf{d}_j^T \cdot (\mathbf{d}_c \wedge {}^W \mathbf{d}_i)} \end{cases}$$

**Step 4:** Obtain 3D target point in ECEF coordinate frame (section II-D)

$${}^W \mathbf{Target}_{3D} = \frac{\Sigma_{P_{int_j}}}{\Sigma_{P_{int_i}} + \Sigma_{P_{int_j}}} \cdot ({}^W \mathbf{p}_i + \lambda_i \cdot {}^W \mathbf{d}_i) + \frac{\Sigma_{P_{int_i}}}{\Sigma_{P_{int_i}} + \Sigma_{P_{int_j}}} \cdot ({}^W \mathbf{p}_j + \lambda_j \cdot {}^W \mathbf{d}_j)$$

**Step 5:** Evaluation the Euclidean distance between two points projected in the global frame in case of  $\lambda_i$  and  $\lambda_j$  are positive. The  $thr$  value is a metric physical distance in  $mm$ .

**if**  $\|({}^W \mathbf{p}_j + \lambda_j \cdot {}^W \mathbf{d}_j) - ({}^W \mathbf{p}_i + \lambda_i \cdot {}^W \mathbf{d}_i)\| < thr$  **then**  
    **return**  ${}^W \mathbf{Target}_{3D}$   
**end if**

where the input state vector is defined as:

$$\nu_{i,j} = \left[ \overbrace{P_i, \mathbf{R}_i, d_i}^{Robot_i}, \overbrace{P_j, \mathbf{R}_j, d_j}^{Robot_j} \right] \quad (7)$$

With the jacobian we can combine the uncertainty in the state variables  $N_{i,j}$  to covariance of  $P_{int_i}$  and  $P_{int_j}$ .

$$\mathbf{N}_{i,j} = diag[\Sigma_{P_i}, \Sigma_{R_i}, \Sigma_{d_i}, \Sigma_{P_j}, \Sigma_{R_j}, \Sigma_{d_j}] \quad (8)$$

$$\begin{aligned} \Sigma_{P_{int_i}} &= J_i \cdot \mathbf{N}_{i,j} \cdot J_i^T \\ \Sigma_{P_{int_j}} &= J_j \cdot \mathbf{N}_{i,j} \cdot J_j^T \end{aligned} \quad (9)$$

As seen in the algorithm the covariance of the both intersection points is used in the determination of the 3D measurement by weighting the uncertainty of each of them (see figure 4) in opposition to classic stereo mid-point triangulation method.

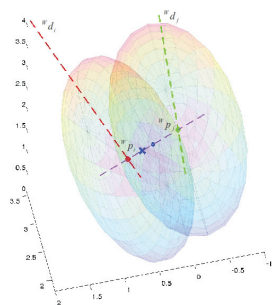


Fig. 4. Snapshot from the covariance 3D ellipse of  $P_{int_i}$  and  $P_{int_j}$  and the intersection point obtained from the algorithm. Mid-Point Triangulation method (blue dot). Triangulation based on the state covariance value (blue cross). Perpendicular vector  ${}^W \mathbf{d}_c$  to  $({}^W \mathbf{d}_i, {}^W \mathbf{d}_j)$  (purple line).

### III. EXPERIMENTAL SETUP

#### A. Outdoor Scenario

To evaluate the proposed multi-robot collaborative stereo the chosen experimental scenario was a non-urban area with several landscape elements, e.g., vegetation, water, rocks, bushes and some semi-urban structures such as gravel paths.



Fig. 5. Experimental Scenario



Fig. 6. Static target tracking by the robot TIGRE

The target tracking used during the experimental tests was an orange life jacket (see figure 6) with a size of  $37\text{cm} \times 67\text{cm}$  equipped with a RTK GPS Septentrio L1 L2 able to provide in post-process a centimeter-accuracy lower than  $10\text{cm}$ . This will allow to evaluate the results from the cooperative stereo and consider the target position as a external ground-truth.

#### B. Vehicles

The robot TIGRE (see figure 7) is an autonomous ground robot for exploration and activity in unstructured environments. The vehicle has electric propulsion and is equipped with an on board processing Quad Core Intel(R) Core(TM) i5 CPU 750 @ 2.67GHz, 4GB RAM, running a Linux operating system, wireless communications, infra-red thermographic camera, laser rangefinder, two visible spectrum cameras in a rigid stereo baseline ( $\sim 0.76$  meters) with a pixel resolution of  $1278 \times 958$ , Novatel GPS receiver and IMU Microstrain.

The MAV (Micro Aerial Vehicle) (see figure 8) is a helicopter driven by four rotors, symmetric to the center of



Fig. 7. TIGRE - Terrestrial Intelligent Ground Robotic Explorer



Fig. 8. Asctec@ Pelican MAV

mass equipped with a Flight Control Unit (FCU) for data fusion (GPS and IMU) and flight control, an onboard 1.6 GHz Intel Atom Based Embedded Computer, 802.11n Wifi and a monocular camera from IDS UEye LE with a resolution of  $1280 \times 1024$ . Both vehicles are running Linux and the ROS framework as a middleware for communication, parameters and monitoring of all processes. It is also crucial for the whole system to work the accurate time synchronization between all robots involved in the cooperative stereo.

### IV. RESULTS

In this section we describe the results obtained from two experimental cases that were performed in an outdoor scenario with a static target. The fact that we are using a static target was due to the importance of evaluating the quality of results from stereo triangulation with a rigid baseline (IV-A) and the paper proposal method with a multi-robot collaborative stereo (IV-B) in a similar context able to be reproduced.

#### A. Experiment I: Stereo rigid known baseline

For this experimental case, a stereo rigid baseline available at TIGRE was used to track the target. This means that the MAV was not available, so the results will express the quality of perception from TIGRE that was at a distance of  $\sim 35$  meters from the static target (see figure 6) and moving towards with speed of  $0.4 \text{ m/s}$ .

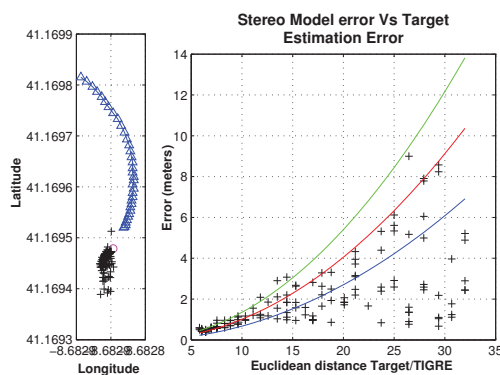


Fig. 9. Target estimation error for a stereo rigid known baseline. **Left:** TIGRE GPS trajectory (blue triangle), target GPS RTK position (magenta circle). Estimate position of the target (black cross). **Right:** Estimation position error related to the target (black cross) compared with the stereo model error (green, red and blue lines).

As expected and considering the reference[15], the perception accuracy of the TIGRE target tracking followed the stereo model error:  $\epsilon_z = \frac{z^2}{b \cdot f} \cdot \epsilon_d$  where  $\epsilon_z$  is the depth error,  $z$  is the

depth,  $b$  the baseline,  $f$  the focal length in pixels and  $\epsilon_d$  the matching error in pixels. The stereo model error is expressed in the lines from figure 9 on the right to different values of  $\epsilon_d$  and the black crosses the estimation position error related to the target. Figure 10 presents the stereo vision covariance for three instances related to the target position. We observe that the covariance decreases with shortening the distance and the bearing angle is consistent even for large distances. It became clear that was not possible to have a good accuracy for target tracking with local perception due to the normally ( $\sim 1$  m) available rig baseline.

### B. Experiment II: Multi-Robot Cooperative Stereo

Supported by the monocular MAV camera both robots are able to obtain a flexible stereo baseline using the proposed multi-robot collaborative stereo framework detail in section II. The experiment was composed of several steps: TIGRE detected the target and shared the estimation position to MAV, MAV moved based on the information provided by TIGRE to the top of the target and remained on the top based on local perception, MAV shared a 3-tuple  $({}^W \mathbf{p}_{i,C}, {}^W \mathbf{R}_i, \{{}^W \mathbf{d}_i\})$  to TIGRE in order to in a cooperative way estimate 3D target position. Results are showed in figures 11 and 12.

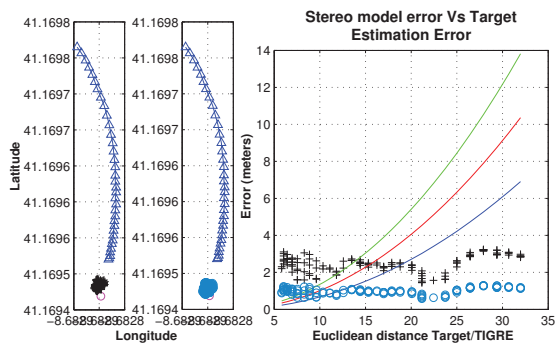


Fig. 11. Target estimation error with Multi-Robot Cooperative Stereo. **Left:** TIGRE GPS trajectory (blue triangle), target GPS RTK position (magenta circle). Estimate position of the target for each method: Mid-Point Triangulation (black cross) and State Covariance Sigma Value (blue circle). **Right:** Estimation position error related to the target with Mid-Point Triangulation Method (black cross) and State Covariance Sigma Value Method (blue circle) compared with the stereo model error (green, red and blue lines).

Comparing the results from section IV-A with IV-B, it is possible to observe that the proposal framework with cooperative dynamic stereo baseline reduced dramatically the target estimation error. This improvement is even more noticeable if we compare the results between figures 9 and 11 when applied the method based on state covariance sigma value (blue circle) detailed in section II-D. From figure 12 we can observe that the resulting uncertainty in 3D target is dominated by the MAV uncertainty mainly caused by the low cost GPS error ( $\sim 2$  m).

### V. CONCLUSIONS

In this work we present a framework for multi-robot real-time 3D high dynamic target estimation in outdoor scenarios. The proposed framework provides the following functionalities:

- Determination of 3D target measurement and associated uncertainty from image measurements from two cameras in robots and robots localization as well as the associated uncertainties;
- Mechanism to help the target search and identification in the image processing blocks in robots with low computational capacities;
- Mechanism to help the matching and association of 2D targets
- Better understanding of how the several sources of uncertainty contributes to measurement uncertainty

We demonstrate the advantages of this approach by comparing a stereo rigid baseline standalone target tracking with the proposed multi-robot cooperative stereo between a micro aerial vehicle (MAV) and an autonomous ground vehicle (AGV). The Field experimental cases, show that our proposal framework with cooperative dynamic stereo baseline reduces dramatically the target estimation error. This novelty will allow in future to establish an information framework for the formation control of multi-robot system. Additionally, this cooperative perception framework when integrated in a multi target tracking architecture, like a DDF, will endows it with a fast track initialization and more robust data association layer in highly dynamic scenarios.

### ACKNOWLEDGMENTS

The authors acknowledge the support given by the ISEP-IPP and INESC TEC to this project. This work is financed by the ERDF - European Regional Development Fund through the COMPETE Programme and by National Funds through the FCT - Portuguese Foundation for Science and Technology within project FCOMP-01-0124-FEDER-022701 and under Perception-Driven Coordinated Multi-Robot Motion Control Project with reference PTDC/EEA-CRO/100692/2008.

### REFERENCES

- [1] Markus W. Achtelik, Stephan Weiss, Margarita Chli, Frank Dellaerty, and Roland Siegwart. Collaborative stereo. In *Proc. IEEE/RSJ Int Intelligent Robots and Systems (IROS) Conf*, pages 2242–2248, 2011.
- [2] D.Blake Barber, JoshuaD. Redding, TimothyW. McLain, RandalW. Beard, and ClarkN. Taylor. Vision-based target geo-location using a fixed-wing miniature air vehicle. *Journal of Intelligent and Robotic Systems*, 47, 2006.
- [3] A.J. Davison, I.D. Reid, N.D. Molton, and O. Stasse. Monoslam: Real-time single camera slam. *Pattern Analysis and Machine Intelligence, IEEE Transactions on*, 29 (6):1052 – 1067, June 2007.
- [4] G. Di Leo, C. Liguori, and A. Paolillo. Covariance propagation for the uncertainty estimation in stereo vision. *Instrumentation and Measurement, IEEE Transactions on*, 60(5):1664 – 1673, May 2011.
- [5] Brian J. Julian, Michael Angermann, Mac Schwager, and Daniela Rus. A scalable information theoretic approach to distributed robot coordination. In *Intelligent Robots*

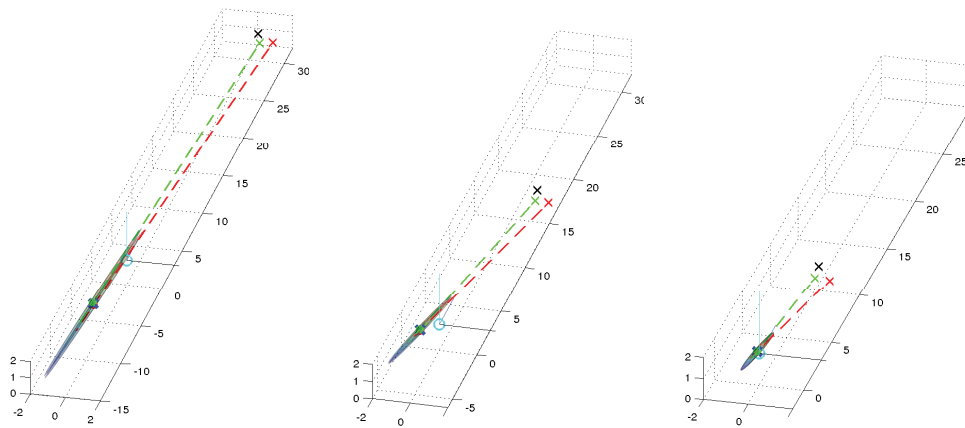


Fig. 10. Snapshot from the stereo vision covariance 3D ellipse for three instances of the experiment I. Red and green crosses are respectively the left and right camera position related to the global frame. The blue circle represent the TARGET RTK GPS position.

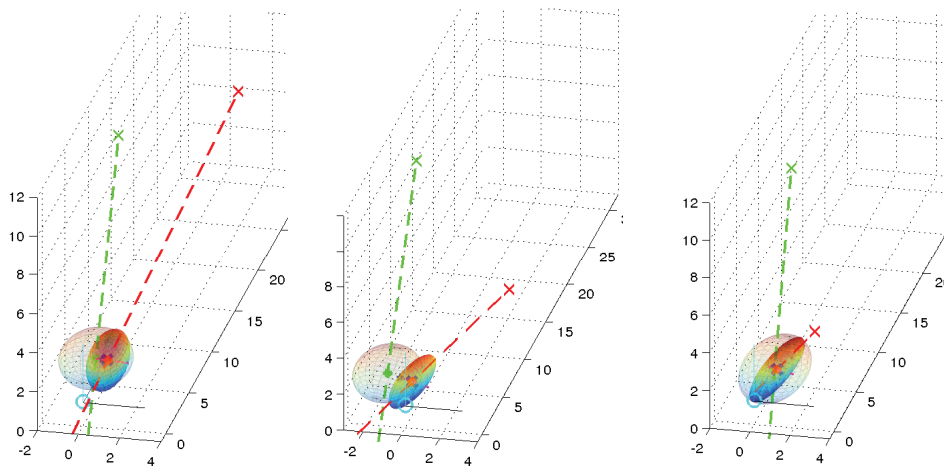


Fig. 12. Snapshot from the stereo vision covariance 3D ellipse for three instances of the experiment II. Red and green crosses are respectively the left and right camera position related to the global frame. The blue circle represent the TARGET RTK GPS position.

and Systems (IROS), 2011 IEEE/RSJ International Conference on, pages 5187–5194, Sept 2011.

- [6] G. Klein and D. Murray. Parallel tracking and mapping for small ar workspaces. In *Mixed and Augmented Reality, 2007. ISMAR 2007. 6th IEEE and ACM International Symposium on*, pages 225–234, 2007.
- [7] Aleksandr Kushleyev, Vijay Kumar, and Daniel Mellinger. Towards a swarm of agile micro quadrotors. In *Proceedings of Robotics: Science and Systems*, Sydney, Australia, July 2012.
- [8] A. Marino, F. Caccavale, L.E. Parker, and G. Antonelli. Fuzzy behavioral control for multi-robot border patrol. In *Control and Automation, 2009. MED '09. 17th Mediterranean Conference on*, pages 246 – 251, 2009.
- [9] L.-L. Ong, T. Bailey, H. Durrant-Whyte, and B. Upcroft. Decentralised particle filtering for multiple target tracking in wireless sensor networks. In *Information Fusion 11th International Conference on*, pages 1 – 8, July 2008.
- [10] M. Schwager, B. J. Julian, M. Angermann, and D. Rus. Eyes in the sky: Decentralized control for the deployment of robotic camera networks. 99(9):1541–1561, 2011.
- [11] J.H. Sutcliffe, P. Riseborough, and H. Durrant-Whyte. Decentralised data fusion applied to a network of unmanned aerial vehicles. In *Information, Decision and Control*, 2002.
- [12] Fumin Zhang and N.E. Leonard. Cooperative filters and control for cooperative exploration. *Automatic Control, IEEE Transactions on*, 55(3):650 – 663, March 2010.
- [13] Ke Zhou and S.I. Roumeliotis. Multirobot active target tracking with combinations of relative observations. *Robotics, IEEE Transactions on*, 27(4):678 – 695, 2011.
- [14] Danping Zou and Ping Tan. Coslam: Collaborative visual slam in dynamic environments. *Pattern Analysis and Machine Intelligence, IEEE Transactions on*, 35(2):354 – 366, Feb. 2013.
- [15] Frahm J.M. Mordohai P. Pollefeys M. iz£Gallup, D. Variable baseline/resolution stereo. *IEEE Conference on Computer Vision and Pattern Recognition*, 2008.

# Cooperative Robotics: Passes in Robotic Soccer

Gustavo Corrente, João Cunha, Ricardo Sequeira, Nuno Lau *Member, IEEE*

**Abstract**—The coordination necessary to make a pass in CAMBADA, a robotic soccer team designed to participate in the RoboCup Middle-Size League (MSL), is presented in this paper. The approach, which relies on information sharing and integration within the team, is based on formations, flexible positionings and dynamic role and positioning assignment. Role assignment is carried out locally on each robot to increase its reactivity. Coordinated procedures for passing and setplays have also been implemented. With this design, CAMBADA reached the 3rd place in RoboCup'2010 and RoboCup'2011. Competition results and performance measures computed from logs and videos of real competition games are presented and discussed.

## I. INTRODUCTION

As robots become increasingly available in different areas of human activity, researchers are naturally prompted to investigate how robots can cooperate with each other in order to perform different tasks. Moreover, progress in wireless communication technologies enables information sharing and explicit coordination between robots. These are basic capabilities needed to support sophisticated cooperation and coordination algorithms. Given this increasing availability of robots and communication technologies, multi-robot systems have, in the last two decades, been receiving more and more attention from researchers [1], [2], [3].

Interest on multi-robot systems is further justified by the advantages they offer with respect to single robots. First, some tasks are simply too difficult or impossible to be carried out by a single robot. In other cases, by providing a larger work force, multi-robot systems can carry out tasks faster. Multi-robot systems also facilitate scalability, as larger problems can often be solved by adding more robots to the team. Finally, through their inherent redundancy, multi-robot systems offer robustness, as they may still work when a team member is damaged or malfunctioning.

A prime environment for the application of coordination approaches are the RoboCup robotic soccer competitions. In the context of a soccer match, robotic or otherwise, the epitome of coordination is a passing situation. Passing is a coordinated behavior involving two players, in which one kicks the ball towards the other, so that the other can continue with the ball. This paper describes the approaches to enable

Gustavo Corrente was a researcher with ATRI/IEETA, Universidade de Aveiro, Portugal, and is currently with Nokia Siemens Networks Portugal, Aveiro, Portugal. (e-mail: gustavo@ua.pt)

João Cunha and Nuno Lau are with the ATRI/IEETA as well as with the Department of Electronics, Telecommunications and Informatics, Universidade de Aveiro, Portugal. (e-mails: joao.cunha, nunolau@ua.pt).

Ricardo Sequeira was a researcher with ATRI/IEETA, Universidade de Aveiro, Portugal, and is currently with Novabase, Lisboa, Portugal. (e-mail: rps@ua.pt)

passes in robotic soccer implemented within the framework of the CAMBADA<sup>1</sup> [4] project at the University of Aveiro.

This paper is organized as follows: Section II presents the hardware and software architectures of CAMBADA players and provides details on the main software components involved in individual decisions of the players. Section III discusses cooperation approaches by other teams of the Middle Size League. Section IV describe the adopted coordination methodologies. Section V presents the behaviours developed for passing and receiving a ball. Section VI discusses competition results and various performance measures. Section VII concludes the paper.

## II. PLATFORM DESCRIPTION

The CAMBADA team competes in the RoboCup Middle-Size League (MSL). The MSL is one of the most challenging leagues in RoboCup. Robotic players must be completely autonomous and must play in a field of 12 m × 18 m. Teams are composed of at most five robots with a maximum height of 80 cm. Human interference is allowed only for removing malfunctioning robots and re-entering robots in the game.

The CAMBADA robots were designed and built at the University of Aveiro. The hardware is distributed in three layers which facilitate replacement and maintenance.

The components in the lower layer, namely motors, wheels, batteries and an electromechanical kicker, are attached to an aluminum plate placed 8 cm above the floor. The second layer contains the control electronics. The third layer contains a laptop computer, at 22.5 cm from the floor, a catadioptric omnidirectional vision system, a frontal vision system (single camera) and an electronic compass, all close to the maximum height of 80 cm.

The players are capable of holonomic motion, based on three omnidirectional roller wheels with a top speed of 2 m/s. The mentioned vision system allows detecting objects, the ball, players, and field lines on a radius of 5 m around each player. Each player also carries encoders, battery status sensors and, for detecting if the ball is kickable, an infra-red presence sensor.

An image of a CAMBADA robot can be seen in Figure 1.

Following the CAMBADA hardware approach, the software is also distributed. Therefore, five different processes are executed concurrently. All the processes run at the robots processing unit in Linux.

Processes communicate by means of an RTDB<sup>2</sup> [5] which is physically implemented in shared memory. The RTDB is

<sup>1</sup>Cooperative Autonomous Mobile robots with an Advanced Distributed Architecture

<sup>2</sup>Real-Time DataBase



Fig. 1. A CAMBADA robot.

a data structure which contains the essential state variables to control the robot. It is divided in two regions, the local and shared regions.

The local section holds the data needed by the local processes and is not to be broadcasted to the other robots. The shared section is divided between all running agents to contain the data of the world state as perceived by the team. Each sub-divided area is allocated to one robot where it stores the perceived state of the world. There is also one area specific for the coach information. As the name implies the shared section is broadcasted through the team. Each agent transmits its own shared section, always keeping all RTDBs with updated information. This allows information sharing among the team.

The RTDB implementation guarantees the temporal validity of the data, with small tolerances.

The software architecture is depicted in Figure 2.

The processes composing the CAMBADA software are:

- The *Vision* process which is responsible for acquiring the visual data from the cameras in the vision system, processing and transmitting the relevant info to the CAMBADA agent. The transmitted data is the position of the ball, the lines detected for localization purposes and obstacles positions. Given the well structured environment the robots play in, all this data is currently acquired by color segmentation [6], [7].
- *Agent* is the process that integrates the sensor information and constructs the robot's worldstate. The agent

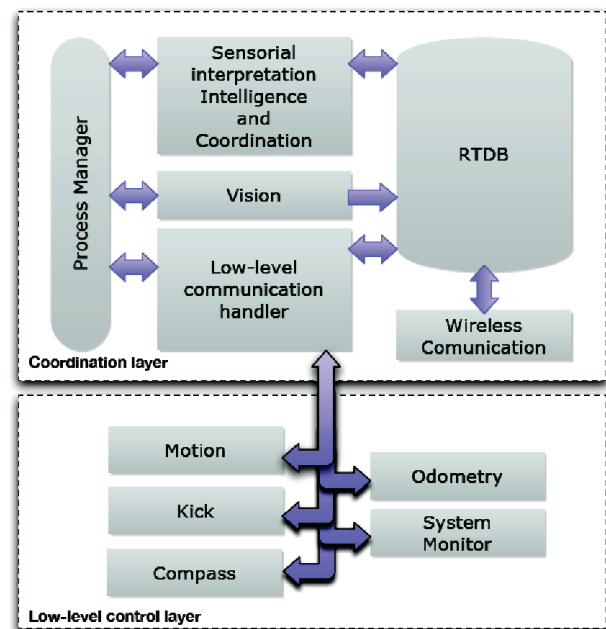


Fig. 2. The CAMBADA software architecture

then decides the command to be applied, based on the perception of the worldstate, accordingly to a pre-defined strategy [8].

- The *Comm* process handles the inter-robot communication, receiving the information shared by the team-mates and transmitting the data from the shared section of the RTDB to the team-mates [9], [10].
- *HWcomm* or hardware communication process is responsible for transmitting the data to and from the low-level sensing and actuation system.
- The *Monitor* process checks the state of the remaining processes relaunching them in case of abnormal termination.

Given the real-time constraints, all process scheduling is handled by a library specifically developed for the task, *pman*, process manager [11].

### III. COOPERATION IN THE MIDDLE SIZE LEAGUE

In the MSL teams use different approaches to deal with the cooperation and coordination problems. Until now, MSL teams have shown limited success in implementing and demonstrating passes. In RoboCup'2004, some teams had already implemented passes, but the functionality was not robust enough to actually be useful in games [12], [13]. Besides the CAMBADA team, the first teams capable of making passes in free play were RFC Stuttgart(former COPS) [14] and Brainstromers Tribots [15]. More recently, the game rules were adapted to enforce cooperation, and it is currently mandatory to perform a pass in order for a team to transition from its defending half-field to the opponent half-field.

The CAMBADA team uses a dynamic role-base architecture with a formation [16]. The main role is the Striker which is the player closest to the ball, the remaining players use the

role Midfielder. The strategic positions are assigned according to the priority to the closest player available. In offensive set pieces CAMBADA team already use passes, using the role Replacer and Receiver achieving cooperation [16].

The Brainstormers Tribots roles are initially assigned by the Teamcontrol which also decides what formation to use depending on the number of robots in the field and robots preferences [17]. Their coordination is based on centralized decision. One robot is the master and decides which set play to use. The master is usually the robot closer to the ball. When deciding which robot to be master there is a possibility to have an ambiguity. The first robot to request it to the centralized Teamcontrol module gets it and if there is more than one robot request at the same time the one with lower shirt number gets it. In defensive plays they use a defensive rotation. It is the master that evaluates the environment and demands a rotation once they have been overplayed through the sideline. This means that the first line of defense is no longer between the ball and the goal. This rotation makes the robots change their roles. When they have the ball the master robot is the one with ball possession. It is the only robot that can request a role exchange for itself and only the master can start a set play like a pass. These decisions are transmitted using keywords. In order to apply this approach during a game all robots must know all possible actions and associate them to keywords.

The RFC Stuttgart team uses dynamic role assignment during the game with subroles so it is possible to have two robots with the same role (Defender, Forward) but with different subroles (Left Defender, Right Defender, etc) [18]. The list of roles is defined before each game. Cooperation is achieved through a modified Interaction net.

Another team to use cooperation is the Tech United team. Their approach is based on a dynamic role assigner [19]. A module called Strategy Decider will pick a formation (e.g. one keeper, two defenders, two attackers) and the roles based on the information of the world state. Then the Role Assigner will assign each role to the most suitable robot. This choice is based on positions, of the entire team and of the ball, and if the robot is fully operational or not. After the role is assigned another module takes charge, the Behavior Executer. This module will use the information of the world state in order to act. The selection of strategy and role assignment is based on weights defined before each game.

Another approach is taken by the Carpe Noctem team. They have developed a new specification language, ALICA<sup>3</sup> [20]. Behaviors are modeled using this language. Each robot will estimate the decisions of the teammates and will act based on those [21]. Communication corrects any wrong assumption. The language supports a degree of commitment for strategies with several robots. A pass requires a higher degree of commitment than deciding who attacks and who defends. The path planning used to calculate the movements of the robots uses shared information like teammates and obstacles positions to achieve a more accurate path [22].

<sup>3</sup>A Language for Interactive Cooperative Agents

#### IV. COORDINATION FOR PASSING

The CAMBADA coordination model is based on sharing the world state between all robots. Each robot has its own world state, that integrates its own perception with the world state broadcasted by the teammates [23], [16].

The Decision architecture is based on Roles, that provide a way to perform high-level tasks. Each role is a combination of Behaviors (ie: Move, Pass, Kick, ReceiveBall) that decompose the high-level tasks. The management of behaviors in each role is made by using a finite state machine or an utility function.

In free play, the CAMBADA team use four roles: Goalie, Midfielder, Striker, Receiver. In a normal situation there are five robots in the field: one Goalie, one Striker and three Midfielders. The Goalie is used to defend the goal from opponent shots, avoiding the team to suffer goals. The Striker is the active role, that pursuits the ball and tries to dribble it near to the opponent goal to perform a shot. The remaining robots have the Midfielder role, that allow them to move according to a strategic position model defined by our coach agent [16].

The passing situation is a team task that involves two robots, one with the role Striker and the other with the role Receiver. Most of the opponent teams do not show a distributed field occupation, rather following a swarm strategy. Hence, to increase the success of a pass team formations place a midfielder in areas of the field that we expect to be free. Figure 3 shows two attacking situations where the used formations place the Midfielder in a better position to receive the pass.



Fig. 3. Two passing situations in free play. The CAMBADA robots are represented by the circular cyan robots and the opponents by the triangular magenta robots.

Figure 4 shows which roles/behavior/messages are involved in a passing situation. This situation is triggered when the Striker has the ball engaged, the conditions to perform a shot are not favorable and the dribble path is not free.

The Striker evaluates the best robot to pass the ball. His choice is sent to all robots by setting a coordination flag with `TryingToPass_[robotId]` in the shared world state, where `robot_id` is the number receiver. When the chosen robot realizes the flag is set, changes the role from Midfielder to

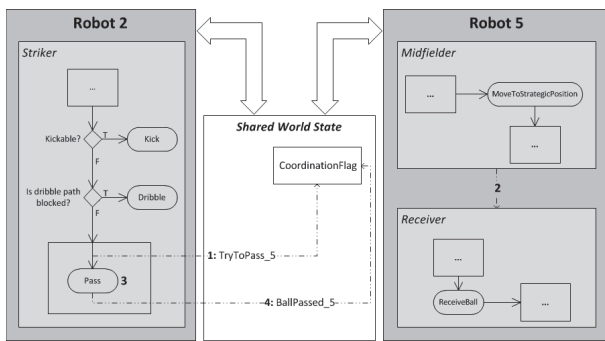


Fig. 4. Distributed state machines involved in a cooperative passing situation from robot 2 to robot 5.

Receiver. The Receiver performs the ball reception behaviour described in section V. When the Striker completes the pass behavior, it updates the coordination flag to Ball-Passed\_[robotId]. This information is used to measure the time since the ball is really passed. If the ball takes too much time to reach the receiver robot, the passing situation is aborted. Another condition to abort the passing situation is if the ball is intercepted (the ball path is different than the expected).

## V. BEHAVIOURS

While efficient coordination between the involved robots and some degree of tactical opportunity are required to perform the process described above, in the end a pass will only be successful as long as the robots are able to perform the necessary actions in each stage of the process. These actions in the CAMBADA software architecture are called *Behaviours*. Examples of behaviours in the CAMBADA architecture are *Move* to a position in the field, *Dribble* or *Kick* the ball. A behaviour can be seen as the basic block of a CAMBADA robot attitude. A behaviour executes a specific task by computing the desired velocities to be applied at the robot frame, activating or not the ball handling device and setting the desired strength to be applied the kicking system.

The various CAMBADA behaviours are:

- **StopRobot** the most basic behaviour, sends zero velocities to all motors, halting the robot.
- **Move** the behaviour that moves the robot to a given position in the field.
- **Interception** the behaviour that intercepts a moving ball, considering its velocity.
- **Dribble** the behaviour executed by the *Striker* role when dribbling the ball.
- **Kick** the behaviour that performs a lob shot to a given position in the field.
- **CatchBall** a behaviour that attempts to get possession of the ball near the outer field lines, without pushing the ball outside the field.
- **GoalieDefend** the goalie exclusive behaviour that tries to prevent conceding goals.

All the CAMBADA behaviours derive from a generic class named *Behaviour*. This class implements the method *execute*

which inserts in the RTDB the different values that will later be translated to the powers to be applied at the various robot actuators. The *calculate* method is implemented by each specific behaviour derived from *Behaviour*.

For the purpose of performing passes in free play, two new behaviours were developed: the *Pass* behaviour, like the name implies passes the ball to another team-mate robot, and the *ReceiveBall* behaviour, that attempts to receive an incoming pass.

### A. Pass behaviour

The *Pass* behaviour receives a position,  $\vec{p}$ , in field coordinates, corresponding to the position of the teammate that will receive the pass. This information is used to calculate the angular error,  $\delta$ , between the heading of the robot passing the ball, relative to the field,  $\theta$ , and the teammate position. This angular error represents how much the robot performing the pass has to reorientate in order to face the receiver and make a pass. This is due to the fact that the kicking device on the CAMBADA robots can only kick straight ahead.

The success of a pass depends heavily on how close the ball will move relative to the robot on the receiving end of the pass. However, as the opponent robots try to get possession of the ball, the passing robot cannot afford to waste time making a fine aim to the receiving robot. Therefore, we want to minimize the angular error  $\delta$  as fast as possible. On the other hand, if a robot makes a pass while rotating, the ball will not follow the desired trajectory. So the robot must rotate fast enough to face the receiver, but at the same time must have a small angular velocity,  $\dot{\theta}$ , when the pass is performed. In order to cope with these requirements the calculated error,  $\delta$ , is supplied to a PD controller. Furthermore, in order to avoid deviations from the desired ball path, the passer rotates around the ball instead of rotating around the center of the robot frame.

Figure 5 presents a visual representation of the *Pass* behaviour, depicting two robots, a passer, with the ball, and a receiver with all the variables used to perform a passing action.

### B. ReceiveBall behaviour

When the process of receiving a pass in free play starts, few assumptions can be made regarding the alignment between the receiver robot and the ball path as well as the robot orientation. Unfortunately, it does not suffice to move the robot to the ball path while facing the ball. Given that the robot body is rigid and the incoming ball travels at high speeds, the outcome of that situation would be the ball hitting the robot and then bouncing away. We need to somehow absorb the ball velocity to avoid such scenarios. Instead of altering the robot body, the solution found was to make the robot move backwards therefore reducing the relative velocity between the robot and the ball upon contact.

The receiver robot tries to face the ball by calculating the angular error,  $\delta$ , between the ball position,  $\vec{b}$ , in field coordinates, and its orientation in the field, similar to the *Pass* behaviour. The error  $\delta$ , is also supplied to a PD-controller

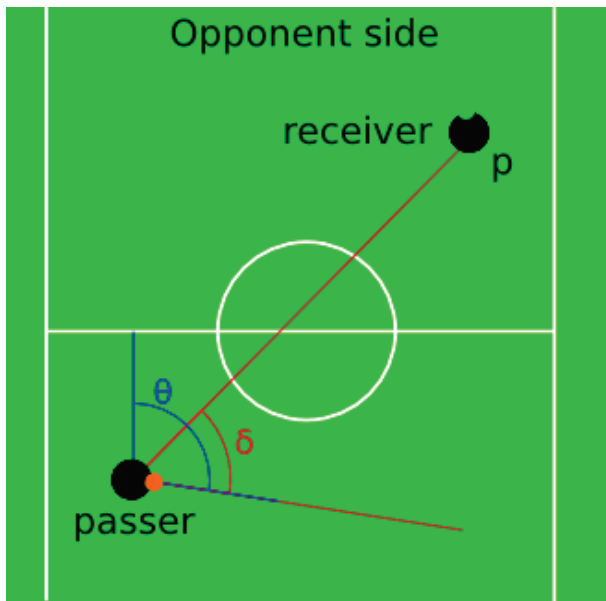


Fig. 5. A visual representation of the *Pass* behaviour.

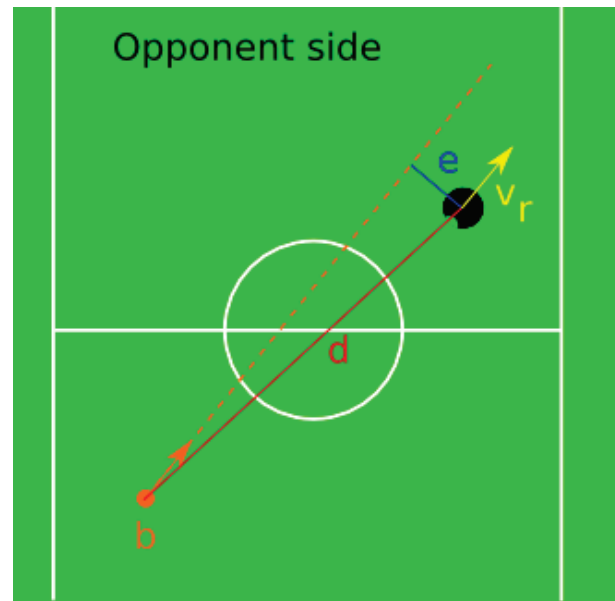


Fig. 6. A visual representation of the *ReceiveBall* behaviour.

in order to make the robot face the ball as fast as possible. Otherwise the robot may not be facing the ball when it is close, failing to receive the pass.

Using the estimation of the ball velocity,  $\dot{\vec{b}}$ , we can anticipate the ball path, assuming a straight path and  $\|\dot{\vec{b}}\|$  to be constant over the ball path. We can then calculate the deviation,  $\vec{e}$ , between the robot position and the ball path. In order to move the robot to the ball path as fast as possible we use another PD controller. This controller uses as input the norm of the calculated deviation,  $\|\vec{e}\|$ . The output of the controller is then projected to a 2D vector with the same direction as  $\vec{e}$ .

In order to absorb the ball velocity we apply an heuristic to make the robot move backwards. We only apply this heuristic when the robot is close to the ball path, as we prefer to have the ball hit the robot and bounce away rather than to have the robot move backwards while far from the ball path. We consider the robot max speed,  $v_{max}$ , and define a parameter  $v_{diff}$ , that represents the desired relative velocity between the robot and the ball upon contact. Therefore the velocity the robot should have to receive a ball,  $\vec{v}_r$ , is  $\dot{\vec{b}} - v_{diff}$ , with saturation on  $v_{max}$ . The value of  $v_{diff}$  used is 0.5 m/s and was obtained empirically.

Assuming the robot is close to the ball path, in other words  $\|\vec{e}\|$ , is small, we check if the distance,  $d$ , between the ball position,  $\vec{b}$ , and the robot position,  $\vec{p}$ , is smaller than the distance travelled in one second at the required velocity to receive the ball,  $v_r$ . This gives the robot one second of time to move backwards and absorb the ball speed.

A visual representation of the *ReceiveBall* behaviour is shown in Figure 6.

## VI. RESULTS

Obtaining results to evaluate the proposed work is a challenging endeavour. First of all, the methodology described

earlier focuses on performing long passes on the MSL field to oppose the slow speed of the CAMBADA robots. However since the authors only have access to a field with the official measures during competitions, we restricted the evaluation to results obtained during soccer matches. On the other, this provides an opportunity to show effectiveness of the proposed approach against different opponents. The CAMBADA team first implemented the passing methodology in 2010. Since then it has been applied in four different competitions. In global passes have been performed in 9 games. These games were analyzed and the results are summarized in Table I.

Total passes	53	100%
Successful passes	37	70%
Unsuccessful passes	16	30%
Goal after pass	14	26%
Dribble after pass	10	19%
Pass after a pass	12	23%
Intercepted passes	1	2%
Ball possession recovered after failed reception	5	9%
Lost ball possession after failed reception	11	21%

TABLE I  
 PASSING PERFORMANCE IN ROBOCUP COMPETITIONS.

The combination of the coordination methodologies described along with the behaviours developed show a relatively high success rate of 70% of all passes performed. Performing passes in free play seems to provide an advantage over dribbling the ball all the way to the opponent goal, since 26% of the passes result in a goal. This shows that placing a Midfielder ahead in the field is strategically advantageous as the robot is in a better attacking position to pose a threat to the opponent team. Additionally, an interesting conclusion is that the swarm based formations used by other teams are seldomly able to intercept passes, proving an opening to teams taking advantage of cooperative skills such as passes.

## VII. CONCLUSION

This paper presented and evaluated the passing coordination methodologies of CAMBADA, one of the top teams in RoboCup MSL world championships (champion in RoboCup'2008, 3rd place winner in RoboCup'2009, RoboCup'2010, RoboCup'2011).

In RoboCup middle size league, several teams follow a swarm strategy to pursuit the ball. These kind of strategy causes clear zones in the field. Combining this fact with the lack of speed of CAMBADA robots, motivates the necessity to improve the team strategy. Using teamwork skills such as passes during free play, allied with a formation with strategic positions exploring free areas of the field allows a cooperative strategy that reduces the importance of speed differences to the other teams.

The described solution is based on information sharing of coordination flags that trigger transitions in pre-defined state-machines, distributed among the robots. Although applied to a robotic soccer environment, the methodology is domain independent, capable of being applied in other domains.

One of the most significant aspects of this work is the integration of the described coordination methodologies in a complex multi-robot system and their validation in the challenging Robo-Cup MSL competition scenario. This contrasts with many other approaches described in the literature, which are often validated in more controlled robotic environments, if not in simulation.

## REFERENCES

- [1] Noreils, F.R.: Toward a robot architecture integrating cooperation between mobile robots: Application to indoor environment. *The International Journal of Robotics Research* **12**(1) (1993) 79–98
- [2] Agmon, N., Kraus, S., Kaminka, G.: Multi-robot perimeter patrol in adversarial settings. In: *Robotics and Automation, 2008. ICRA 2008. IEEE International Conference on*. (may 2008) 2339–2345
- [3] Balch, T., Parker, L., eds.: *Robot teams: from diversity to polymorphism*. A K Peters/CRC Press (2002)
- [4] Neves, A.J.R., Azevedo, J.L., Cunha, B., Lau, N., Silva, J., Santos, F., Corrente, G., Martins, D.A., Figueiredo, N., Pereira, A., Almeida, L., Lopes, L.S., Pinho, A.J., Rodrigues, J.M.O.S., Pedreiras, P.: CAMBADA soccer team: from robot architecture to multiagent coordination. In: *Robot Soccer. INTECH* (2010)
- [5] Almeida, L., Santos, F., Facchinetti, T., Pedreiras, P., Silva, V., Lopes, L.S.: Coordinating Distributed Autonomous Agents with a Real-Time Database: The CAMBADA Project. In Aykanat, C., Dayar, T., Korpeoglu, I., eds.: *Computer and Information Sciences - ISCIS 2004, 19th International Symposium, Kemer-Antalya, Turkey, October 27-29, 2004. Proceedings. Volume 3280 of Lecture Notes in Computer Science.*, Springer (2004) 876–886
- [6] Neves, A.J., Pinho, A.J., Martins, D.A., Cunha, B.: An efficient omnidirectional vision system for soccer robots: From calibration to object detection. *Mechatronics* **21**(2) (2011) 399 – 410 Special Issue on Advances in intelligent robot design for the Robocup Middle Size League.
- [7] Neves, A., Martins, D., Pinho, A.: A hybrid vision system for soccer robots using radial search lines. In: *Proc. of the 8th Conference on Autonomous Robot Systems and Competitions, Portuguese Robotics Open - ROBOTICA'2008, Aveiro, Portugal (April 2008)* 51–55
- [8] Lau, N., Lopes, L.S., Corrente, G., Filipe, N., Sequeira, R.: Robot team coordination using dynamic role and positioning assignment and role based setplays. *Mechatronics* **21**(2) (2011) 445 – 454 Special Issue on Advances in intelligent robot design for the Robocup Middle Size League.
- [9] Santos, F., Almeida, L., Pedreiras, P., Lopes, L., Facchinetti, T.: An Adaptive TDMA Protocol for Soft Real-Time Wireless Communication among Mobile Autonomous Agents. In: *Proc. of the Int. Workshop on Architecture for Cooperative Embedded Real-Time Systems, WACERTS 2004*. (2004)
- [10] Santos, F., Corrente, G., Almeida, L., Lau, N., Lopes, L.: Selfconfiguration of an Adaptive TDMA wireless communication protocol for teams of mobile robots. In: *Proc. of the 13th Portuguese Conference on Artificial Intelligence, EPIA 2007*. (2007)
- [11] Paulo Pedreiras, L.A.: Task Management for Soft Real-Time Applications Based on General Purpose Operating Systems. In: *Robotic Soccer. I-Tech Education and Publishing (December 2007)* 243–252
- [12] Lima, P.U., Custódio, L.M.M., Akin, H.L., Jacoff, A., Kraetzschmar, G.K., Kiat, N.B., Obst, O., Röfer, T., Takahashi, Y., Zhou, C.: Robocup 2004 competitions and symposium: A small kick for robots, a giant score for science. *AI Magazine* **26**(2) (2005) 36–61
- [13] van der Vecht, B., Lima, P.U.: Formulation and implementation of relational behaviours for multi-robot cooperative systems. In Nardi, D., Riedmiller, M., Sammut, C., Santos-Victor, J., eds.: *RobuCup. Volume 3276 of Lecture Notes in Computer Science.*, Springer (2004) 516–523
- [14] Zweigle, O., Lafrenz, R., Buchheim, T., Käppeler, U.P., Rajaie, H., Schreiber, F., Levi, P.: Cooperative Agent Behavior Based on Special Interaction Nets. In: *Proceedings of the 9th International Conference on Intelligent Autonomous Systems 2006, IAS-9, Tokio, Tokio, IOS Press (März 2006)* 651–659
- [15] Müller, H., Lauer, M., Hafner, R., Lange, S., Merke, A., Riedmiller, M.: Making a robot learn to play soccer using reward and punishment. In Hertzberg, J., Beetz, M., Englert, R., eds.: *KI. Volume 4667 of Lecture Notes in Computer Science.*, Springer (2007) 220–234
- [16] Lau, N., Lopes, L., Corrente, G., Filipe, N.: Multi-robot team coordination through roles, positionings and coordinated procedures. In: *Intelligent Robots and Systems, 2009. IROS 2009. IEEE/RSJ International Conference on*. (Oct. 2009) 5841–5848
- [17] Tribots, B.: Tribots: Soccer Strategy. [http://carpenoetm.das-lab.net/sites/default/files/Workshop%20Content/11\\_2010/Tribots-Kooperation.pdf](http://carpenoetm.das-lab.net/sites/default/files/Workshop%20Content/11_2010/Tribots-Kooperation.pdf) (2008) Last visited: 31 of January 2012.
- [18] Buchheim, T., Käppeler, U.P., Lafrenz, R., Oubbati, M., Rajaie, H., Schanz, M., Schreiber, F., Zweigle, O., , Levi, P.: Team Description Paper 2005 CoPS Stuttgart. In: *CD proceedings of RoboCup 2005 Symposium*. (2005)
- [19] Aangent, W., de Best, J., Bukkems, B., Kanters, F., Meessen, K., Willems, J., Merry, R., v.d. Molengraft, M.: TechUnited Eindhoven Team Description 2009. In: *CD proceedings of RoboCup 2009 Symposium*. (2009)
- [20] Skubch, H., Wagner, M., Reichle, R.: A Language for Interactive Cooperative Agents. <http://carpenoetm.das-lab.net/dl/doc/ALICA.pdf> (2009) Last visited on: 21 of July 2009.
- [21] Amma, T., Baer, P., Baumgart, K., Burghardt, P., Geihs, K., Henze, J., Opfer, S., Niemczyk, S., Reichle, R., Saur, D., Scharf, A., Schreiber, J., Segatz, M., Seute, S., Skubch, H., Triller, S., Wagner, M., Witsch, A.: Carpe Noctem 2009 (2009)
- [22] Opfer, S., Skubch, H., Geihs, K.: Cooperative Path Planning for Multi-Robot Systems in Dynamic Domains. In: *Mobile Robots - Control Architectures, Bio-Interfacing, Navigation, Multi Robot Motion Planning and Operator Training. InTech* (Nov 2011) 237–258
- [23] Lau, N., Lopes, L., Corrente, G.: CAMBADA: Information Sharing and Team Coordination. In: *Proc. of the 8th Conference on Autonomous Robot Systems and Competitions, Portuguese Robotics Open - ROBOTICA'2008, Aveiro, Portugal (April 2008)* 27–32

# Unknown-Color Spherical Object Detection and Tracking

Anže Tropan, Eduardo Guerreiro, Francesco Celiberti, Gonçalo Santos, Aamir Ahmad and Pedro U. Lima

*Institute for Systems and Robotics, Instituto Superior Técnico, Lisboa, Portugal*

**Abstract**—Detection and tracking of an unknown-color spherical object in a partially-known environment using a robot with a single camera is the core problem addressed in this article. A novel color detection mechanism, which exploits the geometrical properties of the spherical object's projection onto the image plane, precedes the object's detection process. A Kalman filter-based tracker uses the object detection in its update step and tracks the spherical object. Real robot experimental evaluation of the proposed method is presented on soccer robots detecting and tracking an unknown-color ball.

## I. INTRODUCTION

Detecting and tracking relevant objects in a known or unknown environment forms a vast area of research not only in the domain of image processing and computer vision [1] [2] [3] [4], but also in that of mobile robotics [5] [6] [7] [8]. Often the objective in the former is to classify complex objects based on their color and shape irregularities [1]. However, in mobile robotics the focus is more on computationally fast methods for object tracking (including detection) and thereby using the objects' information to achieve other complex goals, e.g. robot's self-localization [7] and high-level decision making [9]. The gain in an object tracker's execution speed is due to using the object's shape as a prior knowledge and/or using less-complex shaped objects, e.g. spheres. Although it is often practical to assume the presence of less-complex shaped objects in most environments, the same cannot be true with regard to the object's color. Moreover, the lighting conditions of the environment irregularly change the apparent colors of the objects over time rendering the prior knowledge of the object's color useless.

In this article we present a method to solve the problem of detecting and tracking spherical-shaped objects in a partially-known environment without the necessity of the object's color information as a prior knowledge of the tracker. The partially-known environment implies that the most dominant colors contributing to the environment's background are known beforehand. The method essentially consists of the following three modules:

- automatic color detection of a spherical-shaped object,
- spherical object detection method and
- a Kalman filter-based (KF) tracker that uses the spherical object detection method in its update step.

The automatic color detection, which consists of a sweep over the HSV color space, is performed only once before initiating the tracker. Therefore, the object should be in the

field of view of the camera at the beginning of the tracking process. The detected color is subsequently used by the spherical object detection method which along with the KF-based tracker runs continuously to track the object. Since the automatic color detection method itself is computationally fast, it can be scheduled to run intermittently without the need of manual intervention in environments where the lighting changes frequently causing the apparent color of the object to change. In order to experimentally validate our proposed method, the tracker was implemented on real soccer robots to track an unknown-color soccer ball.

The rest of the article is organized as follows. In Section II we briefly overview the existing literature in the context of object detection and tracking. The novel contributions of the article concerning automatic color detection is presented in Section III along with the spherical object detection and the KF-based tracker's theoretical details. Real robot experimental results are presented in Section IV, followed by Section V where we conclude the article with comments on future work.

## II. RELATED WORK

An extensive literature exists in the area of object detection where researchers have explored concepts ranging from contour recognition, e.g., Hough transform (HT) [10] to structure tensor techniques [4]. While some of these assume a prior knowledge of the object's color [8], innovative algorithms have been proposed recently to overcome this assumption, e.g. [5] [6]. In [5] the authors present a color histogram mismatch-based method to distinguish a spherical object of known size from the background. This removes the dependency on the prior color information and enables the spherical object detection in 3D space. However, since its accuracy depends on the number of pixels required to perform the histogram mismatch (the higher the number of pixels used, the better the accuracy is) at every frame, the execution speed is adversely affected causing the method to be inefficient for real-time applications.

In [11] the authors present a circular HT-based method to identify the circular projections of the spherical object to detect them. Apart from being computationally expensive, the method explicitly requires a fine-tuning of the edge-detection system, required by the HT, every time the lighting condition of the environment changes. A possible solution to this problem is proposed in [12], where the image projection of the spherical object is an exact ellipse and radial and rotary scan lines are used to look for matching color variations to detect the outer

edge of the ellipses. The method is fast and suitable for real-time detection of unknown-color spherical objects. However, it is too specific to a certain kind of vision system that consists of a special mirror with a hyperbolic part in the middle, a horizontal isometric mirror and a vertical isometric mirror in the outer parts. In this article we show that our method is fast, adapts automatically to lighting changes in the environment and requires an easily available perspective lens-based camera making it diversely usable.

### III. DETECTION AND TRACKING MECHANISM

To detect and track a specific type of object in an image, some of its characteristics must be known beforehand. These are usually the object's shape and color. In this article we deal with spherical shaped objects, henceforth referred simply as objects. Detecting a spherical object assuming a prior knowledge of its color is a relatively easy and previously solved problem. However, in order to solve the generic problem of detecting objects in any lighting condition, the known-color assumption needs to be dropped. Our solution to this problem involves automatic color detection (ACD) of the object before initiating its detection and tracking process. This consists of sweeping the *hue-saturation-value* (HSV) color space in *hue* intervals, and then applying the color detection mechanism, explained further, to each *hue* interval. The output of this method is the most likely *hue* interval that corresponds to the color of the object. This process should be repeated after a pre-determined time interval to adapt to varying lighting conditions of the environment in which the detection is done. Since the ACD is a fast method ( $< 1$  second) the tracker can easily afford to execute the ACD without affecting its own execution speed. The resulting *hue* interval information is then used by the object detection mechanism (ODM) by filtering each image frame using only that *hue* interval.

The approach mentioned above includes the use of only a perspective lens-based camera fixed to the robot and pitched down towards the ground plane (GP). The GP is where the robot moves (translates on the GP's  $X - Y$  plane and rotates around an axis passing through the robot's center of mass and perpendicular to the ground plane). To calculate the distance to the object from the robot we use the perspective transformation between the the image frame and the GP, assuming that the robot is at the origin of the coordinates and the object is on the GP. This allows a linear pixel-to-meter relationship for every pixel belonging to the GP. Once the pixel corresponding to the object's contact point with the GP is known (by the ODM), we use the aforementioned relationship to calculate the distance to it in meters. Furthermore, using simple geometric calculations, the object's center's coordinates in the robot-centric frame of reference is calculated. Finally, the ODM acts as a classifier for the update step of a KF-based tracking method to track the object's position and velocity. The robot's odometry is used in the KF's prediction step.

As mentioned previously, we assume that the detection and tracking is done in a partially known environment meaning that the GP consists of a few dominant colors which contribute to a large, useless part of the image. Assuming the prior knowledge

of this information, we simply eliminate their corresponding image pixels, facilitating a much faster ACD of the object and the ODM.

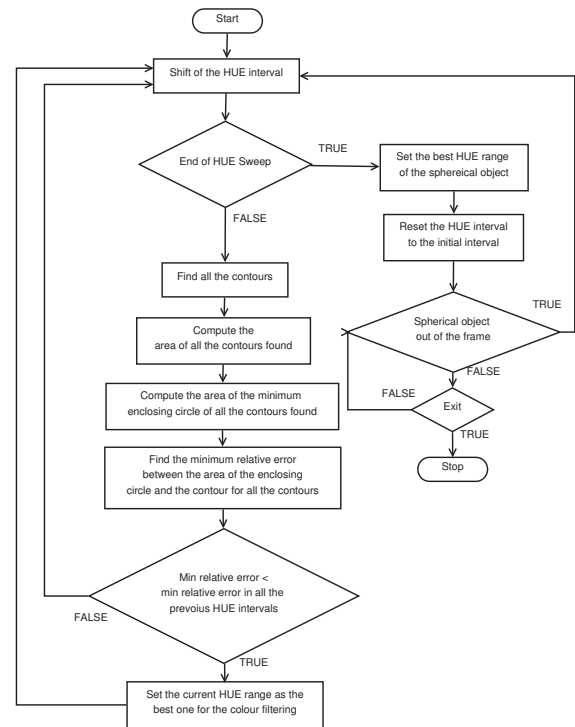


Fig. 1: Automatic color detection algorithm

#### A. Automatic Color Detection (ACD) Mechanism

The ACD operates only on the first image (also assuming that the object is present in that image) but can be executed later if required, as mentioned previously. At first the acquired image frame is blurred to remove noise. A color filter (consisting of the known dominant colors of the GP) is applied to this to remove the regions consisting of the GP background. This leaves only the object to be detected along with other objects which might be present on the GP. Note that a rather trivial assumption here is that the GP's dominant color is not the same as that of the object. Subsequently the following two steps are performed:

- **Sweep of the HSV color space in *hue* intervals:** Consecutive color filters are applied for every interval in the *hue* range. Although the *hue* space is swept in the tonality in intervals of ten, the *value* and *saturation* intervals are constant in order to get different intensities for each color. For each *hue* interval we do the following. Take the GP color-filtered image and re-filter it for the *hue* interval in consideration. The output image now consists only of the pixels belonging to

that *hue* interval. We then find the contours on this output image. If the area of any contour is less than a certain predefined threshold value, it is discarded as noise. We then compute the minimum enclosing circles for each of the remaining contour and the area of those enclosing circles. The relative error between the area of each enclosing circle and the respective internal contour is also computed. The minimum relative error among all the contours corresponding to that *hue* interval is compared with the absolute minimum relative error from all the previous *hue* intervals (already processed), saving only the smallest.

- **Detecting the color:** After the sweep is finished, the *hue* interval that has the contour with the least relative error is the one corresponding to the color of the object. The entire ACD algorithm detailing these two steps is presented in Figure 1.

The reason why the contour and the *hue* interval corresponding to the least relative error is considered to be that of the object (object to be detected) lies in the circular shape of the object's projection. In an ideal scenario, the contour of the object's projection will be circular in shape and the minimum enclosing circle for that contour will be the contour itself causing the relative error to be zero.

### B. Spherical Object Detection Mechanism (ODM)

Once the color of the object is detected, every subsequent frame is filtered by the *hue* range found by the ACD. The filter consists of a threshold function, which sets a pixel to the value one (white) if it belongs to the *hue* range of the object, and zero (black) in the other case. Further, we compute (after removing noise) the centroid  $(\bar{x}, \bar{y})$  of all the white pixels, resorting to the image's spatial moments. The centroid pixel corresponds to the position of the object (center of the spherical object) in the robot's frame, which is the output of the ODM.

$$m_{ji} = \sum_{x,y} I(x,y)x^j y^i$$

$$\bar{x} = \frac{m_{10}}{m_{00}}, \bar{y} = \frac{m_{01}}{m_{00}}$$

### C. Kalman Filter-based Object Tracking

In order to track the object efficiently and robustly we used a standard Kalman Filter (KF). The ODM is used as the measurement source for the object's position and is used in the KF's update step. For the prediction step, the motion of the robot and that of the object was taken into account. Most of the KF's mathematical details presented here are adapted from [13].

The object's motion is assumed to be a constant velocity plus zero mean Gaussian acceleration noise model and the robot is assumed to move with a constant linear and angular velocities with negligible accelerations. The conversion of the object's velocity from the global frame to the robot frame is done as follows.

Let  $v_o^r$  denote the object's velocity in the robot's frame,  $v_o^g$  denote the object's velocity in the global frame,  $v_r$  denote the robot's linear velocity (always in global frame) and  $\omega_r$  denote the angular velocity of the robot about an axis passing through its center of mass and perpendicular to the GP.  $p_o^r$  denotes the position of the object in the robot frame. The differentials of these variables are denoted in the dot-format.

$$\begin{cases} v_o^r = v_o^g - v_r - \omega_r \times p_o^r \\ \dot{v}_o^r = \dot{v}_o^g - \dot{v}_r - \dot{\omega}_r \times p_o^r - \omega_r \times v_o^r \end{cases} \quad (1)$$

Since the the robot's and the tracked object's accelerations are assumed to be zero, i.e.  $\dot{v}_o^r = \dot{v}_r = \dot{\omega}_r = 0$ .

$$\dot{v}_o^r = -\omega_r \times v_o^r \quad (2)$$

To obtain the object's velocity in the robot frame, the robot's velocity adds negatively to the object's velocity in the global frame. An intuitive reasoning is that a static object (implying zero global velocity) would be seen as moving in the opposite direction of the robot's velocity direction when the object is viewed from the robot frame. The robot's angular velocity also affects negatively to the apparent object movement in the robot frame for the same reason.

The state to be estimated by the KF is denoted by  $\mathbf{x}$  where  $\mathbf{x} = [p_o^r \ v_o^r]^\top = [p_{o_x}^r \ p_{o_y}^r \ v_{o_x}^r \ v_{o_y}^r]^\top$ , which consists of the 2D position and velocity of the object in the robot's frame of reference. The discrete time state transition model and the observation model is given by (3). Henceforth  $(t)$  associated to any variable denotes its value at the timestep  $t$ .

$$\begin{aligned} \mathbf{x}(t) &= \Phi(t)\mathbf{x}(t-1) + \Gamma(t)u(t) \\ \mathbf{z}(t) &= H(t)\mathbf{x}(t) \end{aligned} \quad (3)$$

where

$$\Phi(t) = \begin{bmatrix} \cos(\Delta\theta) & \sin(\Delta\theta) & \Delta t \cos(\Delta\theta) & \Delta t \sin(\Delta\theta) \\ -\sin(\Delta\theta) & \cos(\Delta\theta) & -\Delta t \sin(\Delta\theta) & \Delta t \cos(\Delta\theta) \\ 0 & 0 & \cos(\Delta\theta) & \sin(\Delta\theta) \\ 0 & 0 & -\sin(\Delta\theta) & \cos(\Delta\theta) \end{bmatrix},$$

$$\Gamma(t) = \begin{bmatrix} \frac{-\Delta t \sin(\Delta\theta)}{\Delta\theta} & \frac{\Delta t (\cos(\Delta\theta) - 1)}{\Delta\theta} \\ \frac{\Delta t (\cos(\Delta\theta) - 1)}{\Delta\theta} & \frac{-\Delta t \sin(\Delta\theta)}{\Delta\theta} \\ 0 & 0 \\ 0 & 0 \end{bmatrix},$$

$$H(t) = \begin{bmatrix} 1 & 0 & 0 & 0 \\ 0 & 1 & 0 & 0 \end{bmatrix}, \quad (4)$$

$\Delta t$  is the time interval between timestep  $t$  and  $t-1$ ,  $\Delta\theta$  is the angular displacement and  $u(t) = [u_x(t) \ u_y(t)]^\top$  is the linear displacement of the robot between those timesteps acquired



Fig. 2: Perspective lens-based camera mounted on top of a soccer robot

from the robot's odometry measurement.  $z(t)$  denotes the object's observation measurements obtained at the  $t^{\text{th}}$  timestep from the ODM.

The KF's prediction step and the update step are given by (5) and (6), respectively. The prediction is performed whenever new odometry readings are acquired and the update is performed when the object's measurements are obtained by the ODM.

- *Prediction Step*

$$\begin{aligned} \bar{\mathbf{x}}(t) &= \Phi(t)\mathbf{x}(t-1) + \Gamma(t)u(t) \\ \bar{\mathbf{P}}(t) &= \Phi(t)\mathbf{P}(t-1)\Phi(t)^\top + \mathbf{Q}(t) \end{aligned} \quad (5)$$

- *Update Step*

$$\begin{aligned} \mathbf{K}(t) &= \bar{\mathbf{P}}(t)\mathbf{H}(t)^\top (\mathbf{H}(t)\bar{\mathbf{P}}(t)\mathbf{H}(t)^\top + \mathbf{R}(t))^{-1} \\ \mathbf{x}(t) &= \bar{\mathbf{x}}(t) + \mathbf{K}(t)(z(t) - \mathbf{H}(t)\bar{\mathbf{x}}(t)) \\ \mathbf{P}(t) &= (\mathbf{I} - \mathbf{K}(t)\mathbf{H}(t))\Phi(t)\bar{\mathbf{P}}(t) \end{aligned} \quad (6)$$

The *a priori* and the *a posteriori* error covariance matrices are represented by  $\bar{\mathbf{P}}(t)$  and  $\mathbf{P}(t)$  respectively. Both were initialized as identity matrices, whereas the process noise covariance matrix,  $\mathbf{Q}$ , and measurement noise covariance matrix,  $\mathbf{R}$ , are based on the ODM's measurement and odometry errors.  $\mathbf{K}$  denotes the Kalman gain and  $\mathbf{I}$  denotes an identity matrix.

#### IV. TESTBED, IMPLEMENTATION AND RESULTS

##### A. Testbed and Implementation

Our experimental testbed is the RoboCup Middle Sized League (MSL) where one of the most important prerequisites for the soccer playing robots is to detect and track the soccer ball which is a spherical object. As the official rules of the MSL have evolved, one of the major technical challenges in the recent years is to detect and track an unknown color ball. This makes MSL a suitable choice for implementing and evaluating the method proposed in this article. We used one of our omnidirectional soccer robots for the implementation of the proposed algorithm. The robots acquire new odometry readings every 30 milliseconds. To perform the ball's detection,

a perspective lens-based camera (see Figure 2) was fixed on top of the robot at a height of 80cm above the GP and pitched down at an angle of  $40^\circ$  w.r.t the GP. Images from this camera were acquired at 30 frames per second (fps). All involved distance computations are based on the perspective camera projection model. An example of the distortion-corrected image from this camera is presented in the Figure 3. All the robot's softwares run on a Sony Vaio laptop, equipped with an Intel Core i3 2.2GHz (quad core) CPU and 4GB of RAM, which is connected to the robot's sensors and actuators through plug-and-play connections (USB and Firewire).

The ACD, ODM and the KF-based tracker were implemented using the robot operating system (ROS) and OpenCV libraries for image processing related processes. Green and white were considered as the dominant color in the background and were filtered out before the ACD was initiated.

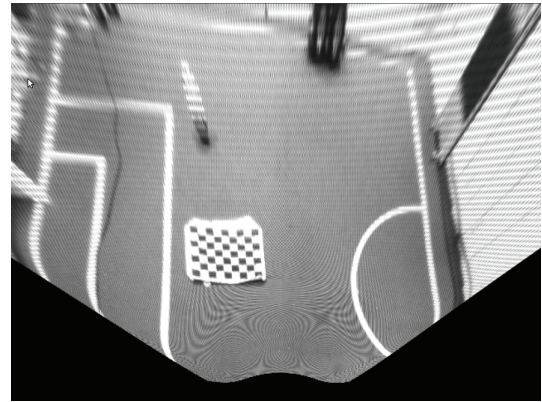


Fig. 3: An example of the distortion-corrected image from the perspective camera.

##### B. results

Experiments were conducted for various balls (note that every ball was uniformly colored, meaning without any significant patterns on it), each of a different color. The robot was able to successfully detect and track the balls upto 6m from itself. Table I shows the range in which the robot was able to detect and track 2 different balls. In Figure 4 we show a series of three images to demonstrate the ACD process. In the first image a red colored ball (color unknown to the detection system) is placed in the field of view of the robot's camera. The second image shows result of filtering the background dominant colors: green and white. The third image shows the contours detected on the remaining image, the enclosing circles on those contours and eventually the chosen circle with the minimum relative error corresponding to the actual ball and its color (marked with fluorescent green color on the image).

We further present the statistical results of the KF-based tracker's implementation in case of the red ball for three separate experiments.

**Experiment 1:** In this experiment the ball was first placed in the field of view of the robot (as it is necessary for the ACD)

Colour	Start Distance (m)	End Distance (m)
Red	2.0	6.2
Yellow	2.0	4.1

TABLE I: Range of tracking achieved by the proposed method on two different balls.

and then moved around the MSL field while the robot was kept static. The robot was able to track the ball successfully even in the case of short-term occlusion. The plots in the Figure 5 present the ball's estimated distance to the robot during the experiment and the KF's innovation over time. The region marked *Occlusion* in the plot of Figure 5 shows the sharp increase in the filter's innovation during the period in which the ball is occluded from the camera's field of view.

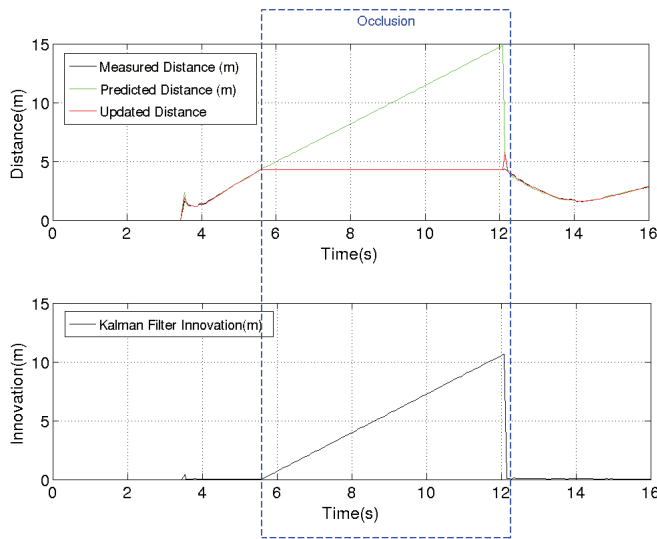


Fig. 5: Results of **Experiment 1** where only the ball was moved while the robot was static.

**Experiment 2:** In this experiment the ball was kept static while the robot was rotated around its central axis perpendicular to the GP so that initially the ball is in the robot's camera's field of view, loses it during the robot's rotation and eventually gets it back in the field of view. Results of this experiment is plotted in the Figure 6 where we show the estimated distance to the ball from the tracking robot, the bearing to the ball w.r.t the robot's heading and its corresponding residual referred to as the KF's angular innovation.

**Experiment 3:** In this experiment both the ball and the robot were moved, however, the ball never left the camera's field of view. Results of this experiment are plotted in the Figure 7 which show both the estimated distance to the ball from the robot and the filter's innovation. From this results we infer that the innovation was slightly noisy (variance of  $\sim 7 \text{ cm}^2$ ) but with a low mean of  $\sim 3 \text{ cm}$ . The reason behind the higher variance lies in the constant velocity plus zero mean Gaussian acceleration noise model used in the KF for the ball's

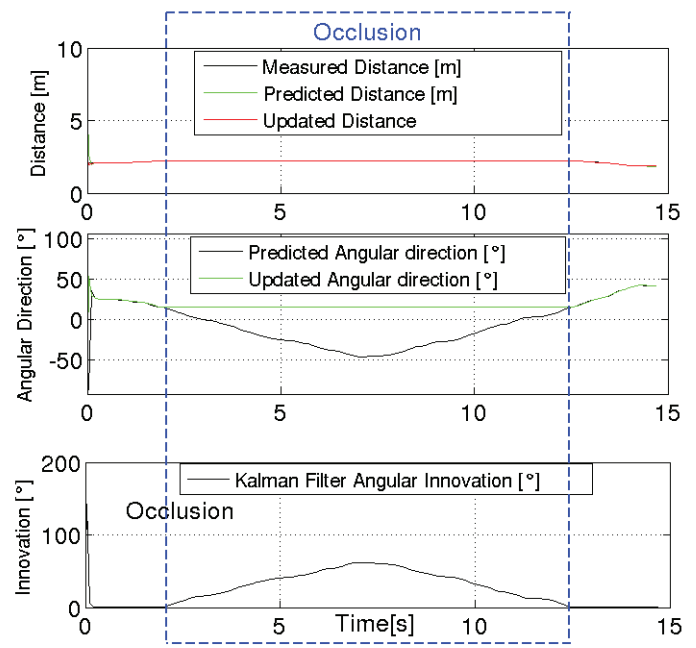


Fig. 6: Results of **Experiment 2** where the ball was static while the robot was rotated around its central axis perpendicular to the ground plane.

motion update. To cope with the erratic movements of the ball, that causes the spikes in the corresponding innovation plot, a more sophisticated motion model would be required, e.g, a mechanism that switches between different motion models depending on the predicted trajectory of the tracked object.

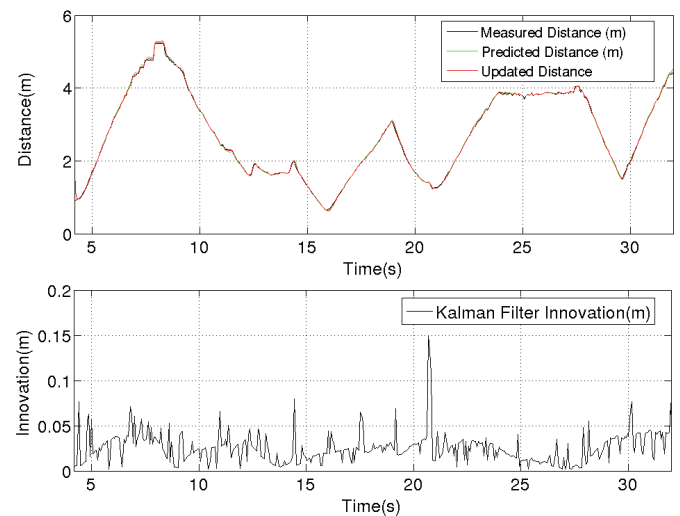


Fig. 7: Results of **Experiment 3** where both the ball and the robot move.

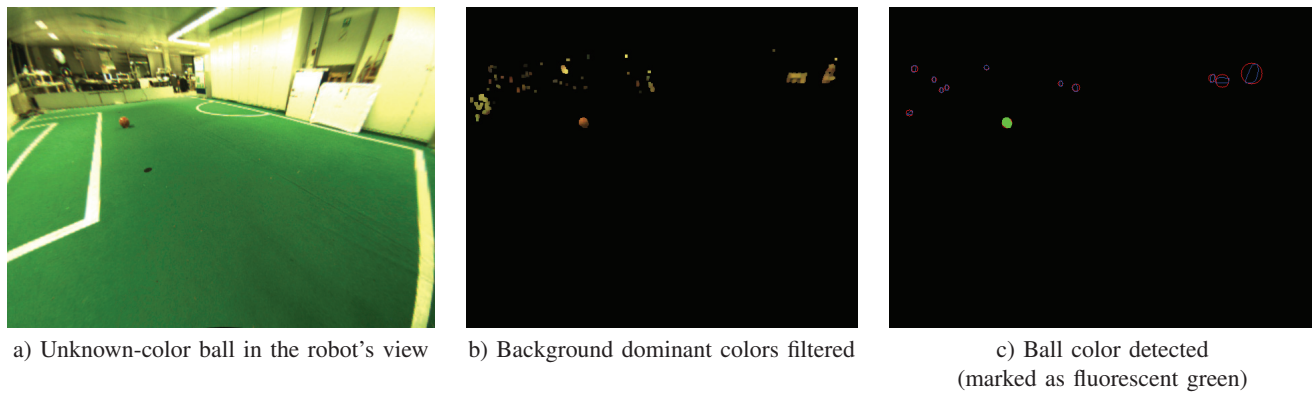


Fig. 4: Demonstration of the automatic color detection (ACD) process.

## V. CONCLUSIONS AND FUTURE WORK

In this article we presented a novel method to automatically detect the color of a spherical object before detecting and tracking it using a Kalman filter-based tracker. The fast execution speed of the color detection method enables it to be executed periodically while running the tracker to cope with the changes in the lighting conditions of the environment. The method was implemented on the soccer playing robots to track unknown-color soccer balls with successful results. A few points that could be enumerated for the purpose of future work are as follows.

- In order to deal better with occlusions and to have a smoother trajectory of the tracked object, cooperation among multiple robots and innovative motion models are required, e.g. an alpha-beta filter [14]. It is a steady-state form of the nearly constant velocity filter. Since an erratically moving object is affected by random positive-mean acceleration, a good object motion model needs to take this effect into account.
- Although the camera is pitched down in our application, it still detects some irrelevant areas of the environment. A possible future improvement would be to choose a configuration where the camera's field of view is better optimized to make use of the maximum possible image space.

## ACKNOWLEDGMENT

This work was funded in part by *Fundação para a Ciência e a Tecnologia* (ISR/IST pluriannual funding) through the PIDDAC Program funds.

## REFERENCES

- [1] C. Lemaitre, M. Perdoch, A. Rahmoune, J. Matas, and J. Miteran, "Detection and matching of curvilinear structures," *Pattern Recognition*, vol. 44, no. 7, pp. 1514 – 1527, 2011. [Online]. Available: <http://www.sciencedirect.com/science/article/pii/S0031320311000148>
- [2] O. Carmichael and M. Hebert, "Shape-based recognition of wiry objects," in *Computer Vision and Pattern Recognition, 2003. Proceedings. 2003 IEEE Computer Society Conference on*, vol. 2, June 2003, pp. II – 401–8 vol.2.
- [3] V. Ferrari, T. Tuytelaars, and L. V. Gool, "Object detection by contour segment networks," in *Proceeding of the European Conference on Computer Vision*, ser. LNCS, vol. 3953. Elsevier, June 2006, pp. 14–28.
- [4] M. Donoser, S. Kluckner, and H. Bischof, "Object tracking by structure tensor analysis," in *Pattern Recognition (ICPR), 2010 20th International Conference on*, Aug. 2010, pp. 2600–2603.
- [5] M. Taiana, J. Santos, J. Gaspar, J. Nascimento, A. Bernardino, and P. U. Lima, "Tracking objects with generic calibrated sensors: An algorithm based on color and 3d shape features," *Robot. Auton. Syst.*, vol. 58, no. 6, pp. 784–795, Jun. 2010. [Online]. Available: <http://dx.doi.org/10.1016/j.robot.2010.02.010>
- [6] M. Wenig, K. Pang, and P. On, "Arbitrarily colored ball detection using the structure tensor technique," *Mechatronics*, vol. 21, no. 2, pp. 367 – 372, 2011,  $\{\text{ce:title}\}$ Special Issue on Advances in intelligent robot design for the Robocup Middle Size League;  $\{\text{ce:title}\}$ . [Online]. Available: <http://www.sciencedirect.com/science/article/pii/S0957415810001297>
- [7] D. Gohring and H.-D. Burkhard, "Multi robot object tracking and self localization using visual percept relations," in *Intelligent Robots and Systems, 2006 IEEE/RSJ International Conference on*, Oct. 2006, pp. 31–36.
- [8] A. Ahmad and P. U. Lima, "Multi-robot cooperative object tracking based on particle filters," in *Proc. of the European Conference on Mobile Robots (ECMR 2011)*, Örebro, Sweden, Sep 2011.
- [9] J. Messias, M. Spaan, and P. Lima, "Multi-robot planning under uncertainty with communication: a case study," in *Multi-agent Sequential Decision Making in Uncertain Domains*, 2010, workshop at AAMAS10.
- [10] J. Matas, C. Galambos, and J. Kittler, "Progressive probabilistic hough transform," 1998.
- [11] D. A. M. Antnio J. R. Neves and A. J. Pinho, "A hybrid vision system for soccer robots using radial search lines," in *Proc. of the 8th Conference on Autonomous Robot Systems and Competitions, Portuguese Robotics Open - ROBTICA'2008*, Aveiro, Portugal, 2008.
- [12] H. Lu, H. Zhang, J. Xiao, F. Liu, and Z. Zheng, "Arbitrary ball recognition based on omni-directional vision for soccer robots," in *RoboCup 2008: Robot Soccer World Cup XII*, ser. Lecture Notes in Computer Science, L. Iocchi, H. Matsubara, A. Weitzenfeld, and C. Zhou, Eds. Springer Berlin Heidelberg, 2009, vol. 5399, pp. 133–144. [Online]. Available: [http://dx.doi.org/10.1007/978-3-642-02921-9\\_12](http://dx.doi.org/10.1007/978-3-642-02921-9_12)
- [13] Z. Marinho, J. Messias, and P. U. Lima, "Multi-object tracking based on histogram classifier and kalman filtering," in *ISR/IST Internal Report*, 2012.
- [14] W. D. Blair, "Design of nearly constant velocity track filters for tracking maneuvering targets."

# Diagonal Walk Reference Generator based on Fourier Approximation of ZMP Trajectory

Rui Ferreira<sup>1,3</sup>, Nima Shafii<sup>2,3</sup>, Nuno Lau<sup>1,4</sup>, Luis Paulo Reis<sup>2,5</sup>, Abbas Abdolmaleki<sup>1,2,4</sup>

<sup>1</sup>IEETA - Instituto de Engenharia Eletrónica e Telemática de Aveiro, Universidade de Aveiro

<sup>2</sup>LIACC - Laboratório de Inteligência Artificial e Ciência de Computadores, Universidade do Porto

<sup>3</sup>DEI/FEUP - Departamento de Engenharia Informática, Faculdade de Engenharia, Universidade do Porto

<sup>4</sup>DETI/UA - Departamento de Eletrónica, Telecomunicações e Informática, Universidade de Aveiro

<sup>5</sup>DSI/EEUM - Departamento de Sistemas de Informação, Escola de Engenharia da Universidade do Minho  
[rui.ferreira@fe.up.pt](mailto:rui.ferreira@fe.up.pt), [nima.shafii@fe.up.pt](mailto:nima.shafii@fe.up.pt), [nuno.lau@ua.pt](mailto:nuno.lau@ua.pt), [lpreis@dsi.uminho.pt](mailto:lpreis@dsi.uminho.pt), [abbas@ua.pt](mailto:abbas@ua.pt)

**Abstract**— Humanoid robots should be capable of adjusting their walking speed and walking direction. Due to the huge design space of the controller, it is very difficult to control the balance of humanoids walk. The position of the Zero Moment Point (ZMP) is widely used for dynamic stability measurement in biped locomotion. The reference trajectory of the Center of Mass (CoM) of a humanoid can be computed from a predefined ZMP trajectory. In order to generate the CoM trajectory, many researchers represent the ZMP equation using the motion equations of simple physical system, e.g. the cart-table model. A Fourier series approximation based method, which generates the CoM trajectory, was previously proposed for straight and curve walking. This paper extends these techniques to generate side and diagonal walking. In order to generate diagonal walking, straight and side walking are combined. The proposed CoM generation approach was tested on a simulated NAO robot. Experiments indicate that the method is successful in generating stable side and diagonal walking. Comparison results of the proposed method with ZMP preview control method show the benefits of the proposed technique.

**Keywords**— Biped Walking; Trajectory generation; diagonal walking;

## I. INTRODUCTION

Humanoid robots are designed with high mobility capabilities. Wheeled locomotion is not appropriate for many human environments, such as stairs and areas littered by many obstacles. However, humanoid robots, due to a larger number of joints are able to avoid obstacles, and attain a wider variety of postures. Therefore, considering this advantage, humanoid robots can function and fulfill their tasks more easily than wheeled robots in domestic areas. In addition, due to the fact that biped locomotion is similar to human movement, people interact more easily with humanoid robots than with other types of robots.

Even though biped locomotion has advantages in many aspects, it is still not used in real common tasks, such as industrial and military activities. A humanoid robot contains many degrees of freedom which increase the dimension of the controller's design space. Due to the huge controller design space, as well as being an inherently nonlinear system, it is very difficult to control the balance of the humanoid robot during walking. The ZMP [1] criterion is widely used as a stability measurement in the literature. For a given set of walking trajectories, if the ZMP trajectory keeps firmly inside the area covered by the foot of the support leg or the polygon

containing the support legs, the given biped locomotion will be physically feasible and the robot will not fall over during walking. Biped walking can be achieved by modelling the predefined ZMP references to the possible body swing or CoM trajectory. The possible CoM can be calculated by a simple model, approximating the bipedal robot dynamics, such as Cart-on-a-table or inverted pendulum model [2].

There is no straightforward way to compute CoM from ZMP by solving the differential equations of the cart-table model. The approaches presented previously, on how to tackle this issue, are organized into two major groups, optimal control approaches and analytical approaches. Kajita has presented an approach to find the proper CoM trajectory, based on the preview control of the ZMP reference, which makes the robot able to walk in any direction [3]. This is a dominant example of the optimal control approach. Some analytical approaches were also developed based on the Fourier series approximation technique, which can create straight walking reference [4] [5]. Recently this reference generation technique has been improved, and tested on the real humanoid robot to generate curve walking [6].

Although making a humanoid robot walk in a straight or curved line is very important and motivating for researchers, generating other types of walking such as side and diagonal walking can improve the ability of a humanoid robot to avoid obstacles. To the best of our knowledge, there is no method based on Fourier approximation to generate side and diagonal walking. Therefore, the contribution of this paper is to extend the Fourier based straight walking approach in [4] [5] into a side and diagonal walking generation approach. In order to create diagonal walking with desired speed, a combination of straight and side walking is required. The speeds on X and Y directions are varied according to user input, which allows the robot to change its walking direction. In order to test its performance, the proposed walking reference generation system is applied to the NAO simulated robot.

In this paper, the results are compared to another well-established method, the ZMP preview control approach. There are also no published studies which compare the outcome results of Fourier based approaches, with the results of the ZMP preview control approach. The experimental results outlined in this paper demonstrate that better side and diagonal walking can be achieved than has previously been achieved in the ZMP preview control approach. The remainder of paper is organized as follows. The next section outlines cart on the table

model and how it can be used for humanoid walking. Section 3 explains the preview controller applied to the biped walking. The diagonal walking reference trajectory generation method based on Fourier approximation is described in Section 4. Experimental and comparison results are presented in Section 5. General conclusions and future work are discussed in the last section

## II. CART-TABLE MODEL APPLIED ON THE BIPED WALKING

Many popular approaches used for joint trajectory planning for bipedal locomotion are based on ZMP stability indicator and cart-table model. ZMP cannot generate reference walking trajectories for walking directly but it can indicate whether generated walking trajectories will keep the balance of a robot or not. Nishiwaki proposed an approach to generate walking patterns by solving the ZMP equation numerically [7]. Kajita assumed that biped walking is a problem of balancing a cart-table model [2], since in the single supported phase, human walking can be represented as the Cart-table model or linear inverted pendulum model [3].

Biped walking can be modeled using the movement of ZMP and body swing. The robot is in balance when the position of the ZMP is in the support polygon. When the ZMP reaches to the edge of the polygon, the robot loses its balance. Biped walking can be achieved by modeling of the desired ZMP to the possible CoM. The body swing can be approximated by using dynamic model of a Cart-on-a-table.

Cart-table model has some assumptions and simplifications in its modeling. First, it assumes that all masses are concentrated on the cart. Second, it assumes that the support leg does not have any masses and represents itself as a massless table. Although these assumptions seem to be far from reality, modern walking robots usually have heavy bodies, with electronics circuits and batteries inside. Therefore the effect of leg mass is relatively small. Fig. 1 shows how robot dynamics is modeled by a cart on a table.



Fig. 1. Schematic view of Cart-table model and a humanoid robot

Two sets of cart-table are used for 3D walking. One is for movements in frontal plane; another is for movements in coronal plane. The semantic view of a cart-table is shown in fig. 2.

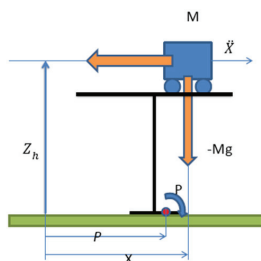


Fig. 2. Schematic view of Cart-table model and a humanoid robot

The position of Center of Mass  $M$  is  $x$  and  $Z_h$  defined in the coordinate system  $O$ . Gravity  $g$  and cart acceleration  $\ddot{x}$  create a moment  $T_p$  around the center of pressure (CoP) point  $P_x$ . Equation (1) gives the sum of the torques at point P.

$$T_p = Mg(x - P_x) - M\ddot{x}z_h \quad (1)$$

We know from [8] that when the robot is dynamically balanced, ZMP and CoP is in the same point, therefore the amount of the moment in the CoP Point must be zero  $T_p=0$ . By Assuming the left hand side of equation (1) to be zero, equation (2) from position of the  $P_x$  and  $x$  can be derived. As mentioned before, to generate proper walking, the CoM must move in coronal plane and another cart-table must be used in  $y$  direction. Using the same assumption and reasoning, equation (3) can be obtained. Here,  $y$  index denotes the movement in  $y$ .

$$P_x = x - \frac{Z_h}{g}\ddot{x} \quad (2)$$

$$P_y = y - \frac{Z_h}{g}\ddot{y} \quad (3)$$

In order to apply cart-table model in a biped walking problem, first the position of the foot during walking must be planed and defined, then, based on the constraint of ZMP position and support polygon, the ZMP trajectory can be designed. In the next step, the position of the CoM from differential equations (2) (3) must be calculated. Finally, inverse kinematics is used to find the angular trajectories of each joint based on the planed position of the foot and calculated CoM.

The main issue of applying Cart-table Model is how to solve its differential equations. Even though theoretically CoM trajectory can be calculated by using the exact solution of the Cart-table differential equations, Applying calculated trajectory is not straightforward in a real biped robot walking because the solution consists of unbounded functions *cosh*, and the obtained CoM trajectory is very sensitive to the time step variation of the walking gait.

An alternative robust CoM trajectory generation method can be found in [4][5], in which the solution of the Cart-pole model differential equation is approximated based on Fourier representation of the ZMP equation. Kajita et. al [3] also presents a very applicable approach to calculate the position of the CoM from the cart-table model. This approach is based on the preview control of the ZMP reference which will be presented in the next section.

## III. PREVIEW CONTROL APPROACH

In this section, the ZMP Preview Control Approach proposed by Kajita et al. will be explained [3], An extended explanation on its stability analysis is presented by Wieber [9]. The jerk  $\ddot{\ddot{x}}$  of the cart areas of the system is assumed as input  $u$  of the cart table dynamics ( $\ddot{\ddot{x}} = u$ ). Considering this assumption, the ZMP equation (2) can be converted to a strongly appropriate dynamical system which is presented in (4)

$$\frac{d}{dt} \begin{pmatrix} \dot{x} \\ \dot{y} \\ \dot{z} \end{pmatrix} = \begin{pmatrix} 0 & 1 & 0 \\ 0 & 0 & 1 \\ 0 & 0 & 0 \end{pmatrix} \begin{pmatrix} x \\ \dot{x} \\ \ddot{x} \end{pmatrix} + \begin{pmatrix} 0 \\ 0 \\ 1 \end{pmatrix} u \quad (4)$$

$$P = \begin{pmatrix} 1 & 0 & -\frac{Z_h}{g} \end{pmatrix} \begin{pmatrix} x \\ \dot{x} \\ \ddot{x} \end{pmatrix}$$

For the Cart table system, a digital controller is designed that allows the system output to follow the reference input. Digital controller input and error signal can be determined by equation (5).

$$u(k) = -G_i \sum_{i=0}^k e(i) - G_x x(k) \quad (5)$$

Here,  $G_i$  and  $G_x$  are assumed as the gain for the ZMP tracking error and the gain for state feedback respectively.  $x$  is the state of the system and denotes CoM positions,  $x = [x \ \dot{x} \ \ddot{x}]^T$ .  $k$  denoted the  $k^{th}$  sample time. Fig. 3 shows the block diagram of the system.

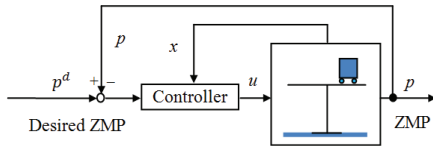


Fig. 3. ZMP Preview control Diagram

It was reported that the controller of equation (4) cannot follow the reference ZMP sufficiently. The main cause of this issue is the inherent phase delay. For addressing this problem, the original digital controller is redesigned in equation (6).

$$u(k) = -G_i \sum_{i=1}^k e(i) - G_x x(k) - \sum_{j=1}^{NL} G_p p^d(k+j) \quad (6)$$

The third term consists of the planned ZMP reference up to  $NL$  samples in future. The approach is called preview controller since the controller applies future information. The gain  $G_p$  is called the preview gain and its profile towards the future is shown in Fig. (4) The magnitude of the preview gain declines quickly with time. Therefore the ZMP preference can be neglected in the far future.

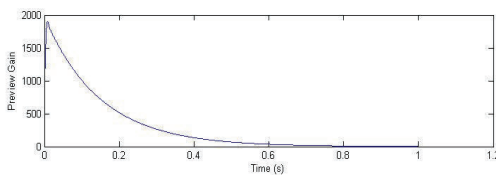


Fig. 4. Gain calculated based on the preview controller

#### IV. FOURIER SERIES APPROACH

In this section the work in [4] is extended to endow the robot with a diagonal walk. First, the reference trajectory for the ZMP is formulated, and then it is approximated by using Fourier series. Finally, the position of the CoM is obtained by solving the differential equations (2) (3) of the cart-table

dynamics while the source term  $P$  is assumed as the approximated ZMP.

In order to determine the reference trajectory of the ZMP, first the ZMP trajectory in a normal diagonal walk is analyzed. Fig. 5 shows the position of feet, on the ground plane, over  $t$  seconds.

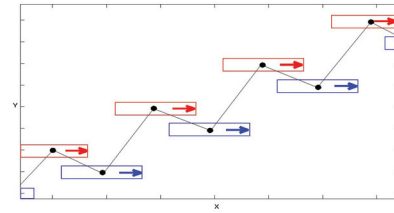


Fig. 5. Foot steps of a diagonal walking

To better understand the ZMP trajectory, ZMP movement is decomposed along  $X$  and  $Y$  axis, giving the advantage to illustrate them as functions of time. Figures (6) and (7) show the ZMP trajectories of  $X$  and  $Y$ , respectively.

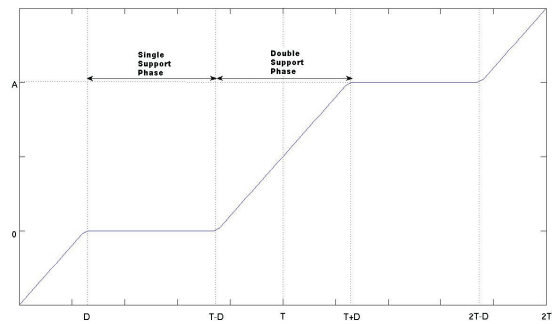


Fig. 6. ZMP trajectory in X direction

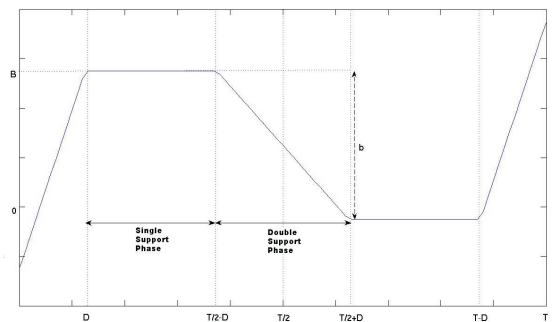


Fig. 7. ZMP trajectory in Y direction

ZMP trajectories can be seen as the combination of periodic and non-periodic component. Figures (8) and (9) illustrate the periodic and non-periodic components of the ZMP trajectories in the  $X$  and  $Y$  direction, respectively.

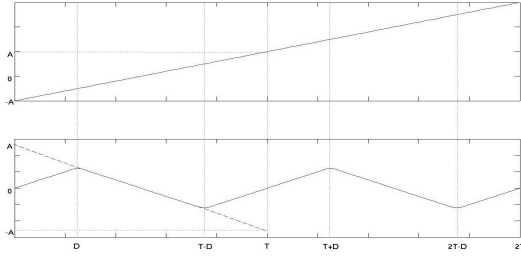


Fig. 8. ZMP component in X direction

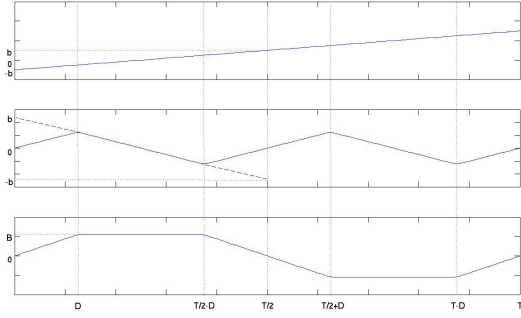


Fig. 9. ZMP component in Y direction

In order to employ Fourier series limited to a certain number of terms, continuous periodic functions are needed. Figures (8) and (9) are employed to determine the equations (7) and (12) for formulating the ZMP reference trajectory in X and Y direction respectively. The equations from (9) to (11) and from (14) to (23) formulate periodic components of the trajectory. The non-periodic component of the ZMP trajectories are presented in equations (8) (13).

This formulation design enhances the approach presented in [4] by adding a double support phase to formulate the ZMP trajectory, allowing to control the amount of double support phase using the parameter  $D$ . The parameters used in the ZMP trajectory formulation are listed in table (1) as well as a brief description of each one.

TABLE I. FORMULATION PARAMETERS

Parameter	Description
T	Period
A	Amount of displacement in X direction
B	Distance between both feet when walking straight
b	Amount of displacement in Y direction
D	Amount of time to be in double support phase

$$ZMP_x^{ref}(t) = f_{x1}(t) + \sum_{i=1}^3 f_{2,i}(t) \quad (7)$$

$$f_{x1}(t) = \frac{A}{T} \left( t - \frac{T}{2} \right) \quad (8)$$

$$f_{x2,1}(t) = A \left( \frac{1}{2D} - \frac{1}{T} \right) \cdot t \cdot (u(t) - u(t-D)) \quad (9)$$

$$f_{x2,2}(t) = A \left( \frac{1}{2} - \frac{1}{T} \right) (u(t-D) - u(t-(T-D))) \quad (10)$$

$$f_{x2,3}(t) = A \left( \frac{1}{2D} - \frac{1}{T} \right) \cdot (t-T) \cdot (u(t-(T-D)) - u(t-T)) \quad (11)$$

$$ZMP_y^{ref}(t) = f_y(t) + \sum_{i=1}^5 (f_{y2,i}(t) + f_{y3,i}(t)) \quad (12)$$

$$f_{y1}(t) = \frac{b}{T} \left( t - \frac{T}{2} \right) \quad (13)$$

$$f_{y2,1}(t) = \frac{2b \left( \frac{T}{4} - D \right)}{DT} \cdot t \cdot (u(t) - u(t-D)) \quad (14)$$

$$f_{y2,2}(t) = -\frac{2b}{T} \cdot \left( t - \frac{T}{4} \right) \cdot \left( u(t-D) - u \left( t - \left( \frac{T}{2} - D \right) \right) \right) \quad (15)$$

$$f_{y2,3}(t) = \frac{2b \left( \frac{T}{4} - D \right)}{DT} \cdot \left( t - \frac{T}{2} \right) \cdot \left( u \left( t - \left( \frac{T}{2} - D \right) \right) - u \left( t - \left( \frac{T}{2} + D \right) \right) \right) \quad (16)$$

$$f_{y2,4}(t) = -\frac{2b}{T} \cdot \left( t - \frac{3T}{4} \right) \cdot \left( u \left( t - \left( \frac{T}{2} + D \right) \right) - u(t-(T-D)) \right) \quad (17)$$

$$f_{y2,5}(t) = \frac{2b \left( \frac{T}{4} - D \right)}{DT} \cdot (t-T) \cdot (u(t-(T-D)) - u(t-T)) \quad (18)$$

$$f_{y3,1}(t) = \frac{B}{D} \cdot t \cdot (u(t) - u(t-D)) \quad (19)$$

$$f_{y3,2}(t) = B \left( u(t-D) - u \left( t - \left( \frac{T}{2} - D \right) \right) \right) \quad (20)$$

$$f_{y3,3}(t) = -\frac{B}{D} \cdot \left( t - \frac{T}{2} \right) \cdot \left( u \left( t - \left( \frac{T}{2} - D \right) \right) - u \left( t - \left( \frac{T}{2} + D \right) \right) \right) \quad (21)$$

$$f_{y3,4}(t) = -B \left( u \left( t - \left( \frac{T}{2} + D \right) \right) - u(t-(T-D)) \right) \quad (22)$$

$$f_{y3,5}(t) = \frac{B}{D} \cdot (t-T) \cdot (u(t-(T-D)) - u(t-T)) \quad (23)$$

The next step is to determine the Fourier series of equations (7) and (12). For this we used the definition of the Fourier series given by (24).

$$f(t) = \frac{a_0}{2} + \sum_{n=1}^N [a_n \cos(nt) + b_n \sin(nt)] , N \geq 1 \quad (24)$$

The results are given by equations (25) and (26) which are approximated ZMP trajectories using Fourier series definition (24).

$$ZMP_x^{fourier}(t) = \frac{A}{T} \left( t - \frac{T}{2} \right) + \sum_{n=1}^N \left[ b_{n,x} \sin \left( \frac{2n\pi}{T} t \right) \right] , N \geq 1 \quad (25)$$

$$ZMP_y^{fourier}(t) = \frac{b}{T} \left( t - \frac{T}{2} \right) + \sum_{n=1}^N \left[ b_{n,y} \sin \left( \frac{2n\pi}{T} t \right) \right], N \geq 1 \quad (26)$$

Where

$$b_{n,x} = \left( \frac{2A \sin \left( \frac{2n\pi}{T} \times DSP \right)}{T \cdot DSP \cdot \left( \frac{2n\pi}{T} \right)^2} \right) \quad (27)$$

$$b_{n,y} = \left( \frac{2 \sin \left( \frac{2n\pi}{T} \times DSP \right)}{T \cdot DSP \cdot \left( \frac{2n\pi}{T} \right)^2} \right) \left( (b - B)(-1)^2 + B + b \right) \quad (28)$$

Finally, it remains to solve the cart-table differential equations (2) and (3) using equations (25) and (26) as source term.

$$y - \frac{Z_h}{g} \ddot{y} = \sum_{n=1}^N \left[ b_n \sin \left( \frac{2n\pi}{T} t \right) \right], N \geq 1 \quad (29)$$

The value of the parameter  $N$  must be a positive integer. The solution will be of the form:

$$y(t) = \sum_{n=1}^N \left[ C_n \sin \left( \frac{2n\pi}{T} t \right) \right] \quad (30)$$

$$\dot{y}(t) = \sum_{n=1}^N \left[ -C_n \left( \frac{2n\pi}{T} \right)^2 \sin \left( \frac{2n\pi}{T} t \right) \right] \quad (31)$$

By substituting equations (30) and (31) to (29), the (32) is obtained.

$$\sum_{n=1}^N \left[ C_n \sin \left( \frac{2n\pi}{T} t \right) \right] - \frac{Z_h}{g} \sum_{n=1}^N \left[ -C_n \left( \frac{2n\pi}{T} \right)^2 \sin \left( \frac{2n\pi}{T} t \right) \right] = \sum_{n=1}^N \left[ b_n \sin \left( \frac{2n\pi}{T} t \right) \right] \quad (32)$$

This equality is true when:

$$C_n - \frac{Z_h}{g} \left( -C_n \left( \frac{2n\pi}{T} \right)^2 \right) = b_n \quad (33)$$

Solving for  $C_n$  and substituting to (30) we get the particular solution for the second order differential equation:

$$y(t) = \sum_{n=1}^N \left[ \left( \frac{b_n}{\left( 1 + \frac{Z_h}{g} \left( \frac{2n\pi}{T} \right)^2 \right)} \right) \sin \left( \frac{2n\pi}{T} t \right) \right] \quad (34)$$

To get the CoM equation all we have to do is to solve the differential equation (29) but changing the right side of the equation with the corresponding ZMP equations (25) and (26). The results are given by equations (35) and (36).

$$CoM_x(t) = \frac{A}{T} \left( t - \frac{T}{2} \right) + \sum_{n=1}^N \left[ \left( \frac{b_{n,x}}{\left( 1 + \frac{Z_h}{g} \left( \frac{2n\pi}{T} \right)^2 \right)} \right) \sin \left( \frac{2n\pi}{T} t \right) \right] \quad (35)$$

$$CoM_y(t) = \frac{b}{T} \left( t - \frac{T}{2} \right) + \sum_{n=1}^N \left[ \left( \frac{b_{n,y}}{\left( 1 + \frac{Z_h}{g} \left( \frac{2n\pi}{T} \right)^2 \right)} \right) \sin \left( \frac{2n\pi}{T} t \right) \right] \quad (36)$$

## V. RESULTS AND DISCUSSIONS

According to section 2, the CoM reference trajectory is obtained by solving the Cart-Table model. Position trajectories of the swing foot are generated through Bézier curve based on predefined footsteps. The swing foot orientation is kept parallel to the ground to reduce the effect of the contact force. Joint angles are calculated based on swing foot positions and CoM references by using inverse kinematics, then joints are controlled by simple independent PID position controllers. The detailed explanation of the techniques, used for inverse kinematics and control of the swing foot positions, can be found in [10] [11].

In this study, a simulated NAO robot is used in order to test and verify the approach. The NAO model is a kid size humanoid robot which has 58 cm height and 21 degree of freedom (DoF). The link dimensions of the NAO robot can be found in [12]. The simulation is carried out by RoboCup soccer simulator, rcssserver3d, which is the official simulator released by the RoboCup community, in order to simulate humanoids soccer match. The simulator is based on Open Dynamic Engine and Simspark [13].

According to literature, there are no published studies to compare the performance of the Fourier based ZMP approximation approach and ZMP preview control approach. In order to test and compare the performance of aforementioned approaches, several robot walking scenarios were designed, in which the simulated NAO robot walks with different speeds from 0 to 0.6 m/s in different directions. The scenarios are designed for different speeds with 0.15 m/s increment in X and Y direction, while the overall speed should not exceed the maximum speed. Parameters used in the walking scenarios are presented in Table 2.

TABLE II. PARAMETERS OF WALKING SCENARIO

Parameters	Value
Step Period	0.2 s
Step Height of the swing foot	0.02 m
Step Size in X direction	3, 6, 9, 12 cm
Step Size in Y direction	3, 6, 9, 12 cm
Percentage of the Double Support Phase (DSP) to the whole step time	15 %
Time of whole walking	4 s, 20 steps
Height of the inverted pendulum ( $Z_h$ )	0.22 cm

All walking scenarios are simulated in the same machine with the same specification. Mean Absolute Error (MAE) of the predefined reference ZMP trajectory and computed ZMP using the two approaches are presented in table 3. The number of the Fourier terms denoted by  $N$  is assumed to be 8. The incremental times of the preview control loop denoted by  $dt$  are assumed to be 0.01, 0.001 and 0.0001.

In average, The MAE in X and Y direction are achieved by the proposed Fourier method are 25 and 3 times less, respectively, than achieved by the preview control approach.

Although by decreasing  $dt$ , the MAE of the preview control will be decreased, but achieving to the performance of the Fourier approach, practically, is not possible. Since the execution time of the algorithm will be increased dramatically. The average and variation of execution times for different specifications on the preview control and Fourier approach are presented in the table 4.

TABLE III. MAE OF COMPUTED ZMP AND REFERENCE ZMP TRAJECORY

Speed (Speed <sub>x</sub> , Speed <sub>y</sub> )	Mean Absolute Error (MAE in X direction, MAE in Y direction)			
	Fourier , N=8	Preview , dt=0.01	Preview , dt=0.001	Preview, dt=0.0001
(0.15,0)	(0.0001167,0.0018)	(0.0044,0.0061)	(0.0031,0.0025)	(0.0022,0.0014)
(0.3 ,0)	(0.0002335,0.0018)	(0.0091,0.0061)	(0.0058,0.0025)	(0.0047,0.0014)
(0.45,0)	(0.0003503,0.0018)	(0.0137,0.0061)	(0.0087,0.0025)	(0.0070,0.0014)
(0.6 ,0)	(0.0004671,0.0018)	(0.0183,0.0061)	(0.0116,0.0025)	(0.0093,0.0014)
(0 ,0.15)	(0 ,0.0018)	(0 ,0.0089)	(0,0.0045)	(0,0.0031)
(0.15 ,0.15)	(0.0001167,0.0018)	(0.0046 ,0.0089)	(0.0029,0.0045)	(0.0023,0.0031)
(0.3 ,0.15)	(0.0002335,0.0018)	(0.0091,0.0089)	(0.0058,0.0045)	(0.0047,0.0031)
(0.45 ,0.15)	(0.0003503,0.0018)	(0.0137 ,0.0089)	(0.0087,0.0045)	(0.0070,0.0031)
(0 ,0.3)	(0 ,0.0018)	(0 ,0.0117)	(0 ,0.0065)	(0 ,0.0049)
(0.15 ,0.3)	(0.0001167,0.0018)	(0.0046,0.0117)	(0.0029,0.0065)	(0.0023,0.0049)
(0.3 ,0.3)	(0.0002335,0.0018)	(0.0091,0.0117)	(0.0058,0.0065)	(0.0047,0.0049)
(0 ,0.45)	(0 ,0.0019)	(0 ,0.0145)	(0 ,0.0085)	(0 ,0.0066)
(0.15 ,0.45)	(0.0001167,0.0019)	(0.0046 ,0.0145)	(0.029,0.0085)	(0.0023 ,0.0066)
(0 ,0.6)	(0 ,0.0020)	(0 ,0.0174)	(0 ,0.00105)	(0 ,0.0083)

TABLE IV. THE AVERAGE (VAR) EXECUTION TIMES OF THE METHODS

Fourier , N=8	Preview , dt=0.01	Preview , dt=0.001	Preview , dt=0.0001
0.0458(1.8482e-006)	0.3013(5.9957e-005)	0.6306(0.0015)	16.5349(0.0014)

After executing the methods for each walking scenarios on the machine, the average execution times for approximating ZMP and generating CoM trajectories, by using the Fourier based approach, was 0.0458 second. It is 15 times faster than the best computation time that could be achieved by using the preview control approach. For a humanoid robot that has limited computational resources, performing a real time task, such as controlling the walking, requires an algorithm with low time complexity like Fourier based approach. CoM reference and CoM position projection on the ground plane for the walking scenario, which has 15 cm/s speed in X direction and 15 cm/s in Y direction, are shown in fig. 10. The generated reference CoM trajectory and executed CoM trajectory by the robot are shown in blue and red lines respectively.

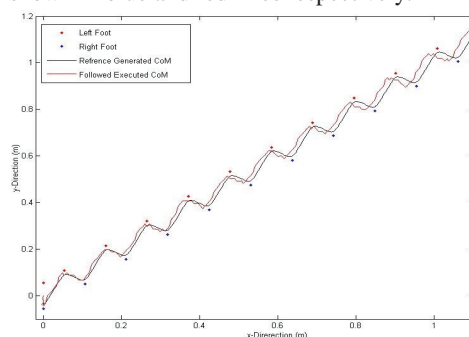


Fig. 10. COM (lines) for the diagonal walk

## VI. CONCLUSIONS AND FUTURE WORK

In this paper an approach to generate the CoM reference trajectory of a diagonal and side walking is proposed. It is the

first time that, by using the Fourier approximation on the predefine ZMP reference, CoM trajectories of diagonal and side walking is achieved. In order to test and validate the results, walking scenarios for the simulated NAO robot with different speeds were presented. The comparison results show that the accuracy and time computation complexity of the proposed method is better compared to the previous approach.

In future work, the proposed method will be tested and implemented on a real humanoid robot. Our aim will be creating an omni-directional walking. Although the experimental results show that the robot can perform forward, side and diagonal walking successfully, extending the approach to make the robot able to do turn in place or curved walking, is also needed, to have a proper omni-directional walking. Following our previous work [14, 15, 16], future work will also be concerned with the application of optimization and machine learning algorithms to improve the results achieved.

## REFERENCES

- [1] M. Vukobratović, D. Jurčić, "Contribution to the synthesis of biped gait" *IEEE Trans. Biomedical Engineering*, vol. 16, no. 1, pp. 1–6, 1969.
- [2] S. Kajita, F. Kanehiro, K. Kaneko, K. Yokoi, and H. Hirukawa, "The 3D linear inverted pendulum mode: a simple modeling for a biped walking pattern generation," in *IEEE/RSJ, IROS 2001*, pp. 239–246.
- [3] S. Kajita, F. Kanehiro, K. Kaneko, and K. Fujiwara, "Biped walking pattern generation by using preview control of zero-moment point," in *IEEE Int. Conf. Robotics and Automation, ICRA, 2003*, pp. 1620–1626.
- [4] K. Erbaturo and O. Kurt, "Natural ZMP Trajectories for Biped Robot Reference Generation," *IEEE Transactions on Industrial Electronics*, vol. 56, no. 3, pp. 835–845, Mar. 2009.
- [5] Y. Choi, B. J. You, and S. R. Oh, "On the stability of indirect ZMP controller for biped robot systems," in *2004 IEEE/RSJ Int. Conference on Intelligent Robots and Systems (IROS)*, 2004, pp. 1966–1971.
- [6] M. Yilmaz, U. Seven, K. C. Fidan, T. Akbas, and K. Erbaturo, "Circular arc-shaped walking trajectory generation for bipedal humanoid robots," in *12th IEEE Int. Workshop on Advanced Motion Control*, 2012, pp. 1–8.
- [7] K. Nishiwaki, S. Kagami, Y. Kuniyoshi, M. Inaba, and H. Inoue, "Online generation of humanoid walking motion based on a fast generation method of motion pattern that follows desired ZMP," in *IEEE/RSJ Int. Conf. Intelligent Robots and System*, 2002, pp. 2684–2689.
- [8] A. Goswami, "Postural Stability of Biped Robots and the Foot-Rotation Indicator (FRI) Point," *The International Journal of Robotics Research*, vol. 18, no. 6, pp. 523–533, Jun. 1999.
- [9] P. Wieber, "Trajectory Free Linear Model Predictive Control for Stable Walking in the Presence of Strong Perturbations," in *2006 6th IEEE-RAS International Conference on Humanoid Robots*, 2006, pp. 137–142.
- [10] R. Ferreira, L.P. Reis, A. P. Moreira, N. Lau, "Development of an Omnidirectional Kick For a NAO Humanoid Robot", *13th Ibero-American Conference on AI, LNAI 7637*, pp 571–580, 2012.
- [11] E. Domingues, N. Lau, B. Pimentel, N. Shafii, L. P. Reis, A. J. R. Neves, "Humanoid Behaviors: From Simulation to a Real Robot", *15th Port. Conf. Artificial Intelligence, EPIA 2011, LNAI 7367*, pp 352–364, 2011.
- [12] D. Gouaillier, V. Hugel, P. Blazevic, C. Kilner, J. Monceaux, P. Lafourcade, B. Marnier, J. Serre, and B. Maisonnier, "Mechatronic design of NAO humanoid," in *Proceedings of the IEEE International Conference on Robotics and Automation (2009)*, 2009, pp. 769–774.
- [13] J. Boedecker, M. Asada, "SimSpark – Concepts and Application in the RoboCup3D Soccer Sim. League," *Aut.Robots*, pp. 174–181, 2008.
- [14] H.Picado, M.Gestal, N.Lau, L.P.Reis, A.M.Tome, "Automatic generation of biped walk behavior using genetic algorithms" In: *IWANN (1)*, Springer LNCS, vol. 5517, pp. 805-812. Springer (2009)
- [15] N.Shafii, L.P.Reis, N.Lau, "Biped walking using coronal and sagittal movements based on truncated Fourier series", (2011) Springer LNAI, Vol. 6556, pp. 324-335.
- [16] L.Cruz, L.P.Reis, N.Lau, A.Sousa, "Optimization Approach for the Development of Humanoid Robots' Behaviors", *IBERAMIA2012*, Springer LNCS, Vol. 7637, pp 491-500, 2012

# Collective Motion Pattern Scaling for Improved Open-Loop Off-Road Navigation

Frank Hoeller, Timo Röhling, and Dirk Schulz

**Abstract**—This paper presents an adaptive navigation system which is able to steer an electronically controlled ground vehicle to given destinations while it adjusts to changing surface conditions. The approach is designed for vehicles without a velocity controlled drive-train, making it especially useful for typical remote-controlled vehicles without upgraded motor controllers. The vehicle is controlled by sets of commands, each set representing a specific maneuver. These sets are combined to form trajectories towards a given destination. While one of these sets of commands is executed the vehicle's movement is measured to refine the geometry of all maneuvers. A scaling vector is derived from the changes in dimensions of the bounding boxes of the assumed and the actual path, which is then used to collectively update all known maneuvers. This enables the approach to quickly adapt to surface alterations. We tested our approach using a 300 kg Explosive Ordnance Disposal (EOD) robot in an outdoor environment. The experiments confirmed that the Collective Motion Pattern Scaling significantly increases the adaptation performance compared to an approach without collective scaling.

## I. INTRODUCTION

In the design of robot systems operating in unstructured outdoor environments special care has to be taken that the robots do not accidentally collide with obstacles in their vicinity. Compared to indoor situations the robot can suffer drastically more damage from the more hazardous surroundings. The risk is increased by different ground surfaces, which have a distinct effect on the wheel grip. The resulting deviation has to be anticipated to ensure the reproducibility of planned motions, and thus making collision avoidance possible.

Additional complications arise for robots which were designed for remote-control. Such robots are usually only equipped with relatively simple motor controllers missing an appropriate servo loop for interpreting velocity commands. Unfortunately, this is a requirement for most classic navigation algorithms. Moreover, the impact of adhesion changes is further intensified by such open-loop controllers because no matter how much the wheel grip, and thus the behavior of the robot changes, there is no feedback of the actual movement. Of course, these problems could easily be solved by using a wheel encoder or similar, but adding such to existing, especially commercial robots is rarely possible. Mostly a time-consuming redesign or an expensive new acquisition are the only options.

In this article we present an approach, which allows a mobile robot with any kind of electronic motor controller to operate in outdoor environments while adjusting to changing surface conditions to provide safety and effectiveness. All components of our system follow a local navigation paradigm and do not need global information on the environment, neither

Frank Hoeller, Timo Röhling, and Dirk Schulz are with the Fraunhofer Institute for Communication, Information Processing and Ergonomics FKIE, Germany



Fig. 1. A Telerob Teodor robot equipped with sensors for basic autonomous navigation.

of surface characteristics nor on obstacles. Instead, the system decides solely based on the robot's sensory input.

The motion planning developed for our robot composes paths by combining predefined Motion Patterns. Each Motion Pattern consists of a set of robot commands and a series of poses that represent the robot's movement when the command set is executed by the controllers. With these Motion Patterns, the local navigation module repeatedly computes trees of command sequences, which are checked for collisions using a real-time costmap. From each tree a path is extracted which brings the robot close to the destination coordinate as fast as possible.

If one is able to measure the robot's motion on the fly, e.g. using SLAM (simultaneous localization and mapping) techniques or an INS (inertial navigation system), one can also monitor movement trajectories. Compared to drive-trains with servo loop that only regard the motor speeds, the results of command sequences can be observed on a larger scale, which allows to tackle the surface traction problem in a novel way: The collected trajectory data is used to update the previously measured movement trajectory of the corresponding Motion Patterns. Furthermore, the detected changes are propagated to all other Motion Patterns by calculating a scaling vector from the alteration in dimensions of a trajectory. The upgraded Motion Patterns are handed over to the planning process and used for the tree generation from then on. Note, that it is not possible to adapt the command sequence to match the desired trajectory because the mapping from trajectories to commands is unknown.

The remainder of this article is organized as follows: After discussing related work in Section II, we introduce our Motion Pattern based local navigation approach in Section III, followed by a description of the learning and collective scaling procedures in Section IV. Before we conclude, we describe some experiments to illustrate the capabilities of our approach. We implemented our approach on a Telerob Teodor EOD robot (Fig. 1) and verified its feasibility in outdoor settings.

## II. RELATED WORK

In the field of outdoor robotics the terrain always is of special interest. The analysis and classification of different surfaces regarding their traversability has been addressed by many different authors. The classification of the different surface types using vibration sensors is very popular because this sensing mode is not vulnerable to lighting or perspective issues. Brooks et al. [1] attached this kind of sensor to axle arms and classified different terrains by traversing them. They used offline learning in combination with a voting mechanism to enable the system to identify a set of different surfaces. Unfortunately, classification approaches of this type can only identify known terrains without deriving information concerning the behavior of a vehicle on the respective surface. The identified terrain type would have to be associated with a parameter set for the trajectory generator in an intermediate step. Furthermore, this would make the navigation dependent on the a priori learned identification data, which would violate the intended local navigation paradigm.

The DARPA Grand Challenge winning robot Stanley [13] also uses a vibration sensor to regulate its maximum speed. Unwilling to catalog every possible terrain type, Stavens et al. evaluate the occurring vibrations to limit Stanley's speed according to observed human driving behaviors [11]. A similar approach is presented by Castelnovi et al. [2], but instead of sensing vibrations the authors used a 2D laser range finder aimed downwards to calculate a ruggedness grade. Based on this result the robot's top speed is reduced, resulting in a decreased number of terrain-related incidents. A combined approach was later proposed by Stavens et al. as an upgrade for Stanley's system [12]. Here a learning component associates vibration intensities with surface profiles measured with a forward-facing 3D laser distance scanner. This way the system can automatically learn terrain-speed-associations. Thus the maximum speed can be adjusted before the vibration sensor detects a surface transition and the vehicle is exposed to less shock. These approaches show several similarities to the technique presented in this paper as the analysis of the ground directly affects the local navigation. Nevertheless, only the maximum translation velocity is altered. Rotation velocities are not addressed at all, which is not necessary for a robot like Stanley.

Another interesting approach by Martinelli et al. [6] also uses laser range finders, but in combination with SLAM and Kalman filter techniques. The system is able to determine the systematic component of the odometry error by using the wheel encoder readings and the estimated SLAM position. The non-systematic error, which is more interesting in outdoor applications, can also be determined by a Kalman filter applied on a history of robot states. These are provided by the former Kalman filter, making the estimation indirectly dependent on wheel encoders and closed-loop control.

Crusher, a six-wheeled robot for extreme outdoor environments also suffered from trajectories differing from planned paths. Seegmiller et al. proposed an approach to automatically calibrate a dynamic model [10]. It linearizes the nominal vehicle model and then calibrates the dynamics to explain the observed prediction residuals using a Kalman filter. Their system, just as our system, takes advantage of the precise short-term localization sensors like GPS and INS. Although

results are impressive, their approach is again tailored to a velocity driven model which unfortunately is not applicable to our robot.

Instead of laser range finders, stereo cameras are also widely used. In [4] a planetary rover navigation suit is presented which uses this type of camera to (besides handling the path planning) classify the terrain and obstacles around the rover. In addition, the system is able to predict wheel slippage based on the same visual data. Again, the used algorithm can only recognize differences to known surfaces, which is negligible if the robot happens to be on a sparse planet. Furthermore, high velocities are not in the focus of planetary rovers yet, thus most rover systems are not suited for other applications.

The combination of motion templates and learning has been used widely in the area of walking robots. In this field, learning techniques are mostly applied to improve walking policies that were derived from simulations [7] or observed from human walking [8]. Furthermore, due to the complexity of biped locomotion, every walking robot is equipped with many sensors to determine its stance and to allow closed-loop control.

Similarly, the concept of motion template based learning has also been employed to simplify the learning of complex motions [9]. In contrast to our approach the templates are parameterized, so they can be adjusted to fit the desired trajectory. This implies a feasible correlation between parameter input and drive-train behavior.

## III. LOCAL NAVIGATION WITH MOTION PATTERNS

The core of the overall approach is a local navigation planning component that directly controls the robot and steers it on a collision-free path from its current position to a given destination in configuration space. For this purpose special precautions for the open-loop motor controllers have to be taken. Since remote-controlled robots lack a velocity regulator circuit, the control commands influence the motor power directly. This induces that their outcome depends on many factors and is far too complex to compute in an online approach. To make motion planning still possible, we introduce Motion Patterns. The first component of a Motion Pattern  $MP$  is a series of robot control commands  $U = (u_1, \dots, u_T)$ . A command  $u_t$  can be of any type and dimension: when used with a Teodor robot they are motor power commands, when controlling a car they probably are throttle position and steering angle. A command sequence  $U$  is immutable, which implies that Motion Patterns cannot be parameterized e.g. regarding their velocity. The second component of a Motion Pattern is an array of oriented relative positions  $R = (\Delta r_1, \dots, \Delta r_T)$ . It represents the trajectory on which the robot would theoretically move when the command series is sent to the robot, so each pose  $\Delta r_t$  describes the relative position of the robot after it executed the command sequence from  $u_1$  to  $u_t$ . The Motion Patterns can now be combined to form motion paths  $P = (R_1, \dots, R_k)$ . Of course it has to be checked if concatenated Motion Patterns fit together so that no harsh velocity change creates unexpected movement trajectories. The created paths can then be checked for collisions e.g. by using

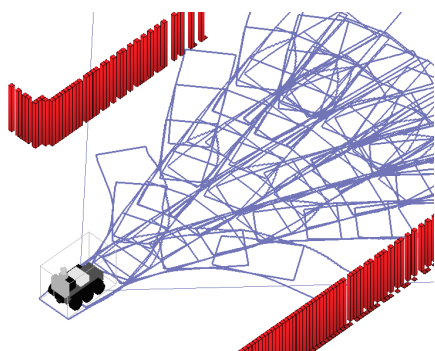


Fig. 2. A planning tree of collision free paths that has been build using Motion Patterns in an 2-dimensional simulated environment.

an occupancy grid [5]. The corresponding sequence of series of commands  $C_P = (U_1, \dots, U_k)$  can be merged to a large array of robot commands which can be executed by the robot sequentially. Notice that the number, shape, and complexity of Motion Patterns are not restricted, but definitely have an impact on the planning process. In general, with fewer patterns a larger range can be covered, while more patterns increase the quality of the resulting paths. Since basic navigation capabilities were sufficient for the following learning algorithm, minimal a set of five Motion Patterns was used, which consisted of command series representing a forward, a left, and a right movement, an acceleration, and a deceleration.

Based on the model above, we can now also build a collision-free tree of Motion Patterns and extract the best path towards the destination. The path planning process is described in detail in [5] and an example tree generated by this technique can be seen in Fig. 2. The theoretical principles of a very similar navigation approach are examined in [3] extensively.

#### IV. MOTION LEARNING USING COLLECTIVE MOTION PATTERN SCALING

A problem arising from our kind of local navigation is its sensitivity to surface and traction changes. Motion Patterns are created for specific surfaces only. And it is unlikely that the surface or the surface's condition always remains constant, especially in outdoor scenarios. As a result, the driven and the previously recorded trajectories may differ.

To compensate for this, the local navigation has been extended by a learning mechanism. While the command set of a selected Motion Pattern  $MP^*$  is executed, the robot's reactions are measured. For this purpose the robot's movement trajectory  $M$ , consisting of the  $x$ ,  $y$  and  $\varphi$  deltas, is recorded. The saved trajectory  $R_{MP^*}$  inside the Motion Pattern  $MP^*$  can directly be updated with this updated measurement. This technique was combined with an exponential smoothing (see below) to form the first version of the learning Motion Pattern based local navigation. The potential of this basic system has been shown in [5]. Both learning approaches, the basic version from [5] and the improved version discussed here, as well as the planning mechanism assume, that applied Motion Patterns yield in similar trajectories repeatedly. The exponential smoothing can cope with singular discontinuities, but it is not able to handle continuously changing results, i.e. occuring on slopes or rough terrain. Both methods are computationally simple and the calculation effort is negligible compared to the time needed for path planning.

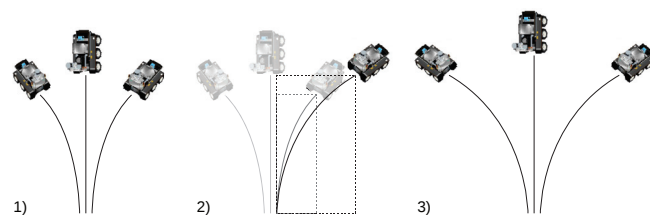


Fig. 3. Evolution of a Motion Pattern set with three patterns: 1) Initial set before a Motion Pattern is chosen and executed. 2) After measuring a Motion Pattern's ( $MP^*$ ) result the bounding box changes are analyzed. 3) All Motion Patterns are scaled yielding to a new set.

The trajectory update inside the Motion Pattern can be regarded as information gain. We would like to propagate this additional knowledge to all other Motion Patterns as well to improve the adaption speed considerably. For this purpose we calculate a vector of scaling factors  $V = (x_s, y_s, \varphi_s)^T$  by comparing the recently measured trajectory and the prediction  $R_{MP^*}$  saved inside the Motion Pattern  $MP^*$ .  $x_s$  and  $y_s$  regard the positions inside the trajectory, and  $\varphi_s$  the trajectory's yaw information. The first approach would be to compare the final pose of the measured trajectory  $M$  and the predicted trajectory from  $MP^*$  to compute these factors. Unfortunately, this would decrease the robustness for trajectories which have a final lateral position close to its initial value (e.g. double-lane change maneuvers). In these cases, it is likely that the measurement noise exceeds the position change, which would generate enormous scaling factors. A similar problem occurs for patterns which only include a movement in only one dimension, e.g. forward motions or in-place turns. Although these patterns can be scaled, they cannot be used to calculate a reasonable scaling vector  $V$  because their movement in the unaddressed axes is only caused by noise and would again generate exaggerated scaling factors. For this reason, patterns like these are taken out of the learning process, because it is not possible to gain information from something, that did not change. To address the former case of this problem, the length and the width of the bounding boxes ( $BB$ ) around the two considered trajectories are used to calculate the scaling factors  $x_s$  and  $y_s$ . The yaw scaling factor  $\varphi_s$  is calculated similarly to the position factor: here the interval between the minimum and maximum of all recorded yaw angles is used. Now we can compute a quotient for every dimension and compose the scaling vector  $V$ :

$$V(M, MP^*) = \begin{pmatrix} x_s \\ y_s \\ \varphi_s \end{pmatrix} = \begin{pmatrix} \frac{\text{Length}_{BB}(M)}{\text{Length}_{BB}(MP^*)} \\ \frac{\text{Width}_{BB}(M)}{\text{Width}_{BB}(MP^*)} \\ \frac{|\text{AngleInterval}(M)|}{|\text{AngleInterval}(MP^*)|} \end{pmatrix} \quad (1)$$

This vector can now be used to collectively scale all Motion Patterns making it possible to update even yet unregarded Motion Patterns. An example application is illustrated in Fig. 3. In this manner the knowledge of change of movement behavior is propagated without the need to wait for every Motion Pattern to be chosen and executed, reducing the adoption time notably.

In both cases, without and with Collective Motion Pattern Scaling, the new predictions are integrated in the Motions Patterns' existing trajectory using a component-by-component exponential smoothing function. This allows continuous learning and at the same time smooths minor surface variations to

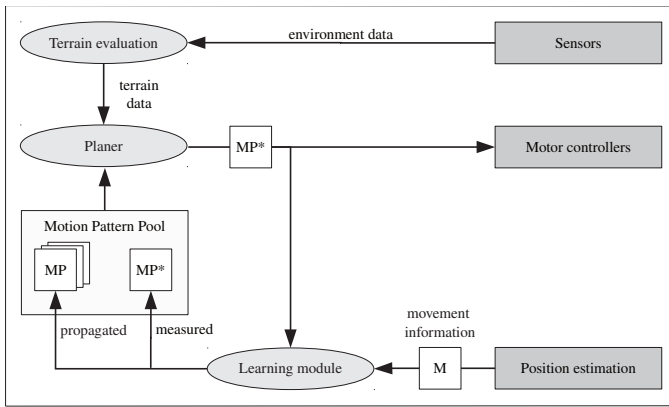


Fig. 4. A flowchart showing the navigation process and the integration of the propagation mechanism. When Motion Pattern  $MP^*$  is chosen, it is used to update its own and all other prediction trajectories.

prevent an oscillating learning behavior:

$$R_{p,t} = (1 - w)M_{p,t} + (w)R_{p,t-1} \quad (2)$$

with  $0 \leq w < 1$ . Here  $M_{p,t}$  is a new trajectory for a Motion Pattern  $p$  at time  $t$ , measured or derived by collective scaling.  $R_{p,t-1}$  represents the existing prediction of the pattern and  $R_{p,t}$  the updated prediction. To limit the impact of new measurements  $w$  is introduced. Setting it to 0.5 turned out to work fairly well. The whole learning approach is outlined in Figure 4 and Algorithm 1. Fig. 4 depicts how the learning mechanism is integrated in the navigation process.

---

**Algorithm 1** Collective Motion Pattern Scaling

---

```

1: while inMotion do
2:   get next Motion Pattern  $MP^*$  from planner
3:   send  $MP^*$  to motor controllers and record motion
4:   let  $M$  be the recorded robot motion
5:   calculate scaling vector  $V$  ▷ see eqn (1)
6:   UPDATEMOTIONPATTERN( $MP^*$ ,  $M$ )
7:   for all other MotionPatterns do
8:     UPDATEMOTIONPATTERN( $MP$ ,  $MP \cdot V$ )
9:   end for
10: end while

11: procedure UPDATEMOTIONPATTERN( $mp$ ,  $update$ )
12:   let  $w$  be the impact reduction
13:    $mp \leftarrow (1 - w) \cdot mp + (w) \cdot update$  ▷ see eqn (2)
14: end procedure
    
```

---

The idea behind this mechanism is that changes in road grip in general affect the forward and lateral movement achieved when executing a command sequence, and that these changes can be approximately captured by the bounding box around the resulting trajectory. Although we disregard it in our learning approach, there certainly is a relation between the length and the width of a trajectory: If the ground surface changes from a sticky to a slippery nature, an executed turn would be wider than before. The resulting bounding box of the trajectory would be longer and correspondingly narrower. But to model this relation more information about the shape of the trajectory would be needed. By the nature of our approach, these are not available, so further detailed analysis of the trajectory

would require more computational time, which at the moment is beyond the time frame of our online application. Surface transitions are likely to change also the orientation of the robot while executing a Motion Pattern. To be able to predict complete poses, the position scaling technique is reduced to one dimension and applied again to the orientation values. In a one-dimensional space a bounding box diminishes to an interval enclosing all occurring yaw angles.

Although not required for the learning technique presented here, it is reasonable that most sets of Motion Patterns contain a number of symmetric patterns, e.g. a left and a similar right turn. If one of these patterns is executed and measured, a very precise prediction for the other is generated, which lessens the error margin of the approximation and thus increases the effectiveness of the collective scaling.

## V. EXPERIMENTS

The system described in the previous chapters has been tested in simulations but using data from a real robot. The Collective Motion Pattern Scaling algorithm proposed here is compared with its predecessor, whose performance is shown in [5]. To demonstrate the performance of the learning and prediction techniques a controlled environment is essential. Although this might be realizable in simulations, the authors have chosen a different approach.

### A. Testing Approach

The following experiment aims at investigating the results of the two mentioned algorithms on a transition from a surface  $A$  to another surface  $B$ . To maximize the quantitative outcome of the experiments the data acquisition was separated from the algorithm tests. For this purpose, the different surfaces were traversed separately to collect data sets for each surface. Later, these sets are used in combination to simulate surface transitions.

In the data collecting stage the robot executed a large number of Motion Patterns on different ground surfaces, one surface at a time. The driven trajectory of each Motion Pattern was collected, resulting in a sample set  $RP_S$  of 300 recordings per Motion Pattern for every considered surface  $S$ . As preparation for the second stage a set of averaged Motion Patterns is calculated from the 300 recordings for each  $RP_S$ . The result is a set of Motion Patterns  $IP_S$  with very precise trajectory predictions for the regarded surface  $S$ . When reproducing a terrain change from a surface  $A$  to a surface  $B$ , the set  $IP_A$  is used as initial Motion Pattern database representing the already learned surface type  $A$ .

For the next step a test sequence  $TS$  of Motion Patterns, which is executed after the virtual terrain change, has to be determined. To show the propagation capabilities, two sequences were chosen and are used alternately. Each sequence consists of three turning patterns resulting in a left-left-right and accordingly a right-right-left motion. Note that the left and the right turn Motion Patterns roughly are mirrored equivalents and have a total length of about a second. The test sequence has to be compiled of turning patterns because straight movements only allow one-dimensional corrections (see Section IV). For each run of the test sequence the initial Motion Pattern database  $IP_A$  is used to create identical starting conditions.

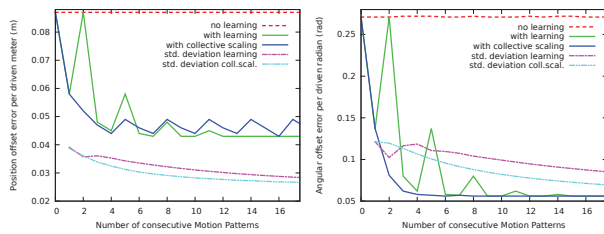


Fig. 5. Error developing of a Teodor robot changing from cinder to grassland during an experiment with extended run-time.

In the next step the test sequence  $TS$  is processed one pattern after another. Before a Motion Pattern's command sequence is sent to a robot, the two algorithms to be tested already have a prediction of the prospective trajectory. The accuracy of these trajectories will be inspected. Instead of sending the command sequence of each Motion Pattern to a real robot and recording its motion anew, the pattern is processed offline: In exchange for the online motion recording, we use a random trajectory recording from the initially measured collection of trajectories  $RP_B$  of surface  $B$ . The trajectory is given to the two algorithms to initiate the learning process to update their predictions for the next request. We assume that the trajectories recorded for a pattern on one particular surface are exchangeable i.e. that the trajectories are randomly distributed given a surface. This allows us to do quantitative evaluations using sampling techniques. Further, this enables us to easily process larger numbers of test repetitions.

The processing of the test sequence is repeated 30,000 times. The random trajectories from  $RP_B$  are chosen anew every time, but in a fashion that both learning algorithms receive the same data in every run. At the end of every pattern of  $TS$ , the final position of the recording is compared with the two position predictions provided by the two learning algorithms.

A disadvantage of this simulation method is that surface changes can only be simulated in between Motion Patterns, which is unlikely to happen in the real world. But even in the likely cases the learning mechanisms would adjust the trajectory predictions in the right direction, still reducing planning error margins. The learning process would only be slowed down, and both algorithms would be affected in the same way.

### B. Testing Results

The input data for this simulation study was recorded using a tracked Telerob Teodor EOD robot which was upgraded with obstacle sensors to enable autonomous behavior (Fig. 1). In addition, an OxTS RT3002 INS was installed to enable easy and precise movement recordings. For the first phase of the experiment the robot was operated on the following four surfaces to collect the data for the sample sets  $RP_S$ : tarmac, grassland, chunky gravel, and volcanic cinder (commonly used for soccer fields). During the experiment the robot always moved at its maximum speed of about 1.0 m/s. The generated sample sets were used to simulate all possible surface transitions.

Table I shows a comparison of four processing methods including a naive and an omniscient policy: a) no learning while keeping the database, b) single pattern learning from [5],

c) learning with collective scaling, d) a priori correctly chosen pattern database with learning deactivated showing the minimal possible errors. The error reduction percentages for the normal learning and the learning with collective scaling are presented in Table II. As in the simulated experiment, the reduction of the orientation error is noticeably higher than the position error reduction. The angular error reduction ranges from 7.3 % up to 27.9 % with one exception that probably resulted from similar surface properties. The position error reduction on the other hand only reaches 17.8 % at best, but is normally below 10 %, sometimes even negative. The measured orientation error values are quite large, but it has to be kept in mind that these are normalized. Just as the position error are scaled with respect to the number of driven meters, the rotation errors are scaled with respect to the covered angle. For the patterns examined here the scaling factor is around 3.

Note that the position error reduction can artificially be improved by increasing the pattern length, taking advantage of the large orientation error reduction. When the pattern length is doubled most of the negative position error reductions raise well above zero. To keep the results realistic, these oversized patterns were not used.

Fig. 6 depicts the error distributions of the two tested approaches when changing from cinder to grassland as an example. The distribution of the position error is not as well formed as the distribution of the angular errors, but still a shift towards small errors can be seen. Most of the error distributions of the other transitions with a crucial reduction look similar.

Since both learning algorithms use the same exponential smoothing function, both errors will correlate with the minimal error if the experiment is continued long enough. Fig. 5 shows the error development of the two algorithms when the chosen Motion Pattern sequence is processed repeatedly without resetting the initial pattern database. Both algorithms reach the minimal error during the extended time span, but especially in the beginning the differences are very large. This confirms that the beginning phase is crucial for a fast adaption, and encourages the concentration on this phase. The position error graph also reveals the reason for the poorer performance of the position estimation: After reaching a value of about 0.045 m, the error begins to oscillate in a range of approx. 0.005 m. These 5 mm are the error caused by the propagation of the Collective Motion Pattern Scaling. At this point the algorithm has reached its highest absolute accuracy; even when extending the Motion Pattern length, the amplitude does not increase.

The long-term experiment also enables us to evaluate the variance of the occurring errors. After the first three patterns the standard deviation with collective scaling is higher than the standard deviation of the simple learning method. This is caused by the exponential smoothing: When it is used, it intentionally prevents instant adaption and generates intermediate trajectory predictions while converging towards the measured behavior. When adding collective scaling, these intermediate predictions appear more often due to the greater number of adjusted Motion Patterns, especially immediately after a surface transition. As soon as the adaption to a new surface is completed, the deviation decreases and stays below the deviation of the simple method.

TABLE I. RESULTS OF THE SIMULATIONS: POSITION (FIRST ROW) AND ORIENTATION (SECOND ROW) ERRORS OF ALL POSSIBLE TRANSITIONS. VALUES DENOTE THE ERROR PER DRIVEN METER/RADIAN. A) NO LEARNING, B) SIMPLE LEARNING, C) COLLECTIVE SCALING, D) OMNISCIENT.

to from	cinder				tarmac				grassland				gravel			
	a)	b)	c)	d)	a)	b)	c)	d)	a)	b)	c)	d)	a)	b)	c)	d)
cinder	-	-	-	-	0.043	0.043	0.042	0.035	0.087	0.077	0.063	0.039	0.063	0.061	0.058	0.046
	-	-	-	-	0.041	0.043	0.042	0.037	0.271	0.226	0.162	0.067	0.164	0.147	0.126	0.099
tarmac	0.059	0.055	0.056	0.041	-	-	-	-	0.060	0.057	0.051	0.039	0.054	0.054	0.057	0.046
	0.107	0.100	0.091	0.030	-	-	-	-	0.204	0.172	0.129	0.067	0.113	0.111	0.109	0.099
grass	0.108	0.093	0.085	0.041	0.071	0.064	0.060	0.035	-	-	-	-	0.063	0.060	0.059	0.046
	0.372	0.313	0.231	0.030	0.256	0.214	0.154	0.037	-	-	-	-	0.165	0.151	0.133	0.099
gravel	0.060	0.056	0.055	0.041	0.045	0.044	0.046	0.035	0.064	0.060	0.057	0.039	-	-	-	-
	0.191	0.166	0.134	0.030	0.090	0.079	0.066	0.037	0.136	0.119	0.098	0.067	-	-	-	-

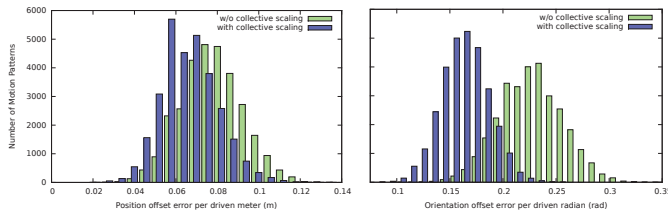


Fig. 6. Result of a simulation: The position (left) and orientation (right) error distribution of a Teodor robot changing from cinder to grassland without and with collective scaling.

TABLE II. THE POSITION (FIRST ROW) AND ORIENTATION (SECOND ROW) ERROR REDUCTIONS OF THE TRANSITION EXPERIMENTS (99% CONFIDENCE).

transition from / to	cinder	tarmac	grassland	gravel
cinder	-	1.5 %	17.8 %	3.4 %
	-	18.5 %	27.9 %	13.5 %
tarmac	-0.5 %	-	10.3 %	-4.9 %
	8.5 %	-	24.9 %	1.2 %
grassland	9.1 %	5.0 %	-	-1.1 %
	26.0 %	27.8 %	-	7.3 %
gravel	0.3 %	-5.4 %	4.5 %	-
	18.4 %	15.6 %	17.2 %	-

## VI. SUMMARY AND CONCLUSION

In this paper we presented an adaptive navigation system based on predefined motion templates called Motion Patterns. The system has the ability to incorporate the actual robot movement into the Motion Patterns. The updating process is not limited to the actually driven Motion Pattern. In most cases the system is also able to derive adjustment information for all other patterns as well. The soundness of our approach has been shown in a simulation study using real-world data. The system proved it can efficiently learn the robot's behavior after transitions between different surface types while outperforming the previous approach without collective scaling. Future work will focus on further improving the performance of the motion learning and adapting mechanisms. Decomposing a Motion Pattern's recorded trajectory in a series of straight lines and connection angles could lead to an improved geometrical understanding.

## REFERENCES

[1] C.A. Brooks and K. Iagnemma. Vibration-based terrain classification for planetary exploration rovers. *Robotics, IEEE Transactions on*, 21(6):1185 – 1191, December 2005.

[2] M. Castelnovi, R. Arkin, and T.R. Collins. Reactive speed control system based on terrain roughness detection. In *Proc. of the IEEE*

*International Conference on Robotics & Automation (ICRA)*, pages 891 – 896, April 2005.

[3] E. Frazzoli, M.A. Dahleh, and E. Feron. Maneuver-based motion planning for nonlinear systems with symmetries. *Robotics, IEEE Transactions on*, 21(6):1077 – 1091, Dec. 2005.

[4] D. Helmick, A. Angelova, and L. Matthies. Terrain adaptive navigation for planetary rovers. *J. Field Robot.*, 26:391–410, April 2009.

[5] F. Hoeller, T. Röhling, and D. Schulz. Offroad navigation using adaptable motion patterns. In *International Conference on Informatics in Control, Automation and Robotics (ICINCO)*, June 2009.

[6] A. Martinelli, N. Tomatis, A. Tapus, and R. Siegwart. In *Proc. of the IEEE/RJSJ International Conference on Intelligent Robots and Systems (IROS)*, volume 2, pages 1499 – 1504 vol.2, Oct. 2003.

[7] J. Morimoto and C.G. Atkeson. Nonparametric representation of an approximated poincaré map for learning biped locomotion. *Auton. Robots*, 27(2):131–144, 2009.

[8] J. Morimoto, J. Nakanishi, G. Endo, G. Cheng, and C. G. Atkeson. Poincare-map-based reinforcement learning for biped walking. In *Proc. of the IEEE International Conference on Robotics & Automation (ICRA)*, pages 2381–2386, 2005.

[9] G. Neumann, W. Maass, and J. Peters. Learning complex motions by sequencing simpler motion templates. In *Proc. of the International Conference on Machine Learning (ICML)*, 2009.

[10] Neal Seegmiller, Forrest Rogers-marcovitz, Greg Miller, and Alonzo Kelly. A unified perturbative dynamics approach to online vehicle model identification.

[11] D. Stavens, G. Hoffmann, and S. Thrun. Online speed adaptation using supervised learning for high-speed, off-road autonomous driving. In *Proc. International Joint Conference on Artificial Intelligence (IJCAI)*, 2007.

[12] D. Stavens and S. Thrun. A self-supervised terrain roughness estimator for off-road autonomous driving. In *Proc. Conference on Uncertainty in AI (UAI)*, pages 13–16, 2006.

[13] S. Thrun, M. Montemerlo, H. Dahlkamp, D. Stavens, A. Aron, J. Diebel, P. Fong, J. Gale, M. Halpenny, G. Hoffmann, K. Lau, C. Oakley, M. Palatucci, V. Pratt, P. Stang, S. Strohband, C. Dupont, L.-E. Jendrossek, C. Koelen, C. Markey, C. Rummel, J. van Niekerk, E. Jensen, P. Alessandrini, G. Bradski, B. Davies, S. Ettinger, A. Kaehler, A. Nefian, and P. Mahoney. The robot that won the darpa grand challenge. *Journal of Field Robotics*, 23:661–692, 2006.

# Localization and Navigation of a Mobile Robot in an Office-like Environment

Paulo Alves<sup>\*</sup>, Hugo Costelha<sup>\*†</sup>, Carlos Neves<sup>\*‡</sup>

<sup>\*</sup>Escola Superior de Tecnologia e Gestão de Leiria, Instituto Politécnico de Leiria, Leiria, Portugal

<sup>†</sup>Robis, INESC TEC, Porto, Portugal

<sup>‡</sup>INESCC, Coimbra, Portugal

PauloFernando.Alves@edp.pt, {hugo.costelha, cneves}@ipleiria.pt

**Abstract** - This article focuses on the localization and navigation of a mobile differential robot in an indoor office-like environment. These are fundamental issues to service robotics, which is a branch with a strong market growth. The work implements a vision tracking system, environment mapping, route planning and navigation for an autonomous robot application inside services buildings. One goal of the methodology is its application with low cost equipment. The test bed chosen was a Pioneer P3-DX robot [16] in a service building, with an attached USB webcam, pointed at the ceiling to take advantage of the position of the light fixtures as natural landmarks. The robot location is estimated through two distinct probabilistic methods: a particle filter, when there is no information about the starting location of the robot, and the Kalman filter, given the convergence of the particle filter. Both methods use the detection of light fixtures together with the robot kinematics as information to estimate the pose. The mapping of the environment and its obstacles is obtained from the localization estimates and the information gathered by ultrasound sensors, representing the entire navigation space discretized in the form of an occupation grid. Planning the navigation path is determined by a simple search algorithm, namely the Wavefront algorithm, based on the information contained in the occupancy grid. For a given path, navigation is performed with obstacle avoidance using the virtual forces method. Replanning is used to recover from local minima situations.

**Keywords:** *Mobile Robots, Localization, Navigation, Mapping, Office Environment.*

## I. INTRODUCTION

Mobile robotics is currently considered a major area of interest, where there is a great willingness by the scientific community to develop its state of the art. Moreover, its interdisciplinary nature and the complexity of the associated problems make this advance depend on the development of mathematical tools, sensors, actuators and the materials themselves, which limit their progress. Whichever vehicle you want to use an autonomous behavior in, whether in health care, assistance at home, industry or even in an office environment, the basis of their performance includes localization and navigation tasks. In the particular case of offices, despite the circulation of a significant number of people, the environment is highly structured, with unique features which facilitate localization and navigation.

Mobile robots have unique capabilities to perform tasks requiring mobility that can be automated, freeing humans to other more creative activities [11]. Today there are several tasks already automated in different areas, such as the mapping and monitoring of land surface [1], large-scale agriculture [3], environmental monitoring [20] and industry [2]. On the other hand, there are high risk tasks or ones which are even impossible to accomplish by humans, such as the verification of explosive devices [5], the exploration and mapping of areas contaminated by biological or nuclear waste to assess the damage [15], or even space exploration of distant celestial bodies [13]. There are other emerging application areas, such as personal assistance [21], rehabilitation and entertainment. For this type of applications to be possible with some degree of autonomy, robots must be equipped with various types of sensors (force sensors, inertial sensors, GPS, odometry, distance sensors or vision), to feedback the work environment perception. The robot movement can be made either by wheels or tracks, on land robots, propellers or wings, for aerial robots, and control surfaces or propellers for aquatic robots. Whether on land, air or water, two fundamental problems coexist: localization and navigation. These two problems are interdependent and crucial for autonomous mobile robotic systems to interact with the physical world correctly by extended periods of time.

In [18] a filter of Simultaneous Localization and Map Building SLAM [12] is presented, which successfully exploited a low cost vision system, with means to improve dead reckoning pose estimate and maintain a correct estimate of the pose of a mobile robot for constructing a map of the environment. As in the present work, limited resources of hardware and low cost vision were used. These limitations impose the use of image processing algorithms involving low processing requirements. To avoid the computational complexity, the paper proposes a fast algorithm for feature extraction which includes the lens distortion model from the SLAM filter. In this methodology, as well as in the present work, the light fixture positions were used as natural landmarks. Unlike the present work, in [18] the light fixture poses are not known a priori and will be mapped during navigation. Present work provides a better accuracy in pose estimate, since light fixture poses are known instead of calculated based in detection and pose estimation.

This paper proposes the application of various methods to solve the problem of localization and navigation of a Pioneer P3-DX mobile differential robot in an indoor environment (the robotics laboratory and adjoining hallways of *Escola Superior de Tecnologia e Gestão*, ESTG, from the Polytechnic Institute of Leiria). It describes an autonomous navigation algorithm, requiring only the indication of the destination point. The algorithm takes advantage of the environment structure elements using low cost sensors, while minimizing the use of techniques which are computationally expensive, so as to be used in systems with limited computational resources. This work aims to be the base for a guide robot or an autonomous system at ESTG.

The problem of localization was divided into two distinct situations: when there is confidence in the estimate of the real pose and when that confidence is insufficient. In the situation where there is a good confidence in the pose estimate, a Kalman filter [10][14] is used, which is a unimodal estimator, allowing to correct the accumulation of odometry errors during navigation. When there is insufficient certainty in the pose estimation, a Particle Filter [10] is used, which is a multimodal estimator that assumes that the robot can be in a number of possible poses. To use these probabilistic methods one needs information about the environment. As one of the goals is to save computational and economic resources, an off the shelf artificial vision system was used, with a video webcam mounted on top of the robot, pointing at the ceiling in order to recognize the light fixtures as natural landmarks.

For a planned navigation one needs to determine waypoints and, therefore, the occupation of the workspace must be integrated in the model. With this goal in mind, a representation of space was implemented in the form of an occupancy grid, where every cell represents the probability of occupation of the corresponding space. This grid is updated based on the distance information provided by the ultrasound sensors and actual pose estimate, as long as the localization estimate confidence is acceptable. Determining the path to follow is implemented with the Wavefront algorithm, based on the information in the occupancy grid. Finally, the virtual forces method is used to execute the planned path, taking into account the distance information from ultrasound sensors to avoid unexpected obstacles.

Aiming to give the work a strong portability and reuse, and given current trends in the field of robotics, the implementation of this system was based on the ROS environment [19]. It is a development environment which provides a set of libraries and tools that facilitate the implementation of mobile robotics applications. This includes a strong abstraction layer of the hardware, peripheral drivers, data viewers, messaging, package management, and makes easier the reuse and publication of the developed work. This software is available under various open source licenses, mainly the BSD license.

The remainder of this paper is organized as follows. Section II addresses the issues of artificial vision, recognition of objects in images from the webcam and the representation of objects as natural landmarks in the robot

coordinate frame. Section III deals with localization, divided in global localization and accumulation of errors correction. Section IV details the mapping of the environment in the form of an occupancy grid. Section V describes the planning algorithms and path execution with unexpected objects avoidance, while Section VI describes the use of the ROS environment. Conclusions and future works are presented in Section VII.

## II. ARTIFICIAL VISION

One of the goals of this work was the use of low-cost equipment and algorithms that do not require high computational resources. For this purpose one used the recognition of elements of the ceiling, namely the pose of light fixtures, as illustrated in Fig. 1. Generally there are no obstacles between the robot and these, allowing for an easier and consistent detection. Moreover the fact that this type of structure typically exists in any office-type environment, allows the developed algorithms to be used generally for indoor service robots.



Fig. 1. Workspace plan with the light fixtures location.

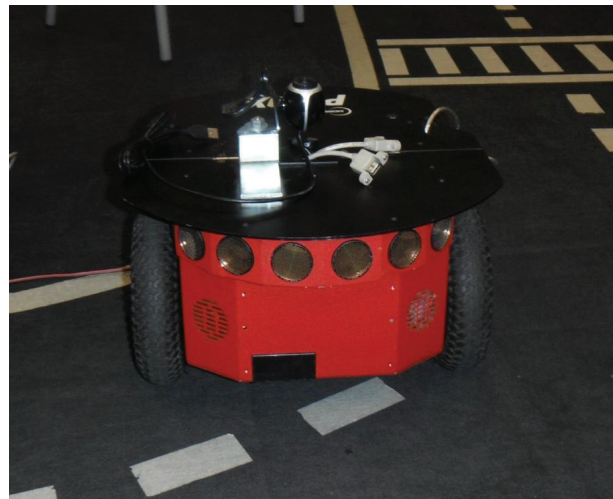


Fig. 2. Webcam mounted on top of the robot.

The vision system used in this work is based upon a low cost webcam, mounted on top of a mobile robot, pointed at the ceiling, as illustrated in Fig. 2. The camera transmits the data to the robot PC via an USB connection. The images are processed for the detection of the light fixtures position and orientation on the robot local reference frame, according to an algorithm divided into three steps: feature extraction,

characteristics validation and calculation of the pose in local coordinates.

In order to reduce the computation resources needed, the image is processed in grayscale. To better adjust the image to the lightning conditions the sensor exposure time is controlled to keep the average pixels value in a given range. The algorithm performs feature extraction using information from the luminance level of the pixels of the digitized image. Assuming that a light fixture on, has a high value of luminance, a threshold operation is performed with a high value to distinguish pixels corresponding to a lighted light fixture. Frequently the level of natural illumination is adequate and the lamps are off, or partially off. In this case, the pixels corresponding to an unlighted light fixture has a luminance lower than the ceiling. For detection of these light fixtures another threshold operation is performed, this time with a reduced value and lower than operation. These two operations are combined and the resulting binary image is subject to erosion followed by dilation operations in order to smooth the contours and eliminate small areas. These areas correspond to reflections or small elements too dark or too bright which might be rejected in the validation process.

After these operations a contour detection is done using the Canny algorithm [8] and the calculation of the respective areas. Only contours with sufficient area and length, corresponding to light fixtures dimensions in image units, will be considered. Due to the existence of light fixtures with two lamps with only one lighted up, and light fixtures in corridors containing only one lamp, the width value considered valid lies between the height of the light fixture with two lamps and the height of a light fixture with only one lamp. For these values a tolerance is allowed for the validation operation to be more immune to variations in ambient lighting. This procedure discards objects which do not match light fixtures dimensions, which would have a negative impact in the localization process.

Using OpenCV library functions [7], the contours moments are determined, and then the mass center and the corners of the smallest rectangle that surrounds the entire contour, which provides the orientation as shown in Fig. 3.

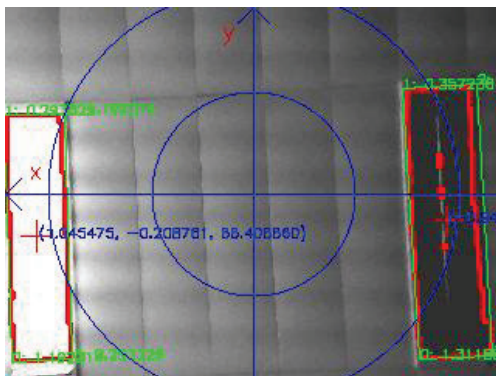


Fig. 3. Results of the light fixtures detection algorithm.

This illustrates the situation in which one light fixture is found on and the other off. The preview of the detected contours are red, the minimum rectangle that surrounds the

contours in green, and the validated information of the light fixture pose in the robot reference frame are shown in blue.

### III. LOCALIZATION

When there is no initial information about the pose of the robot, or the pose estimation confidence is low, one uses a particle filter to solve the global localization problem, which initially generates hypothesis randomly distributed in the available space [4]. Having solved the global localization problem with high enough confidence, the particle filter algorithm is abandoned and the Kalman filter, which is an unimodal estimator, is used instead.

#### A. Global localization

The following describes the application of the particle filter to estimate the robot pose, based on the robot odometry and the pose of the light fixtures detected by the previous method, following the standard three-step approach: prediction, update and resampling.

In the prediction step each particle, which represents a pose hypothesis, is updated based on the information of the robot linear displacement and rotation (odometry), including Gaussian white noise. This particle update is limited to the free map space, since the robot cannot be inside a wall or outside the map.

In the update step, based on the observations of the light fixture, the weight of each particle is calculated. The weight is proportional to the proximity between the expected values for the observations and the values obtained. There is a particular problem that may cause ambiguities, since there is no information about which light fixture was observed; it's assumed that the observed light fixture is the closest from expected position. Two factors are included which help in disambiguation: the orientation of the light fixtures relative to the robot and the space occupation probability for the position of each particle. A noise factor is added corresponding to the observation error model, even when there is no motion. These calculations are represented in equation (Eq.1):

$$w_j = \frac{1}{p(k)} \sum_{i=1}^p(k) \frac{1}{1 + k_d \sqrt{(x_i - \hat{x}_{j_i})^2 + (y_i - \hat{y}_{j_i})^2} + k_\theta \text{abs}(\theta_i - \hat{\theta}_{j_i})} \times P(r_j, c_j) + \text{norm}(\sigma) \quad (1)$$

where  $x_i, y_i$  and  $\theta_i$  correspond to the pose in world coordinates of the landmark  $i$ ,  $\hat{x}_{j_i}, \hat{y}_{j_i}$  and  $\hat{\theta}_{j_i}$  correspond to the landmark  $i$  pose in global coordinates based on the pose of particle  $j$ ,  $k_d$  and  $k_\theta$  are adjustable gains enabling to vary the weight sensitivity to errors in position and orientation,  $P(r_j, c_j)$  is the probability of the space corresponding to particle  $j$  position to be free, where  $(r_j, c_j)$  is the pair row / column corresponding to the position of the particle  $j$  in the occupancy grid, and  $\text{norm}(\sigma)$  is an independent factor representing the observation noise. After

this procedure the weight of all the particles is then normalized so that the sum of all weights is one.

The resampling step consists in replicating the best 10% of particles over the worst 10%. It was further introduced a random redistribution of 5% of the worst particles, to enable recovering from situations where no particles were placed near the robot true pose.

To estimate the pose, one considered clusters of particles with a circular boundary with a radius smaller than the minimum distance between light fixtures, to distinguish the different groups associated with each light fixture possible sighting (see Fig. 4 for an example). The first cluster starts with the particle with the highest weight. Then, for each particle in order of importance, one checks if it lies within the boundaries of an existent cluster. If so, it is considered to belong to that cluster and contribute to its accumulated weight. If the location of the particle is far from existing clusters, it starts a new cluster with the same procedure. At the end of this process all particles will be part of a given cluster, even if it consists of only one particle. The weight of each cluster will be the sum of all weights of the particles that are associated with it. The estimated pose is the average pose of all particles poses of the cluster with higher weight. Generally available clustering techniques, such as K-means [9] or Nearest Neighbor are used with good results, but these are computationally intensive, which is contrary to our goal of having an algorithm with a low computational demand.

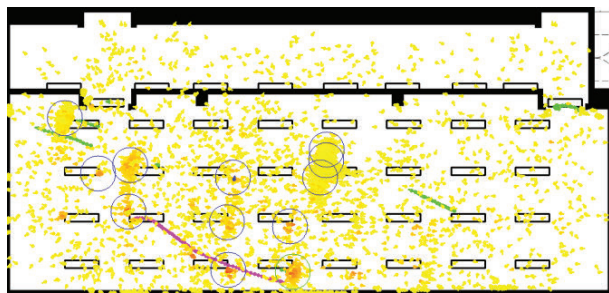


Fig. 4. Particle distribution.

#### B. Localization update after global localization

Having solved the global localization problem, the particle filter is abandoned and the Kalman filter started. The main advantage is the processing time, much lower in the case of the Kalman filter (in our case in the order of tens of ms for each iteration, while the particulate filter takes between 200 and 300 ms by iteration, meaning a factor between 20x and 30x). This happens because in the Kalman filter the calculations are made only for one pose, whereas in the particulate filter calculations are done for all particles. The computational resources are then more available for mapping the environment and navigation (recall that mapping is not done while the robot is not confident enough in its pose estimate). Note that generally the robot only has to perform the global localization when starting, meaning that most of the time it is using the Kalman filter and not the particle filter. Given that the system is non-linear, the Extended Kalman Filter is used, as described in [10]. Here the state of the system to estimate is the robot pose, the

control signal are linear and angular velocity from odometry and the external information is the observed pose of the light fixtures, in world coordinates.

Fig. 5 shows loop closure navigation through the robotics laboratory at ESTG of the robot in teleoperation mode. Localization process started with the particle filter (green) and switched to Kalman filter (blue) after convergence. The odometry data is represented in magenta.

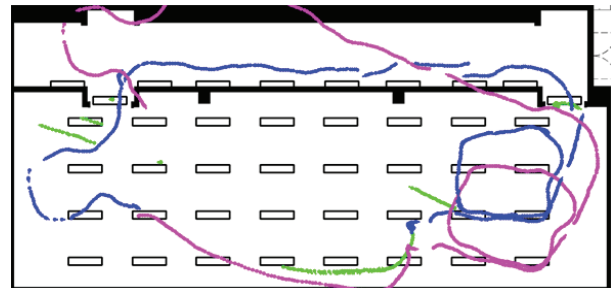


Fig. 5. Loop closure navigation.

#### IV. OCCUPANCY GRID

Space is represented as an occupancy grid based on the estimated pose provided by the localization algorithm and only when there is an acceptable degree of confidence in the estimate. Otherwise the occupancy grid is not updated.

For each distance measurement using the ultrasound sensors one assumes that the volume of the sonar beam, until the measured distance, is likely free space. If the measurement is smaller than the maximum range, at this distance, space is likely to be occupied. For the sake of reducing the computational complexity, one chose to consider only a line segment starting in the sensor with its orientation and ending after the measured distance.

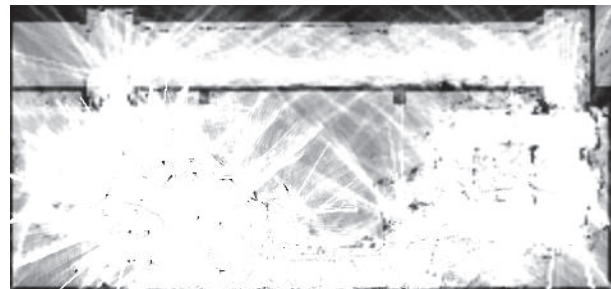


Fig. 6. Occupancy grid.

Regarding the resolution of the sonar sensor and the ultrasonic dispersion cone, a 10 pixel/m resolution to the occupancy grid was chosen. This satisfies the compromise between a good representation of space occupation and processing resources. An example of the occupancy grid is shown on Fig. 6.

#### V. NAVIGATION

After solving the localization problem, one needs to compute the movements required for the robot to reach the

desired pose. This question can be divided in two: deciding which way to go and determining the execution speed.

The Wavefront algorithm [10] was chosen for path planning, since it is one of the simplest solutions that guarantees finding a path if it exists, with immunity to local minima situations. Furthermore its use is possible because the navigation environment is discretized as an occupancy grid. The operating principle of the algorithm is essentially as follows: initially each cell considered as occupied is labeled with the value 1, and each free cell with the value 0. The cell corresponding to the target is labeled with the value 2. In the first step, all cells surrounding the target, using eight-connectivity, are labeled with the value 3. In the next step all cells with the value 0 which involve the value 3 are labeled with the value 4. These causes a "wavefront" to grow from the target cell where, in each iteration, all the cells in the "wavefront" have the same path length, in pixels, from the target cell. This procedure terminates when the "wavefront" reaches the starting point.

To account for the size of the robot, the occupancy grid must be expanded to configuration space, which consists in expanding the occupied space for the robot action radius, as showed in Fig. 7. In order to smooth the navigation trajectory, a temporary objective for navigation is defined, advanced relative to the current position on the path. To do so, the current position on the path was considered as the closest cell to the robot's position in the path set. The objective will be a number of cells along the path, determined by the compromise between a smoother trajectory, and the correct following of the planned path, given existing obstacles. Fig. 9 shows an example of a full planned path.

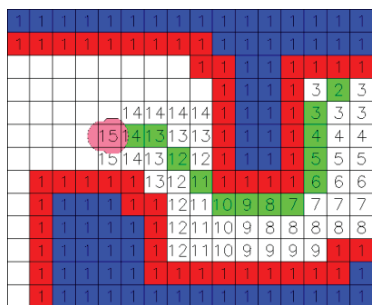


Fig. 7. Path in configuration space

While navigating the path defined above, unexpected obstacles can be founded. To account for this situation, one

uses the information from the ultrasound sensors through the method of virtual forces [6] [17]. When an obstacle is detected on the path ahead, or close to it, its position is associated with a virtual repulsive force and the temporary navigation goal is associated with a virtual attractive force. The orientation of the robot is obtained from the resultant of these forces.

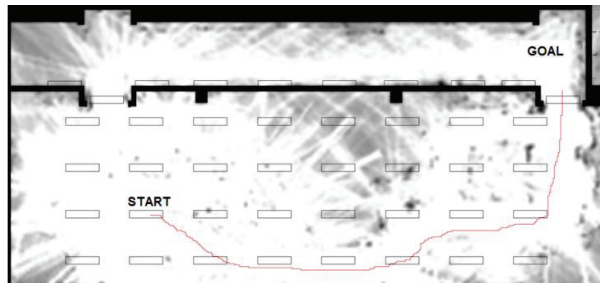


Fig. 9. Path determined by the Wavefront algorithm.

## VI. ROS ENVIRONMENT

To carry out the implementation of these methodologies, we used the ROS [19] development environment from Willow Garage. As stated previously, it consists of a development environment which provides a set of libraries and tools that facilitate robotic applications, especially in mobile robotics. It includes a nearly total abstraction of the hardware, peripheral drivers, data viewers, messaging and package management. Its architecture contemplates the existence of nodes, consisting in applications with the ability to publish and subscribe to topics, which are a type of data bus for transmitting information via messages with predefined data structures.

For the communication with the hardware of the Pioneer P3-DX robot one used the *p2os* node [22], while the *uvc\_camera* node [23] was used to access the webcam, both nodes were provided by the ROS community. The remaining software and algorithms were implemented in the *main\_node*. The representation of the full system structure is illustrated in Fig. 8, where the used nodes and topics are marked in red. This implementation allows using the onboard computer to perform all the computations, but also allows the use of external, or even multiple, computers in the future if needed, with only minimal changes in the configuration

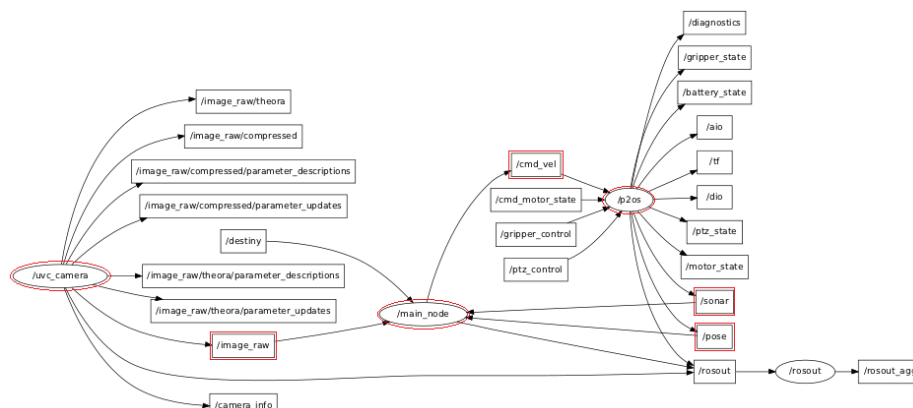


Fig. 8. Full ROS system structure.

## VII. CONCLUSIONS AND FUTURE WORK

A localization and navigation system was implemented to perform general tasks in office-like environments. This system maintains a correct estimate of the robot's pose in real-time, being able to correct the error accumulation of intrinsic sensors and estimate its own pose if this information is not provided in advance.

Artificial vision is used with a common video camera for recognizing ceiling light fixture fixtures as external landmarks, whose poses are known a priori. However, given the similarity between the various fixtures and the symmetry of those poses, the determination between the real and the corresponding fixture detected is strongly dependent on the robot's estimated pose. This may generate erroneous matches, leading to ambiguity and getting reasonable confidence in a pose that may not be real. Also, the ambient lighting conditions can lead to false detections that can compromise severely the location and hence the mapping of the environment. Nevertheless, the continuous movement of the robot combined with the particle filter used for global localization and the Kalman filter localization update, given the localization estimate confidence, allows the robot to recover when lost, and resume its normal operation.

For determining a safe and short path an occupancy grid was kept and updated with information of the space occupation likelihood. This map is updated based on the distance information of ultrasound sensors and pose estimate when this estimate has sufficiently high confidence. Based on the information of this occupancy grid the path to follow is determined with the Wavefront algorithm.

Finally, while performing the determined path, this system reacts to unexpected obstacles such as people or objects left in previously free space. To avoid these obstacles one used the virtual forces method for navigation, resuming the path whenever possible.

To speed up localization it would be interesting to explore matching techniques directly from the camera images or contours with a representation of the light fixtures and other ceiling elements, as air vents and fire detectors. This avoids significant movement without detection of landmarks, resulting in faster convergence for the particle filter and more accuracy for the Kalman filter and mapping. Furthermore, it is also expected to be more immune to erroneous detections caused by reflections, foreign objects or anomalous lighting conditions. This is difficult to combine with a high number of particles because it has to be done for each particle, which leads to a large consumption of processing resources, unavailable on the Pioneer 3-DX robot standard platform.

As a follow up of the present work, one plans to use the developed work as a base for specific tasks, such as an autonomous guide or carrier robot.

## REFERENCES

- [1] Ahmad, A., & Samad, A. (2010). Aerial mapping using high resolution digital camera and unmanned aerial vehicle for Geographical Information System. Signal Processing and Its Applications (CSPA), 2010 6th International Colloquium on .
- [2] Angerer, A., Hoffmann, A., Schierl, A., Vistein, M., & Reif, W. (2010). The Robotics API: An object-oriented framework for modeling industrial robotics applications. International Conference on Intelligent Robots and Systems (IROS), 2010 IEEE/RSJ.
- [3] Arguenon, V., Bergues-Lagarde, A., Rosenberger, C., Bro, P., & Smari, W. (2006). Multi-Agent Based Prototyping of Agriculture Robots. International Symposium on Collaborative Technologies and Systems.
- [4] Arulampalam, M. S., Maskell, S., & Gordon, N. (2002). A tutorial on particle filters for online nonlinear/non-Gaussian Bayesian tracking. IEEE Transactions on Signal Processing.
- [5] Baumann, M., Hunter, J., Hannum, D., & Horton, R. (2004). Robohound™ remote explosives detection. Conference on Security Technology. 38th Annual 2004 International Carnahan.
- [6] Borenstein, J. (1991). The Vector Field Histogram – Fast Obstacle Avoidance for Mobile Robots. IEEE Transactions on Robotics and Automation, Vol. 7, No.3.
- [7] Bradsky, G. R.; Pisarevsky, V.; Bouguet, J. Learning OpenCV: Computer Vision with the OpenCV Library. Springer, 2006.
- [8] Canny, J. (1986). A Computational Approach to Edge Detection. IEEE transactions on pattern analysis and machine intelligence, vol. Pami-8, no. 6.
- [9] S. P. Lloyd, "Least Squares Quantization in PCM," IEEE Trans. Information Theory, vol. 28, 129-137, 1982.
- [10] Choset, H., Lynch, K. M., Hutchinson, S., Kantor, G., Burgard, W., Kavraky, L. E., et al. (2004). Principles of Robot Motion – Theory, Algorithms and Implementations. MIT Press.
- [11] Couto, M. S. (2010). Localização e Navegação entre Robôs Móveis. Dissertação para a obtenção do Grau de Mestre em Engenharia Mecânica - Instituto Superior Técnico.
- [12] Dissanayake, M. W., Newman, P., Clark, S., Whyte, H., & Csorba, M. (2001). A Solution to the Simultaneous Localization and Map Building (SLAM) Problem. IEEE Transactions on robotics and automation, Vol. 17, NO. 3, June 2001.
- [13] Grotzinger, J. P., Ba, J. C., Blake, D. F., & all, e. (2011). Mars Science Laboratory Mission and Science. Space Sci Rev DOI 10.1007/s11214-012-9892-2.
- [14] Kalman, R. E. (1960). A new approach to linear filtering and prediction problems. Journal of Basic Engineering 82 (1), 35–45.
- [15] Manocha, K., Pernalet, N., & Dubey, R. (2001). Variable position mapping based assistance in teleoperation for nuclear cleanup . IEEE International Conference on Robotics and Automation. Proceedings 2001 ICRA.
- [16] Mobile Robots, A. (2010). Pioneer 3 Operations Manual.
- [17] Neves, C. C. (1998). A Generalized Framework for the Analysis of System Architectures in Autonomous Robots. Telford Research Institute Department of Electronic and Electric Engineering University of Salford, UK.
- [18] Panziera, S., Pascucci, F., & Ulivi, G. (2003). Vision based navigation using Kalman approach for SLAM. Proc. of the 11th International Conference on Advanced Robotics.
- [19] Quigley, M., Gerkey, B., Conley, K., Faust, J., Foote, T., Leibs, J., et al. (2009). ROS: an open-source Robot Operating System. ICRA workshop.
- [20] Rahimi, M., Pon, R., Kaiser, W., Sukhatme, G., Estrin, D., & Srivastava, M. (2004). Adaptive sampling for environmental robotics. IEEE International Conference on Robotics and Automation.
- [21] Srinivasa, S. S., Ferguson, D., Helfrich, C. J., Berenson, D., Collet, A., Diankov, R., et al. (2009). HERB: a home exploring robotic butler. Springer Science+Business Media, LLC 2009.
- [22] [http://www.ros.org/wiki/p2os\\_driver](http://www.ros.org/wiki/p2os_driver)
- [23] [http://www.ros.org/wiki/uvc\\_camera](http://www.ros.org/wiki/uvc_camera)

## Design of a 3DOF Passive Rotating Platform for the Adaptive Motion Planning of a Single-Legged Robot

Zhenli Lu

**Abstract**— A 3 DOF (Degrees Of Freedom) passive rotating platform and a simulator with position controller were developed as the stimulus input for a simulated single leg robot system to realize COP (Center Of Pressure) based motion control. The platform contains a board mounted on a tripod by a ball joint. A magnetic tracking sensor is mounted on the board to get the orientation of the rotating platform. The virtual reality tracking system records the rotating information of the platform in real time. According to the orientation of the real platform, the information of the magnetic sensor is used to control a simulated rotating platform. Using the real and virtual rotating platform systems, some experiments were carried out to realize the adaptive motion planning of the simulated single-legged robot.

### I. INTRODUCTION

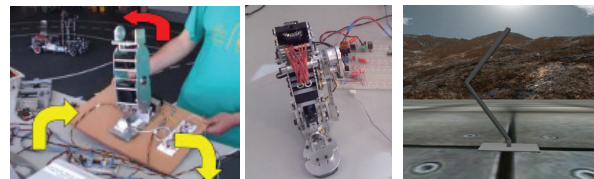
Humanoid robots have been widely developed and studied in universities and research institutes. The research topics on humanoid robot are not only with regard to mechanical and electrical system design, but also motion control and learning [1]. Designing stable walking control methods for biped robot is one of the most difficult research issues [2]. One of the tasks involved in designing algorithms for bipedal robot locomotion is to assess their effectiveness at maintaining balance in a changing environment [3, 4]. To simulate a dynamic environment, a method is used to allow free rotation of the platform by a human operator. For example, in Fig.1 (a) a robotic leg using a Center Of Pressure (COP) controller [5] may be tested for maintaining balance as the human-user continuously rotates the platform in three dimensions under the leg. Having a human-in-the-loop to operate over the platform is a way to imitate an uneven and unstructured environment. The goal is to develop a control algorithm that provides enhanced robustness using the four force sensors (i.e. FlexiForce with U.S. Patent No.6,272,936 ) placed at the bottom of the robotic leg (i.e. part of leg that makes contact with the surface, usually a robotic foot). The global objective is to maintain balance by specifying a desired COP location and a desired hip height profile in the sagittal plane. The force sensors are used to estimate the real COP coordinates. The control system regulates the joint actuators by relating the joint velocities to the error between the desired and the current position of the COP in the X and Y direction, and between the desired and the actual hip position in the Z direction [6].

While developing new mechanical system of the humanoid robot at University of Aveiro, as shown in Fig.1 (b)

Z. Lu is with the Institute of Electronics and Telematics Engineering of Aveiro, University of Aveiro, Aveiro, 3810-193, Portugal, and with the Shenyang Ligong University, Shenyang, 110168, P.R.China (phone: 351-234-370-531; fax: 351-234-370-545; email: zhenli.lu@ua.pt).

[3], a YARP (Yet Another Robot Platform) [7] - based simulated leg model was also developed, as shown in Fig.1(c) to allow COP based motion control experiment and test algorithms before the real leg is built.

Besides improving the performance of the humanoid robot platform, designing the environmental stimulus device for the robot leg motion control is also a very interesting research topic. As a stimulus device, it can generate and record the independent trajectory of pitch, yaw and roll axes. The device to imitate shaking ground information is shown in Fig.1 (a). It is a board rotated by the researcher which is adopted in a robotic experiment to verify the COP leg control methods. It is the interface to realize the “human-in-the-loop” robot experiment. Human movement in the cooperation with robot is difficult, even impossible, to be recreated. Capability to record helps in performing offline evaluation of changes in the environment and corresponding changes in robot's configuration parameters for maintaining balance.



(a) Former demonstration (b) New mechanical system (c) Simulated leg

Figure 1. Leg robot system.

In the context of the current example, the platform is simply a flat board. Such boards are usually supported by stable platforms that support rotational movements.

Ideally, a suitable platform would need to meet following requirements:

1. The platform should be able to perform passive and random rotation in the direction of pitch, yaw and roll, and these rotations can occur either independently or simultaneously;
2. The rotating motion can be read and recorded in real time;
3. The platform should support a board to support the experimental object;
4. The platform should allow active participation of a human operator in controlling the movement of the board (human-in-the-loop interaction); and
5. The rotating axis of pitch, yaw and roll are interacting in one point.

Most of the existing support platforms with rotation capability are designed as the base of a camera. The standard platforms are: manually-driven terrace (passive rotation, see Fig.2 (a)), and motor-driven cloud terrace (active rotation, see Fig.2 (b)).

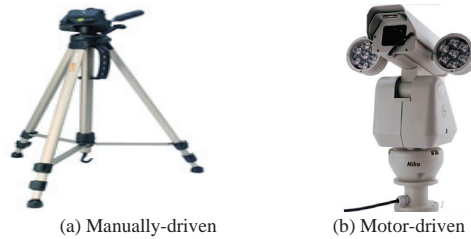


Figure 2. Typical rotating cloud terrace.



Figure 3. 3 DOF input device.

The manually-driven cloud terrace platform can not record its rotating trajectory, and using the motor-driven cloud terrace, it is not possible to realize passive rotation while recording the board trajectory. Two exceptions to these limitations are 3 or 6 DOF input devices, as shown in Figure 3. The PHANTOM haptic device (Fig. 3(a)) allows trajectory tracking in real-time but can not support a board. If it is required to rotate in pitch, yaw and roll, the rotational axes of manually-driven and motor-driven cloud terraces as well as PHANTOM like devices do not cross in one point. The 9000 series of APEM contactless joystick (Fig. 3(b)) are designed for applications that demand proportional control with the lower possible profile below the pane. It uses contactless, inductive sensing and circuitry. If we attach a board on the top of the joystick, the payload and the board itself will break down the sensing circuitry. With the given mechanics in 9000 series of APEM, they can not be directly used to support a payload greater than 0.5kg.

In their current form, these devices are not suitable for being directly adopted for the COP-based human-in-the-loop leg motion control experiments.

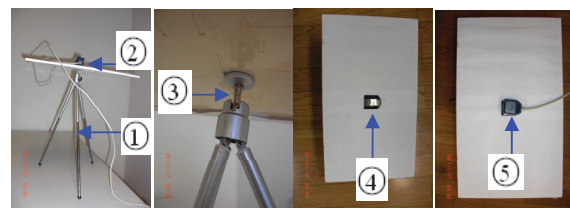
The platform in this paper is designed to meet all the mentioned requirements. It is composed of a scalable tripod with a passive ball joint and a board mounted on the ball joint with a screw bolt. With specific slot on the passive ball joint, the passive platform can realize independent movement of pitch, yaw and roll. WinTracker, a 3D virtual reality tracking system is selected from the existing 6 DOF sensory system [8, 9], and its magnetic sensor is attached to the board to get ball joint Trajectory. The 3D virtual reality tracking system provides the position, and orientation of the rotating board.

Within YARP framework and the general conception of iCub simulator [10-12], the simulator for the rotating platform was developed. The position controller was also designed to control the simulated platform to rotate around pitch, yaw and roll axis.

The human-in-the-loop interface was designed such that when the real platform is rotated by hand, the angle information is recorded by the 3D virtual reality tracking system and sent to the computer, where the position controller of the simulator adopts them as input to rotate the simulated platform. As a primary application, the experiments where the position controllers developed with YARP protocol use the output value of the real rotating platform motion to control simulated platform to realize the COP based adaptive motion control of the simulated leg.

The remainder of this paper is organized as follows: In section II, the passive rotating platform is specified. Section III presents the mixed reality application of this passive rotating platform on COP-based adaptive motion control of a single leg robot. The experiment results are addressed in section IV. Finally, the conclusions and future works are discussed in section V.

## II. SYSTEM SPECIFICATION OF THE ROTATING PLATFORM



### A. Mechanical System

Figure 4. Mechanical system.

- ①: Scalable tripod, ②: Rotation board, ③: Passive ball joint and its slot,
- ④: Standard strip, ⑤: Magnetic sensor.

The rotating platform, as shown in Fig.4, is composed of a scalable tripod, a passive ball joint and a board connected with the ball joint with a tightening screw in joint hedge. The parameters of the rotating platform are shown in Table I.

TABLE I. PARAMETERS OF THE PROTOTYPE OF ROTATING PLATFORM

Dimension of the board: $L_b \times W_b \times H_b$ (cm)	37×23×0.6
Radius of the ball joint: $R_b$ (cm)	0.5
Height of the tripod: $H_s$ (cm)	36

The magnetic sensor is fixed to the surface of the board. The rotating trajectory of the platform is recorded by the magnetic sensor and sent to the computer through the 3D virtual reality tracking system. Low price, simple mechanical and electrical system, free rotation in pitch yaw and roll, and easily recording trajectory in real time are the key aspects of the stimulus device.

B. Control System

The hardware in the control system of the rotating platform is shown in Fig.5. The main component is Wintracker, a 3D virtual reality tracking system. Although Wintracker is a 6 DOF tracking system with three magnetic sensors, in this study, only the rotation information is being used to record the platform trajectory of pitch, yaw and roll axis. The position information can also be taken as a potential function of the rotating platform for robot motion control.

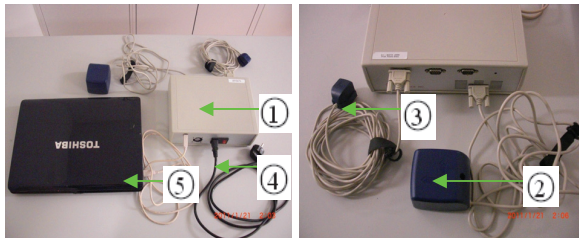


Figure 5. Control system hardware.

①: Control box, ②: Magnetic sensor transmitter, ③: Magnetic sensor receiver, ④: Power line, ⑤: Computer connected by the USB line.

1) Hardware Specification of Wintracker

Wintracker has three magnetic sensory receivers with mounting clips. The magnetic sensor transmitter sends magnetic information. In this rotating platform, one magnetic sensor is put on the top of the board. When the platform is rotated, the origination relationship between the transmitter and the receiver can be recorded and sent to the computer.

The system parameters are listed in Table II. Since it is a magnetic tracker, the system signal can be influenced by metallic objects. Based on the application area and mechanical system integration requirements, similar devices, such as accelerometer-based tracking system, optical-based tracking system and potentiometer-based tracking system can also be adopted to record the trajectories of different passive rotating platforms. This design avoids the excessive use of complex mechanical and electrical parts.

TABLE II. SYSTEM PARAMETERS OF WINTRACKER

<b>Weight : <math>W</math> (Kg)</b>	4.6
<b>Electronics unit : <math>L_e \times W_e \times H_e</math> (cm)</b>	32×20×12
<b>Transmitter : <math>L_t \times W_t \times H_t</math> (cm)</b>	5.5×5.5×5.8
<b>Cable length of transmitter: <math>L_c</math> (m)</b>	4.5
<b>Operating temperature: <math>T</math> (°C)</b>	10~40
<b>Update rate: <math>R_u</math> (outputs/second)</b>	90(1),45(2),30(3)
<b>Operating Voltage: <math>O_v</math> (V)</b>	85~264

2) Data Specification of Wintracker

The data recorded by WinTracker is shown in Table III, that contains the information for Cartesian coordinates of position, Euler angles, quaternion and orientation. In this research, we only use the information of azimuth, elevation and roll angles, as shown in Fig.6. In the rotating platform system, the pitch rotation means to rotate the X axis from +Y to +Z; the yaw rotation means to rotate the Y axis from +X to -Z; and the roll rotation means to rotate the Z axis from +X to +Y.

TABLE III. DATA SPECIFICATION OF WINTRACKER

<b>Position</b> (accuracy in 0.0001 m)	<b>Position X: <math>X</math> (m)</b>
	<b>Position Y: <math>Y</math> (m)</b>
	<b>Position Z: <math>Z</math> (m)</b>
<b>Attitude</b> (accuracy in 0.01 Deg)	<b>Azimuth Attitude: <math>A</math> (Deg)</b>
	<b>Elevation Attitude: <math>E</math> (Deg)</b>
	<b>Roll Attitude: <math>R</math> (Deg)</b>
<b>Orientation</b>	<b><math>Q_w</math> : quaternion component <math>W \times 10000</math></b>
	<b><math>Q_x</math> : quaternion component <math>X \times 10000</math></b>
	<b><math>Q_y</math> : quaternion component <math>Y \times 10000</math></b>
	<b><math>Q_z</math> : quaternion component <math>Z \times 10000</math></b>

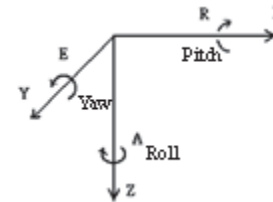


Figure 6. Coordination system.

3) Interface Function Specification of Wintracker

In this study, Wintracker is supplied with Windows compatible data capture software. The sensor data can be saved in a file or as an input to other program in real time. As a functional demonstration, the platform is rotated by hand in one direction, from pitch, yaw to roll and then rotated in arbitrary direction to realize a complex behavior. The joint trajectory is recorded and sent to the computer, and the signal can be easily separated into independent axis data, as shown in Fig.7. The signal can be also recorded with a timer defined by world step size in ODE (Open Dynamic Engineering).

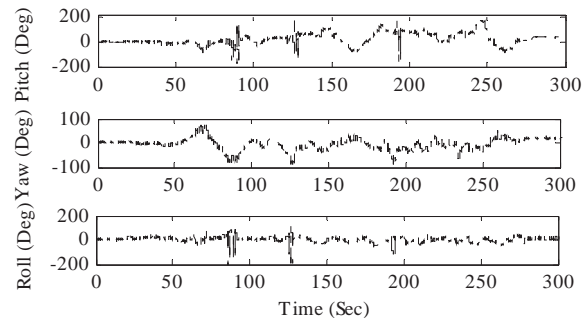


Figure 7. Trajectory of rotating movement.

III. THE MIXED REALITY APPLICATION ON COP-BASED ADAPTIVE MOTION CONTROL OF A SINGLE LEG ROBOT

A. Development of the simulated rotating platform

YARP is an open source middleware which contains a set of software libraries, protocols, and tools to keep modules and devices clearly decoupled. The architecture of the simulator is realized as a set of YARP executables, and models are connected by the YARP port.

In our study, YARP is adopted as the framework to build the simulated leg robot system with COP based motion controller. In this simulation system, a simulated rotating platform is developed with a position controller. The simulated platform is composed of a board and a stick fixed on the ground, as shown in Fig.8 (a). It can also work together with the simulated leg robot [5], as shown in Fig.8 (b).

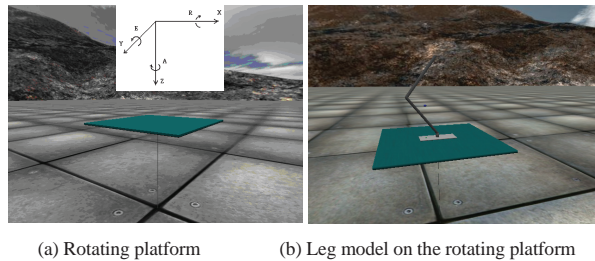


Figure 8. Simulated system.

The simulated platform can be controlled by three independent joint position controllers (software modules developed with YARP protocol) to realize the rotation of pitch, yaw and roll.

#### B. Interface specification of the mixed reality system

The diagram of the control system of the mixed reality system is shown in Fig.9. The trajectory of rotation of pitch, yaw and roll are used as the input of the position controller with the help of Wintracker software. Based on the protocol of YARP, the controller can get its input and command the simulated rotating platform. The rotating platform and the leg model are independent. Based on the force information, the COP controller can plan the motion of the robotic leg to adapt it to the rotating platform.

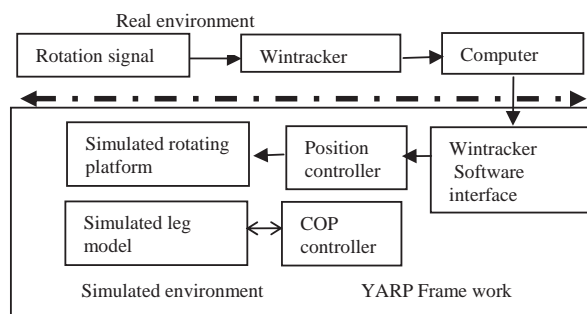


Figure 9. Control system block diagram.

#### IV. EXPERIMENT RESULT

Together with the rotating platform, some experiments were carried out to validate the COP balance controller of the simulated leg. The whole experiment system is shown in Fig.10.

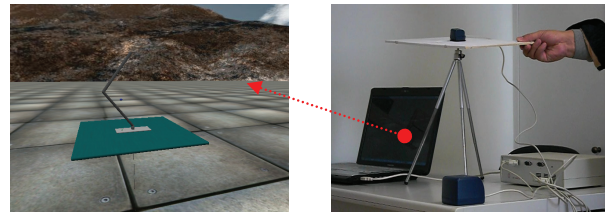


Figure 10. Experiment system.

Table IV presents the parameters of the single leg robot with the posture shown in Fig.10.

TABLE IV. ROBOT MODEL PARAMETER

The length of the foot : $L_f(m)$	0.13
The width of the foot : $W_f(m)$	0.054
The length of upper part of the leg : $L_{upper}(m)$	0.2
The length of lower part of the leg : $L_{lower}(m)$	0.2
The number of DOF of ankle joint: $N_{ankle}$	2
The number of DOF of knee joint: $N_{knee}$	1
The value of front force sensor: $F_l(N), F_r(N)$	2.23, 2.23
The value of back force sensor: $B_l(N), B_r(N)$	0.45, 0.45

#### A. Experiment in static environment

The goal of the experiment is let the leg move along a reference trajectory. The starting point of  $COP\{x,y\}$  and  $COG\{z\}$  is (0.04,0,0.18), and the target point of  $COP\{x,y\}$  and  $COG\{z\}$  is (-0.04,-0.01,0.15), where COG means Centre of Gravity. Because COP controller parameter setting depends on motion task[5], by trial and error, a set of values (6,10,6) are selected as Proportional gain of joint controller in knee, lateral ankle, ankle. The corresponding experiment result are shown in Fig.11. The execution time in simulation is 5 second.

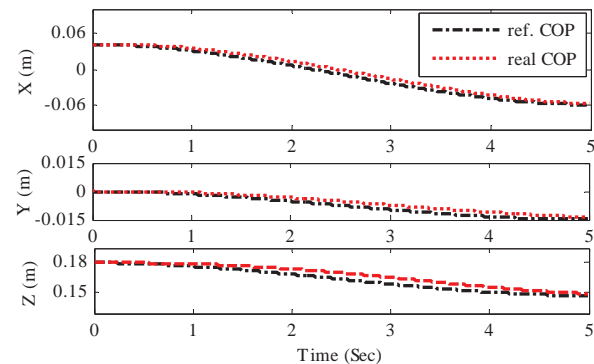


Figure 11. COP trajectory.

The leg robot motion during this experiment are shown in Fig.12. The experiment result validates the performance of the COP controller during realizing this motion task.

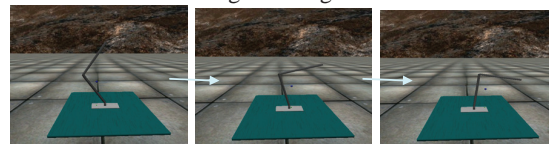


Figure 12. Snapshots of the movement sequence.

*B. Experiment with rotating the simulated platform*

Based on the parameters of the COP controller, another experiment was carried out. The reference (0, 0, 0) is set at the center of the robot foot. The target of the controller is to make the COP to follow a fixed point (0.04, 0, 0.18) on the foot. When the platform is rotated, the controller plans the velocity of the joint to change the posture of leg and keep the COP in the same position of the foot. Here we use the sine function to generate the signal for one joint. The reference trajectory is shown in Fig.13.

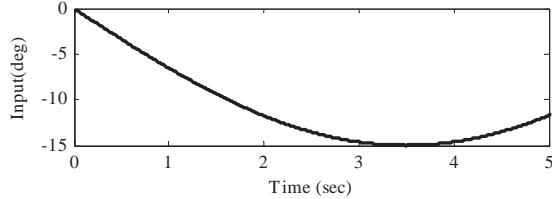


Figure 13. Control signal of pitch rotation.

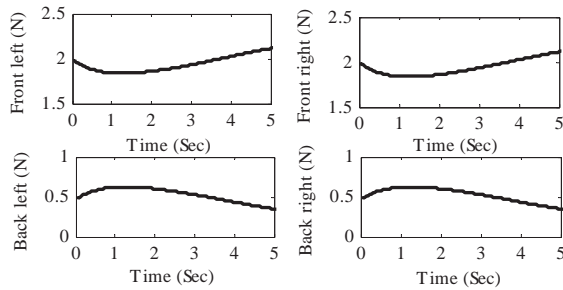


Figure 14. The ground reaction forces.

Based on the sensory information, as shown in Fig.14, we can calculate the reference COP, as shown in Fig.15.

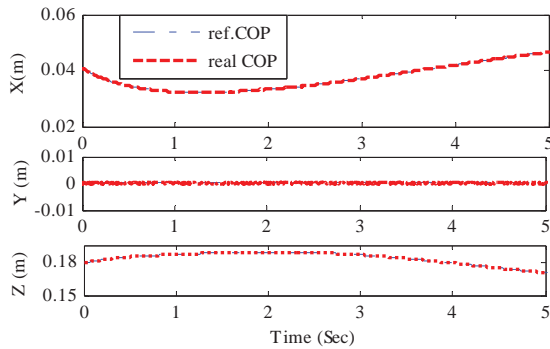


Figure 15. The real and reference COP coordination.

The real COP and reference COP can generate the error to make the COP controller generate different signal, as shown in Fig.16, to control the robot joint to move. From Fig.15 and Fig.16 we can see the robot can use the COP-based controller to regulate its posture so as to keep balance on the changing board.

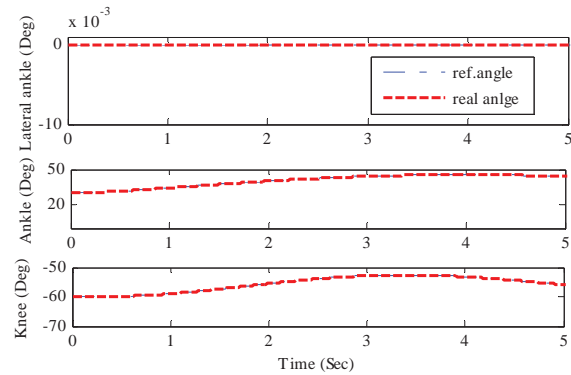


Figure 16. The joint input signal of the robot.

*C. Experiment with input from the real rotating platform*

The output of the platform, as shown in Fig.17, can be adopted as the stimulus for the simulated rotating platform, as shown in Fig. 18.

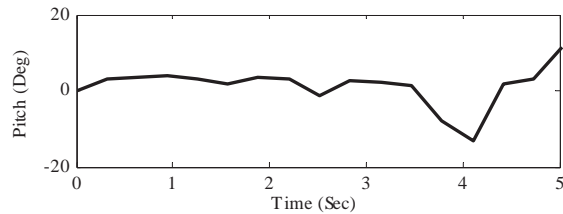


Figure 17. Output of the rotating platform

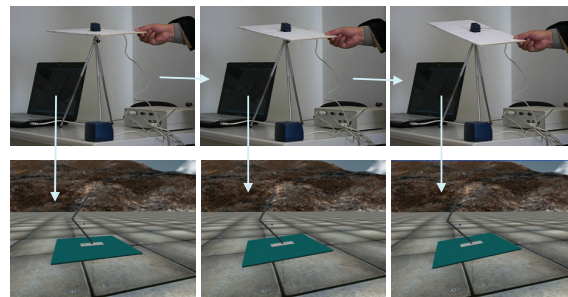


Figure 18. The experiment result.

Based on the result during the development of the prototype of rotating platform and the primary application in a mixed reality application on robot leg motion control, some issues are discussed as follows.

*1) Zero position calibration for the simulated rotating platform*

Since the rotating platform is mounted on top of a passive ball joint, it is difficult to find its physical zero position. In this study, when new experiment is carried out on the real and simulated platform, we need the following two steps to realize the zero position calibration for the simulator. Firstly, the real platform is fixed at a reference zero position and we

run the simulator, thus the position value of real platform is recorded and converted to joint values of the simulated platform. Secondly, the real joint values of last experiment are set as the zero position error correction value for joints of the simulated platform controller. Thus when we rotate the real rotating platform from the reference zero position, the simulated rotating platform can start its rotation from its zero position.

## 2) Stability analysis

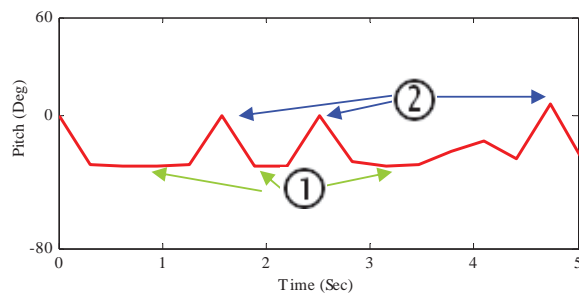


Figure 19. Movement of the rotating platform.

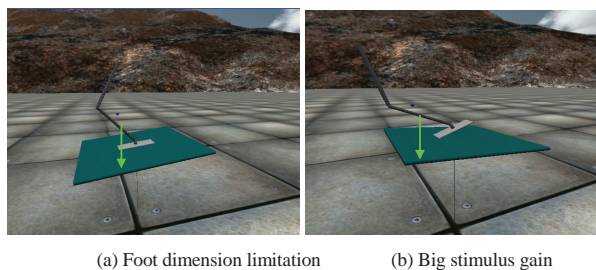


Figure 20. Falling down.

Two situations shown by marker ① and marker ② in Fig. 19 can make the robotic leg loose its balance in the COP-based motion planning experiment. Firstly, the platform is inclined too much, thus make the real COP reaches the borderline of the foot, as shown in Fig. 20 (a). Secondly, the stimulus signal changes too quickly, the error of the system is beyond the limitation of COP controller to keep the balance of the leg, as shown in Fig. 20 (b). This study shows the advantage that simulated system can give help on avoiding damage real robot in adaptive motion experiment.

## V. CONCLUSION

This paper presented a new method to build a simple 3DOF passive rotating platform instead of a complex mechanical and electrical device. The magnetic tracking sensor system was used as the key component to record the rotation information and send it to a computer. Within YARP framework, the simulator for the 3 DOF rotating platform was built with the position controllers, which can receive the data from the tracking sensor system and take it as the joint control information to the simulator. The mixed reality application on COP-based adaptive motion control of a

single-legged robot has shown the potential application of the developed 3DOF passive rotating platform for human-in-the-loop robot experiments.

In the future, the position, and orientation provided by WinTracker can provide additional information to realize adaptive bipedal locomotion control in changing environment.

## ACKNOWLEDGMENT

This work is partially funded by FEDER through the Operational Program Competitiveness Factors - COMPETE and by National Funds through FCT - Foundation for Science and Technology in the context of the project FCOMP-01-0124-FEDER-022682 (FCT reference PEst-C/EEI/UI0127/2011). The author is supported by the FCT grant under CIENCIA2007 (Post Doctoral Research Positions for the National Scientific and Technological System).

The author thanks P. Dias, F. Silva, A. Chauhan, and L. Lopes for the technical support and help.

## REFERENCES

- [1] K. Kawamura, S. Gordon, "From Intelligent Control to Cognitive Control", in Proceedings of 11th International Symposium on Robotics and Applications (ISORA) 2006, July24-27, 2006, pp.1-9, Budapest, Hungary.
- [2] S. H. Collins, M. Wisse, A. Ruina, "A three-dimensional passive-dynamic walking robot with two legs and knees", *International Journal of Robotics Research*, 20, 607-615, 2001.
- [3] V. Santos, R. Moreira, M. Ribeiro, F. Silva, "Development of a Hybrid Humanoid Platform and Incorporation of the Passive Actuators", in Proc. 2010 IEEE International Conference on Robotics and Biomimetics (ROBIO2010), 2010.12, pp.679-684, Tianjin, China.
- [4] C. Maurer, T. Mergner, B. Bolha, F. Hlavacka, "Vestibular, visual, and somatosensory contributions to human control of upright stance", *Neurosci Lett*, 281:99-102, 2000.
- [5] Z. Lu, F. Silva, Y. Zhang, Q. Wang, L. Lopes, "A COP-based Controller for Adaptive Motion Planning of a Single-Legged Robot", in Proc. 2012 IEEE International Conference on Robotics and Biomimetics (ROBIO2012), 2012.12, 42-47, Guangzhou, China.
- [6] M. Ruas, P. M. Ferreira, F. Silva, V. Santos, "Local-Level Control of a Humanoid Robot Prototype with Force-Driven Balance", *Proc. IEEE-RAS Int. Conference on Humanoid Robots HUMANOID2007*, 29 Oct-1 Nov, 2007, pp.551-556, Pittsburgh, USA.
- [7] G. Metta, P. Fitzpatrick, L. Natale, "YARP: Yet Another Robot Platform." *International Journal of Advanced Robotic Systems*, Vol. 3, No. 1 (2006), ISSN 1729-8806, pp. 043-048.
- [8] VR SPACE INC. © Wintracker III ® USER'S MANUAL, MAR 2010.
- [9] E. Chen, "Six Degree-of-Freedom Haptic System for Desktop Virtual Prototyping Applications", In Proceedings of the First International Workshop on Virtual Reality and Prototyping, pp. 97-106, June 1999, Laval France.
- [10] P. Fitzpatrick, G. Metta, and L. Natale, "Towards Long-Lived Robot Genes. Robotics and Autonomous Systems", Volume 56(1), pp. 29-45, Elsevier, 2007.
- [11] V. Tikhonoff, A. Cangelosi, P. Fitzpatrick, G. Metta, L. Natale, F. Nori, "An open-source simulator for cognitive robotics research: The prototype of the iCub humanoid robot simulator", 2008, Proceedings of IEEE Workshop on Performance Metrics for Intelligent Systems Workshop (PerMIS08).
- [12] N. Greggio, A. Bernardino, C. Laschi, J. Santos-Victor, P. Dario, "Real-Time 3D Stereo Tracking and Localizing of Spherical Objects with the iCub Robotic Platform", *Journal Of Intelligent & Robotic Systems* - 63 : pp.417-446 (2011).

# EKF-based visual self-calibration tool for robots with rotating directional cameras

João Ribeiro, Rui Serra, Nuno Nunes, Hugo Silva and José Almeida  
INESC TEC - INESC Technology and Science  
(formerly INESC Porto) and ISEP/IPP - School  
of Engineering, Polytechnic Institute of Porto  
Rua Dr Antonio Bernardino de Almeida, 431, Porto, Portugal  
Email: {joao.ribeiro,nuno.nunes,ruiserra,hsilva,jma}@lsa.isep.ipp.pt

**Abstract**—Autonomous mobile robots perception systems are complex multi-sensors systems. Information from different sensors, placed in different parts of the platforms, need to be related and fused into some representation of the world or robot state. For that, the knowledge of the relative pose (position and rotation) between sensors frames and the platform frame plays a critical role. The process to determine those is called extrinsic calibration. This paper addresses the development of automatic robot calibration tool for Middle Size League Robots with rotating directional cameras, such as the ISePorto team robots. The proposed solution consists on a robot navigating in a path, while acquiring visual information provided by a known target positioned in a global reference frame. This information is then combined with wheel odometry sensors, robot rotative axis encoders and gyro information within an Extend Kalman filter framework, that estimates all parameters required for the sensors angles and position determination related to the robot body frame. We evaluated our solution, by performing several trials and obtaining similar results to the previous used manual calibration procedure, but with a much less time consuming performance and also without being susceptible to human error.

## I. INTRODUCTION

In this paper, we present an EKF based solution, for the development of a visual auto-calibration tool to fully calibrate all rotative axis, angles and offsets of a ISePorto MSL Robot [2].

Robot Calibration is an important and complex task, that needs to be performed, in order for the robot to be able to complete tasks in Robocup semi-structured environment. This calibration procedure consists on defining sensors and active mechanisms inter-relationships but also defines their relation with a global robot body frame.

The ISePorto robots, are complex robots that pose an interesting challenge for obtaining a well-established calibration procedure, since it has many different sensors, namely: 2 cameras for visual perception, a low cost 3-axial Inertial Measurement Unit (IMU), laser range sensor (only for the goalkeeper) and odometry sensors(wheel encoders). The ISePorto robot all possess two rotative axis one for the kicker camera and kicking mechanism and other for the head camera.

The main objective, behind this type of rotation mechanism is to facilitate cooperative play (passing) between robot team members but also to artificially increase robot cameras field-of-view(fov), to allow a better robot self-localization using

field landmarks and also a more efficient obstacle detection.

There are several ways to perform specific calibration procedures, such as the work of Ling [3], that allows to retrieve camera extrinsic parameters through the use of vanishing lines, thus being able to calibrate camera orientation, position and focal length parameters.

Others, like Zhang [8] or Shen and Wang [6] presented algorithms to calibrate the extrinsic parameters of a camera by minimizing total control-point errors. The algorithms minimized control-point errors of the pixels in the image plane and also of the object points in the 3D physical space. Those papers addressed the problem of determining the initial calibration on a off-line procedure. However, for Robocup applications where the extrinsic parameters can change during game-play or as with the use of cameras in cars, the parameters must be determined in real time. Examples of approaches in those scenarios are the work of Martinelli [4] and Wu [7], but not supporting rotating cameras in moving vehicles.

Another developed special purpose robot calibration tool supporting cameras that can change dynamically its configuration in the robot, is the one developed by Pradeep et al [5] to calibrate a multi-arm multi-sensor PR2 robot, through bundle adjustment. They estimated a set of system parameters by acquiring poses of known targets in the world. However, this approach is not applicable for on-line calibration.

In the MSL scenario, the previous calibration method of the ISePorto Robots consisted on a sequence of manual procedures, see figure 1:

- First, concerning the imaging part of the procedure, camera information measurements were acquired through out a sequence of images that were processed off-line, in order to obtain robot camera calibration parameters(intrinsic and extrinsic parameters), this procedure was performed using J.Y.Bouget [1] toolbox.
- Second, the robot is placed on a mechanical frame, specially design to physically align all rotative robot axis, so information regarding motor encoder position can be acquired. The value read from the kicker axis encoder, is defined as the initial bearing angle of the kicker device. Where all camera (head and kicker) pose related angles will be referenced to.
- Third, the one remaining angle to be estimated, is the



Fig. 1. ISePorto robot positioned on the calibration frame

inter-relationship angle that relates the kicker rotative device with head rotative device. For estimating this angle one aligns the robot with a field line and compensates manually the related offset between the two cameras.

The problem with this type of calibration, is that is very time consuming but most of all is very sensible to human error.

The objective of this research is to develop a auto-calibration tool, that can be executed off-line or in future work on-line, that copes with all robot parameters (robot state, camera Kicker and camera Head) estimation, namely:

$$\left[ \theta_w, h_{kc}, d_{kc}, \psi_{kc}, \theta_{kc}, \phi_{kc}, h_{hc}, d_{hc}, \psi_{hc}, \theta_{hc}, \phi_{hc} \right]^T \quad (1)$$

Where  $\theta_w$ ,  $h_{kc}$ ,  $d_{kc}$ ,  $\psi_{kc}$ ,  $\theta_{kc}$ ,  $\phi_{kc}$ ,  $h_{hc}$ ,  $d_{hc}$ ,  $\psi_{hc}$ ,  $\theta_{hc}$  and  $\phi_{hc}$  are respectively robot's pitch and both cameras height, displacement, yaw, pitch and roll.

For that purpose we developed an EKF auto-calibration tool that is based on odometry readings of the robot encoders and camera update visual measurements to a world fixed target. This calibration tool allows us to estimate all necessary robot parameters that are somewhat related to the robot body frame. Moreover, presented results clear shown that this new method is more accurate and provides a robust parameter estimation being 6 times faster than our previously used manual procedure. Other advantage is that EKF parameter filter convergence is achieved very quickly and with very few necessary measurements.

In this paper, in section II our proposed solution is explained. The calibration procedure and the feature processing algorithm are shown along with the EKF equations for the parameters estimation.

The results from several trials are compared to the old calibration method in section III. Also some figures displaying parameter EKF estimation results are shown, in order to correctly evaluate our proposed system performance.

Finally, in section IV conclusions and some insights about future work are also presented.

## II. AUTO-CALIBRATION TOOL

Our solution, contrary to the previous procedure does not depend on the robot positioning inside a fixed mechanical frame. Instead, the robot is placed manually on the floor with the cameras forward looking a chessboard. Afterwards, a circular movement is executed around the positioned chessboard. During this robot motion, we must assure that the

robot cameras always keep the target inside their field of view. Information from the wheel encoders and also images sequence are acquired for EKF post-processing.

In figure 2, a overall representation of our system is presented. The robot sensor (cameras, gyro and odometer encoders), are used to collect data to estimate all robot parameters. This information is then fused within an Extended Kalman filter framework. While gyro and odometry information is used directly in the predict stage of the EKF filter. Visual Information is related to the observation model and data association.

### A. Vision

To get the feature points from the chessboard images, an algorithm was developed based on OpenCV function *cvFindChessboardCorner*. These features will be used as EKF observation in order to update our state variables by comparing each feature point to the predicted chessboard points based on encoder measurements. However, we need to get feature points from OpenCV displaced in the same order, or otherwise, we will not be able to compare the board predicted points with the observed ones. To ensure this condition an order correction algorithm was developed.

The adopted order for the chessboard point is represented in the left side of figure 3 and it's one of the eight possible orders that OpenCV outputs in his chessboard detection function. So the first step of our algorithm is to check if the chessboard points come in a 6x9 format using the cross product (2), between vectors  $V_{1,2}$ (points 1 and 2) from the chessboard and vector  $V_{1,7}$  (points 1 and 7) to know if the points need to be transposed or not.

$$\frac{\vec{V}_{(1,2)} \times \vec{V}_{(1,7)}}{\|\vec{V}_{(1,2)}\|} > threshold \quad (2)$$

In a second step we need to check if the points are in the correct direction using a similar cross product equation (3). If the points are in the wrong direction an vertical mirror is performed to put them in the right order.

$$\vec{V}_{(1,2)} \times \vec{V}_{(1,7)} > 0 \quad (3)$$

At this point, we already have the points in the right position and only need to check if they are starting in the correct order or if is necessary to invert the array. To perform such procedure, we need to use the predicted board points as reference to verify the correct order.

In the right side of figure 3 we can see the correction from the wrong order, red line, to the correct order, green line with the algorithm described above.

### B. Robot parameters estimation EKF

The state of the EKF include all the calibration parameters and the robot state, and is:

$$x = \left[ RobotState \quad CamKicker \quad CamHead \right]^T \quad (4)$$

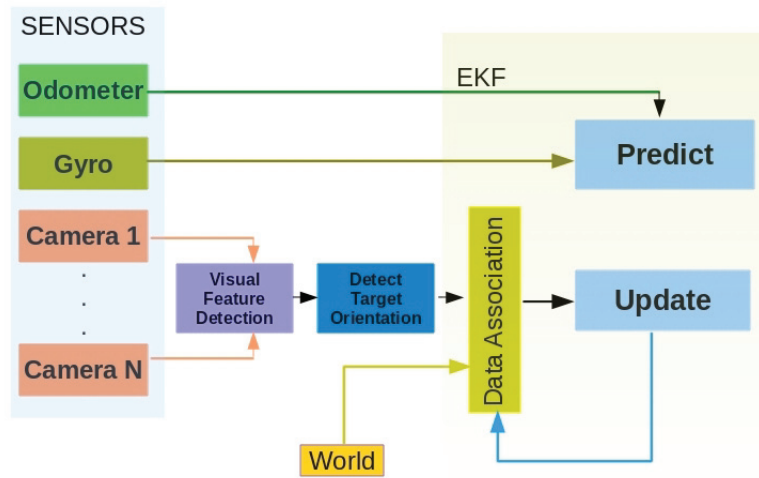


Fig. 2. Auto-Calibration tool framework

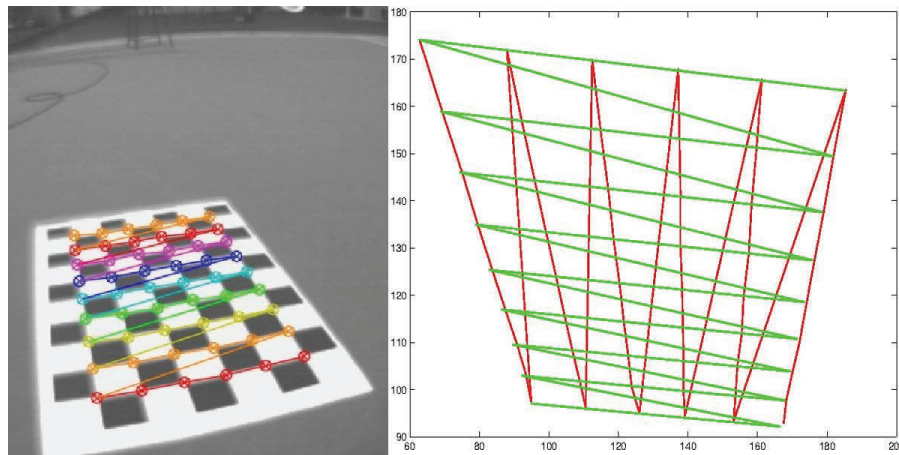


Fig. 3. OpenCV chessboard detection algorithm and matlab order correction

Being,

$$RobotState = \begin{bmatrix} x_w & y_w & \phi_w & \theta_w & \phi_{a1} & \phi_{a2} \end{bmatrix} \quad (5)$$

Where,  $x_w$ ,  $y_w$ ,  $\phi_w$ ,  $\phi_{a1}$  and  $\phi_{a2}$  are respectively robot's  $x$  position,  $y$  position, orientation, kicker angle related to the base and head angle related to the base that are retrieved from robot's encoders in order to predict the position of the chessboard points related to the robot during robot's path.

And,

$$CamKicker = \begin{bmatrix} h_{kc} & d_{kc} & \psi_{kc} & \theta_{kc} & \phi_{kc} \end{bmatrix} \quad (6)$$

$$CamHead = \begin{bmatrix} h_{hc} & d_{hc} & \psi_{hc} & \theta_{hc} & \phi_{hc} \end{bmatrix} \quad (7)$$

Where,  $CamKicker$  and  $CanHead$  are the extrinsic parameters of the cameras relating to the rotating referential of the Kicker and Head, and are constituted by the height  $h_*$ , distance to the rotating axis  $d_*$ , and 3 angles  $\psi_*$ ,  $\theta_*$ ,  $\phi_*$  defining the rotation to the camera frame.

In figure 4 we can see the axes that constitute the ISePorto MSL robot. The gray colored axis is the world axis, the green and red are respectively robot and kicker axes, the violet is the kicker camera axis and in the top we have the yellow and blue axes that are respectively head rotation axis and head camera axis.

$$x(k) = f(x(k-1), u(k)) + v(k) \quad (8)$$

- $x(k)$  → state vector
- $f$  → state transition function
- $u(k)$  → controls (inputs)
- $v(k)$  → process noises which are assumed to be zero mean multivariate Gaussian noises with covariance  $Q$

$$f = \begin{bmatrix} x_w + dx_w, y_w + dy_w, \phi_w + d\phi_w, \theta_w, \phi_{a1} + d\phi_{a1}, \\ \phi_{a2} + d\phi_{a2}, h_{ck}, d_{ck}, \psi_{ck}, \theta_{ck}, \phi_{ck}, h_{ch}, d_{ch}, \psi_{ch}, \theta_{ch}, \phi_{ch} \end{bmatrix}^T \quad (9)$$

$$z(k) = h(x(k)) + w(k) \quad (10)$$

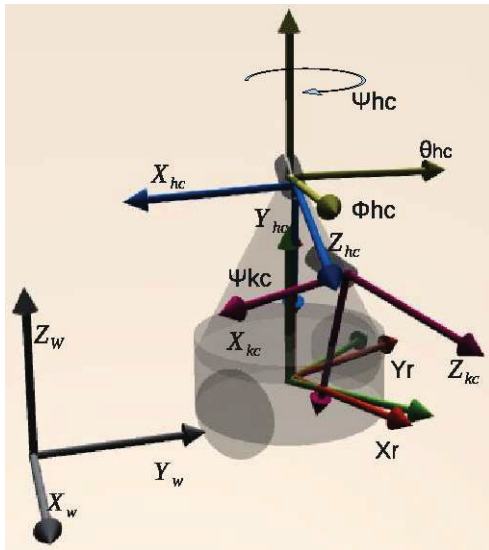


Fig. 4. Definition of referentials in the ISePorto robot

- $z$  → measurement model
- $h$  → observation model
- $w$  → observation noises which are assumed to be zero mean multivariate Gaussian noises with covariance  $R$

We considered the following angles representation (11), using Z(yaw),Y(pitch),X(roll) orientation convention:

$$\begin{bmatrix} \phi \\ \theta \\ \psi \end{bmatrix} = \begin{bmatrix} Roll \\ Pitch \\ Yaw \end{bmatrix} \quad (11)$$

In order to be possible to work with all the different axes we need to relate them with each other. To do so, some rotation and translation matrices are applied.

To relate the robot axis with the world axis the rotation and translation matrices in (12) and (13) are used.

$$R_r^w = \begin{bmatrix} \cos(\psi_r) & -\sin(\psi_r) & 0 \\ \sin(\psi_r) & \cos(\psi_r) & 0 \\ 0 & 0 & 1 \end{bmatrix} \quad (12)$$

$$T_r^w = \begin{bmatrix} \cos(\psi_r) & -\sin(\psi_r) & 0 & Px_r \\ \sin(\psi_r) & \cos(\psi_r) & 0 & Py_r \\ 0 & 0 & 1 & 0 \\ 0 & 0 & 0 & 1 \end{bmatrix} \quad (13)$$

$$R_b = R\psi_b \cdot R\theta_b \cdot R\phi_b \quad (14)$$

For the robots to have better traction, they have some looseness in the base pitch. Due to this, the base referential can't be the same as the robot referential.

The (15) and (16) equations are the rotation and translation matrices from the kicker to the base.

$$R_k^b = \begin{bmatrix} \cos(\psi_k) & -\sin(\psi_k) & 0 \\ \sin(\psi_k) & \cos(\psi_k) & 0 \\ 0 & 0 & 1 \end{bmatrix} \quad (15)$$

$$T_k^b = \begin{bmatrix} \cos(\psi_k) & -\sin(\psi_k) & 0 & 0 \\ \sin(\psi_k) & \cos(\psi_k) & 0 & 0 \\ 0 & 0 & 1 & 0 \\ 0 & 0 & 0 & 1 \end{bmatrix} \quad (16)$$

$$R_{kc}^k = Rkc_{\psi}^k \cdot Rkc_{\theta}^k \cdot Rkc_{\phi}^k \quad (17)$$

$$T_{kc}^k = \begin{bmatrix} & kickerdist_x \\ R_{kc}^k & kickerdist_y \\ & h_{kc} \\ 0 & 0 & 0 & 1 \end{bmatrix} \quad (18)$$

$$T_{kc}^w = T_r^w \cdot T_b^r \cdot T_k^b \cdot T_{kc}^k \quad (19)$$

To project a point seen from the kicker camera in the world, the intrinsic matrix and a translation matrix from the kicker camera to the world are multiplied.

$$PPMkicker = A \cdot T_{kc}^{wT} \quad (20)$$

$$R_{hc}^h = R\psi_{hc}^h \cdot R\theta_{hc}^h \cdot R\phi_{hc}^h \quad (21)$$

$$T_{hc}^w = T_r^w \cdot T_b^r \cdot T_k^b \cdot T_h^k \cdot T_{hc}^h \quad (22)$$

The projected point seen from the head camera in the world, can be obtained using the equation (23).

$$PPMhead = A \cdot T_{hc}^{wT} \quad (23)$$

The equation (24) is used to project one point from the world in to the image in homogeneous coordinates.

$$P_{cam} \begin{bmatrix} x \\ y \\ z \end{bmatrix} = PPM_{cam}(x) \cdot Pw \quad (24)$$

And to predict a 2D point from the world in the image using the robot state, the equation (25) can be used.

$$P_{img} = \begin{bmatrix} x_{imgi} \\ y_{imgi} \end{bmatrix} = h'(x, Pw) = \begin{bmatrix} Pcam_x \\ Pcam_z \\ Pcam_y \\ Pcam_z \end{bmatrix} \quad (25)$$

This way,  $\hat{z}$  is the concatenation of all the predicted chessboard points from the world into the image referential, based the robot state, in our observation model  $h$  (26).

$$\hat{z} = \begin{bmatrix} P_{img1} \\ \vdots \\ P_{imgn} \end{bmatrix} = h \left( x, \begin{bmatrix} P_{chess1} \\ \vdots \\ P_{chessn} \end{bmatrix} \right) \quad (26)$$

$$= \begin{bmatrix} h'(x, P_{chess1}) \\ \vdots \\ h'(x, P_{chessn}) \end{bmatrix}$$

The jacobian from our observation model is obtained by using equation (27).

$$\nabla_x h \left( x, \begin{bmatrix} P_{chess1} \\ \vdots \\ P_{chessn} \end{bmatrix} \right) \quad (27)$$

### III. RESULTS

Several experiences were performed to evaluate the accuracy and performance consistency of our proposed auto-calibration EKF based tool, The trials consisted on performing a circular path around the chessboard while fusing vision with odometry and giro information within a standard EKF framework algorithm.

The obtained results displayed in table I, clearly show that the performance obtained using the auto-calibration tool is similar to the one obtained by the previously used manual calibration procedure.

However, while the manual procedure is very time consuming, with an average of 30 min spent per robot. The auto-calibration tool only spends five minutes on average per robot. Moreover, this new approach is less sensible to human factor, due to the fact that humans do not interfere on the data gathering procedure.

The following EKF results were obtained during one of auto-calibration experiments.

In figure 5, one can observe the robot position estimated using the EKF auto-calibration tool, while comparing with robot odometry position, both displayed trajectories are very similar, but the displayed auto-calibration tool trajectory exhibits less error when compared to the real circular robot trajectory performed by the robot. It is also presented the robot pitch estimation based on the features retrieved from the chessboard during the robot trajectory. It is important to refer that the ISePorto robot has a free-wheel in the rear and so the robot tend to exhibit a dynamic behavior concerning robot pitch angle, that should be continuously estimated even during MSL matches.

In figure 6 is displayed the estimated robot the Euler angles or the kicker camera and their covariance during the experience. It is important to state that the displayed Euler angles

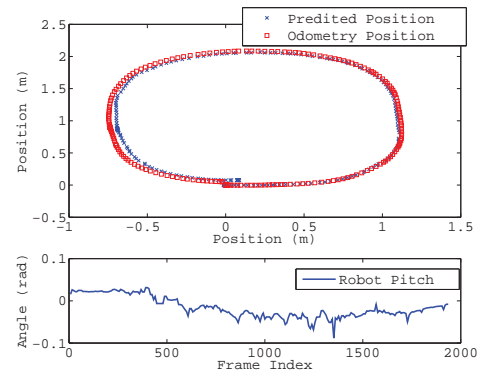


Fig. 5. Robot position and pitch estimation

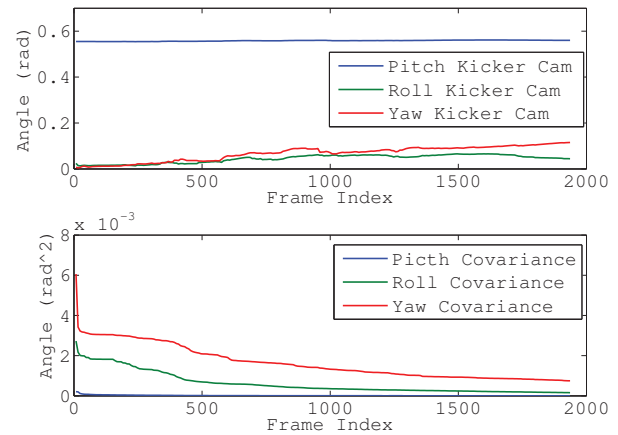


Fig. 6. Kicker camera Euler angles estimation

estimation present a rapid convergence to their estimated values. This characteristic is clearly displayed in almost all EKF-filter estimated parameters. All presented angles were also estimated for the head camera, but were not displayed here for simplicity.

Other two parameters estimated by the EKF are the height and displacement of both cameras, when related to the robot body frame. The results for the kicker camera along with their covariance are presented in figure 7.

Finally, as a way to demonstrate our EKF innovation, figure 8 shows an example of innovation of  $x$  and  $y$  (corner feature) of a chessboard point with  $2\text{-}\sigma$  estimated error bounds during this trial.

### IV. CONCLUSIONS AND FUTURE WORK

In this paper, a vision based auto-calibration tool for the robots with rotating directional cameras, such as the ISePorto robots, was presented. The proposed solution allows to fully calibrate all robot camera parameters (extrinsic) and camera related angles in an autonomous fashion during only a short period of time. This calibration poses a complex and interesting problem within the Robocup MSL, due to the several rotative axis that the ISePorto robots possess.

TABLE I  
 AVERAGE CALIBRATION RESULTS AND THEIR STANDARD DEVIATION COMPARED TO THE MANUAL CALIBRATION

	$h_{kc}$	$d_{kc}$	$\theta_{kc}$	$\phi_{kc}$	$\psi_{kc}$	$h_{hc}$	$d_{hc}$	$\theta_{hc}$	$\phi_{hc}$	$\psi_{hc}$
<b>Manual Calib.</b>	0,5016	0,1125	0,5461	-0,0218	-0,0263	0,6638	0,0636	0,4998	-0,0426	-0,0307
<b>Average auto</b>	0,5003	0,0968	0,5548	-0,0238	-0,0496	0,6587	0,0485	0,5086	-0,0429	-0,0564
<b>Std. Deviation</b>	0,0020	0,0027	0,0063	0,0099	0,0125	0,0031	0,0021	0,0070	0,0121	0,0122

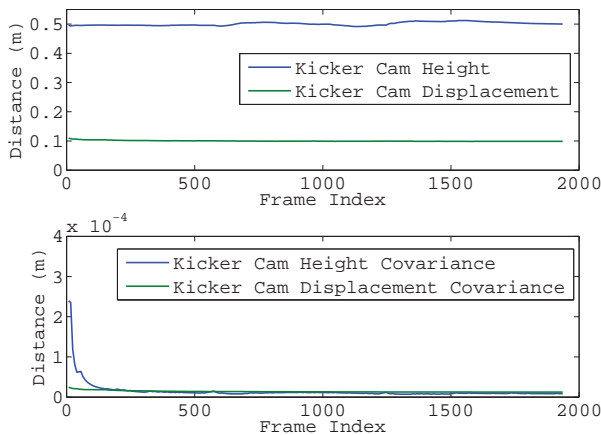


Fig. 7. Kicker camera height and displacement estimation

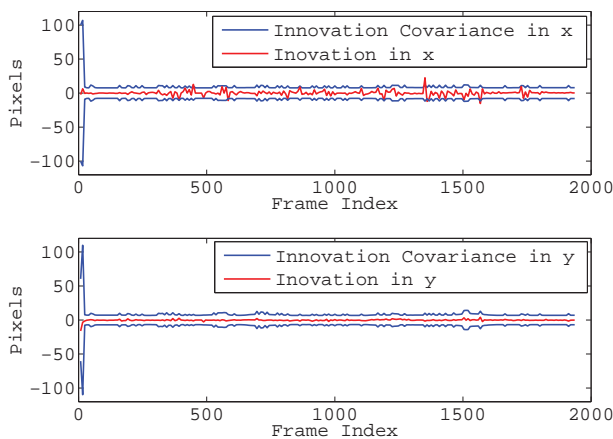


Fig. 8. EKF innovation compared with the  $2\text{-}\sigma$  error bounds

Our proposed method only requires the robot to describe a circular trajectory around one chessboard placed on the ground while gathering vision, gyro and wheel encoder information, that is fused within an Extended Kalman filter framework, that estimates all necessary robot parameters.

The results obtained, using the new calibration method were very similar to the ones obtained by the previously used manual calibration method. During the conducted experiments standard deviation of the parameters was very low, thus allowing to conclude that the auto-calibration tool provides robust estimation results.

One important factor, that had a major influence on the

choice of using an Extended Kalman Filter framework, and not recurring to an optimal batch estimator such as the Maximum Likelihood Estimator(MLE), is that even during the games and specially due to robot collisions, the calibration parameters can change. By using an Extended Kalman Filter approach, one can in future work use an on-line approach that instead of using a chessboard to find feature points for the estimation, uses field lines to provide visual information, thus being possible to adjust and calibrate the robot on-line.

Another future work novelty, would be the introduction of Inertial Navigation System(INS) information within the EKF framework in order to provide a better robot position and pitch angle estimation. This type of approach can also be in future work extended to other types of robots, specially service robots that possess multiple joints and rotative axis.

#### ACKNOWLEDGEMENTS

The authors acknowledge the major support given by the ISEP-IPP Institution and by the INESC TEC, to this project. This work is financed by the ERDF European Regional Development Fund through the COMPETE Programme (operational programme for competitiveness) and by National Funds through the FCT Fundação para a Ciência e Tecnologia (Portuguese Foundation for Science and Technology) within project FCOMP - 01-0124-FEDER-022701.

#### REFERENCES

- [1] J. Y. Bouguet. Camera calibration toolbox for Matlab, 2008.
- [2] Andre Dias, Jose Almeida, Alfredo Martins, and E.P Silva. Traction characterization in the robocup middle size league. *IEEE Robotica 2007 - 7th Conference on Mobile Robots and Competitions*, 2007.
- [3] Wang Ling Ling and Tsai Wen-Hsiang. Camera calibration by vanishing lines for 3-D computer vision. *IEEE Transactions on Pattern Analysis and Machine Intelligence*, 13(4):370–376, April 1991.
- [4] Agostino Martinelli, Davide Scaramuzza, and Roland Siegwart. Automatic self-calibration of a vision system during robot motion. In *ICRA 2006*, pages 43–48, 2006.
- [5] Vijay Pradeep, Kurt Konolige, and Eric Berger. Calibrating a multi-arm multi-sensor robot: A bundle adjustment approach. In *International Symposium on Experimental Robotics (ISER)*, New Delhi, India, 12/2010 2010.
- [6] Yuan Shen, Xiqin Wang, Huadong Meng, and H. Zhang. Camera Extrinsic Parameter Calibration by Minimizing Total Control-Point Errors. *International Conference on Computer Vision, Beijing, China*, 2005.
- [7] Meng Wu and Xiangjing An. An automatic extrinsic parameter calibration method for camera-on-vehicle on structured road. In *Vehicular Electronics and Safety, 2007. ICVES. IEEE International Conference on*, pages 1 –5, dec. 2007.
- [8] Zhengyou Zhang and One Microsoft Way. Flexible camera calibration by viewing a plane from unknown orientations. *Proceedings of the Seventh IEEE International Conference on Computer Vision*, 00(c):666–673 vol.1, 1999.

## Visual Detection of Vehicles Using a Bag-of-Features Approach

Pedro Pinto<sup>1</sup>, Ana Tomé<sup>2</sup>, Vitor Santos<sup>3</sup>  
*DEM<sup>1,3</sup>, IEETA<sup>2,3</sup>*  
*University of Aveiro*  
*Aveiro, Portugal*  
*pempd@ua.pt<sup>1</sup>, ana@ua.pt<sup>2</sup>, vitor@ua.pt<sup>3</sup>*

**Abstract**—This paper presents and evaluates the performance of a method for vehicle detection using a bag-of-features methodology. The algorithm combines Speeded Up Robust Features with a Support Vector Machine. An optimization to the bag-of-features dictionary based on a genetic algorithm for attribute selection is also described. The results obtained show that this method can successfully address the problem of vehicle classification.

**Keywords**—Intelligent vehicles; Object recognition; Machine learning algorithms; Support vector machines; Genetic algorithms;

### I. INTRODUCTION

The car manufacturers have increasingly been adopting more Advanced Driver Assistance Systems (ADAS) in order to make their vehicles safer. The development of vision based methods for efficient obstacle detection and classification is one of the current research trends towards this goal.

In the literature the problem of detecting a car in an image is usually divided in two steps, hypothesis generation followed by hypothesis verification or classification. In the former, a Region of Interest (ROI) with a potential target is determined. Multiple methods can be used like sliding-window, saliency detection or an external laser as seed. This work focuses on the second step, where image features are extracted from the ROI and a supervised learning algorithm determines if a vehicle is present.

Multiple techniques have been applied for hypothesis verification. Some appearance based methods rely on statistical analysis to extract the relevant information that define the target objects. In [1] the author implemented eigencars, an algorithm that uses Principle Component Analysis (PCA) to compute eigenvectors and reduce the dimensionality of the input space. Other methods detect distinctive and robust points of interest on the image. In [2] the authors present a method which combines HOG (Histogram of Oriented Gradient) features with a Support Vector Machine to successfully identify obstacles on the road. In [1] and [3], the authors implemented algorithms based on the Viola–Jones object detection framework. This framework uses Haar-like features and a cascade of classifiers to speed up the recognition process.



Figure 1. Image sample from the dataset

The algorithm presented in this paper distinguishes itself by following a bag-of-features approach and also combining SURF features with a Support Vector Machine for vehicle classification.

### II. ALGORITHM

Bag-of-features [4] [5] is a popular approach for classification due to its simplicity and performance. It uses the frequency of descriptors rather than spatial features to describe and classify an image. This method is inspired by document classification methods where word frequency is often preferred in detriment of semantic meaning [6]. Bag-of-features follows the same idea, using a dictionary of visual words that are image features.

Before feature extraction the ROI was pre-processed by converting to grayscale and its histogram equalized to enhance the contrast. The visual vocabulary is based on Speed-Up Robust Features (SURF) [7]. SURF shares some similarities with SIFT (Scale-Invariant Feature Transform) combining an interest point detector with a descriptor that is scale and rotation invariant. However, because it is designed for performance, it is faster and more suitable for a real-time environment.

#### A. Dictionary

The dictionary is a set of visual features. These are computed around points of interest which are detected by approximating the scale-normalized determinant of the

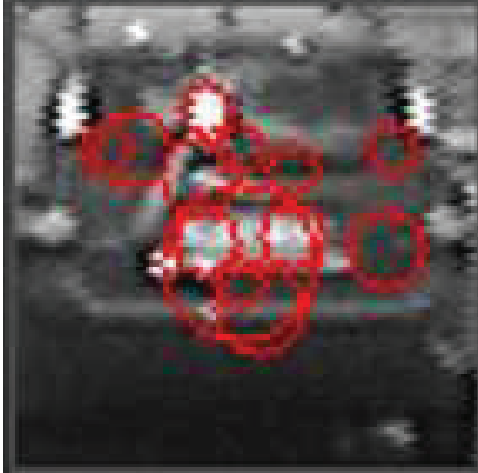


Figure 2. Points of interest of a ROI

Hessian. This is a scale invariant blob detector characterized by good computational performance and accuracy.

Because the feature space is continuous, it is not feasible to generate all possible combinations using a brute-force approach. The solution was to sample features from a dataset that included images with and without vehicles. The dictionary is then formed by clustering all the visual features using K-means, the centroids of each clusters are the entries of the dictionary. The use of a clustering algorithm reduces the variable number of features to a more compact fixed sized set. Naturally the number of clusters is a design parameter of the system and it is experimentally evaluated in this work.

### B. Classification features

In bag-of-words classification strategies the features at the input of the classifier are achieved by post-processing the basic features (semantic features) detected in documents [4]. In this case the dictionary provides the means to compute these high-level features. Then by characterizing each ROI with a set of visual features and after matching them in the dictionary a histogram of the frequencies of the entries of the dictionary is constructed. The matching of a visual feature (SURF feature vector) to the dictionary is achieved by using the K-NN (K Nearest neighbor) strategy using Euclidean distance measures. In this case K is equal to 1, which corresponds to approximating to the closest visual word. Furthermore notice that the classification feature vector will now have the size of the dictionary overcoming then the problem of having different number of points of interest per frame.

These entries of the classification vector were normalized by dividing the absolute frequencies by the dictionary size. Since the vector components are all of the same magnitude, normalization should not be a relevant factor.

Naturally there is another tradeoff that needs to be addressed, increasing the size of the dictionary results in classification features with more attributes and a more complex classifier. Several dictionaries sizes were tried in order to determine a suitable value.

### C. SVM

Image classification is done using a SVM (Support Vector Machine) [8]. This is a supervised learning algorithm that supports non-linear classification. This is due to "the kernel trick", a kernel function defined with the original that provides the means to work in the new space of higher dimension where a linear separation can be made. An example is RBF (Radial Basis Function) kernel where  $\sigma$  is an user-defined parameter (Eq. 1).

$$k(x_1, x_j) = \Phi^T(x_i)\Phi(x_j) = \exp(-0.5\|x_i - x_j\|^2/\sigma) \quad (1)$$

Non-linear kernels require that the subset of the training data (the so called support vectors) be stored to perform the decision on every new data example  $x$ . The decision is taken computing Eq. 2.

$$\sum_i^{N_s} \lambda_i y_i \Phi^T(x_i)\Phi(x) + b \quad \begin{array}{l} \geq 0 \Rightarrow \text{class 1} \\ < 0 \Rightarrow \text{class 2} \end{array} \quad (2)$$

Where  $N_s$  is the number of support vectors  $x_i$  and naturally the pair  $(x_i, y_i)$  belongs to this subset of the training set. The  $y_i = 1, -1$  represents the label values. Finally  $\lambda_i$  and  $b$  are parameters learned, in conjunction with the selection of the support vectors, also during the training phase.

On the other hand, Linear SVMs are less computationally demanding, at least after the training phase, because only the coefficients  $w$  that determine the separation need to be stored. In this particular case, where there is no mapping, the previous equation simplifies by computing  $\sum_i^{N_s} y_i \lambda_i x_i$ . The decision is now  $w^T x + b$ , the support vectors do not need to be available. This is an important issue for on-line applications.

The SVM was trained using as input the frequencies of the dictionary's features. ROIs with cars should have higher frequencies of certain features not present in other images. In addition, each dictionary item is an attribute, which means the SVM will have as many dimensions as the dictionary size.

### D. Optimization

In a second step, an optimization was introduced in order to improve the performance and robustness of the learning algorithm. An attribute selection optimization based on a genetic algorithm was performed.

Genetic algorithms are biologically inspired search methods. A population of chromosomes is submitted to an evolutionary process for several generations in order to improve a fitness metric. Each chromosome is formed by a string of binary genes that can recombine with others (crossover) or suffer random changes (mutation). The probability of crossover increases with the chromosome fitness, directing the search towards the goal. Mutation is a way of introducing diversity and avoiding a fast convergence for a local minimum.

The dictionary was optimized by generating a 1024 feature set using the K-means clustering algorithm. In the genetic algorithm each chromosome represented a mask of enabled visual words. The result of the optimization is therefore a combination of visual features from the initial 1024 feature set. Attribute selection helps to tune the dictionary so that only the most relevant features are included.

### III. RESULTS

#### A. Implementation

This algorithm was implemented in C++ using the OpenCV library [9]. OpenCV is a widely used open source library for real-time computer vision. It focus on image processing but also includes machine learning algorithms, like the K-NN or SVM used in this implementation.

#### B. Dataset

The algorithm was validated with a dataset of images collected by Miguel Oliveira on a previous research project [3]. It contains 2265 images: 828 with at least one car and 1434 with no car. For the first group a manual segmentation has been performed [3], which provides the coordinates of regions of interest (ROI) to be further processed (Fig. 1). In the case of regions of interest without cars a random squared ROI with a size between 50 and 200 pixels is considered.

The dataset was divided in three subsets: a training dataset (70%), a validation dataset (20%) and a test dataset (10%). The training dataset is used to generate the predictive model. The validation dataset is used to perform the attribute selection optimization. Finally the test dataset is used to evaluate the algorithm performance.

Fig. 2 shows examples of interest points extracted using SURF from a ROI. These are identified by red circles.

#### C. Algorithm performance metrics

Precision and recall are best visualized using a confusion matrix. Precision reflects the number of correctly identified ROIs relative to the total amount classified as having a vehicle. Recall is the percentage of correctly identified positive ROIs from the universe of the total ROIs with vehicles. However, these performance metrics are not sufficient, as they could lead to erroneous conclusions. As an example, an algorithm that classifies all the ROIs as positive has a high recall but a low precision. On the other hand, an

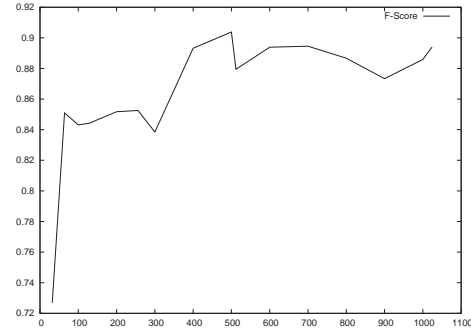


Figure 3. Algorithm performance relative to the dictionary size (without genetic optimization)

algorithm that classified correctly one ROI and all the others as negative would have a high precision but a low recall. The solution is to use F-score, which combines both metrics as defined by Eq. 3.

$$F - score = 2 \frac{precision \times recall}{precision + recall} \quad (3)$$

#### D. Dictionary size

Determining an adequate size for the dictionary is important as a very small dictionary may not be expressive enough and a very large dictionary not only consumes more computer resources but can also introduce learning problems because of the high number of dimensions.

Several dictionary sizes were tested within the range of 32 to 1024 visual words. Fig. 3 shows that performance increases with dictionary size until a value of about 100 visual words. After that, the algorithm performance does not improve significantly. We have found 128 words to be a good compromise between recognition performance and computational load.

#### E. SVM kernels

SVMs support non linear classification using the "kernel trick". In this study, both linear and a RBF kernels were evaluated.

1) *Linear kernel*: In the linear kernel dot product is done in input space. The linear kernel is defined by Eq. 4.

$$K(x_i, x_j) = x_i^T x_j \quad (4)$$

Tables I and II show the results obtained for the test dataset using a 128 words dictionary.

Table I  
 CONFUSION MATRIX FOR THE TEST DATASET USING A LINEAR KERNEL

	Predicted positives	Predicted negatives
Actual positives	70	12
Actual negatives	22	39

Table II  
 PERFORMANCE MEASUREMENTS OF THE TEST DATASET USING A  
 LINEAR KERNEL

Precision	0,760870
Recall	0,853659
F-score	0,804598
Time (seconds)	0,02

2) *RBF kernel*: RBF kernel maps the input space into a space of higher dimension using a gaussian function.

Tables III and IV show the results obtained for the test dataset using a 128 words dictionary. The results show that RBF kernel performs better then the linear kernel.

Table III  
 CONFUSION MATRIX FOR THE TEST DATASET USING A RBF KERNEL

	Predicted positives	Predicted negatives
Actual positives	66	16
Actual negatives	11	50

Table IV  
 PERFORMANCE MEASUREMENTS OF THE TEST DATASET USING A RBF  
 KERNEL

Precision	0,857143
Recall	0,804878
F-score	0,830189
Time (seconds)	0,01

#### F. Dictionary optimization

To further improve the results, attribute selection was applied to the dictionary using a genetic algorithm. Each chromosome was implemented as a mask where each gene enabled or disabled a visual word. The fitness metric used was the F-score and in our tests it reached a maximum value of 0.903703. However, we could not make the algorithm converge.

#### IV. CONCLUSION

This study focused on studying the applicability of a bag-of-features methodology to the problem of vehicle recognition.

The experiments have shown that the proposed algorithm is able to successfully classify vehicles with performance metrics above 80%. On the other hand, the tuning of the dictionary using attribute selection did not produce the desired results. This can be explained by the fact that a genetic algorithm can take a high number of iterations until reaching an optimized genotype.

It was also shown that the choice of the kernel in the SVM learning algorithm is relevant for the performance of the algorithm. The RBF kernel obtained better figures than the linear kernel.

This work aimed to achieve a simple and effective method for hypothesis verification through a bag-of-features approach. We used a dataset with already segmented regions as the input. In the future, the authors plan to investigate efficient algorithms for hypothesis generation based on salient regions. The final goal is to have an algorithm able to recognize and track road obstacles in real-time.

#### REFERENCES

- [1] L. Dlagnekov, "Video-based car surveillance: License plate, make, and model recognition. MSc. U. C. San Diego," 2005.
- [2] D. Balcones, D. F. Llorca, M. Á. Sotelo, M. Gavilán, S. Álvarez, I. Parra, and M. Ocaña, "Real-Time Vision-Based Vehicle Detection for Rear-End Collision Mitigation Systems," *Lecture Notes in Computer Science*, vol. 5717, no. 2009, pp. 320–325, September 2009.
- [3] M. A. R. de Oliveira, "Development of a foveated vision system for the tracking of mobile targets in dynamic environments. MSc. Thesis. University of Aveiro," 2007.
- [4] L. Fei-Fei, R. Fergus, and A. Torralba, "Recognizing and learning object categories, cvpr 2007 short course," Cambridge, MA, 2007.
- [5] J. R. R. Uijlings, A. W. M. Smeulders, and R. J. H. Scha, "Real-time bag of words, approximately," in *In Proc. ACM Int'l Conf. Image and Video Retrieval, Santorini Island, Greece*, 2009.
- [6] Y. Zhang, R. Jin, and Z.-H. Zhou, "Understanding bag-of-words model: a statistical framework," *International Journal of Machine Learning and Cybernetics*, vol. 1, pp. 43–52, 2010.
- [7] H. Bay, T. Tuytelaars, and L. V. Gool, "Surf: Speeded up robust features," in *In Proc. ECCV, Graz, Austria*, 2006, pp. 404–417.
- [8] C. J. Burges, "A tutorial on support vector machines for pattern recognition," *Data Mining and Knowledge Discovery*, vol. 2, pp. 121–167, 1998.
- [9] G. Bradski and A. Kaehler, *Learning OpenCV: Computer Vision with the OpenCV Library*. Cambridge, MA: O'Reilly, 2008.

# Base Pose Estimation using Shared Reachability Maps for Manipulation Tasks

Daniel Di Marco, Oliver Zweigle, Paul Levi

University of Stuttgart, Dept. Image Understanding, Universitätsstr. 38, 70569 Stuttgart, Germany

Email: dimarco | zweigle | levi@ipvs.uni-stuttgart.de

**Abstract**—Manipulation tasks for robots with a robotic arm and a mobile base are one of the most error-prone operations in service robotics. Especially for low-cost robots with a small reachable workspace of the arms, the selection of base poses for reaching tasks is a challenging problem. In this paper, we focus on the estimation of base poses for robots such that they are able to reach a given end effector target pose using space-efficient discretizations of the robots workspace, so-called reachability maps. We further present a method to share these reachability maps among robots by storing them on a cloud-database, annotated with a semantic description. These are then integrated in a knowledge-based task execution system for service robots. Last, we conclude with the results of an experiment showing the cooperation of robots of different hardware making use of each other's reachability maps.

## I. INTRODUCTION

One of the most important tasks of service robots to assist us in daily household chores some day will involve fetching objects in unstructured environments. A recurring problem in this context is the estimation of base poses, from which the robot is able to reach towards an object. Robots that will be working autonomously in these kinds of environments will need to be able to reason about possible locations for reaching tasks. Another interesting case is the cooperation of multiple robots. Assume for instance the task of handing over an object from one robot to another, where the robots have different manipulator hardware. In order to solve this task robustly, each robot needs to know about the reachable workspace of the other, such that suitable base poses might be chosen.

From a more pragmatic point of view, a lot of service robots used in research labs are built based on the same manipulator hardware. As an example the robots used in [1], [2] and TUM's Rosie robot [3], to name a few, are all using the KUKA Light Weight robot arm and could thus profit from sharing knowledge about the arm's capabilities.

We formulate three requirements necessary for reaching our goal of sharing this kind of knowledge among different robots:

- **Completeness:** The reachability information shared by the robot needs to be complete in the sense that it is sufficient to fully reproduce the workspace of the manipulator.
- **Representation Efficiency:** It should be efficiently encoded for storage size, such that it can be transmitted quickly over wireless networks.
- **Uniqueness:** The reachability information has to be uniquely mapped to the manipulator hardware it describes, to allow for efficient search.

In this paper we present a method to create discretized reachability maps for service robots, with the goal to calculate viable base poses for grasping tasks, and propose to store them on a database to make them usable for other robots as well.

### A. Related Work

The problem of estimating suitable base poses for reaching tasks by discretizing the workspace of a mobile manipulator has been investigated by several researchers in the past semi-decade. One of the earlier publications to make use of a discretized workspace in a similar way to the approach presented in this paper is [2]. The basic idea is to discretize the workspace of a robotic manipulator into discrete parts and fit primitives describing the reachability of each part of the workspace. One of the main goals is to find meaningful structures in the manipulator's workspace (so called *capability maps*) and to find elements of the workspace which are well suited for manipulating objects. The discretization of the workspace is done by subdividing it into small cubes. Multiple rotations are randomly sampled for each of these cubes, and the results of the inverse kinematics are stored. In contrast, we use a deterministic approach to sample rotations. As we will use the word *capability* in a broader sense in this paper, we will call maps of this kind *reachability maps* instead further on.

Another influential work on this topic is [4]. The authors use a set of randomly selected base poses in order to learn a success model for reaching towards a goal pose, taking into account external parameters that influence the outcome of grasping actions (e.g. the uncertainty of the robot's self-localization and the expected object pose). In contrast, in this paper we consider the object position to be known in advance and do not require learning phases for the grasping task.

The approach to estimating base poses from a discretized reachability workspace described in sections II-A to II-C is related to Diankov's work in OpenRAVE<sup>1</sup>, described in [5, ch. 4.4]. Here, a kernel density estimation to cope with aliasing effects from the workspace discretization is used. However, our work differs in the discretization step in that it discards some information to achieve a more efficient representation and in the way these are used.

The authors of [1] use the method from [2] to capture a manipulator's workspace. Their main focus is on defining a quality measure for the *graspability* of an object at a specific pose, i.e. how well a specific pose is reachable by a robotic manipulator. This way, they can find e.g. placement poses for objects which are most suitable to manipulate these objects.

<sup>1</sup><http://www.openrave.org>

## B. Contributions

As can be seen from the previous section, reachability maps are useful for multiple tasks found in service robotics. In terms of computation power, they also are very costly to generate. Thus it makes sense to generate them once and share them in an easily accessible way, as proposed in this paper. We consider the main contributions of this paper to be as follows: The integration of reachability maps for base pose estimation in a distributed information system in order to share the workspace information for cooperative tasks executed on different robots. We further describe a space-efficient representation, annotated with semantic information and provide a heuristic method to make use of these.

## II. APPROACH

### A. Discretizing the Workspace

In order to efficiently reason about possible base poses for grasping tasks, we first need to approximate the workspace of the robot, which we call *reachability map*. This map will describe the workspace usable by the manipulator. We follow a somewhat common approach to achieve this (as it was used in e.g. [5], [2]): Approximate the workspace as a cube with the manipulator's base in the center, then subdivide this cube into smaller cubes according to a predefined resolution. For selecting a set of evenly distributed orientations from the space of rotations  $SO(3)$  for the end effector, the algorithm described in [6] is used.

Having selected a set of 6D poses in this manner, we run an inverse kinematics solver on each pose. Currently, there are interfaces for two different IK solvers implemented; one for using the analytical solvers generated by the OpenRAVE framework, and another implementation that calls the ROS inverse kinematics solving interface. All data visualizations shown in the rest of this paper were generated using data supplied by the ROS IK interface, and the the experiments presented in section IV made use of it as well.

We represent the results (i.e. for each manipulator target pose in the workspace, one binary value specifying whether an IK solution could be found or not) as a bit vector. Note that we thus discard the information on how many solutions are found for each manipulator target pose, in contrast to [5], in order to obtain a more efficient representation of the workspace. Neither are the manipulator target poses stored explicitly, though these can be reproduced using additional parameters of the discretization step. We therefore store the spatial and rotational resolution and the transformation matrix for the transformation between the base and the manipulator coordinate system in YAML format<sup>2</sup> in a second file. The bitvector is then compressed using the *libbzip2*<sup>3</sup> library and stored, resulting a highly space-efficient representation (for example, the file for storing the reachability map for the PR2's left arm in a resolution of 0.05 m and 576 rotations representing 76,406,976 poses, occupies only  $\sim 112$  kB of storage space). Fig. 1 shows a visualization for the workspace for the left arm of Willow Garage's PR2 robot with a resolution (i.e. the side length of the subdivision cubes) of 0.05 m and a workspace side length of 1.26 m.

<sup>2</sup><http://www.yaml.org>

<sup>3</sup><http://bzip.org>

Depending on the chosen resolution, the computation time required for this step are often quite extensive (i.e. in the order of magnitude of multiple hours). Thus this operation is done off-line only once and its results are then stored for later access.

### B. Calculating Base Poses

From the discretization of the reachable workspace obtained in the previous section, we can select possible base poses for a given end effector target pose. Let  $p$  be the target end effector pose, with  $r_p$  being a quaternion representing its rotation in  $SO(3)$  and  $t_p = (x_p, y_p, z_p)$  its  $\mathbb{R}^3$  position. Assume that  $t_p$  is given in a coordinate system whose  $z$ -axis is pointing upwards, with its origin on the height of the floor (i.e. the *world* frame).

Our goal in this step is to find 6D poses marked as reachable in the discretized workspace such that the inverse of the transformation given by the considered pose is a suitable base pose for the robot. We narrow down the search space in several ways:

- Since the robot base can only be rotated around the  $z$  axis, the rotation from the target base to a viable target rotation in the discretized workspace likewise must only be a rotation around the  $z$  axis. The rotation axis can be easily determined from the quaternion representation that is used for storing rotations. Thus, rotations with rotation axis components for the  $x$  and  $y$  components are filtered from the workspace.
- The height of the target pose  $z_p$  defines the "slices" of the reachability map we need to take into consideration. As we are working with floating point numbers, we take the two slices  $s_1$  and  $s_2$  of the workspace neighboring  $z_p$  such that  $s_1 < z_p < s_2$ . The rest of the reachability map is consequently not relevant for finding a base pose for the given reaching task.

Subsequently the system iterates through the reachability map filtered in this way, checking each candidate pose for applicability. With  $T_{cand}^o$  being the affine transformation corresponding to the candidate pose under consideration and  $T_{torso}^{base}$

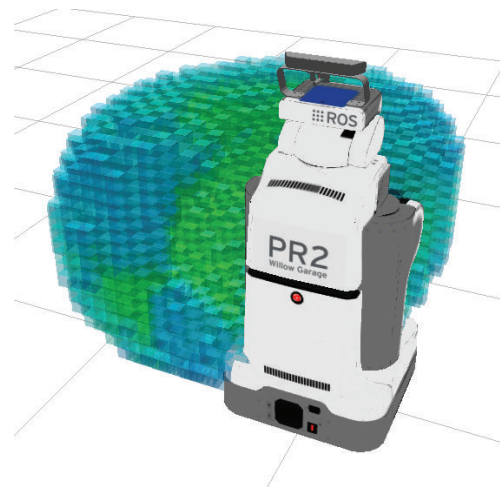


Fig. 1. PR2 left arm workspace. The green cubes represent a high, blue cubes low number of different end effector rotations.

being the homogenous 4x4 transformation matrix from the robot base to coordinate system of the manipulator workspace, the base pose is:

$$T_{basepose} = T_p \cdot (T_{torso}^{base} \cdot T_{cand}^o)^{-1} \quad (1)$$

The resulting transformation matrices represent a set of possible base poses to fulfill the reaching task.

### C. Kernel Density Estimation

The base poses from the previous step could directly be used for manipulation tasks. However, as they are based on the workspace discretization, they are limited to the discretization resolution. Thus, coarse workspace discretizations will give less possible base poses than finer discretizations. Further, in order to assess different base poses for their adequacy for reaching to the target pose, we need to define a measure for this adequacy first. A reasonable approach to assign a base pose a quality measure in this context is to count the number of different base rotations from which the robot can reach towards the goal.

To compensate these problems, the result of this step will be a weighted map of possible 2D positions and orientations, created from an estimation of the continuous probability distribution for the base poses estimated. The weight of each pose will encode its adequacy for reaching towards the target 6D pose  $p$ . To create such a representation, one option is to create a histogram on the base poses from the previous section. As the underlying reachability map is discrete, we need to account for aliasing effects that will occur, though. Like [5], we therefore chose to apply a multivariate kernel density estimation method (e.g. [7]) to estimate a continuous probability distribution from a discrete set of values.

The possible base poses calculated in the previous step II-B are used as observations as input to the kernel density estimation. To efficiently estimate the kernel density, we adopted the *nuklei* library<sup>4</sup> (see also [8]). We extended the library to make use of the following kernel definition.

To encode a robot's base pose (translation in  $\mathbb{R}^2$  + yaw orientation) in a multivariate density estimation, a product kernel of the form as described is used (refer to [8] for a more detailed description):

$$\mathcal{K}(x; \mu, \sigma) = \mathcal{L}(x_t; \mu_t, \sigma_t) \mathcal{O}(x_r; \mu_r, \sigma_r) \quad (2)$$

$\mathcal{L}$  is the location kernel for positions in  $\mathbb{R}^2$  and  $\mathcal{O}$  is the orientation kernel, respectively.  $\sigma_t, \sigma_r$  is the bandwidth for the translational and the rotational kernels, respectively. In the current implementation, both kernel functions are referencing a triangular shape function  $\mathcal{T}$  (defined in the *nuklei* library) using the euclidean distance for the position kernel and the angular distance for the orientation kernel:

$$\mathcal{L}(x_t; \mu_t, \sigma_t) = \mathcal{T}\left(\sigma_t, \sqrt{(x_t - \mu_t)^2}\right) \quad (3)$$

$$\mathcal{O}(x_r; \mu_r, \sigma_r) = \mathcal{T}\left(\sigma_r, d_{ang}(x_r, \mu_r)\right) \quad (4)$$

$$\mathcal{T}(\sigma, d) = \begin{cases} 0 & \text{if } d > 2\sigma \\ \frac{1-d}{2\sigma} & \text{otherwise} \end{cases} \quad (5)$$

<sup>4</sup><http://nuklei.sourceforge.net>

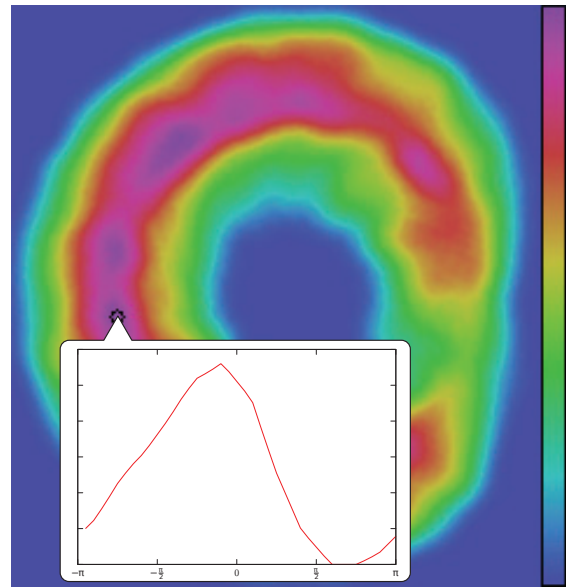


Fig. 2. Kernel Density Distribution Visualization, based on the kinematic properties of PR2's left arm. The colors encode the number of orientations that allow to reach the origin (blue means the robot cannot reach the target, purple represents positions with various feasible orientations). The plot shows the weights for different orientations of the robot at the marked base position.

with  $x_t$  and  $\mu_t$  being positions in  $\mathbb{R}^2$ , and  $x_r$  and  $\mu_r$  being rotations around the world coordinate system's  $z$  axis.  $d_{ang}(\alpha, \alpha')$  is the minimal angular distance between  $\alpha$  and  $\alpha'$ . The choice of a triangular shape function as opposed to e.g. a Gaussian kernel function is motivated by a faster evaluation.

A common question when applying kernel density estimation methods is the selection of the bandwidth parameter  $\sigma$ . As we want to mitigate potential aliasing problems originating in the discretization of the workspace, it is sensible to make the bandwidth depending from the resolution of the reachability map.

An exemplary visualization for the result of this estimation is given in Fig. 2. In the main image, the possible base positions on the floor are represented. They are graded by the adequacy (as defined above) for reaching towards the center of the image, pointing to the right at the height of the arm base. The graph shown in Fig. 2 illustrates the weights for different orientations at the marked position.

### D. Selecting Base Poses

Having acquired the base pose distribution as described in the previous section, there are several ways to generate a base pose for the grasp action. The main problem to cope with is that a discretization of the rotational space, used in section II-A, is finite, whereas the space of possible target orientations for the end effector is not. Thus there are possible target end effector poses where the orientation is not well represented in the discretization of the rotational space, increasingly so on more coarse workspace discretizations. It is therefore necessary to allow for differences between the given target orientation and the available rotations in the reachability map. Note that this will lead to result false positives, i.e. base poses from which the target cannot be reached.

**Random Sampling:** The base pose distribution suggests a straightforward solution for finding a viable base pose by weighted sampling, also used in [5]. I.e. to determine a viable base pose one can select a position by weighted sampling from the 2D position distribution first (e.g. by inverse transform sampling), then likewise draw an orientation from the orientation distribution at the chosen position. This allows for an efficient, stateless sampling of many potential base poses, but will be sub-optimal on a real robot when a low-weighted pose is chosen. Also, commonly used navigation and localization methods working on real sensor data are not guaranteed to exactly achieve a given target pose, but will typically reach the goal only within a certain margin.

**Scored Sampling:** The discretization of the workspace might lead to problems at the borders of the base pose distributions. Thus a more pragmatic heuristic would be to take the environment of candidate poses into account. We found the following heuristic to significantly increase the success rate: A set of  $n$  base pose candidates  $c_1, \dots, c_n$  is randomly sampled as described in the previous paragraph. Each candidate pose gets a score  $s(c_i)$  which is the product of the score  $s_t(c_i)$  for its translational component and  $s_r(c_i)$  for its rotational component. The scores depend on the weights of the neighbors for both cases; i.e.  $s_t(c_i)$  is the sum of scores for  $c_i$ 's neighbors in position inside a certain radius.  $s_r(c_i)$  is the sum of scores for the orientation weights around the sampled orientation. Note that the scoring process can also be easily extended to incorporate features like the distance to the nearest obstacle or a learned success rate.

To make sure only valid base poses (i.e. those that are not inside a wall or other obstacles), are generated from the base pose distribution we need to merge it with a map of the environment. In most robotic systems in use today, a 2D occupancy grid generated by a SLAM process is the representation of choice for those maps (see e.g. [9]). Because the occupancy grid map is used for navigation and localization, the base pose distribution obtained in the previous step needs to be aligned to it in terms of orientation and scale. This is easy to achieve with the kernel density estimation, as mentioned in the previous section.

As the kernel density estimation resulted in an approximation of a continuous probability distribution for viable base poses, we can sample it with the same resolution as any given occupancy grid map. Merging the grid map  $o$  with this base pose distribution  $d$  is then straightforward using the product rule.

### III. SHARING REACHABILITY MAPS

The RoboEarth project, described in [10], aims to provide a platform to share and exchange knowledge among robots. Among the information shared are descriptions of objects (e.g. feature descriptors for object detection), environments (semantic descriptions as well as occupancy grid maps) and robot descriptions (capabilities and components). Its backbone is a Apache Hadoop-based database, accessible via the world wide web<sup>5</sup>. The language used for describing the knowledge to be shared is based on the W3C standard OWL, and is described in [11]. Every piece of data stored on the database is annotated

---

```

Individual:
<http://www.robearth.org/kb/amigo.owl#AmigoArmLeft>

Individual: ReachabilityMap_11_07_29_15_08_35_185
Types:
  ReachabilityMap

Facts:
  providesReachabilityMapFor
  <http://www.robearth.org/kb/amigo.owl#AmigoArmLeft>,
  creationDateTime "11_07_29_15_08_35_185"^^xsd:string,
  workspaceCubeResolution 0.05f
  workspaceQuatResolution 0.25f
  workspaceApproxReach 1.26f
    
```

---

Fig. 3. OWL annotation for the reachability map of the AMIGO [15] robot's left arm.

with a semantic description using this language. A Sesame server [12] is integrated into the database, so that semantic and taxonomic queries formulated in the SeRQL query language [13] can be answered.

#### A. Storage in the Database

Robots and their capabilities are described by the Semantic Robot Description Language (SRDL, [14]) in our system. Compared to e.g. URDF (Unified Robot Description Format<sup>6</sup>) from the ROS framework, SRDL allows describing a robot's hardware parts in terms of its meaning and the capabilities it enables for the robot. As described in [11], it enables reasoning about the capabilities of a given robot platform in a specific situation, and inferring missing requirements to fulfill a specific task.

We store the binary reachability map file in the database, along with an annotation referring to the semantic robot description of the robot to allow searching using SeRQL queries. Fig. 3 shows an example of such an annotation.

This representation enables an effective sharing and exchange among robots. We show that by comparing its properties with the requirements formulated in section I:

- **Completeness:** The reachability maps represent a discretized version of the workspace with a given resolution. The experiments in the following section show that this approximation is sufficient to use for base placement tasks.
- **Representation Efficiency:** The choice of a compressed bit vector for representing the workspace results in file sizes in the order of magnitude of several hundred kilobytes. Files of this size can be transmitted over wireless networks in a matter of seconds.
- **Uniqueness:** While there can be multiple reachability maps for the same manipulator stored in the database, which might differ in resolution or only time of creation, every one is annotated with the manipulator ID and fulfills the uniqueness criterion.

Currently, there are multiple reachability maps for the PR2 and the AMIGO robot stored in the database.

<sup>5</sup><http://api.robearth.org>

<sup>6</sup><http://www.ros.org/wiki/urdf>

### B. Base Pose Correction for Manipulation Tasks

The small size of the workspace discretizations together with the expressive semantic description in the database allows for an efficient retrieval on demand during run-time. We make use of this circumstance in the integration of a failure handling method for manipulation tasks in the execution framework described in [16]. To recap shortly, abstract task descriptions are described in terms of OWL classes and instances which can refer to semantic descriptions of objects, robot descriptions etc. The task descriptions are translated to an executable robot plan in the robot plan description language CPL [17], based on Common Lisp. During execution, the sub-actions forming the execution plan are annotated with the OWL identifiers of the objects involved: e.g. the robot manipulator in manipulation actions, or the object class identifiers in object detection subtasks.

Manipulation tasks are prone to failure, in our experience, often due to an inability of the robot to reach to the target pose because of localization or navigation issues. We implemented a straightforward failure handling method to compensate for these problems making use of the database and the efficient workspace representation described in the previous sections.

If during task execution an error condition is signaled that represents an “cannot reach target pose” error, the implementation poses a SeRQL query to the database using the robot manipulator OWL id to retrieve a workspace discretization file. The query has the following form (namespaces have been omitted for conciseness):

```
SELECT source FROM CONTEXT source {S}
  rdf:type (re:ReachabilityMap);
  re:providesReachabilityMapFor {amigo:AmigoArmLeft}
USING NAMESPACE re=..., amigo=...
```

If no suitable workspace file is found, the action fails. Otherwise, a base correction pose is selected with the scored random sampling approach described in section II-D and the manipulation action is started again.

## IV. EXPERIMENTS

### A. Base Pose Estimation Method

This experiment tries to compare the base pose estimation method described in section II-D. The open source driver implementations for Willow Garage’s PR2 robot were used to simulate the robot during the trials. For each method, 1000 base poses were selected, with a reaching target in the origin of the world coordinate system and a random height offset and a random end effector orientation. After the robot was teleported to one of these base poses, the inverse kinematics solver was called to move the manipulator to the reaching target. A try was considered successful if the manipulator could be moved to the target pose.

Table I shows the results for both methods and several workspace resolutions. The resolution is given as the side length of the cubes and the number of sampled rotations (see section II-A) It demonstrates that the voted sampling approach described in section II-D has a significantly positive effect on the failure rate, when compared to the random sampling approach. It also shows the impact of different resolutions for the reachability maps; both the quality of the base estimation and the difference between random and voted sampling decrease with lower resolution.

TABLE I. BASE POSE SELECTION FAILURE RATES FOR DIFFERENT WORKSPACE RESOLUTIONS AND DIFFERENT BASE POSE ESTIMATION METHODS FOR THE PR2 ROBOT.

method	translational res.	rotational res.	failure rate
Random Sampling	0.05 m	576 rot.	0.179
Scored Sampling	0.05 m	576 rot.	0.003
Random Sampling	0.10 m	76 rot.	0.561
Scored Sampling	0.10 m	76 rot.	0.116

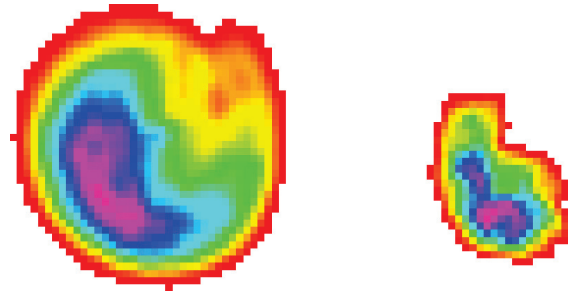


Fig. 4. Comparison of base pose distributions for PR2 (left) and AMIGO (right). Red stands for low, purple for a high density of base poses.

### B. Use Case: Robotic Handover

In this section, the experiment for showing a use-case for the approaches described in this paper is presented. Consider as a scenario two robots with different manipulators, where one robot is handing over an object to the other. To do so, both need to move one of their manipulators to approximately the same position. The problem is then to find base poses for both robots from which they can reach the handover position.

The two robot platforms used are the PR2 robot and the AMIGO prototype robot built by TU Eindhoven (described e.g. in [15]). Fig. 5 shows a visualization of both robots during a simulated handover. Because the AMIGO has a very limited workspace due to the fixed installation of the arms (see Fig. 4 for a comparison), this combination is interesting for the task at hand.

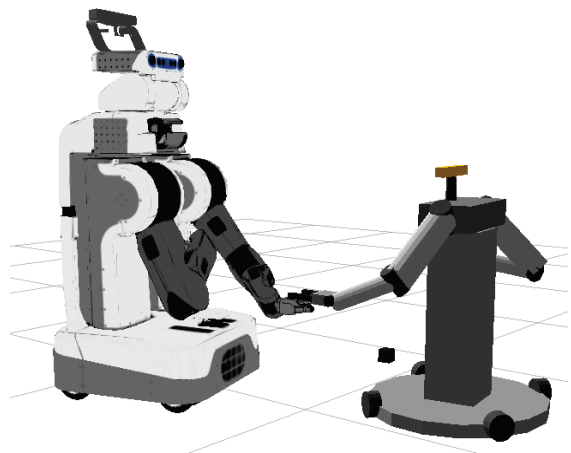


Fig. 5. PR2 (left) and AMIGO (right) during simulated handover with their left arm, respectively

As we do not have both robots available for use, the experiment is carried out in simulation. The experiment process is as follows:

- A handover height  $h$  is chosen randomly, such that there is at least one reachable pose in the workspace of both PR2 and AMIGO at this height. The reachable pose for the AMIGO is selected as  $p_{amigo}$ . The target reaching pose for the PR2  $p_{pr2}$  is defined as having an offset of  $-0.05$  m in  $z$  direction, while its orientation is rotated  $180^\circ$  around the  $z$ -axis.
- We generate base pose distribution maps for both target poses, using the respective workspace discretization for each robot. In order to avoid selecting base poses such that both robots stand on the same place, the distribution map for the PR2 is subtracted from the one for the AMIGO and vice versa. For each robot, 10 base poses are then estimated from the base pose distribution maps using the scored sampling approach from section II-D.

The process is repeated 100 times. In our experiment, the joint failure rate was 14.5%, where the rate for the AMIGO was 14.2% and for the PR2 0.3%. The difference between the failure rates for both robots lies in the fact that the validity for the pose estimated for AMIGO is checked first. If the first check fails, the trial counts as failed.

## V. CONCLUSIONS AND FURTHER WORK

We presented a system that efficiently discretizes the workspace of a robotic manipulator, and shares them to be used by different robots. We also described methods making use of them for estimating suitable base poses for reachability tasks. Two experiments were provided to show the validity of the approach, one of which was showing a possible use case for the work described in this paper. Overall, the system allows to discretize the workspace of a robotic manipulator once and store it in a space-efficient manner on a database, thus allowing an easy re-use for other robots or services.

A worthwhile idea for future work would be to integrate OpenRAVE's powerful *ikfast* [5] module, which allows generating analytical IK solvers from a manipulator's URDF description, onto the database servers. Using this module, the system could discretize the robot's workspace without requiring redundant information given by the user. To help with providing the semantic information necessary for the database, there are tools that are able to convert a URDF robot specification to a basic SRDL description.

We also strive for a deeper integration of the system into the knowledge representation framework, e.g. to be able to automatically infer that downloading the reachability map is necessary by integrating the system to make use of the capability matching using semantic robot descriptions described in [11].

## ACKNOWLEDGMENT

The research leading to these results has received funding from the European Union Seventh Framework Programme FP7/2007-2013 under grant agreement no 248942 RoboEarth.

## REFERENCES

- [1] S. Ruhl, A. Hermann, Z. Xue, T. Kerscher, and R. Dillmann, "Graspability: A description of work surfaces for planning of robot manipulation sequences," in *Robotics and Automation (ICRA), 2011 IEEE International Conference on*. IEEE, 2011, pp. 496–502.
- [2] F. Zacharias, C. Borst, and G. Hirzinger, "Capturing robot workspace structure: representing robot capabilities," in *Intelligent Robots and Systems (IROS), 2007. IEEE/RSJ International Conference on*. IEEE, 2007, pp. 3229–3236.
- [3] M. Beetz, U. Klank, A. Maldonado, D. Pangercic, and T. Rühr, "Robotic roommates making pancakes-look into perception-manipulation loop," in *IEEE International Conference on Robotics and Automation (ICRA), Workshop on Mobile Manipulation: Integrating Perception and Manipulation*, 2011, pp. 9–13.
- [4] F. Stulp, A. Fedrizzi, L. Mösenlechner, and M. Beetz, "Learning and reasoning with action-related places for robust mobile manipulation," *Journal of Artificial Intelligence Research (JAIR)*, vol. 43, pp. 1–42, 2012.
- [5] R. Diankov, "Automated construction of robotic manipulation programs," Ph.D. dissertation, Carnegie Mellon University, Robotics Institute, August 2010. [Online]. Available: [http://www.programmingvision.com/rosen\\_diankov\\_thesis.pdf](http://www.programmingvision.com/rosen_diankov_thesis.pdf)
- [6] A. Yershova, S. Jain, S. LaValle, and J. Mitchell, "Generating uniform incremental grids on so (3) using the hopf fibration," *The International journal of robotics research*, vol. 29, no. 7, pp. 801–812, 2010.
- [7] D. Scott, *Multivariate density estimation: theory, practice, and visualization*. New York: Wiley, 1992.
- [8] R. Detry, D. Kraft, O. Kroemer, L. Bodenhagen, J. Peters, N. Krüger, and J. Piater, "Learning grasp affordance densities," *Paladyn. Journal of Behavioral Robotics*, 2011.
- [9] S. Thrun, W. Burgard, and D. Fox, *Probabilistic Robotics (Intelligent Robotics and Autonomous Agents series)*, ser. Intelligent robotics and autonomous agents. The MIT Press, Aug. 2005.
- [10] M. Waibel, M. Beetz, J. Civera, R. D'Andrea, J. Elfving, D. Galvez-Lopez, K. Häussermann, R. Janssen, J. Montiel, A. Perzylo *et al.*, "RoboEarth," *Robotics & Automation Magazine, IEEE*, vol. 18, no. 2, pp. 69–82, 2011.
- [11] M. Tenorth, A. Perzylo, R. Lafrenz, and M. Beetz, "The RoboEarth language: Representing and Exchanging Knowledge about Actions, Objects, and Environments," in *Robotics and Automatic (ICRA), 2012, IEEE International Conference on*, Saint Paul, USA, 2012.
- [12] J. Broekstra, A. Kampman, and F. Van Harmelen, "Sesame: A generic architecture for storing and querying rdf and rdf schema," *The Semantic WebISWC 2002*, pp. 54–68, 2002.
- [13] J. Broekstra and A. Kampman, "SeRQL: a second generation RDF query language," in *Proc. SWAD-Europe Workshop on Semantic Web Storage and Retrieval*, 2003, pp. 13–14.
- [14] L. Kunze, T. Roehm, and M. Beetz, "Towards semantic robot description languages," in *IEEE International Conference on Robotics and Automation (ICRA)*, Shanghai, China, May, 9–13 2011.
- [15] J. Lunenburg, S. van den Dries, J. Elfving, R. Janssen, J. Sandee, and M. van de Molengraft, "Tech United Eindhoven Team Description 2012," in *RoboCup Team Description Papers 2012*, 2012.
- [16] D. Di Marco, M. Tenorth, K. Häussermann, O. Zweigle, and P. Levi, "Roboearth action recipe execution," in *12th International Conference on Intelligent Autonomous Systems*, 2012.
- [17] M. Beetz, L. Mösenlechner, and M. Tenorth, "CRAM – a cognitive robot abstract machine for everyday manipulation in human environments," in *IEEE/RSJ International Conference on Intelligent Robots and Systems*, 2010.